Title
Metal-Organic Framework-Based Colorimetric Gas Sensors toward an Improved Indoor Air Quality Monitoring

Author
Davey, Adrian Kentrell

Publication Date
2023

Peer reviewed|Thesis/dissertation

Metal-Organic Framework-Based Colorimetric Gas Sensors toward an Improved Indoor Air Quality Monitoring

by

Adrian Davey

A dissertation submitted in partial satisfaction of the
requirements for the degree of

Doctor of Philosophy

in

Chemical Engineering

in the

Graduate Division

of the

University of California, Berkeley

Committee in charge:

Professor Markita Landry, Co-Chair
Professor Bryan D. McCloskey, Co-Chair
Professor Jeffrey R. Long

Spring 2023

Abstract

Metal-Organic Framework-Based Colorimetric Gas Sensors toward an Improved Indoor Air Quality Monitoring

by

Adrian Davey

Doctor of Philosophy in Chemical Engineering

University of California, Berkeley

Professor Markita Landry, Co-Chair
Professor Bryan McCloskey, Co-Chair

As respiratory illness infections and related environmental antagonisms continue to beleaguer our contemporary moment, the construction of low-cost, scalable, highly sensitive, remarkably selective, ultralow power, and user-friendly technologies for detecting hazardous chemical species indoors remains imperative. Namely, the accumulation of carbon dioxide (CO_2) and select volatile organic compounds (VOCs) in indoor settings is associated with deleterious human health conditions, such as fatigue, headaches, and irritation of the throat. While commercialized indoor gas detectors exhibit desirable analyte sensitivity and long-term sensing endurance, these devices characteristically suffer from cost, bulk, and power requirements. Toward addressing these limitations, this work introduces amine-functionalized, dye-loaded metal-organic framework (MOF)-based chemical sensors whose color change upon exposure to indoor analytes produces a more passive, smaller, cheaper, and simpler alternative to existing technologies.

In this dissertation, the iterative synthesis and spectroscopic characterization of color-based, MOF-based indoor analyte sensors are accomplished toward the realization of an ideal sensor for an improved indoor air quality monitoring. Chapter 1 situates the relationship among indoor CO_2 and indoor VOCs in the ongoing Coronavirus disease 2019 (COVID-19) pandemic, illustrating the range of detrimental realities for human and environmental health. To best articulate the stakes of structured public health violence, the chapter engages an interdisciplinary analysis of power in which antiblack worldbuilding is linked to previous, present, and emerging environmental violence and human unwellness. Once certain predatory formations are more concretely assigned answerability for air-based violence, the chapter closes with attendant scientific interventions and provides the rationale for the development of color-based chemical sensors to preempt adverse exposures to indoor analytes.

Abstract

Chapter 2 introduces a first-generation colorimetric gas sensor composed of a MOF, primary amine, dye, and methanol blended, drop-cast on cellulose filter paper, and exposed to indoor levels of CO_2 (700 parts per million, ppm, and up). Here, the pristine MOF—the zeolitic imidazolate framework-8 (ZIF-8) consisting of zinc (Zn^{2+}) cations tetrahedrally coordinated by 2-methylimidazolate ($Hmim^-$) organic linkers—serves as the highly-porous adsorbent with known physisorptive affinity to CO_2. Following its unstirred, room temperature synthesis, ZIF-8 is blended with the primary amine, ethylenediamine (ED), and the dye, phenolsulfonpthalein (PSP, or phenol red). The capacity of the resulting sensor, termed PSP-ED/ZIF-8, to effectively function in plausible indoor air conditions is probed via several characterization techniques. Powder X-ray diffraction (PXRD) is used to demonstrate the long-term chemical stability of ZIF-8 in the basic environment created from the addition of ethylenediamine. Moreover, scanning electron microscopy (SEM) is used to define the morphological properties of PSP-ED/ZIF-8 in relation to the molar ratio of the ZIF-8 metal : ZIF-8 linker : methanolic solvent precursors, as well as the post-synthetically incorporated colorimetric ingredients. A LabView-enabled gas dosing apparatus (coupled with a nondispersive infrared, NDIR, gas sensor to substantiate gas levels, humidity, and temperature) is implemented to deliver a range of CO_2 levels (700-7,500 ppm) under various humidity (0-80% RH) at room temperature to PSP-ED/ZIF-8 drop-cast on cellulose filter paper. Through smartphone video recording, qualitative assays of gas-exposed PSP-ED/ZIF-8 are collected, with an increasing intensity of the fuchsia-to-yellow color change observed with increased concentrations of CO_2. In realizing that the perceived color change is only permissible in the presence of the MOF, Brunaeur-Emmett-Teller (BET) surface area analysis is performed to evaluate the role of high surface area on ZIF-8's ability to accommodate both ethylenediamine and phenol red, as well as provide sorption sites for indoor CO_2. Finally, an *ex-situ* ultraviolet-visible (UV-Vis) diffuse reflectance spectroscopic technique is achieved to quantify how the Kubelka-Munk, F(R), values at 443 and 570 nm resonant with phenol red change relative to each other as the concentration of CO_2 and humidity levels are modified. Despite immediate and increasing responses of PSP-ED/ZIF-8 to 700 ppm CO_2 (and up) in dry environment, qualitative color assays and quantitative UV-Vis measurements exhibit a largely suppressed color change in the presence of humidity. To improve the colorimetric gas response across humidity, a revised sensor recipe is accomplished.

In Chapter 3, an enhanced colorimetric indoor CO_2 sensor is attained through the direct incorporation of phenol red into the ZIF-8 metal and linker precursor broth. The orange crystals formed, PSP:ZIF-8, are then blended with ethylenediamine to form a second-generation sensor, ED/PSP:ZIF-8. Collected PXRD patterns, as well as Fourier transform infrared (FTIR) spectroscopic transmittance scans, confirm the structural integrity of ZIF-8 in both PSP:ZIF-8 and ED/PSP:ZIF-8. In addition, SEM and transmission electron microscopy (TEM) demonstrate the fourfold increase in size of ZIF-8 crystals upon growth in a phenol red-loaded methanolic precursor mixture (compared to the PSP-ED/ZIF-8 first generation chemical sensor). Reimplementation of the LabView-based gas apparatus demonstrate a significantly more intense fuchsia-to-yellow color change of the ED/PSP:ZIF-8 sensor than the PSP-ED/ZIF-8 sensor upon exposure to indoor CO_2 levels (600 ppm and up) across humidity (0-80% RH). To better elucidate these assays, the smartphone-gathered images are read into a MATLAB script and decomposed into their respective red-, green-, and blue (RGB) distributions, which both confirms a stronger color change in the second-generation sensor *and* enables a reasonable approach with which to

index color change data for the optimal indoor gas sensor. In addition to this approach, an *in-situ* UV-Vis diffuse reflectance spectroscopic technique is developed in which room-temperature Kubelka-Munk spectra at 443 and 570 nm are *directly collected* as indoor levels of CO_2 are exposed to both first- and second-generation sensors across humidity, as well as in the presence of VOCs (acetone). Consistent with the qualitative assays, ED/PSP:ZIF-8 exhibits a stronger color change than the first-generation sensor in dry CO_2, CO_2 and VOC environment, and humid CO_2. However, compared to its dry CO_2 and CO_2+VOC colorimetric response, ED/PSP:ZIF-8 still displays a noticeably suppressed color change at heightened humidity. To initially determine differences in the sensing performance of the first- and second-generation sensors, washing studies are conducted in which both sensors are successively washed with methanol. Upon collecting FTIR spectroscopic scans with each wash, the nitrogen-hydrogen (N-H) stretching vibrations indicative of ethylenediamine disappear in both sensors, which suggests the localization of ethylenediamine to the external surface of ZIF-8 in both sensors. Similarly, in a second washing experiment, both sensors are washed with methanol and replenished with (i) fresh methanol, (ii) fresh methanol and ethylenediamine, and (iii) fresh methanol, ethylenediamine, and phenol red. Upon being replenished in these three ways, both sensors are exposed to dry CO_2. Neither sensor responds to CO_2 upon sole replenishment in methanol, which reaffirms the probable location of ethylenediamine to the external surface area of ZIF-8. However, when both sensors are washed and replenished with an ethylenediamine methanolic solution, only the ED/PSP:ZIF-8 sensor recovers its original color change (whereas the PSP-ED/ZIF-8 sensor does not). Once both phenol red and ethylenediamine replenish the sensor (in methanol), the PSP-ED/ZIF-8 partially recovers its colorimetric gas response from its fresh state. These observations imply that phenol red is located on the external surface of ZIF-8 in the first-generation sensor (but inside the internal pore cavities in the second-generation sensor). Given the unresolved hypothesis of phenol red location between both sensors (as well as how phenol red binds to ZIF-8 in general and the underlying chemical sensing mechanism informing the color change), mechanistic studies are pursued.

Chapter 4 details an exhaustive set of spectroscopic analyses used to (i) distinguish the first- and second-generation colorimetric gas sensors and (ii) examine the role of surface basicity (or inclusion of ethylenediamine) on the thermodynamics of phenol red adsorption to ZIF-8 for colorimetric indoor analyte monitoring. The first half of this chapter involves the use of carbon, hydrogen, nitrogen, and sulfur (CHNS) elemental analysis to discern how much phenol red adsorbs to ZIF-8 between the first- and second-generation sensors. A gas-dosed FTIR spectroscopy is later implemented to investigate the physisorptive and chemisorptive nature of ZIF-8 and ethylenediamine-modified ZIF-8 exposure to dry CO_2. The second half of this chapter uses a liquid-phase UV-Vis spectroscopy to distinguish the adsorption isotherms of room temperature phenol red adsorption onto ZIF-8 (with and without ethylenediamine). In addition, FTIR spectroscopy is implemented to discern whether the presence of ethylenediamine controls how phenol red binds to the ZIF-8 adsorbent. This chapter concludes with an introduction of second-harmonic spectroscopic techniques to evaluate the Gibbs free energy of adsorption (ΔG_{ADS}) of phenol red to ZIF-8 (with and without ethylenediamine) to illustrate how the components of the "full" colorimetric gas sensor interact to bind indoor CO_2. In addition, X-ray photoelectron spectroscopy (XPS) is briefly discussed toward evaluating MOF/dye/amine interactions.

Once the internal workings of the previous sensors are elaborated, Chapter 5 describes a third-generation sensor prepared from the admixture of ZIF-8 species crystallized from precursor

solutions blended with different dyes. Specifically, a universal pH indicator (mixed with phenol red) produces an improved sensor with a strong colorimetric CO_2 response in low and intermediate humidity. To simulate indoor air conditions more closely, this sensor is exposed to CO_2, humidity, and acetone, and its response is quantified via an *in-situ* UV-Vis diffuse reflectance spectroscopy.

Chapter 6 completes the dissertation with a summary of key results and recommends future studies involving multi-color, multi-transduction MOF-based analyte sensing.

This work presents a novel, proof-of-concept colorimetric sensor whose optimization and characterization are accomplished through coupled spectroscopies toward the eventual creation of an ideal indoor analyte sensor for widespread use.

Table of Contents

Table of Contents

Table of Contents

Table of Contents

Acknowledgements

In typical Adrian fashion, anybody who knows me can anticipate what will be written here. Y'all know what it is lol.

I want to first start off by thanking my labmates (graduate researchers, postdoctoral researchers, and undergraduate researchers) whose brilliance, meticulousness, and care made this dissertation possible. Firstly, I would like to thank Dr. Steven Delacruz. When I was still very new to graduate school, you spent a lot of time with me to ensure that my UV-Vis measurements proceeded smoothly using the LabView system (and asked me important chemical engineering questions about reversibility, equilibrium, etc. with respect to the colorimetric gas sensors and the *ex-situ* gas dosing technique). More than that, though, you were a warm, attentive person who invited me into conversation every day and became someone with whom I constructed a meaningful, long-lasting friendship. Thank you for your efforts toward building community within the lab and for being interpersonally committed to all of us. (And let's be clear: them cakes from Sheng Kee BAKERY? Absolutely delicious every time). Thank you for the *many* Zoom calls and checking in on me after you graduated and affirming me. From conversations about our favorite manga to favorite food to the unremitting violence in the World, I sincerely appreciate more than you know. Thank you to Dr. Leslie Chan for welcoming me into the lab right after my prelim exams and being so encouraging as I first began my research journey here. Thank you to Dr. Zhou Li, Dr. Aifei Pan, Dr. Yong Xia, Dr. Sikai Zhao, Dr. Yuhui Xie, and Dr. Siyi Cheng for your critical research support, delicious meals together, cherished laughter, and compassion. To Isaac Zakaria: thank you for all the rich conversations, for literally saving me mid-UV-Vis experiment when the UV-Vis enclosure was stuck (I was shook because you know I needed those data LMAO), and your support of undergraduate researchers within the group. I am so proud of not just your commitment to practicing rigorous science, but to living with a certain ethics that compels you into action. Thank you to Dr. Yaprak Ozbakir and Dr. Jihoon Chung for your tremendous help with my metal-organic framework research, warmth, and genuine conversations. Thank you to Alireza Pourghaderi for your *realness* (not too many people can claim that in the College of Chemistry…yeah, I said it lol), research support with all the colorimetric imaging using the LabView apparatus, and support with co-facilitating the FTIR spectrometer at the Catalysis Center. You really showed up for me (and Isaac) in the strongest way (even when you were at risk in the process), and I can't thank you enough for what you did for the both of us. Thank you to Stuart McElhany for your help with running the FTIR spectrometer at the Catalysis Center and with collecting SEM images for the multi-generation colorimetric gas sensors. Thank you, also, for many conversations that I found very important.

Mentorship is an experience of building unique, wonderful bonds that I immensely cherish. As a mentor, it is not just truly rewarding to watch your mentee grow in holistic ways, but to also experience learning *from* and *with* your mentee. Throughout this doctoral journey, I was truly

grateful to have met and grown alongside five amazing scholars. Thank you to Sanket Swamy for working with me on developing the first-generation colorimetric gas sensor and collecting the UV-Vis diffuse reflectance data for our first article published in 2021. Thank you to Tayler Hunter for your incredible work on the third-generation ZIF-8-based colorimetric gas sensor using UV-Vis diffuse reflectance spectroscopy and FTIR spectroscopy. I am so proud of you for going to Anaheim in Fall 2022 and presenting your work at the Annual Biomedical Research Conference for Minoritized Scientists (ABRCMS), as well as your fantastic leadership in the Black Students in Health Association (BSHA) at UC Berkeley in which you connected Black scientists across the Bay Area. Thank you to Ishan Gupta for your Python-based colorimetric analysis scripts, inquisitive character, candor, and many shared laughs. Thank you to Kushaan Bahl for your incredible work in Summer 2021 studying ZIF-93-based colorimetric gas sensing, always asking fantastic questions, and seriously attending to the social dimensions of this research. Finally, I would like to thank Cameron Mollazadeh, a student whom I had the pleasure of GSI'ing in Spring 2021 in Chemical Engineering Thermodynamics and mentoring thereafter. You are a fantastic researcher (shout out to you also for presenting at ABRCMS in Anaheim!) and an extremely caring person who thinks critically about how to show up real beyond academia. Keep being you!!

Thank you to all my research collaborators who made my research possible. IMMENSE SHOUT OUT to Natalie Lefton and Branden Leonhardt for helping me set up my carbon dioxide and acetone cylinders with your *in-situ* UV-Vis spectroscopic instrument. (Chapter 2, Chapter 3, Chapter 4, and Chapter 5 *deeply* rely on this technique, so thank you so much)! Thank you to Matt Dods, Dr. Katie Engler, and Dr. Michael Ziebel of Professor Jeffrey Long's research group for assisting me with understanding inorganic chemistry related to my research, assisting with PXRD pattern collection, and preparing me for my qualifying exam in September 2020. Thank you to Dr. Hendrik Ohldag for introducing me to NEXAFS and helping me concretize efforts toward elucidating the chemical sensing mechanism of my dye- and amine-loaded MOF-based sensors. Thank you to Dr. Andreas Siebert and Mario Gotters for assisting me with late-night XPS spectra collection using the synchrotron radiation at BL 11.0.2 at the ALS in Fall 2022. Thank you to Dr. Derek Popple, Dr. Chunhui Dai, and Dr. Salman Kahn for helping me collect SEM and TEM images toward differentiating the first- and second-generation sensors. Many thanks are given to Dr. Elena Kreimer of the Microanalytical Facility, who collected CHNS elemental analysis data to quantify phenol red adsorption onto ZIF-8 (across sensor generations) and to evaluate dye/MOF adsorption differences with and without ethylenediamine. Thank you to Dr. Nick Settineri for assisting me with PXRD pattern collection at the CheXray facility in the College of Chemistry. Thank you to Dr. Chithra Asokan for being an AWESOME manager of the UC Berkeley Catalysis Center and actively constructing a network of graduate students with training on various spectroscopic techniques toward advancing modern chemical research. I thoroughly enjoyed teaching other folks how to collect FTIR transmittance spectra and interpret their results. Thank you also for teaching me how to use the variable temperature UV-Vis spectrophotometer toward understanding the adsorption thermodynamics on dyes onto ZIFs for colorimetric indoor gas detection. I also thank Liana Klivansky of the Molecular Foundry for training me on the use of BET surface area characterization tools toward clarifying the critical function of ZIF-8 as the adsorbent species for colorimetric gas monitoring. Many thanks are given to Erika Riffe, who introduced me to second harmonic spectroscopic techniques (which can do REALLY COOL

STUFF that I still am so curious about)! I am so excited to see what you will continue to learn from this technique related to dyes, MOFs, and amines. Thank you for enriching scientific conversations and being a truly wonderful person. Thank you to Hanxiao Liu, who I met after a Berkeley Sensor & Actuator Center (BSAC) presentation and provided me with critical insights toward hydrophobizing my indoor carbon dioxide sensors to minimize humid interference.

I want to use this space here to personally thank all of my research mentors. Thank you first to Dr. Bruce Shapiro, who welcomed me into your lab when I was sixteen-years-old to study ribonucleic acid structure prediction (2013-2014). I still remember just finishing AP Chemistry and being extremely enthusiastic to apply what I had learned into my first research endeavor (and this one involved CODING)! Thank you for writing letters of recommendation for me and being involved in my research journey a whole decade later. Thank you to Professor Christopher Hennigan, who served as my principal investigator for my sustained research in aerosol chemistry at UMBC (2015-2018). I really appreciate your support as I navigated my undergraduate career, especially as I was performing the daunting task of selecting, applying, and visiting graduate programs. Thank you to Dr. Erin Lavik for MANY things. You gave me really affirming feedback when I discussed the energy-based research I did in Berkeley in 2017. In this same class, you had us do an exercise that made us really sit with our sense of purpose, as well as to whom we're committed and with whom we build community. Thank you for constantly checking in on me, introducing me to Dr. Stian Rice (who's also AMAZING), being candid with me about so many topics, sincerely listening to me, and always showing up with fervor toward helping. As someone who's also taking COVID-19 very seriously, it meant a lot that William appreciated that I wore a mask during my colloquium presentation (and that William understands the significance of COVID-conscious existing from a disability justice perspective). Thank you to you and Stian for providing me with so much advice regarding post-graduate life (especially related to a possible future in the academy). Thank you to Dr. Xiang Gao, my research mentor when I first started graduate school. Having known nothing about MOFs (as well as most of the techniques associated with their characterization), I really appreciate your commitment to teaching me, guiding me, and encouraging me shortly before your graduation. Thank you to Dr. Monika Blum, who met with me many times to discuss my research project, develop XPS experiments toward differentiating the first- and second-generation sensors, and assigning me beamtime for such experiments. Connecting with you, visiting the ALS, and working with X-rays were truly some of the highlights of this Ph.D. (Thank you also for giving us the leftover Halloween candy as we did this very long experiment)!! I am very excited to read more about the work that is done at BL 11.0.2 using the liquid jet technique! Thank you to Professor Bryan McCloskey for what was my favorite research summer *ever* in 2017 in which I studied photo-electrocatalysis and used all of the thermodynamics and kinetics knowledge that I learned during my junior year of college. Thank you for writing letters of recommendation, caring about my research, welcoming me into your lab after I was kicked out of mine *with eight months left to graduate* (**reader: we will return to this ejection because WHEW CHILE),** and providing me with resources to finish all the characterizations I needed to write this dissertation. Thank you to Professor Jeffrey Long for inviting me to build great relationships with your students, sharpening my inorganic chemistry knowledge, welcoming me to use your characterization techniques, and encouraging me to use advanced techniques to answer critical questions related to dye/MOF location for colorimetric gas sensing. Thank you to

Acknowledgements

Professor Kwabena Bediako for welcoming me into your office in late 2019, being interested in my work, and offering support. I really appreciate your engagement during my qualifying exam in 2020.

As a Black graduate student, it is quite difficult to have meaningful support within antiblack institutions such as the University of California. While I was here, I encountered multiple Black faculty who demonstrated a genuine care for me. Thank you to Audrey Knowlton for calling me years ago in early 2017 to welcome me into the Amgen Scholars Program, which was the first time I really got to see the West Coast. You've been the embodiment of kindness: every time we speak, I feel absolutely loved, heard, and affirmed. Thank you for the meals at Angeline's Louisiana Kitchen, opportunities to meet with other Black scholars, and conversations both on Zoom and in-person. Thank you to Dr. Brice Yates for being the first person within the College of Chemistry who *got it*. Wasn't afraid to say "antiblackness" or "white supremacy," and who challenged the College of Chemistry on its insufferable, paternalistic white progressivism. Thank you for organizing virtual space for the Black graduate students of the College of Chemistry to assemble and freely share our thoughts about this antiblack environment. I appreciate the phone calls and Zoom calls that you routinely made time for to check in on me. Thank you to Professor Cesunica Ivey, who is truly *the* example of the type of Black professor I wish I had encountered before the end of my degree. I wept in the late afternoon talking to you because I was used to being scolded for my political worldview (sometimes from other Black administrators/faculty committed to respectability). However, not only did you affirm me, but you took me seriously as a co-intellectual and created space for us to be honest about the antiblack World. Thank you for being transparent with me, for attending my colloquium presentation, and affirming me through it all.

During my doctoral experience, I encountered multiple reasons worth risking repeatedly. In addition to the state-based violence enacted during the ongoing COVID-19 pandemic—leaving most folks vulnerable to food and housing precarity—the antiblack, ableist, queerphobic, classist, and xenophobic commitments of the University of California compelled me and others to strike *twice*: #COLA4All (2019-2020, starting at UC Santa Cruz) and the SRU-UAW statewide strike (November – December 2022). While many of my colleagues in the College of Chemistry chose to preserve white supremacist decorum and direct their attention to holiday parties, "wine and cheese" events, insincere recruitment weekends, and Chem Keg events (while scarcely intervening upon any of the violence within and beyond the department), some of us chose to risk (even when our careers were absolutely compromised in the process). I would like to first thank Black graduate students across the University of California who collectively named the antiblackness within the union *and* challenged the multiracial coalitionist betrayals characteristic of the antiblack progressive market of California. Moreover, I want to thank said Black graduate students for refusing to adopt analyses that mystify Black suffering and instead studying and absorbing Black radical politics attendant to the abolition of the University (and, of course, the abolition of "the World"). Thank you to Gene, Shah, Semassa, and Xavier for the multiple meetings, laughs, and collective thinking. Thank you to Juleon for your amazing efforts around the "No" vote campaign and connecting folks across departments across the campus. Thank you to Zein for carrying that *iconic* megaphone and being unapologetic about the antiblackness of the university and the union (are these two entities even dissociable at the end of the day? They both are antagonists to

Blackness…OOP)! The flowers you gave me were beautiful; the hugs we shared (and will continue to share) are full of warmth. Thank you for inviting me over to have a wonderful meal. (As I type this message, I look forward to our anime night)! You are brilliant, kind, and sweet, and I am immensely grateful that we met in this life. To Tenley—you are truly one of my faves. Since connecting in the Twitter Space years ago, I have really appreciated our continued political growth together. Thank you for exchanging voice notes with me routinely (you know I LOVE a voice note)! Your laugh brings me a lot of joy and I really enjoy spending time with you. Thank you for making time to rewatch movies in our adulthood (like *Antz* and *The Hunger Games*) and juxtapose our present thoughts with those from when we were younger (and possessed different political understandings). The card you gave me the day of my colloquium presentation was incredibly sweet. Thank you for driving from Santa Cruz to support me in person. :)

Thank you to the four people within the Department of Chemical & Biomolecular Engineering who showed up and did the damn thing in ways that *nobody* else would: Helen Bergstrom, Dr. Anthony Abel, Jeremy Adams, and Joshua Hubbard. Since my early days in this program, we worked together to name violence and manifest better realities for graduate students in ways to which many folks were hostile. We've been gossiped about, screamed at, lied on, exiled, surveilled, and worse. Helen, thank you for being the **ONE** person in our cohort who really cared about me—seriously. Thank you for remembering my birthday and bringing cupcakes. Thank you for inviting me to celebrate your birthday. Thank you for reminding me to rest. Thank you for organizing with me in #COLA4All and the 2022 strike. Thank you for your *integrity*—something that most folks are lacking. Anthony, thank you for your humor, for your *tremendous* efforts to get us paid more (because faculty members are just soooo benevolent and seek to ensure we have a livable wage without us demanding such, right????), and for deeply understanding the role of political education. Jeremy, thank you for your kind energy, support in both strikes, and political education commitments. Thank you to Katie Latimer for leading the #STEM4COLA space in 2020 and leading important teach-ins on the function of the University. Thank you to Marcelo Garzo Montalvo for organizing with me in #STEM4COLA, introducing me to Science and Technology Studies, teaching me about the origins of Ethnic Studies at UC Berkeley, informing me about the origins and objectives of the Westernized university, and thinking collectively about what "the sciences" mean to us. Thank you to Xóch for connecting with me outside of Stanley Hall and supporting the "No" vote strike folks. More so, thank you for the conversations about abolition of the state and what's necessary of us in this ever-expanding hellscape. Finally, I want to thank everybody involved with #COLA4All Strike University (2020) and the "No" vote strike squad (2022). Thank y'all for refusing to defend that which can't love us (but can *only harm us*)—the University.

When I moved to Berkeley in August 2018 to commence this Ph.D. in Chemical Engineering (an interesting life choice, right?), I attended Black Graduate Student Orientation within the first week of arriving. That single event was probably the most important decision of my life between 2018 and 2023. In attending that event in early August 2018, I befriended Black people with whom I forged community as I then dwelled some 2,700 miles away from my hometown. To Angélica M. Pagán, thank you for the many ki's, trips to Cheesecake Factory, driving down the Pacific Coast Highway to see all of California, and scolding me for "always being in that damn lab" (LMAO)!

(And yes, I saw you said some "Dexter's lab" in the Zoom transcript of my colloquium sksksksksksk). I am so excited to see you again soon on the East Coast! Thank you to Christian White for your beautiful laughter, fellow anime stanning, campus leadership, and kindness. Marsalis Gibson, Soliver Fusi, and Raymond Blackwell: thank y'all for all the work we did together as MARS. The meetings, mourning, laughter, silence… everything meant and still means so much to me. Shout out also to Debra Gore-Mann and Adele Caballero for your support of Black graduate students in STEM navigating the unethical domain of our educational spaces. Darius Gordon, thank you for the amazing vacation in Jamaica, watching HTGAWM, and having all the Zoom ki's. You made being in California truly special for me. Thank you to THEE Dr. Henry L. Washington, Jr.—you were one of the first people I met in California. You challenged me to grow in so many ways, and I am so thankful for you. You are hilarious, loving, brilliant, and attentive. I am so proud of you and look forward to linking again once I return to the East Coast! To Reuben Hogan, Kai Littlejohn, and Taylor Harris: thank y'all so much for the LITTEST summer in 2017 and supporting me (I still can't believe we did a whole photoshoot at UCLA on our way to get late-night snacks. Truly iconic). Tara Montgomery, thank you for the Friday burrito nights at Ida L. Jackson House (and literally saving me from getting hit by a car)! I was so glad that you could make my colloquium in person, and I appreciated your warm hugs. Thank you to Ean Hall, Shaniqua Cartwright, Devin Guillory, Letitia Carpenter, and Sharifa Taylor for the meals had together, nights spent together (in Berkeley, Oakland, and LA), and showing up to events I was hosting with all the love and support. Thank you to Donez Horton-Bailey for both in-person and virtual support as we navigated this Ph.D. Dr. Josiah Yarbrough—as soon as I met you during the Stanford visit weekend in early 2018, I knew we'd be friends. You are incredibly funny (with the best laugh ever), you are kind, you are brilliant, and you are very genuine. (We really shoulda ended up in the same program)!!! Thank you for supporting me in all the ways and always making time to catch up and affirm each other. Thank you to Kristen Gardner for your support as a fellow Graduate Student Mentor in the SEED Honors Program, as well as constantly sending kindness my way. Thank you to Christian Hosam and Norris Davis for the laughs and love sent (in-person and via Instagram). Thank you to Reubén Perez for being so kind and talking manga and supporting me with incredibly affirming messages. To Naomi Yonas: you are a younger sibling to me, and watching you grow has been amazing. You challenge institutions; you are a scholar and you have an immense love for Black folks. Each day, you make me proud. Thank you for supporting me in myriad ways. To Dr. Meron Tesfaye, thank you for truly loving me: for introducing me to Black folks across the Bay Area, discussing our dreams, holding each other (literally), and discussing the latest episode of The View (you know I could write a *whole* dissertation on that show LMAO). Thank you to Professor Faheemah Mustafaa for being in community with me and affirming me as I navigated the antiblackness of California. Thank you to Dr. Oyinkansola Romiluyi for affirming my sense of direction regarding this PhD, guiding me, affirming me, hugging me, externalizing our feelings together, and encouraging me through everything. Thank you to Lorenzo Washington for the iconic photoshoots, welcoming me (and others) into your house for food and drinks, experiencing that period we went to the movies and saw everything in 2019, discussing lots of anime and manga, grubbing all the time together, and the many conversations. Thank you to J'Anna Lue for reminding me to TAKE A NAP (I know you're laughing reading this skjsksksk). I deeply respect you for your honesty and thank you for the conversations about political struggle related to (and beyond) our disciplines. Thank you to

Acknowledgements

Lidya Gebremeskel and Ayah Hassan for cheering me on in my final years in the College of Chemistry and being so kind. Thank you to Robyn Jasper for spending so much time with me reflecting on antiblackness within the University, the Bay Area, and the World. I laugh a lot thinking about our earlier years at UMBC and how we'd always run into each other at the store. Thank you for being real as hell every time. I really appreciate you and can't wait to see you again :) Thank you to Holly Johnson for building community with me in my final years in the Bay Area, for organizing with me, and for all the lovely voice notes. Thank you as well to every other Black person in the Bay Area who changed my life in all the ways from our connection(s).

MANY THANKS are given to the Black communities which I formed at my undergraduate institution, the University of Maryland Baltimore County (UMBC). Thank you to Keith McNamara, Jr.—my bestie, fellow Wawa sub sandwich consumer, sweet friend, sharer of many laughs, brilliant thinker, fellow photoshoot-er (and we ate EVERY TIME!), and more. There are so many memories we have, and I am so glad we met in the Summer of 2014. Thank you for ALWAYS being there, always cheering me on, challenging me, being real as hell, encouraging me to rest, inviting me to chill at your house, sharing commentary on every movie we saw, and having serious conversations about what it meant to navigate the world as Black folks. Thank you to Nahum Meherete: a beautiful friend whom I first encountered in Susquehanna Hall full of jokes and a care for community grounded in love. Thank you for always making time to hang out (throwback to the three nights you, Keith, and I went to Arundel every day because why tf not?), supporting all the events I was involved in (during and post-UMBC), the many Zoom calls while I was in grad school listening to and affirming me and inviting me into new events happening in your life, all the conversations about manga and anime (yes, I'm still behind on *One Piece*), and candid conversations also about this antiblack World. (Now, I *do* believe that you are responsible for the anti-Frederick County disposition at UMBC, but—as the scholars say—that matter is "beyond the scope of this dissertation"). Thank you to Georgina Stephanie—chile, where do EYE BEGIN? You are an icon, a legend, the moment… wow. From the iHop ki's to the phone ki's to the Zoom ki's to navigating UMBC Chemical Engineering (whew chile *again*) to sharing pretty much every meme from *The Real Housewives of Atlanta*—thank you for literally being the sweetest friend. I thoroughly enjoying being in your presence and I can't wait to reunite and spend a day in the bookstore: flipping the pages, smelling the books, sharing the ones we've selected with each other. To Jessica M. Vaden: GWORL!!!! A Scorpio icon, a chemical engineer, a dancer, a BAKER, a community builder… you are that gworl, TRULY. Literally since the summer of 2014, we've had many amazing times together (and one thing about it—we were gon end the semester with a piggyback picture)! I'll never forget when a snowstorm hit Maryland *right before* we left for the NSBE National Convention and you told me to calm down and get myself together. Thank you for that, and for reminding me to *live*. Thank you for inviting me to sit with the things you're navigating, too, and sending me all the affirming voice messages and prayers. I look forward to the day we are on stage together again (hey, Pangea)! I love you deeply <3 Thank you to my mentee and whole child, Howard Nicholson, III. When I was first assigned to be your Meyerhoff peer mentor in 2016 and I met you, I knew that this relationship wasn't going to be a conventional mentorship about excelling as a student, getting internships, and finding grad school programs. I knew that we would be family, and I thank you for being so loving, so phenomenal, and so hilarious. You make me so proud every time we talk. I admire your commitment to

community: family, friends, and others. You have *no idea* how shook I was when you appeared in the colloquium room during my presentation. I wish nothing but for more love to embrace you in this left (and the next). Many thanks to Abenezer Wudenhe and Meshach Hopkins, my fellow M26 cohort members with whom I built amazing memories in college and who continued to show up for me post-undergraduate. Thank you both for the Zoom calls we did throughout the (ongoing) pandemic: holding each other, sitting in silence, reflecting, and growing. Y'all move with such love that inspires and moves me. Thank you to my mentors, Dr. Matt Shirley and Dr. Kendall Queen (aka DeeJay Q), for making my UMBC experience lit as hell *and* checking in on me after y'all graduated and after I graduated. Thank you, Matt, for making sure that I succeeded academically at UMBC and for affirming when I confided in you about antiblack professors. You're a fantastic listener and you are wise as hell and I grow so much every time we chat. And KENDALL—now. The way you are THEE DJ of all time. My on-campus birthday party all them years ago was absolutely one of the best birthdays I ever had. Thank you for welcoming me to come visit y'all in Philly right before I graduated from UMBC in 2018. You've constantly been someone who instills joy in my life (and the lives of others). Thank you for making time to process so much with me (and Matt, Jessica, and Keith) over Zoom in the years following UMBC. Thank you to my Meyerhoff Summer Bridge Mentors, Mayowa Balogun and Dr. Niambi Brewer, who routinely checked in on me during this Ph.D. and provided powerful advice as I navigated this (scam) called "the twenties." Thank you also to Dr. Gwenaëlle Thomas for rooting for me since I was seventeen at UMBC (I still remember you coming to our freshman seminar and saying one of the realest things I'd ever heard and remain glad that you said and that I heard). You are amazing in all the ways, and I am incredibly inspired by the myriad ways you advocate for Black STEM scholars *everywhere* both virtually and in-person. Thank you to Dr. Lydia Grmai for so many things: one of my favorite memories is sitting with you outside after you and fellow Meyerhoff alumni came to speak with us, and I shared several misgivings I had. You were incredibly affirming and really lifted me up. I am so appreciative of how you've shown up for me in grad school: every meme sent via Twitter and IG, every text, every email, everything. You are phenomenal! Thank you to Dorian Frazier for all of the memes, screenshots (IG/Twitter sksksksks), and honest conversations about the academy. I strongly admire your clarity, compassion, and courage. Thank you for sitting with me and refusing to mystify *why* academia (among everything else) *must be abolished*. Thank you to Kelsi Lawson for all the kind things you said to me about being your TA, for cheering me on throughout this Ph.D., for attending my colloquium, for helping me with job applications, and for having incredibly sharp political analysis. Thank you to Lauren Robinson for being the keeper of the "mfn goodz," a NSBE icon, a UMBC icon, and a genuine soul committed to establishing sincere Black community wherever you are. I am so glad that you are in my life! I would like to thank everybody in the UMBC chapter of the National Society of Black Engineers (NSBE) with whom I had (and have) beautiful community. I would like to thank the UMBC Meyerhoff Scholars Program for preparing me to pursue a Ph.D. in Chemical Engineering and connecting me with amazing Black folks with whom I would have community. Special thanks are given to Mrs. Earnestine Baker, with whom I've shared delicious meals (hey Angeline's, again!) and been vehemently supported for years now. One thing I know for sure is that you are incredibly protective of us and will say *anything* to *anybody*: don't care if it's a president, chancellor, etc. (pretty iconic, if you ask ME!) Thank you for caring about me, sending many text messages, having many phone calls… I tell my parents all

the time what you told me when I told you I was headed to UC Berkeley. Everything you said was true. <3

Here, I would like to thank my friends across the globe! Thank you to Cearrah L. Sherman for being an amazing friend since high school: inviting me to the house to cackle and eat (and watch me fall asleep half-on-the-couch), having fun at all the track meets, preparing for the Mr. TJ competition (there is so much to be said about that night and the choreography we REHEARSED, okay?!!), the trips to Salisbury, watching *Brotherly Love* too many times (lol), and the many iHop missions. Thank you to Khiarra Watkins for being a great friend since high school and processing with me what it meant to navigate STEM as Black folks. Thank you to Marcus thee Sowell for the many memories since Ballenger Creek Middle School: all the sports events, memes (shout out to Lois Griffin), meals, phone calls, and more. I'm looking forward to seeing you soon and being incredibly unserious everywhere we go (because why not)? Thank you to Sarah Coleman for being a real one since FMBC, meals together, inviting me to your house all the time, and cheering me on as we both departed from Maryland. Many thanks to Kellen Haile for all the linkups in Frederick, Zoom calls, and supportive text mages. Thank you to Dr. Ivón Padilla-Rodriguez for showering me with sincerity since we first met. You got me through this Ph.D. with so many supportive discussions (text and Zoom), discussions of delicious food, checking in on me, and *really seeing me*. I want you to always remember that your work is critical, thorough, and IMPORTANT!!! I can't wait to visit you and Steven soon! :) Thank you to Nicel for visiting me in the Bay Area and all the Zoom conversations. Thank you to KeShawn "Well, yes!" Ivory for being truly a comedian, for organizing with me, for sending all the memes, and for having the best taste in music and cuisine. Thank you to Evan C. Brooks for supporting me through all the hardships of this Ph.D., for all the small things (like discussing what we were eating and watching on a given day), for all the Zoom ki's, and for cheering me on every day. Thank you to Kani for your beautiful spirit, for reminding us to disavow antiblack "urgency," and for organizing with me. Thank you to Professor Racheida Lewis for being radiance personified: thank you for your energy at all the NSBE conferences, getting food with me, visiting me in grad school, introducing me to Leo, giving me amazing advice, FLYING TO THE BAY AREA TO SURPRISE ME DURING MY MFN COLLOQUIUM PRESENTATION (the fact y'all had a WHOLE group chat to coordinate sksksksksk), and everything else. Thank you to Dr. Kennedy Goldsborough for checking in on me on IG literally every day during this final year of grad school. I really appreciate the ways in which we virtually held each other over the past year. Thank you to Dominique Smiley for being a ray of sunshine since I first moved to Frederick decades ago, showing up to birthday parties, supporting my writing, and attending anything I was ever doing. I love you and your family so much <3 Thank you to Charles Walker for the many IG voice notes and ki's about literally EVERYTHING! Thank you to Torey for the many Zoom ki's about grad school and God. You are doing phenomenal work and are a phenomenal writer! Thank you to Terrance McQueen for the memes and extremely sweet DMs. Thank to Maimouna Dia for rooting for me since K-12 and being there in many ways (especially on IG)! Thank you to Jovante Anderson for your love, your memes, your poetry, holding and advancing my writing, your kindness, and your being. Thank you to Rickey Terrell for the MANY conversations we've had: processing the antiblackness of STEM, of any "career," always returning to 2020, thinking about our futures, everything. You are someone I am incredibly glad to have met since moving to the Bay Area. I look forward to

linking again in the near future. Thank you to my football homie, David Carlisle, for being an amazing friend to me since elementary school: nights spent at your house eating DOWN, playing video games, and watching movies. It was so lit to link up when you came through to the Bay Area years ago. I'm looking forward to catching up very soon in-person! Thank you to Dr. Carlton Poindexter and Rod Martinez for showing up for me all the way from Maryland and for being real (online and offline) about why all these institutions must go. Thank you to Dr. Derek Platt for encouraging me since I was just leaving UMBC and getting ready for grad school. Thank you for advancing my politics and always having long, clarifying conversations with me regarding Blackness. Thank you to Dr. James Bridgeforth for being the embodiment of kindness: asking me how my day is, affirming me, reminding me to "go get that slice of red velvet cake," encouraging me to try a different ice cream flavor (you know Ms. 'Nilla Bean is an icon), and for admitting that *that* show was worth watching (some of y'all reading this section will IMMEDIATELY know what the show is lmao). Thank you to Gaby Corona for all the daily check-ins, holding me as I processed the violence of the University of California, sharing information about various political discussions with me, and for sending me all the animal videos. Thank you to Dr. Shane Coleman for coming through on the TL when I was getting ate up for my tweet about the origins of STEM and why nobody should be surprised by the politics of folks from STEM (the quote retweets were vicious lmfao). Thank you for your love for Black people—for seriously contending with the antiblackness of "education," for attending to "What are the sciences?", and for taking organizing seriously. Thank you to Dr. Lorena Grundy and Dr. Sarah Yang for cheering me on while y'all were here at UC Berkeley (and after you both graduated). Thank you to Mr. Lance Day for providing a space in high school where I (and other Black students) felt comfortable to have conversations about what we were dealing with as teenagers (and beyond). Thank you for affirming my poetry and reminding me that I am awesome. Thank you to Serendib Early Learning—Mrs. Zoe, Mrs. Farwah, Alexis, Marc, and everyone else—who provided me with genuine community when my family and I first arrived to Frederick, MD. Thank you all for the love decades later. Thank you to Mrs. Tanya Davis and the Frederick County chapter of Delta Sigma Theta Sorority, Inc. for introducing me to the UMBC Meyerhoff Scholars Program, for providing me (and other Black Frederick County high school students) with scholarships, and for cheering us on into adulthood. Many thanks are given to all of my coaches, mentors, barbers, and other community members whom I have met in this life. You all are so important to me, and I thank you for holding me in your life.

There are not enough words for me to express gratitude to my family. To my parents, Avon K. Davey, Sr. and Regina L. Davey: thank you for teaching me that I have a voice (and to use it, which y'all know I do WELL haha), teaching me to possess integrity, and teaching me to be an excellent friend to others. I called the house nearly every day, and y'all answered. To my siblings—Nick, VJ, and Arianna (aka Arianny/Arianka)—thank y'all for being amazing. Nick, thank you for the phone calls, messages, and pep talks. VJ, thank you for being an excellent listener. Arianna, thank you for affirming me, for laughing with me, knowing all the memes, and growing with me. I learn so much from you, and I am so proud of you. I love y'all <3 To my grandparents, Daisy and Trevor, thank you so much for calling and sending lovely cards and celebrating with me. To my Momo, Linda Drewery, and my Paw Paw, Matthews Drewery, Sr.:

thank you both for always having a home grounded in love for Black folks. I still remember when I first got my license and felt so grown driving y'all to the movie theaters (and afterward to Burger King). You both have shown me immense love and I am truly grateful. To my aunts and uncles—Jeremy, Jermaine, Sheca, Matt, Dewanna, and Stacy—thank y'all for sending gifts, hugs, and encouragement from Louisiana, Florida, and California. To my godmother, Ms. Patricia "Pat" Beverly, thank you so much for being here before *I was here*! You've been so truly kind and caring to me and my siblings, attending anything we had going on, caring for us in your home, and being cherished family. I am so excited to be seeing you again soon! To my cousins—Ryan, Jamal, Micah, and Steven—I am so proud of you and am so excited to see y'all grow. Thank you to Coco, Niecy, and all my extended family for your bottomless love. <3

As a spiritual person, I sincerely believe in the power of transcendent relationships—forms of mutual recognition which exceed the descriptions of Westernized science, and which persevere even upon transition from the corporeal realm. **To Isaac L.Y. Adeeku**: you are the closest person I have on this planet, in this cosmos, and wherever else there exists space, time, and whatever else. I've known you since we were early teenagers flipping tires under the June sun during football conditioning in 2011, and I couldn't have experienced a better person to navigate "life" with. From sports to Necktie Club to college to the workforce to everywhere else, you've been there to process, grow, and rebel against antiblack, gendered structures. Thank you for making your home also my home (and thank you to Kofi, Mrs. Adeeku, and Mr. Adeeku). I've spent more nights than I can count at your house (eating WELL, okay???), having incredibly necessary conversations on the couch, and just *thinking*. As a fellow *Bleach* scholar, I am so excited to be thinking with you about this life and the afterlife (and what will become of "us"). Thank you for vacationing with me, weeping with me, dancing with me, celebrating with me… listening and experiencing precious moments of together. As many parts of us died (and continue to die) as we live, I am glad that we have each other to navigate through the dissonance. Thank you for taking the ongoing COVID-19 pandemic seriously when the World demanded the opposite of us. Thank you for welcoming me into your apartment and providing a safe place to watch YouTube movies, eat Lisa's cuisine, grieve the violence occurring across the country, and organizing. "Best friend" is an understatement. Wherever you go, so shall I. Until the End—and after that. **I love you eternally.** **To Andrea S. Constant**: I can hear your laugh as I'm typing this message (where Miranda Killgallen? LMAOOOO). Thank you for being a beautiful, brilliant, compassionate, and real friend from the beginning. I get so excited every time we hop on the phone or send text messages. I love hearing you talk, and I love spending time with you. I love hearing about your day, your goals, what you're reading, all of it. Thank you for truly caring about me: reminding me to rest, holding me up when I was dejected (while also urging me to feel what I felt), making time to ki, sending memes, and experiencing the interesting space that is Black Academic Twitter™ (hahahaha). Thank you for spending many hours on Zoom with me and Isaac: catching up, laughing, grieving, organizing. 2020 really put the three of us through it, and I appreciate you for constructing space for us to attend to our feelings as community. I was so excited when you came to Berkeley in 2019 and I got you show you (and Isaac) around the Bay Area, and we ate s'well. And (you know Imma say it)… "Mmm! That was TEW good… let's get the bill!" I am so ready to dip outta here and return to the East Coast and spend more time with you. Thank you for being there for me through bliss and battle. I love you, love you, LOVE YOU <3 **To Kat/sun Muloma:**

Acknowledgements

Chileeeeeeee… there is so much to say. "If you a mama—! Let's make these plates…in my opinion, Getchör Lichbach!" Thank you for being there for me through every battle. We both have been tried by the Bay Area in myriad ways. However, we stood beside each other and fought back. Thank you for everything: sending flowers, getting me vanilla bean ice cream, surprising me on my 26th birthday with a Zoom ki (a SETUP!!! skskskks), presenting me with *The Broken Earth* trilogy (truly one of the sweetest things anybody has ever done for me), introducing me to your friends, calling me, texting me, videochatting with me, having lunches on campus, and organizing with me. I learn so much from and with you, and I know for sure that we were meant to meet. I thoroughly enjoy thinking with you—discussing things related to both this material realm and the otherworld. Thank you for inviting me into vulnerable conversations. Thank you for challenging me. Thank you for showing up for Naomi, for Mariama, and for so many other young Black folks for whom this antiblack World *must* collapse. I meant everything I said during my birthday Zoom, during my colloquium, and during all the toasts. Thank you for *seeing* me, thinking about me, and loving me. Even as everything collapses and war remains ongoing, I shall stand beside you on the battlefield <3 **To Da'Shaun L. Harrison:** HEY, DA'SHAUN!!! Thank you for your beautiful self, your gorgeous laughter, your musical TASTE, and your treasured love. Since I first followed you on social media years ago, you've been incredibly kind to me. Thank you for all the work you've done on *In the Middle*, *Wear Your Voice* magazine, *Scalawag*, Twitter, and Instagram, and in *Belly of the Beast: The Politics of Anti-Fatness as Anti-Blackness*. Not only do you constantly advance Black political thought with each and every day, but you also sincerely cultivate community with Black folks across the planet and demonstrate care for all of us in ways that make us weep. Thank you for attending my colloquium and sending all the loving comments in the Zoom transcript (which I STILL am screaming at)! I love you and can't wait to see you in person <3 **To Tea Troutman:** HEY, TEAAAAAAAA (AND BELL)!!!! My comrade in a world of extremely unserious climate change studies; my fellow anime pal (still looking forward to the *Bleach* ki!); my fellow fan of a good po'boy… thank you for everything. I love every conversation we have, whether it's on Zoom, a phone call, or ongoing text messages. The way "We're doomed!" gets exchanged each and every time, chile… thank you for caring about me, building community with me, taking seriously what antiblackness is, and inviting me to hold so much with you. You are literally one of the most brilliant people I know, and your work is already galvanizing us into action against the antiblack antagonisms that afflict us. Thank you for your assessments, your precision, and your honesty. I learned (and learn) so much from you, and I am so excited to share space full of laughter with you. I excitedly look forward to connecting in-person soon :)

As I close these Acknowledgements, I want to be clear: **I suffered immensely in acquiring this Ph.D. I am full of both rage and sorrow as I sit here and type these words. I do not construe earning this degree as a conduit toward "Black freedom" (however folks assign meaning here).** I do not believe in "Black resilience" because I do not celebrate suffering that should not exist. I do not desire to esteem "surviving" antiblack systems just to graduate into other antiblack systems. As long as there remains the University of California, and the United States, and the rest of Europe, and the rest of "the World," there will be antiblackness. There will be no delivery from antiblackness through law, the courts, the Oval Office, charismatic leadership, nonprofits, industry, or Celebrity. In earning this degree, I endured disciplining and retaliation from a former adviser for naming violence (eventuating in my dismissal from the research group in September 2022). I

was scolded and talked about in conversations which absolutely employed antiblack logics to portray me as "irrational," "hostile," "cruel," "unfair," "dominating," and other terms. While this violence from my adviser occurred (among other things during this degree), I was scarcely supported by non-Black people who knew and who instead chose their safety over mine. I watched as other violent professors (who shouted at students, harassed students, gossiped about students, and were incredibly disrespectful to guests in the department) remained enabled by fellow faculty and students. Though I first could not comprehend how anyone could construe this space as a "community," I eventually realized that I was wrong. What I eventually came to understand was that white civil society unites around violence. Violence is the constitutive element; without it, there is no World.

In this antiblack World, it is difficult to be the people who choose resistance. Betrayal is forever present, and the path of the rebel is never bereft of punishment. However, I want to use this remaining space to thank some Black radical intellectuals who rejected the ways of this World and morphed me completely: Ida B. Wells, Ella Baker, Fannie Lou Hamer, George Jackson, Dr. Joy James, Dr. Gerald Horne, Dr. Axelle Karera, and Dr. Frank B. Wilderson, III. There are many more Black radical intellectuals, and I thank you all for your gifts.

Because you all are, there is a "we" who will continue to go to battle.

We're at the End.

Chapter 1: Introduction—Situating the Sciences: Symptoms, Structures, and Sensors

Each year, numerous scientific interventions are imagined, implemented, assessed, and optimized to address global challenges in food and water quality, housing, medicine, energy, and other sectors [1]. However, rather than serving as depoliticized implements with which to reproduce existing global arrangements of power, these novel technologies should necessarily be grounded in the *disruption* of antagonistic structural relations and the *realization* of anti-oppressive emergences for life and its surroundings. This dissertation presents a thorough investigation into the fabrication and characterization of three generations of color-based, inorganic chemical sensors sensitive to analytes whose indoor accumulation engenders hazardous conditions for setting occupants. In this first chapter, the (i) acute human health consequences from, (ii) historical violence associated with, and (iii) proposed interventions to indoor analytes (with particular emphasis on carbon dioxide, CO_2) are discussed.

1.1 Symptoms: Indoor Air Quality and Concomitant Suffering

Carbon dioxide (CO_2) is a linear, nonpolar [2], odorless, and colorless molecule largely known to the public as a *greenhouse gas* [3]. When solar energy strikes the earth's surface and transforms into infrared radiation, greenhouse gases (such as carbon dioxide, water vapor, methane, and nitrous oxides) absorb and reradiate this energy as heat into the atmosphere [3-4]. However, the increased generation of these greenhouse gases has precipitated harrowing realities for life on planet Earth [3-4]. Fossil fuel burning, deforestation, cement manufacturing, and other industrialized activities are primarily responsible for heightened global CO_2 emissions over multiple decades (as well as other greenhouse gas evolution), which is linked to *climate change* [5]. Climate change—defined by the Intergovernmental Panel on Climate Change (IPCC) as "any change in climate over time whether due to natural variability or as a result of human activity" [6]—has resulted in an increase in the global mean surface air temperature of ~0.8 °C in the last 50 years [5], as well as a rise in sea level, increased flooding, hurricanes, tornadoes, and the spread of infectious disease [4, 7].

Beyond its association with ongoing climate change concerns, CO_2 has been studied as a target analyte in indoor air quality monitoring. *Indoor air quality* describes the air composition in indoor environments (such as homes, schools, offices, and automobiles) which informs the overall comfort experienced by setting occupants [8-9]. In modern times, the average person in the United States of America spends 90% of their time indoors [8], which necessitates proper measures to maximize wellness throughout enclosed spaces. Human metabolism represents the primary source of indoor CO_2 in non-industrial settings, with exhaled breath composed of ~40,000 parts per million (ppm) CO_2 [10-11]. In addition to releasing CO_2, humans also emit volatile organic compounds (VOCs) into the air via exhalation and dermal channels [12], where VOCs are "compounds that have a high vapor pressure and low water solubility" [13]. Various VOCs, such

as acetone and formaldehyde, are also commonly sourced from a range from indoor items, such as disinfectants, paints, adhesives, furnishings, sealants, and toiletries [12-14].

In recent decades in the United States of America, buildings have been intentionally designed to be "airtight and energy efficient" [15]. However, these energy conservation measures arrived with a significant decline in air exchange rates (or ventilation), which enables an increase in the concentration of indoor chemical species [15]. Under specific ventilation, temperature, and humidity settings, the indoor accumulation of CO_2 and select VOCs has been connected to *sick building syndrome (SBS)*, which includes symptoms such as nasal and optic irritation, fatigue, and headaches [11, 15-18]. In prior literature, the Strategic Management Simulation (SMS) computer-based testing program (operated in a controlled environment under constant temperature and ventilation) indicated a significant reduction in participants' decision-making capacities at elevated CO_2 concentrations [18]. Namely, relative to 2.5 hours of 600 ppm CO_2 exposure, participants exposed to 1,000 and 2,500 ppm CO_2 (produced from the controlled injection of ultrapure CO_2 into experimental rooms) for 2.5 hours expressed decreased performances in Basic Activity, Initiative, Information Usage, Breadth of Approach, and Basic Strategy [18]. Of these lowered scores, participants showed "Dysfunctional" rankings in Initiative and Basic Strategy and borderline "Marginal"/"Dysfunction" rankings in Information Usage and Breadth of Approach upon exposure to 2,500 ppm CO_2 [18]. Other studies attending to in-vehicle air quality associate elevated CO_2 levels indoors (~3500 ppm) during 1-hour driving with an increased driver drowsiness at the wheel and a reduced driver heart rate—factors which increase the risk of traffic accidents [19]. However, discrepancies exist in the literature whether CO_2 (as an isolated molecule)—or its accretion along with indoor air pollutants (such as VOCs from human bioeffluents or household products)—primarily induces perceived poor air quality and human cognitive function [20]. Toward the determination of whether "CO_2 is an innocuous indicator of other harmful indoor pollutants such as volatile organic compounds" or "an active contributor to reduced performance in cognitive tasks" [20], some researchers have conducted experiments in which subjects are exposed to elevated CO_2 levels (1000 and 3000 ppm) through (i) the addition of pure CO_2 into the supply duct and mixed with a high outdoor air supply rate (720 m^3/h) and (ii) the placement of five subjects and an experimenter in rooms in which metabolic CO_2 at reduced ventilation flowrates of 155 and 38 m^3/h could produce 1,000 and 3,000 ppm CO_2 environments, respectively [10]. In the former experimental protocol, occupant bioeffluents were kept low; however, the reduced outdoor supply rates in the latter experimental protocol allowed for higher levels of human bioeffluents [10]. This study concluded that (relative to 500 ppm CO_2 at the same 720 m^3/h ventilation rate) "exposure to added CO_2 at or below 3000 ppm did not cause any significant changes in perceived air quality, acute health symptoms, or cognitive performance during 4.25-h exposures" [10]. However, "[c]ompared to CO_2 at 500 ppm, a reduced outdoor air supply rate that allowed bioeffluents to increase to levels, at which CO_2 increased up to 3000 ppm, significantly reduced the air quality perceived by visitors, increased the intensity of general (neuro-behavioral) acute health symptoms without increasing respiratory or mucous mem-brane symptoms, and affected cognitive performance," largely associating "moderate concentrations of bioeffluents, but not pure CO_2" with "deleterious effects on occupants during typical indoor exposures" [10]. In a parallel study (in which the same experimental protocols described previously [10] are used to control both CO_2 and bioeffluent levels), the addition of pure CO_2 (to

achieve a 3,000-ppm environment) generated an increase in end-tidal CO_2 ($ETCO_2$) and a decrease in heart rate relative to the reference condition; however, no other physiological changes were observed [21]. However, exposure to metabolic CO_2 (3,000 ppm) in the presence of elevated bioeffluent levels produced an increase in $ETCO_2$ and a decrease in heart rate, *as well as* a significant increase in diastolic blood pressure and salivary a-amylase level [21]. Across various studies, VOC emissions—such as "hydrocarbons, alcohols, ketones, and aldehydes" [22]—are associated with sore throats, nausea, and odors [14, 23-24]. Whether CO_2 is a "causative agent" [10] for acute health symptoms—or simply an indicator of inadequate ventilation [10]—remains to be entirely clarified, as future mechanistic studies are required to inform how CO_2 levels characteristically achievable in non-industrial settings (< 5,000 ppm) affect human health [25-26]. However, the objective of this dissertation is not to employ technical means to advocate a particular role that CO_2 (ex. Poor ventilation indicator, "causative agent," etc.) assumes in the sensation of poor indoor air quality [10]. *Moreover, the ableist and capitalist markers associated with scientific framings of "inhibited cognitive function" and "decision-making" must be challenged, disavowed, and abolished.*

The emergence of the novel Coronavirus disease 2019 (COVID-19) pandemic has motivated tremendous efforts to promote excellent air quality to minimize the risk of infection [27-29]. In addition to "physical distancing" and "masking" practices, scientists have recommended proper ventilation in high-occupation areas (such as stores, restaurants, public transit, and offices) to intervene upon the spread of COVID-19 [27-29]. COVID-19 transmission has been studied to occur via droplet and airborne routes, such as sneezing, coughing, eating, and talking [28]. Given these conduits of viral spread, scientific endeavors have developed to investigate relationships between COVID-19, indoor air quality, CO_2, and select VOCs. During the early stages of the pandemic, lockdowns in certain cities increased the time residents spent indoors; however, due to poor ventilation from "domestic energy savings" and increased use of cleaning products, residents experienced immense rises in exposures to total volatile organic compounds [TVOC] [27]. Measuring indoor CO_2 levels toward the evaluation of ventilation has been adapted by some scientists (and other COVID-conscious persons) as a form of risk assessment of COVID-19 transmission [30-32]. As novel COVID-19 variants appear and infections continue, scientists remain inquisitive (and concerned) about sustained and emergent human health complications from prior infection(s). Of persons who have contracted COVID-19, some have developed "Long COVID," which describes the "condition of suffering post-COVID-19 symptomatology" [33] and "a range of persistent symptoms after the acute SARS-CoV-2 infection" [34]. At present, some Long COVID symptoms include fatigue, cardiac abnormalities, headaches, and muscle pain; specifically, Long COVID has been associated with serious impositions on "respiratory, cardiovascular, neurological, gastrointestinal, and musculoskeletal systems" [34]. As scientists worldwide investigate the long-term effects of COVID-19 contraction on the human body—which already have been linked with the exacerbation of some human sensory abilities and reduced mobility of patients [33-35]—an optimal indoor monitoring of CO_2 and VOCs is vital to assess ventilation toward attempted minimization of COVID transmission and to preclude otherwise emergences of SBS symptoms.

In this section, prior studies on the relationship among CO_2, VOCs, indoor air quality, and COVID-19 have been established. However, the scope with which to substantively frame and meaningfully intervene upon these contemporary human health issues must be elaborated in greater detail. In the subsequent section, relationships with power are engaged to illustrate the vectors of violence historically responsible for global health outcomes and to assert the political stakes of modern scientific acts desirous of an efficacious character.

1.2 Structures: Power and Chemistry

Figure 1.1 displays the temporal rise in atmospheric CO_2 levels from the eighteenth century to the twenty-first century [5], with additional focus on the upward trend from approximately 1958 to 2020 in the Keeling curve [36]. In hegemonic climate change discourse, the incline in CO_2 concentrations is ascribed to "anthropogenic emissions," which primarily involve human activities such as industrial operations and processes, agriculture, and transportation [5]. Given the deleterious consequences of rising CO_2 emissions on collective wellness addressed in the previous section [4-7], a logical inquiry of "What is to be done?" has reverberated across the planet. In the past two decades, the "individualization" of environmental responsibility has been championed by state actors, "community groups," and others, challenging each person on the planet to "do their [part]" to mitigate the harms of climate change [37]. The lowering of "carbon footprints," which are related to the magnitude of CO_2 and other carbon-based emissions produced from the activities of an individual and other entities [38], has been significantly structured by such individualist logics [37]. Many "actions" have been grounded in consumerism, with persons electing to "buy organic," "buy local," and "avoid excessive packaging" [38]. While there could exist arguable merits to such consumer behaviors, the underlying modes of violence generating climate change precarity routinely remain unchallenged. In primarily espousing such individualist solutions to freeze the increase of harmful gases, proponents "distract from the fundamentally social and political character of environmental problems, and thus produce responses that are both inadequate environmentally" [37].

In the process of constructing scientific inquiry around these global challenges, intellectuals should become familiar with analyses of *power* through which to appropriately frame "the problem(s)" and to dismiss unimaginative and foundationally limited endeavors disguised as "solutions." Here, *power* involves control over violence and refers to "a matter of controlling decision making in the political arena," involving actors such as "large corporations and banks," "national level political structures," miscellaneous individuals enforcing oppressive structures in quotidian interactions, and others [39]. In the following subsections, the critical formations of the understood "World" and concomitant harms on life will be discussed.

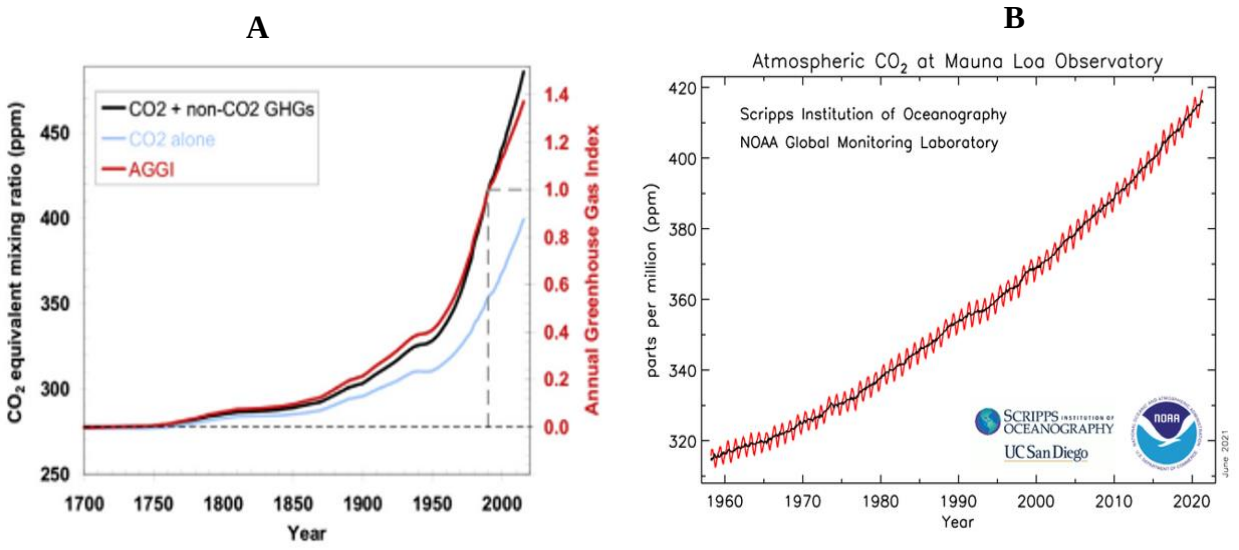

Fig. 1.1. (A) Profiles of CO_2 equivalent mixing ratio (ppm) and Annual Greenhouse Gas Index vs. Year [CO_2 + non-CO_2 greenhouses gases (GHGs), CO_2 alone, and annual greenhouse gas index (AGGI)] **and (B)** Atmospheric CO_2 at Mauna Loa Observatory vs. Year. Fig. 1.1(A) is acquired from Kirk-Davidoff (2018) [5] and Fig. 1.1(B) is acquired from NOAA (2021) [36].

1.2.1. What is the 'World?'

The "World" is not a neutral phenomenon; rather, it is an antiblack arrangement consisting of ceaseless extraction and accumulation, state expansion through identity and technology, necropolitical violence, knowledge subjugation, and genocide. In *Reconsidering Reparations*, Olúfẹ́mi O. Táíwò (scholar of Philosophy) describes "the system of the world" as "a set of inertias, gravities, pressures, and bottlenecks that bound and channel the endless flow of the present: material, money, media, violence, advantage, disadvantage" [40]. "Worldmaking" (or "worldbuilding") entails the evolution and interaction among these flows, informing the sites of antiblack violence understood (and obscured) in the present [40]. While different (and some opposing) views exist on the appropriate frameworks through which to critically examine "the World," the following paragraphs are largely assembled from the works of various radical intellectuals.

There is no "World" without "Europe," which itself should be conceived as a political project of spiritual, epistemic, and somatic dominion (rather than as a mere continent of solely geographical context). In "The Structure of Knowledge of Westernized Universities," Ramón Grosfoguel, Ph.D. (scholar of Ethnic Studies) describes such formations inherent to the "World" in which we exist [41]. Multiple centuries ago, the emergence of Cartesian philosophy—"I think, therefore I am"—generated a "world-historical event" in which the presented "I" replaced the God of "Christendom" as "the new foundation of knowledge" and assumed a "universality" wherein knowledge

production was "unsituated" in "particular social relations" or "from a particular space in the world"[41]. From this foundation, the basis of "objectivity" and "neutrality" would eventually structure and permeate the scholastic institutions descendent from these European logics, as well as dismiss epistemic practices situated in body-politics and geo-politics of knowledge as "… invalid, irrelevant, unserious, that is, inferior knowledge" [41]. Informing the arrogance in the Cartesian philosophy is European colonial expansion, which states: "I conquer, therefore I am" [41]. In the process of global conquest, European men replaced "God as the new foundation of knowledge" and attained "'God-like' qualities that gave them epistemic privilege" [41]. "I think, therefore I am," then, would become united with the "I conquer, therefore I am" position of European colonial expansion, and finally yield "I exterminate, therefore I am" to frame the "modern/colonial world" [41].

In the worldmaking that ensued, Europeans architected the racist, classed, gendered/cisheteropatriarchal, and ableist realities from which there is no refuge. When engaging this political project, one understands that "European civilization, containing racial, tribal, linguistic, and regional particularities, was constructed on antagonistic differences" [42]. With religion functioning before Descartes as "an animating axis of society" [43], the Catholic Monarchy declared the "purity of blood," which was the ethnic cleansing of Jews and Muslims in Al-Andalus, resulting in expulsion from the land, physical disappearing (genocide), and the extermination of Islamic and Judaic spiritual knowledge through coerced conversion and state surveillance ("epistemicide") [41]. Such genocidal programs would also eventuate in the burning of Indo-European women as "witches" in the long sixteenth century, whose oral knowledges of "astronomy, medicine, biology, ethics, etc." grounded in communal land relations were viciously condemned by the "Christian-centric patriarchy" [41].

"Race," while possessing "hazy" and disputed origins [44], would become "the animating axis of society" [43] which permeated all arms of oppression. Such is clear from engagement of *The Dawning of the Apocalypse* by Gerald Horne, Ph.D. (scholar of History). Rather than functioning as a biological identity marker, "whiteness"—or "pan-Europeanism"—emerges as the effective "God" of the modern world, possessing absolute control over the material realities of those differentially designated as "nonwhite" [44]. Through their racialization as "white," Europeans launched *racial capitalism*, which involves the accumulation of "social and economic value" from racialized "others" (particularly, Black and Indigenous persons) [45]. In *Black Marxism,* the late Cedric Robinson, Ph.D. (scholar of Black Studies and Political Science) outlines racial capitalism. As established earlier, "Racism… was not simply a convention for ordering the relations of European to non-European peoples but has its genesis in the 'internal' relations of European peoples. The development, organization, and expansion of capitalist society pursued essentially racial directions, so too did social ideology. As a material force, then, it could be expected that racialism would inevitably permeate the social structures emergent from capitalism" [46]. Moreover, the "creation of capitalism was much more than a matter of the displacement of feudal modes and relations of production by capitalist ones… The social, cultural, political, and ideological complexes of European feudalisms contributed more to capitalism than the social 'fetters' that precipitated the bourgeoisie into social and political revolutions…Indeed, capitalism was less a catastrophic revolution (negation) of feudalist social orders than the extension of these

social relations into the larger tapestry of the modern world's political and economic relations" [46]. Here, we observe that the European sensibilities that colored its pre-capitalist civilizations would still define its capitalist emergences (and structure the modern "World"). Finally, the transformed European bourgeoisie entities [46] that developed were crucial (as "conduits of capitalist expansion") in "determining the direction of investment, establishing political security for such investments, encouraging certain commercial networks and relations while discouraging others" [46].

Racial capitalism engendered a "modern world-system… dependent on slavery, violence, imperialism, and genocide" [47]. Max Liboiron, Ph.D. (scholar of Geography), describes the colonial arrangements of the "World" in *Pollution is Colonialism*. "Colonialism," which involves "relationships characterized by conquest and genocide" through which "colonialists and settlers" seized "access" to land, knowledge, physical bodies, and related resources to advance their projects of domination [48], undergirds the antiblack and anti-Indigenous essence of the "World" that exists (and continues to expand). In the colonization of the Americas, European conquerors constructed the "Indigenous" persona as "a new modern/colonial identity invention that homogenized the heterogeneous identities that existed in the Americas before the arrival of the Europeans" [41]. In the sixteenth century, Indigenous civilizations were engaged as "people without a religion," which necessarily meant "people without a soul" [41]. Through "the Spanish Christian imperial monarchy," debates about the humanity of Indigenous persons ensued [41]. While some argued that Indigenous peoples were "not human" because they "have no sense of private property and no notion of markets" and "produce through collective forms and distribute wealth through reciprocity," others asserted that Indigenous peoples were "human" but existing "in a barbarian stage in need of Christianization" [41]. Despite these debates, Indigenous civilizations of the Americas would remain subjected to epistemicidal/genocidal violence [41] through exposure to European diseases [49], "land dispossession" [50], and state-mandated suppression of their plural forms of knowing.

Antiblackness—the formation of the "Slave"—is the basis for which "the World" will ever possess definition. Pertaining to the capitalist conquests of European worldbuilding, "the Atlantic slave trade" was "integral to the modern world economy," as its "relationship to capitalism was historical and organic rather than adventitious or synthetic" [51]. In becoming "Slaves," captives "traveled not as emigrants seeking new lives in new places but as commodities" [52]. The "blurred and blooded boundaries between captivity, commodification, and diaspora" offered no relief for the Slave transported across the Atlantic, for "one could never completely escape the saltwater, for even once an African captive's own middle passage had ended, the communities where that slave's life played out in the colonial Americas continued to be molded by the rhythm of ships returning to deposit still more bodies" [52]. As with "Europe," "Africa" (in the context of its political function) should not be construed as a natural continent, but as a socially-produced zone of infinite acquisition through which Slave-making (hence, "worldbuilding") occurred and occurs. As an early agent of "pan-European" [43-44] investments in the formation of the antiblack "World," Portugal maintained a "long exploratory enterprise in Africa" in the fifteenth century, which resulted in a 1471 expedition to Africa where Portuguese mariners encountered a region where "huge quantities of the purest gold could be exchanged for cheap trade-goods of cloth and metal"

[52]. "By the end of this sixteenth century," this "whole region from Axim… to the Volta River, encompassing 230 miles, was known as the Gold Coast" [52]. From its inception, the Gold Coast was determined to be a target of established European resource acquisition, which firmly concretized (through war, importation of European firearms, and displacement) the Gold Coast as "a slave coast" [52].

In their rapacious worldbuilding operations, Europeans perpetrated transcontinental ecological shifts that would be implicated in modern environmental apprehensions. In *Saltwater Slavery*, Stephanie E. Smallwood, Ph.D., scholar of History, elaborates how Portuguese mariners transported maize from the Americas to Africa, where the crop "quickly attained a prominent place among the agricultural staples in the Gold Coast" [53]. Maize, along with "other New World plants such as pineapples and sweet potatoes," grew "in abundance" along the coast; the "high yield" and "protein content" of maize "fueled dramatic population growth throughout the southern forest region" that participated in the Atlantic "Slave" market [53]. During the coerced travels of African captives across the Atlantic, "slavers" purposely hauled "dead, ailing or recalcitrant Africans overboard and actively courted shark retinues in order to present survivors with an object lesson in the spectacle of their fellows being degraded to the status of meat" [54]. Throughout these colonial movements of African capital, sharks "[followed] slavers over extended distances," which has compelled some scholars to posit that the Atlantic "Slave" market influenced "the migratory pattern of sharks" [54]. Such "cross-continental exchange" and Slave-making—wherein "the magnitude, variety and longevity of human-induced changes, including land surface transformation and changing the composition of the atmosphere"—would mark the advent of the "modern world-system" (or, as some scholars regard it, the "Anthropocene" era) [55]. The "arrival of Europeans to the Americas" immensely reduced population numbers in the region, with an approximate 54 million people in 1492 shrinking to about 6 million people due to "exposure to diseases carried by Europeans," as well as "war, enslavement and famine" [55]. This occurrence, and the "accompanying… reduction in fire use [that] resulted in the regeneration of over 50 million hectares of forest, woody savanna and grassland with a carbon uptake by vegetation and soils," are suggested to have "significantly contributed to the observed decline in atmospheric CO_2 of 7–10 p.p.m. … between 1570 and 1620 documented in two high-resolution Antarctic ice core records" [55].

In the absence of an attendance to the colonial interests that Europeans (who founded and guarded "whiteness," which effectively denoted a relation as "sovereign" of the "World") possessed in their unthwarted seizure of Earth and cosmic rearrangement of all relations, any proposed environmental "elixir" will surely prove its impotence. Following these paragraphs, which have entailed a brief account of "worldmaking," atmospheric carbon dioxide concentrations (from the Industrial Revolution into the present) will be engaged, with discussion of the role of racial capitalism in producing militarized, technology-based employment sectors wherein state interests (primarily involving war) both contribute to (and obfuscate) these troubling emissions.

1.2.2. Carbon dioxide, capitalism, and war

Outdoor air pollutants in cities, "emitted from on-road and off-road vehicles," as well as from "power plants" and "petrochemical plants," can enter indoor air environments through (i) mechanical ventilation ("driven by a ventilation fan or air conditioner of a dwelling"); (ii) natural ventilation ("driven by prevailing wind flow"); and (iii) infiltration (driven by "cracks and leaks in the building envelope") [56]. As shown in the Keeling curve depicted in **Figure 1.1**, atmospheric CO_2 levels maintain a concerning rise [36]. Given the proposed worries of CO_2 exposure on human health [18-19), an assessment of the effect of outdoor CO_2 levels on indoor CO_2 levels is warranted.

Equation 1.1 shows a simple differential equation involving indoor CO_2 levels and outdoor CO_2 levels (as a function of time, t) [57]:

$$V\frac{dC_{in}}{dt} = Q(C_{out} - C_{in}) + G \qquad \textbf{(Eq. 1.1)}$$

Where:

V is the volume of the indoor space (assumed to be well-mixed),
C_{in} is the indoor concentration of CO_2,
C_{out} is the outdoor concentration of CO_2,
Q is the outdoor air ventilation rate,
And G is the rate of generation of CO_2 from indoor occupant human respiration.

Assuming steady-state conditions for the change in the indoor CO_2 concentration, the transient derivative term can be set to 0 such that **Equation 1.1** simplifies to **Equation 1.2** [57]:

$$C_{in} = C_{out} + \frac{G}{Q} \qquad \textbf{(Eq. 1.2)}$$

Based on these assumptions, the indoor CO_2 concentration (C_{in}) will increase as the outdoor CO_2 concentrations (C_{out}) and the rate of metabolic CO_2 generation (G) increase [57]. Beyond ensuring indoor settings can comfortably accommodate occupants and optimizing ventilation (Q) for such occupation, the impact of increased atmospheric CO_2 emissions on indoor CO_2 levels must be examined. However, to execute such an analysis, the reason for increased atmospheric CO_2 levels must first be elucidated through the work of Andreas Malm, Ph.D., scholar of Human Ecology and author of *Fossil Capital*.

Fossil fuels certainly preside over the "modern-world system" [55]. There presently exists "a vast infrastructure of oil terminals, petroleum refineries, asphalt plants, road networks, gas stations…" [58]. Cars, which mostly "run on fossil energy," are made ubiquitous, as "people travel to work

in cars, go on visits and vacations in cars, drive their shopping lists and shopping bags back and forth in cars…" [58]. It is not happenstance that such a proliferation of these fossil fuel-based vehicles occurred in the twentieth century (whereas "other modes of transportation" were "excluded" or "prevented from rising to dominance") [58]. Such structured technological progressions (and prohibitions) constitute *carbon lock-in*, which is the "cementation of fossil fuel-based technologies, deflecting alternatives and obstructing policies of climate change mitigation" [58]. This work possesses a nontrivial role in the *fossil economy*, which is "an economy of self-sustaining growth predicated on the growing consumption of fossil fuels, and therefore generating a sustained growth in carbon dioxide" [58]. With fossil energy as "the material fuel" for the "fire of modern growth [which] reproduces an economic gas that necessarily ignites as more growth," the fossil economy exists as "a socio-ecological structure, in which a certain economic process and a certain form of energy are welded together" [58]. In its self-sustaining expansion, the fossil economy "appears indistinguishable from life itself," remains "entrenched in the environment," and "conditions the movements of the people inside" [58]. In surely unprecedented (and foreboding) ways, the fossil economy exercises widespread "causal" functions, "most notably the power to alter the climatic conditions on planet Earth" [58]. In the assessment of the functions, an understanding blossoms in that "the power derived from fossil fuels was dual in meaning and nature from the start," with *power* here co-constituted through interpretations as both "a measure of work" *and* as "an authority" or "a structure of domination" [58].

In anticipation of "How did we get here?" emanating from rightfully dismayed co-dwellers of Earth, the elucidator must be explicit in partially analyzing climate through class [59]. Pertaining to modern consternation about climate change, rather than misconstruing "solar radiation" or "volcanic outgassing" as natural phenomena implicated in worldwide shifts, intellectuals should recognize that fossil fuels are "a materialisation of social relations" [59]. As became evident over the centuries, "fossil fuels necessitate waged or forced labour—the power of some to direct the labour of others—as conditions of their very existence" [59]. To illuminate the origins of the fossil economy, the elucidator must investigate the British Industrial Revolution. Britain approximately "accounted for 80 percent of global emissions of CO_2 from fossil fuel combustion in 1825 and 62 percent in 1850" [59]. As is understood by the contemporary sciences, "emissions are cumulative" such that "for every emission added to past output, the atmospheric concentration of the gas increases" [59]. The global "climate system" retains a "long memory," which is reflected in a "messy mix up of time scales" where "every *conjuncture* now combines relics and arrows, loops and postponements that stretch from the deepest past to the most distant future" to potentially "unhinge ice sheets," "thaw permafrost," and "destablise methane hydrates" [59]. This "epoch of diachronicity" must regularly revisit nineteenth-century Britain, whose cotton industry once "impelled its machines with water" [59]. However, British manufacturers eventually turned from water-powered mills to steam engines fired by coal during their Industrial Revolution—a transition which underlined the climate/class material emergences that would eventuate in today's increased atmospheric CO_2 levels and trepidations regarding global wellness [59].

In the situation of water versus coal-powered steam, the embrace of technology as a means to effectuate an understood "general good" would be to mischaracterize power [58]. During the Industrial Revolution, the "transition from water to steam in the British cotton industry did not

occur because water was scarce, more expensive or less technologically potent—to the contrary, steam gained supremacy *in spite of water being abundant, cheaper and at least as powerful, even and efficient*" [60]. While such a transition would appear reasonably unwise, the interests of capital averred an otherwise logic. To the chagrin of British capitalists, the "flow of energy did not halt before the fence of private property" and respected "no deeds or titles" [60]. Such flows, including "running water, light and air," configured *res communes* ("things the property of which belong to no person, but the use to all") insofar as "they were physically impossible to capture for exclusive appropriation and hence must belong to the people collectively: commons ordained by nature" [60]. Despite their upholding of "the principles of private property," British capitalists could not "cut up" flowing nature and "cart it away" for future transactions [60]. In addition, industrialists sought an "independence from the vagaries of the weather," insofar as droughts, floods, and other "extreme weather events" disrupted factorial operations [60]. Due to such caprice with respect to "the supply of water" amid "dry weather," "rainy seasons," and "frost," British capitalists ascertained that "water followed its own clock—not that of the factory" [60].

Whereas flowing water could not be so seamlessly domesticated, coal-powered steam submitted to the British capitalist toward self-sustained economic growth. Unlike the elements of *res communes*, coal was "piecemeal, splintered, amenable to concentration and accumulation," and "divisible," which "made it more appropriate for capital" [61]. Separated from the "waterfall" and the perceived whims of nature, accumulated coal (as "stock") could be "used wherever," such as in the "center of a[n] [urban] population" [61]. While the steam engine did not function solely on coal and "craved water," it did not require "falling or even moving water … just water, be it level, stagnant, even putrid" [61]. Given the canal formations of the late eighteenth century, such water "was within easy reach nearly everywhere" [61]. Of paramount value to the capitalist, however, was the subservience of steam [61]. Praised as a "tractable," "docile," "active," and 'laborious and indefatigable servant," steam served capitalists' interests sans the disadvantages regarding discipline and exhaustion imputed to human laborers [61]. Steam required "no government but fuel" and possessed "no residual existence outside that brought forth by its owners" [61]. Nonetheless, while British fossil capitalists adulated steam for its "virtues," they resented steam's foil—the human worker—whose will to dissent by any means ruptured capital accumulation.

Rebellion ensued throughout the Industrial Revolution among laborers. In the 1820s, expansive lending and overproduction in the "booming cotton industry" precipitated "the panic," inducing harsh competition between companies [62]. As economic disaster struck in the 1830s and 1840s, indocile workers formed unions and mobilized each other in militant formations against bourgeoisie entities [62]. "Ruling classes" were imbued with "fear"—emotionally preoccupied with the horror of coinciding disorder, famine, crime, and revolution [62]. Unlike steam, the noncompliant human worker could disavow "an industrious character" when wronged [62]. However, the British state did not simply relent to organized laborers. In the late 1820s, the British state sentenced those who willfully sabotaged coal mines and steam engines to capital punishment [62]. This measure, the Act of 1827, was used to both (i) hang three men for setting ablaze a power loom mill and smashing "the steam engine with a sledgehammer" and (ii) "acquit defenders of a factory whose bullets had killed besieging rioters, if intention to damage machinery could be established" [62]. Despite promised violence from the British state, workers revolted still [62].

During the general strike of 1842, workers espoused *collective bargaining by riot* and targeted machinery of the fossil economy to seize concessions from industrial capitalists [62].

While penury was a driving force into insurrection, workers were also subjected to hazardous conditions at the factories. Steam engines emitted considerable heat, which elevated temperatures in some factories to "a normal range of 84 to 94 degrees [Fahrenheit]" [62]. Moreover, the indoor accumulation of CO_2 within the "congested factory rooms" engendered an "insalubrity" in the air immensely harmful to the laborers [62]. Despite how "all the smoke, the acid rain, [and] the sulphurous fog literally killed off flora and fauna" in an 1840s Manchester, the bourgeoisie asserted that (i) "suppression of the smoke" could "materially injure important branches of [their] national industry" and (ii) "the quantity of smoke was rather a barometer of prosperity" [62]. Rather than prioritize the holistic wellness of their workers, the British bourgeoisie selected fossil capital. Such blatant disregard for collective health from actors with power would not be trapped within the British Industrial Revolution; rather, it would, too, be a practice of ecological state violence inherent to the adoption of the fossil economy that would proliferate around the globe.

In return to the fossil economy, the notion of "climate as classed" must be reemphasized [59]. In "class societies"—social ensembles in which "the means of production are properties of some people to the exclusion of others"—"productive forces," such as the coal-powered steam engine, "will materialise only *through their being exclusively owned*" [63]. Thus, the "technologies of fossil fuel combustion," as well as the attendant CO_2 emissions, must be grounded in "property relations" to explicate how such forces "change the climate of the earth" from "*their value for their owners* as distant from non-owners" [63]. Here, "property relations" describes "a matrix of positions for the members of the species [through] the means of production" [63]. For example, a worker requires money to survive; to accumulate such monies, the worker will (i) sell their "labour power… for specific periods of time," (ii) acquire a "wage" for labor performed, and (iii) use said wage to purchase goods with which to survive [63]. The worker, then, traverses from Commodity I to Money (M) to Commodity (M) [63]. However, the process is different for "an agent who *starts off* with money" and seeks to accumulate more money [63]. For this agent, they begin with money (M), which is used to purchase "labour power" (L) and "means of production" (MP) as commodities [63]. There then comes production (P), wherein "resources are withdrawn from nature and placed in the hands of workers … to be applied, refined, worked up," involving "raw materials" [63]. Once these resources have been transformed into commodities [C'], they are sold to the market to return profit for the monied agent [63]. Such a circuit (which can be "extrapolated in perpetuity") outlines *the accumulation of capital*, which involves the withdrawing of more and more "biophysical resources" for profit-making [63]. As such, these "capital property relations" engender "the profit," the desire to pursue "the profit," and the push to increase material throughput (or biophysical resource extraction) [63]. Fossil capital accumulates in a similar mechanism, involving "self-sustaining growth" which passes "through the metamorphosis of fossil fuels into CO_2" [63]. In the fossil economy, "for capitalists to burn fossil fuels, there have to be other capitalists specialised in their production, and for the former to burn more, the latter have to deliver it in greater quantities, the two cycles ever intertwined" [63]. Through such relations, capitalists "insert themselves in the metabolism between human beings and the rest of nature" to assert dominance over material reality [63], which is again manifested in modern "carbon lock-in" [58].

While emerging in the British Industrial Revolution, the fossil economy has expanded around the world. In the United States of America—which transitioned into a fossil economy later in the nineteenth century [64]—such technological advancements resulting in increased CO_2 emissions would materialize via transportation and war. Following World War II, "economic growth, population growth, rapid suburbanization, and the closing of some public transit systems" generated the expansion of the U.S. transportation sector [65]. However, this growth also resulted in increased CO_2 emissions with time [65]. Previous work shows that "in 2007, the transportation sector was responsible for a third of U.S. GHG emissions from CO_2 and 28% of global GHG emissions" [66]. Since 1960, "highway travel has grown threefold due to higher population [and] greater number of vehicles per capita" [66]. The U.S. Department of Defense also uses copious amounts of fossil fuel energy to power its "submarine[s], warship[s], tanks, planes, aircraft[s], helicopters and other warfare machinery" [67]. In terms of "average daily oil consumption," the U.S. Department of Defense would rank "34th in the world… coming in behind Iraq and ahead of Sweden" [67]. Given its "open-ended operations around the globe" (known as "the everywhere war"), it is largely "unlikely" that the U.S. military will cease its prodigious use of fossil fuels soon [68]. In analyzing the "carbon boot-print" of U.S. military operations around the world, previous scholars (appealing to anti-war leftist struggles of past social movements) have asserted that "the logics, logistics, and bureaucratic structures embedded in the overarching modalities of the US war apparatus are inextricably tethered to hydrocarbons" [68]. Thus, U.S. imperialism at all times functions to perpetrate climate change devastation [68].

In return to "war," the mid-twentieth century expansion of U.S. technological labor sectors must also be situated. In 1945, Vannevar Bush—Director of the U.S. Office of Scientific Research and Development—wrote a letter to the U.S. President to persuade the U.S. Government to expand and support its scientific infrastructure [69]. In making his case, Bush linked "science" to "the public welfare," where the latter necessarily meant "national security" [69]. Not only did Bush assert that "modern war requires the use of the most advanced scientific techniques," but he also claimed that "there must be more—and more adequate—military research during peacetime" [69]. Bush further grounded his arguments in U.S. capital interests, articulating that "a nation which depends upon others for its new basic scientific knowledge will be slow in its industrial progress and weak in its competitive position in world trade" [69]. With regard to advancements in medical research, Bush also frames his argument as "The War Against Disease" [69]. This militaristic framing, coupled with the arguments regarding "national security" and "industrial progress," establish U.S. scientific enterprise as a state-building project [69]. With government funding secured, U.S. imperialist exceptionalism would found the National Science Foundation (NSF) and expand vocational opportunities for U.S. citizens obtaining training in the political project that became known as Science, Technology, Engineering, and Mathematics (or STEM). More than seven decades subsequent Bush's report, Westernized scientists [41] in climate change studies continue to research plausible avenues to transition to "renewable energy" [68], while minimizing (or simply omitting) any critiques of the material corollaries of U.S. hegemony on planet-scale climate degradation.

As an epoch illustrating an era of the "impact" of human activity on Earth's ecosystems, "the Anthropocene" has been critiqued by multiple scholars. Relating to the concept of "anthropogenic emissions," where *Homo sapiens* (as a species) are collectively made answerable for rising atmospheric CO_2 levels, some scholars have argued that "enormous variations—in space and time, present and past—humanity appears too slender an abstraction to carry the burden of causality" [70]. Instead of assigning "blame" to mankind, Malm articulates in *Fossil Capital* that "[c]apitalists in a small corner of the Western world invested in steam, laying the foundation of the fossil economy; at no moment did the species vote for it either with feet or ballots, or march In Mechanical unison, or exercise any sort of shared authority over its own destiny and that of the earth system" [70]. Attentive to the fact that white British men (who composed a "tiny minority" of *Homo sapiens* in the nineteenth century) bloomed the fossil economy, the scholar invites readers to be specific about social "divisions" among humanity which have always "been an integral part of fossil fuel combustion in the first place" [70].

In the act of taking these "divisions" seriously, what could be learned from assessment not of the "human" (as a *Homo sapiens* biological entity), but of the "Human" (as a sociogenic relation/function)? What could be ascertained in the configuration of "the Human" with respect to carbon emissions and global health? Moreover, who is "the Human"—and what is it *not*? In response to these inquiries, the subsequent section will investigate the antithesis of the Human—Blackness.

1.2.3. Antiblackness: the stakes of environmental ruination

In the process of becoming "Black," African captives (as also sentient commodities) "revealed the boundaries of the middle ground between life and death" and embodied "the limits up to which it is possible to discipline the body without extinguishing the life within" [71]. Smallwood informs the reader in *Saltwater Slavery* that the "violence exercised in the service of human commodification relied on a scientific empiricism always seeking to find the limits of human capacity for suffering, that point where material and social poverty threatened to consume entirely the lives it was meant to garner for sale in the Americas" [71]. Slave traders were quite calculated in measures taken to "preserve" African captives to maximize profit [71]. As "an obvious and effective" means to impede escape, "shackles were an important element in the arsenal of tools" of captors [72]. English traders requested specific "irons" for specific purposes: " 'short irons' binding captives' wrists ensured that slaves could neither raise a hand to strike their tormentors nor seize a weapon, open a door, or scale a wall without great difficulty; 'long irons' around the ankles likewise held captives fast" [72]. Captains directing slave ships even grumbled about "the corrosive effects of humidity" with respect to binding irons, likely apprehensive regarding how such tools "in need of repair" might incite insurrections aboard [72]. In addition to the science of physical binding, captors were "thoroughly scientific" regarding the "food" that captives consumed [73]. Interested solely in the successful exchange of their breathing commodities, slave traders provided "meals whose content and size reflected a calculating balancing the cost of the slaves' maintenance against their purchase price" [73]. At the English factories involved in Slave-making, "slaves generally received a daily allotment of corn dressed with malagetta pepper and palm oil," which was not administered to "support health," but "simply to ensure subsistence"

under the "economic considerations" of the trader [73]. Finally, as "waves of illness and death swept through" an Accra slave prison in the late seventeenth century, "openings [were] cut into the walls for ventilation," though they "did little to counteract the heat and closeness of the air when the rooms grew so crowded" [74].

"Slave-making," however, did not simply consist of routine acts of physical denigration through empirical approaches. African captives experienced *death* in plural form. As Grosfoguel writes in "The Structure of Knowledge of Westernized Universities," Slaves transported to the Americas (characterized as "people without a soul") endured epistemicidal violence, explicitly prohibited "from thinking, praying or practicing their cosmologies, knowledges and world views" [41]. "Un-making" oneself a Slave was impossible. No matter what the captive accomplished—"[w]hether they burrowed their way under prison walls, broke out of the irons on their legs, or swam away from coasting vessels"—"the market" persevered, which meant "escape, did not, in itself, alter slaves' status as a market commodity" and captives remained "extremely vulnerable to recapture and resale" [75]. The Atlantic trade disrupted African "kinship ties," which "were the institutional glue that most immediately bound the self to society" [76]. As a result, "the disappearance of a community member left an absence that portended consequences for both the individual and for those left behind" [75]. Through capture and placement at the "littoral" for exchange across the Atlantic, African captives experienced *social death*, which involved "a severing of ties with familial relations, … kinlessness and subsequent introduction and attachment to the owner's network of kin" [76]. In "the alienation from their society of birth," African captives "had been doomed to social annihilation" [76].

In the episodes following the coordinated trafficking of African captives, Black persons are scattered across the planet in an African diaspora. While some would argue that most Black people are "free" in the twenty-first century insofar as "slavery" has been abolished by their governmental bodies (which is untrue in the United States [77]), what if this argument misunderstands what "slavery"—to be Black—*is*? Frank B. Wilderson, III, Ph.D. (scholar of Rhetoric and African American Studies) encourages us to *not* to think about "Blackness" as biological recordkeeping of African ancestry nor "slavery" as a status dictated through law. Rather, he constructs "Blackness" as "Slaveness"—that is, to be "Black" is to function as the "Slave" with relation the "World" [78-79]. In "The Politics of Pessimism in an Anti-Black World," Wilderson asserts that "Blackness, as a paradigmatic position (rather than as an ensemble of cultural practices) cannot be disimbricated from Slavery" [78]. In a separate engagement [79], Wilderson declares that "antiblack violence is a necessary ensemble of rituals that produces a kind of knowledge for the rest of the World – 'if this happens to me, there would have to be a reason.' We have to be assaulted; we have to be assailed. It's therapy for the rest of the World. It's because we breathe." In this context, the "rest of the World" implies those who are non-Black—thus, "Human." For Wilderson, "the value of the word comes from its opposition," meaning that there can only be a "Human" insofar as there exists a clear definition of what is *not* "Human" [78]. It is with that understanding that the "Slave" as a function congeals [78-79]. Unlike "Humans," there is not contingency to antiblack violence; as civilizations had effigies/sites upon which burnings occur, the Black/Slave is "the breathing effigy of the World" and "the living, breathing destination of the World's aggressivity so that they can live in peace" [79]. Black flesh, then, is simply exposed to

ritualistic acts of violence simply because it is what makes the World coherent [78-79]. "I know I am Human because I am not Black" [79]. Within the Human unconscious, the Black/Slave does not register as another "person" (or "Human") [79]. Expanding Grosfoguel's remark of African captives as "people without a soul" [41], the Black/Slave functions as an organic implement [78-79]. As Wilderson notes, "Whoever heard of an injured plow?" [79]. Given this function of the Black/Slave, Wilderson argues that the antiblackness which establishes "the World" maintains *all Black people everywhere in a position of Slaveness* [78-79]. Such an argument, then, complicates strategies through which attempts at "redress" are implemented. Whereas Humans experience oppression which (with varying levels of structural violence) can be abolished with "the World" intact (such as the worker from the end of capitalism), the Black/Slave will *not* be liberated from antiblackness unless *the World is abolished* (which necessarily means the end of the Human and the Slave) [78-79]. This analytic, known as Afropessimism, acts as a "report… on the paradigm of suffering" [79]. Namely, Afropessimism is a "dangerous theoretical intervention" insofar as it raises the stakes of what is required to meaningfully assess (and end) "Black suffering" in ways that have "shaken and rocked… the assumed foundation of the humanities" [79]. As long as there exists the "World," antiblackness—as it constructs Black as effigy in the Human mind and materializes through capitalist, gendered, imperialist, and ableist logics—will persevere [78-79].

Afropessimism invites us to reassess the "we" implied in the "Anthropocene" pertinent to climate change and the future of planet Earth. In "Blackness and the Pitfalls of Anthropocene Ethics," Axelle Karera, Ph.D. (scholar of Philosophy and African American Studies) presents "new regimes of Anthropocean consciousness" as "disavowing racial antagonisms" and being unequipped to "wrestle with the problem of black suffering" [80]. Due to its "unwillingness to account for past and current imperial injustices" with respect to antiblackness, the Anthropocene ensures "a post-apocalyptic world without any signs of ethical transformation" or "any emancipating value" from antiblackness [80]. While the Anthropocene aims to present a depoliticized "human" who is "grievable both in the present and possible future" due to misgivings about the deleterious effects of climate change on "life," the "unregisterable and therefore un-grievable" nature of "'blackened' life" remains uninterrogated [80]. More so, Karera challenges us to consider that "if blackness is inherently a necropolitical imitation of life that continues to thrust our ethical impulses and inclinations into critical crisis," then "Anthropocean consciousness" which disappears Blackness will "reproduce ant-Black sentiments" [80]. Given the ways in which "Anthropocean ethics" produce a certain pragmatism that ultimately upholds an antiblack social order, Karera proposes that we "complicate our thinking" and resist the allure of establishing "a solution" [80]. Instead, we are called to "stretch our thinking to the limits of their logics, complicate our questions, and investigate the ways in which many of our philosophical commitments to anti-oppression can betray their own potential radicality in thought and action" [80]. Thus, the "we" who recognize the ineluctable presence of antiblackness must not embrace ruse of the "We as human/We as collective all" which appears with seductive intrigue in hegemonic discussions on the environment.

Blackness remains anchored to the "diachronous" [59] aspects of environmental violence. In the Belgian Congo, uranium was mined from Shinkolobwe to construct the atomic bomb and secure "victories" for the Allied Powers in World War II through the bombings of Hiroshima and Nagasaki [81-82]. Under Belgian rule, Congolese Slaves were subjected to an element whose dust

has been associated with lung cancer, respiratory disease, and kidney disease [82]. Uranium mining also has been implicated in soil, air, and water contamination [82]. Elsewhere, "along an 85-mile stretch of the Mississippi River which hosts over 100 chemical, petrochemical, refining and industrial plants," exists Cancer Alley in Louisiana, whose operations expose poor Black U.S. residents to pollution containing carcinogenic toxins [83]. When Hurricane Katrina submerged Black communities and displaced Black people in 2005, white reporters (while perceived to have expressed "sympathy" for "storm victims") condemned "looting" through an appeal to white middle-class sensibilities and demonstrated that "disaster" could not disappear pre-existent antiblack animus [84]. Black people largely form the residents of the Ironbound neighborhood of Newark, New Jersey, where "plumes of vapors" have been found "underneath residents' homes" [85-86]. Ronson Metal Corp., a "a company that once occupied the land where it made cigarette lighters and other products from the 1950s to 1989," left the volatile organic compound, trichloroethylene (TCE), in the groundwater; through vapor intrusion, TCE has infiltrated homes, which has generated alarm regarding long-term exposure and the development of "nerve, kidney and liver damage" [85]. As the COVID-19 pandemic continues to ravage the planet, the antiblack capitalist systems inherent to "the World" continue to heighten the probability of Black contraction of (and death from) COVID-19, especially due to unhoused conditions preventing opportunities to "shelter in place" and a "neoliberal" health care system that prioritizes whiteness and facilitates Black murder through dismissing Black patient medical needs [87].

Given these dismal conditions under which Blackness interfaces with the environment in an antiblack World, one might implore the academy to brainstorm a "solution" through which to conjure an "otherwise" for Blackness. However, as Grosfoguel reminds us, the Westernized university is fundamentally an antiblack and anti-Indigenous site [41]. Joy James, Ph.D. (scholar of Political Philosophy and Africana Studies) declares that "the university is not grounded into the needs of any community in struggle" [88]. Engaging the state university as a "government entity" and the private university as a "corporation," James articulates that neither site produces "new thinking for freedom" [88]. Though certain academic STEM endeavors generate "new theories about genes and about black holes" (among other data), James determines that these are moments of "technology" and "medicine" which are "impressive," but do not necessarily deliver "freedom" to communities in struggle [88]. In "Algorithm of Anti-Racism," James illustrates how "hegemonic progressives" (such as those employed in Westernized universities) configure a "kneeling" and "meek" Black icon whose visible suffering is used to make "Blacks more embraceable" and foster discussions regarding openings for "reconciliation" under U.S. democracy [89]. However, such configurations "erase the militancy" of Black rebels who reject dependency on a "white savior" and who aver that "the World" must be obliterated to be emancipated from the function of Slaveness [89].

As I close this section, I must be clear: this dissertation will not end "the World." In contrast, the origins of this work are more closely aligned with the "hegemonic progressives" [89] whose collaborations with think tanks, focus groups, nonprofits, startups, and other sites of capital accumulation aim to mystify or commodify Black suffering. This thesis is a product of an antiblack Westernized university, UC Berkeley, which still occupies the unceded land of the

Ohlone people. In studying indoor air quality, however, I aim to establish the stakes for what is necessary for *any* scientific intervention to seriously consider antiblackness. However, absent of an overt recognition of "the World" as antagonist and of any serious intention to extinguish "the World," such scientific endeavors ultimately reproduce innocuous "solutions" compatible with the same antiblack arrangements that once transformed Africans into captives.

Now that the antiblack "World" responsible for environmental violence related to indoor air quality, carbon dioxide, and volatile organic compounds has been discussed—as well as the impossibility of conventional "solutions" in effecting "change" for colonized persons—we shall glimpse the scientific system of this dissertation.

1.3 Sensors: Color and Possibility

Carbon dioxide and volatile organic compounds are ubiquitous in our daily lives. For the reasons expressed in the prior sections, however, it is imperative that these molecules are soundly monitored to promote salubrious indoor air. Toward such goals, the construction of *sensors* is pursued, where a *sensor* (which has different definitions in "application perspectives") is a device that measures a phenomenon of interest and provides a "useful output" (called a "signal"), which can be "read by an observer or by an instrument" [90]. Sensors are fabricated and deployed on a global scale across numerous domains, such as in human medicine, food packaging, and ocean acidification [1]. Pertaining to indoor air quality, the nondispersive infrared (NDIR) gas sensor is the commonplace item on the market [91-92]. As shown in **Figure 1.2**, this device measures the concentration of carbon dioxide through the attenuation of infrared radiation [92]. Gas molecules enter through the gas inlet and travel through a gas chamber, where infrared radiation is emitted from an IR source [91-92]. Carbon dioxide absorbs the infrared beams through the Beer-Lambert law [91-92], shown in **Equation 1.3.**

Downstream in the NDIR gas sensor are optical bandpass filters (as shown in **Figure 1.2**), which select specific IR bands to pass through to the detector and prevent others [91-92]. Carbon dioxide possesses an asymmetric stretch of its C=O bond ~2300-2400 cm^{-1} [91-92], which is used via the Beer-Lambert law to measure indoor gas levels. While these devices demonstrate longevity (10+ years of operation) and a lower limit of detection perfect for indoor quality monitoring (< 400 ppm CO_2), NDIR gas sensors have characteristically suffered from (i) expensive cost (> $100.00 USD) and (ii) bulky dimensions (cm length) required to achieve ppm-level detection [91].

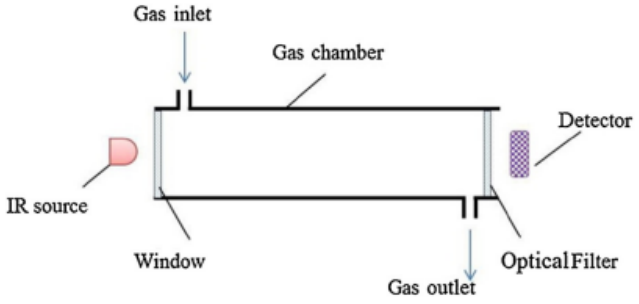

Fig. 1.2. Schematic of a simple NDIR gas sensor. Acquired from Dinh et al. (2016). [92].

$$T = \frac{I}{I_0} = e^{-\varepsilon cL} \quad \textbf{(Eq. 1.3)}$$

Where:
T is the transmittance (%)
I_0 is the input IR beam intensity
I is the beam intensity after traveling through gas molecules to the detector
c is the concentration of CO_2 (ppm)
L is the optical pathlength (cm),
and ε is the molar attenuation coefficient.

The ideal indoor gas sensor should be highly sensitive, highly selective, low-cost (< $10.00 USD), ultralow power, scalable, and simple to operate [93]. Moreover, since users may seek to index "personalized data" over time, this sensor should be compatible with mobile phone technologies such that sensing output can be stored via Internet-based digital communications [1]. Finally, research efforts should be expended to enable the wearability of the sensor, such that the device remains stable and collects reliable data as user surroundings change [94]. In the attempt to satisfy most of these sensing criteria, this work turns to *chemical sensors*. Chemical sensors, "as the result of a *chemical* interaction or process (i.e., a reaction) between the analyte and the device, transforms chemical… information of a quantitative or qualitative type into an analytically useful signal" [95]. In such systems, there is "a sensitive layer that is in chemical contact with the analyte gas," which then generates "a change in the chemistry of the sensitive layer" during exposure to the analyte [95]. Such changes are monitored through a *transduction domain*, which converts such analyte-interface interactions into assessable signals [95]. In this dissertation, *colorimetry* is the primary transduction domain. Colorimetry describes "the science of the measurement of colour" [96]. Here, the "perception of colour" involves the spectral power distribution, S(λ), of the light source, which is "the relative intensity of the illumination at each wavelength in the visible spectrum" [96]. When an object "reflects a certain fraction of the incident light"—expressed as R(λ)—the intensity of light entering the eye, I(λ), describes an interaction of both light source and reflectance terms, which generates the sensation of "color," as displayed via **Figure 1.3.**

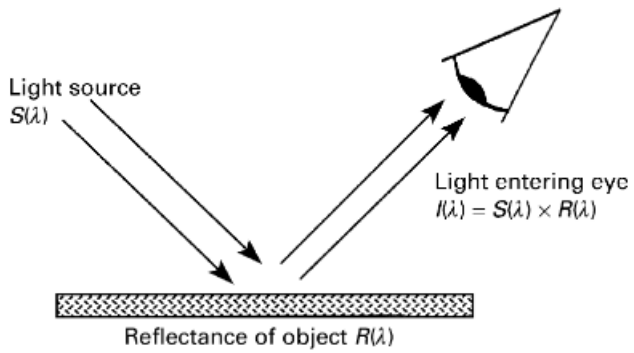

Fig. 1.3. Schematic of "color" through light source, object reflectance, and human eye interaction. Acquired from Gilchrist and Nobbs (2017). [96].

This dissertation studies inorganic, color-based chemical sensors assembled from primarily three components: (a) an adsorbent species, which provides a porous surface area to integrate sensing components and bind analyte species; (b) a reporter molecule, which translates the chemical interaction between the analyte and sensitive layer into a qualitative and quantifiable color change detectable to the naked eye; and (c) a signal enhancer/enabler species, which consists of functional groups incorporated into the sensor to increase sensitivity to select analytes and minimize signal interference from other chemical species in multicomponent systems. Here, the analyte species is indoor carbon dioxide, whose change in concentration is related to a color change detectable via the human eye and spectroscopic techniques.

Colorimetric sensing—alongside "easy fabrication," "quick detection" [97], and "cheap" operation [98]—offers user-friendly assessments required of the ideal indoor gas sensor [93, 97-98]. Through reporter engineering, colorimetric gas sensors can be functionalized to produce select colors in select gas environments (as depicted in **Figure 1.4**). In this dissertation, the research chapters are as follows: Chapter 2 describes the construction and characterization of a first-generation colorimetric indoor gas sensor; Chapter 3 describes the construction and characterization of a second-generation colorimetric indoor gas sensor; Chapter 4 illuminates the underlying chemical sensing mechanism and reporter/adsorbent adsorption thermodynamics involving the established sensors; and Chapter 5 describes the construction and characterization of a third-generation colorimetric indoor gas sensor. In Chapter 6, I conclude the dissertation with an overview of the prior chapters, as well as discuss an outlook for what remains to be accomplished to develop optimal gas sensors to enhance the wellness of life across the planet.

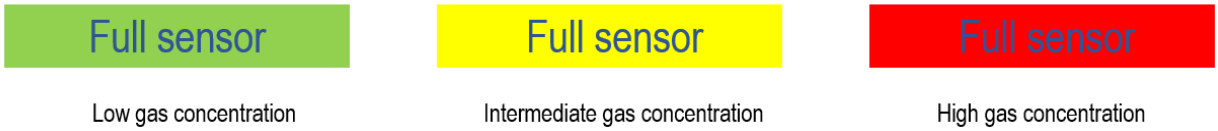

Fig. 1.4. Fundamental expression of the relationship between perceived color and indoor analyte concentration.

Chapter 2: Developing the Prototype: An Amine-Functionalized Zeolitic Imidazolate Framework -8 (ZIF-8)-Based Colorimetric Indoor Carbon Dioxide Sensor

The subject of this chapter is the synthesis and characterization of a first-generation indoor carbon dioxide sensor. This chapter is largely adapted from the manuscript, Davey et al., "Amine-functionalized metal-organic framework ZIF-8 toward colorimetric CO_2 sensing in indoor air environment." *Sensors and Actuators B: Chemical*, **2021**, 130313. DOI: https://doi.org/10.1016/j.snb.2021.130313) [99].

2.1 Introduction to Metal-Organic Frameworks (MOFs)

Metal-organic frameworks (MOFs) are hybrid inorganic-organic compounds constituted from the coordination of metal ions (or clusters) by organic linker (or ligand) molecules (as displayed in **Figure. 2.1**). [99-102]. MOFs are desirable materials because of their "ultrahigh porosity" [100], "enormous internal surface areas" [100], "highly uniform and tunable pore structure and size" [102], and "facile functionalization of metal nodes [and] ligands" [102]. In recent times, MOF research involving "green applications" has been widely investigated, involving "carbon capture," "VOC adsorption," "harmful organic dye" water pollution, and hydrogen (H_2) storage [103]. Throughout this dissertation, MOFs will function as *adsorbents*, which will be elaborated in greater detail in the ensuing section.

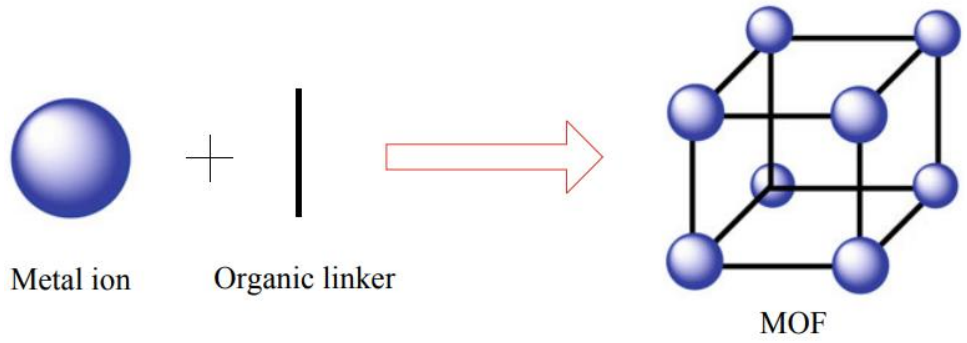

Fig. 2.1. Metal-organic framework (MOF) synthesis from the inorganic component (metal ion) and organic component (organic linker). Acquired from Varma et al. (2022). [102].

2.2 Construction of the First-Generation Sensor, PSP-ED/ZIF-8

2.2.1. Zeolitic imidazolate framework-8 (ZIF-8) as the adsorbent

Zeolitic imidazolate frameworks (ZIFs) are a "subclass of metal-organic frameworks" [104] constructed from transition metal ions tetrahedrally-coordinated by imidazolate ligands [99, 104-

105]. As shown in **Figure 2.2**, "the metal-imidazolate-metal (M-Im-M) angle is similar to the 145° Si-O-Si angle in zeolites, which give these materials 'zeolite-like' topologies" [99, 104-105].

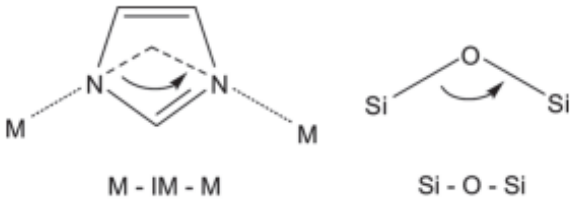

Fig. 2.2. Similarities in the bridging angle between M-Im-M (in ZIFs) as Si-O-Si (in zeolites). Acquired from Park et al. (2006). [105].

The ZIF used in this thesis is the zeolitic imidazolate framework-8 (or ZIF-8), which is synthesized from the reaction of zinc (Zn^{2+}) cations (from zinc nitrate hexahydrate) with 2-methylimidazolate (2-mIm^-) anions (from 2-methylimidazole) in solution [99, 106]. The chemical reaction is represented by **Equation 2.1** [106].

$$Zn^{2+} + 2(2mIm^-) \xrightarrow{mix\ in\ solvent} Zn(2mIm^-)_2 \qquad \textbf{(Eq. 2.1)}$$

As depicted in **Figure 2.3**, ZIF-8 demonstrates a *sodalite (sod)* topology, "comprised of 1.16 nm cages connected through six-membered windows, 0.34 nm in size" [107].

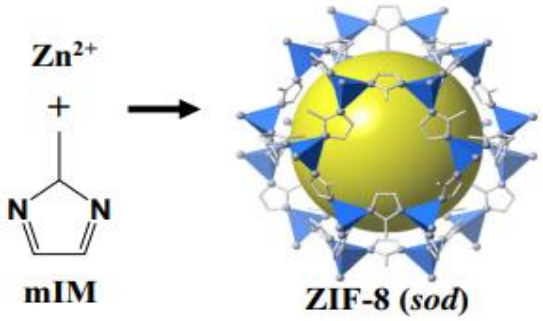

Fig. 2.3. Crystal structure of ZIF-8. Acquired from Lee et al. (2015). [107].

Interactions between MOFs and analytes can occur through "size exclusion" and energetics [108]. Through the "fine tuning of pore size," MOFs can facilitate the separation of gases with similar kinetic diameters [108]. In terms of energetics, MOFs adsorb target species through (a) chemisorption (which involves a "chemical transformation," such as "bond formation") and/or (b) physisorption (which describes how "the guest molecule interacts with the electric field produced by the framework") [108]. For polar guest molecules, the strength of the guest-framework

interaction, E_{int}, is related to the "guest dipole moment, (μ), and the strength of the electric field produced by the host framework ($\boldsymbol{E}_{xyz}$)," shown as **Equation 2.2** [108].

$$E_{int} = -\mu \boldsymbol{E}_{xyz} \quad \textbf{(Eq. 2.2)}$$

For nonpolar molecules (such as CO_2), the guest-framework interaction energy is mediated through the polarizability (α) of the guest molecule, which is related to the induced (or instantaneous) dipole, μ_i, and the applied electric field of the MOF, $\boldsymbol{E}_{xyz}$, as shown in **Equation 2.3** [108].

$$\mu_i = \alpha \boldsymbol{E}_{xyz} \quad \textbf{(Eq. 2.3)}$$

With regard to these MOF-analyte interactions, ZIF-8 is selected toward the construction of an indoor gas sensor because of its excellent selectivity for CO_2 reported in other studies [109-110]. Moreover, molecular simulations have associated preferable CO_2 adsorption sites with regions proximate to the organic linker of ZIF-8 [99, 111]. In addition to its demonstrated affinity for CO_2, ZIF-8 can be widely functionalized and loaded for various applications (while not compromising its crystalline structure), such as through amine-functionalization for effective radioactive iodine removal from the environment [112] and selective dye adsorption for pollutant separations [113]. Thus, because of its intrinsic physisorptive capacity to adsorb CO_2—as well as its demonstrated structural integrity upon the adsorption of other molecules for other research purposes—ZIF-8 is employed as an adsorbent for the integration of colorimetric ingredients (described next) toward indoor CO_2 monitoring.

2.2.2. Phenol red (PSP) as the halochromic compound/dye (reporter)

Halochromic compounds are materials which change color in response to a change in pH as the "external stimulus" [114]. This color change is accomplished through a change in *molecular conjugation*, which involves "the overlap of one p-orbital with another across an intervening sigma bond," which generates "alternating single and double bonds" [115]. This arrangement creates a *conjugated system*, which "is a system of connected p-orbitals with delocalized electrons in compounds with alternating single and multiple bonds" that "may lower the overall energy of the molecule and increase stability" [115]. When a pH change occurs, the degree of conjugation changes in a halochromic compound [116]. Highly-conjugated systems will demonstrate a closeness in energy between ground and excited electronic states such that longer wavelengths of light in the ultraviolet-visible (UV-Vis) region of the electromagnetic spectrum can be absorbed [116]. However, in less conjugated systems, higher energies (thus, shorter wavelengths of light) are required to promote electrons from ground states to permitted excited states [116]. In terms of *color*, the energy of absorbed radiation increases with *decreasing conjugation*: "red, orange, yellow, green, blue, and violet" [116]. Depending on the degree of conjugation, the molecule will

absorb within a particular region of the visible spectrum (and reflect the complementary color) [116].

Phenol red (phenolsulfonpthalein or PSP) is the halochromic compound (or dye) used in this dissertation. The change in molecular structure of phenol red with pH is depicted in **Fig. 2.4** [117]**.** Below pH 6.8, phenol red is yellow (λ_{max} = 443 nm) [118]. Between 6.8 and 8.2 pH units, phenol red is red; with increasing basicity (pH > 8.2), phenol red becomes fuchsia (λ_{max} = 570 nm) [118].

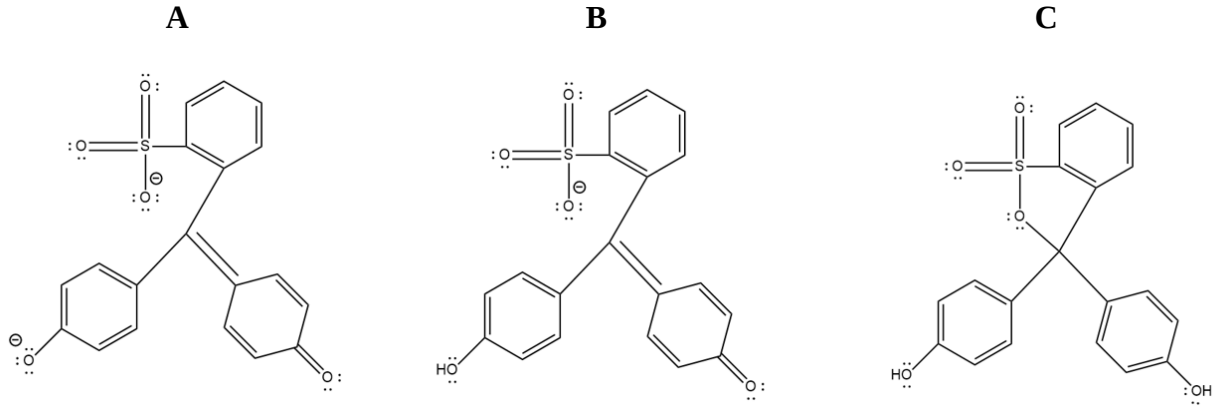

Fig. 2.4. Phenol red (PR) structure with modified pH. **(A)** Basic environment (pH > 8.2); **(B)** Basic to acidic environment (6.8 < pH < 8.2); and **(C)** Acidic environment (pH < 6.8).

In this chapter, phenol red is incorporated as a *reporter molecule* to monitor changes in the adsorbed CO_2 concentration on the surface of functionalized-ZIF-8 sensors through changes in the magnitude of fuchsia-to-yellow transitions observed via the human eye and spectroscopic instrumentation. The subsequent section will discuss the CO_2-affinative group enabling the pH change toward the full realization of the first-generation indoor colorimetric gas sensor.

2.2.3. Ethylenediamine (ED) as the CO_2-affinative group (signal enhancer)

Amine-based technologies remain critical tools for monitoring carbon-based emissions on varied scales [119]. Aqueous amine absorption technologies are implemented on an industrial scale toward CO_2 capture [119]. However, aqueous amine solutions are "highly corrosive" and "incur a high energy penalty for regeneration," which are unfavorable for power plant operations [119]. However, as improvements are made to these technologies, scientists continue to pursue opportunities to optimize amine-based adsorbents to "adsorb CO_2 from dilute and ultra-dilute sources such as flue gas or air" [119]. Through evaluation of adsorption capacity, selectivity, and regenerability, researchers screen "proposed CO_2 adsorbents" [119].

Ethylenediamine (ED) is a primary amine (shown in **Figure 2.5**) which has been loaded into manganese-based MOFs to enhance water stability and carbon dioxide uptake [120], as well as used to functionalize zirconium-based MOFs for "efficient removal of heavy metal ions from water" [121].

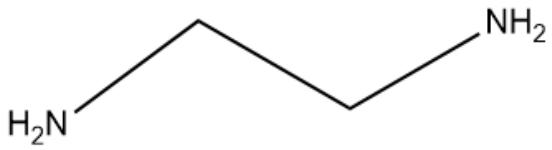

Fig. 2.5. Chemical structure of ethylenediamine (ED).

Here, ZIF-8 is functionalized with ethylenediamine, which enables a chemisorptive mechanism through which to trigger colorimetric activity. In the "Discussion" section of this chapter, proposed mechanisms will be addressed with respect to *how* the color change is achieved upon surface incorporation of ethylenediamine molecules.

2.2.4. Formation of PSP-ED/ZIF-8

The preparation of the first-generation colorimetric indoor carbon dioxide sensor, PSP-ED/ZIF-8, follows the exact recipe described in Davey et al. (2021) [99]. This procedure is adapted from room-temperature methanolic ZIF-8 synthesis achieved by Cravillon et al. [122].

"1.04 g of zinc nitrate hexahydrate [$Zn(NO_3)_2 \cdot 6H_2O$; Fischer Scientific] and 1.04 g of 2-methylimidazole (Hmim, 99%, Sigma-Aldrich) are dissolved in 60 ml of methanol (Fischer Chemical), separately, and then mixed and allowed to react at room temperature overnight (with no stirring). Pristine ZIF-8 crystals are then partially activated, washing three times with methanol using a Beckman Coulter, Inc. Microfuge®18 Centrifuge at 12,000 rpm for 5-min.

"For the synthesis of PSP-ED/ZIF-8 material, a 2% ethylenediamine (99%, Sigma-Aldrich) solution (% v/v) in methanol is produced by adding 400 μl of ethylenediamine to 19.6 ml of methanol. 10 mg of phenolsulfonpthalein (Acros Organics) is then dissolved into this solution. Aliquots of this solution are then mixed with the partially-activated ZIF-8 (80 mg ZIF-8/ml

colorimetric solvent) with prolonged sonication to achieve the PSP-ED/ZIF-8 solution" [99]. Optical images of the material at various stages of synthesis are depicted in **Figure 2.6** [123].

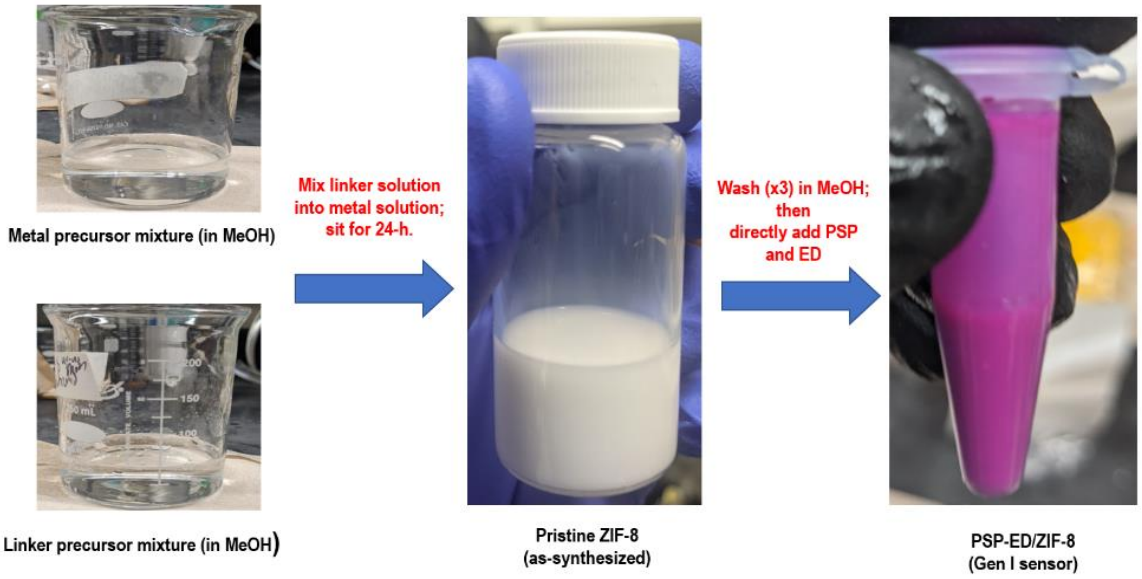

Fig. 2.6. Synthesis of the first-generation sensor, PSP-ED/ZIF-8. Adapted from Davey et al. (2023) [123].

2.3 Experimental Characterization Techniques

This section will describe the various characterization techniques used to exhaustively analyze the structure, morphology, surface area, and colorimetric gas sensing fitness of PSP-ED/ZIF-8.

2.3.1. Powder X-ray diffraction (PXRD)

Powder X-ray diffraction (PXRD) "is a rapid analytical technique primarily used…for the identification of unknown crystalline materials" [124]. X-rays are produced "in a cathode ray tube by heating a filament to produce electrons, accelerating the electrons toward a target by applying a voltage, and bombarding the target material with electrons. When electrons have sufficient energy to dislodge inner shell electrons of the target material, characteristic X-ray spectra are produced. As the sample and detector are rotated, the intensity of the reflected X-rays is recorded. When the geometry of the incident X-rays impinging the sample satisfies the Bragg Equation, constructive interference occurs and a peak in intensity occurs" [124]. Bragg's theory describes the diffraction of monochromatic X-rays [125]. "Bragg's analysis" assumes "that crystals are in layers or atomic planes (lattice plane- *hkl*) are in layers with spacing distance, *d* and produce reflection when incident light or x-ray impinges on the planes of atom. [The] incident beam makes equal angle with corresponding diffracted beam at the lattice plane" [125]. When Bragg's law (shown as **Equation 2.4**) is satisfied, the "path difference lengths equal nλ," and constructive interference occurs such that a diffraction peak intensity is observed [125]. This condition under which Bragg's law is satisfied is demonstrated in **Figure 2.7** [125].

$$n\lambda = 2dsin\theta \quad \textbf{(Eq. 2.4)}$$

Where:
n is the X-ray wavelength (in Å)
λ is the "order of reflection."
d is the spacing distance (Å)
and θ is the angle of the diffraction beam [125].

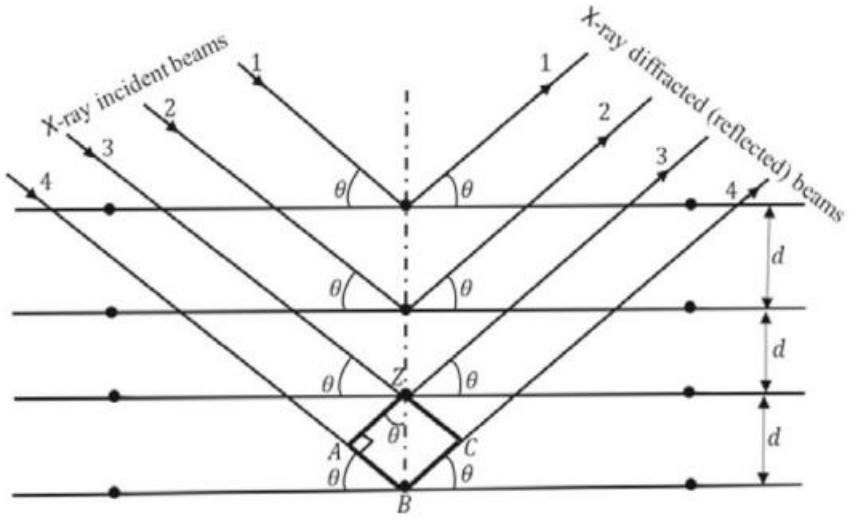

Fig. 2.7. Bragg's theory represented with X-ray diffraction on a sample. Acquired from Ameh (2019) [125].

In this chapter, "Powder X-ray diffraction (PXRD) patterns are collected with a Bruker diffractometer (Cu *K*-α radiation, λ = 1.54 Å, 40 kV, 40 mA)" [99].

2.3.2. Scanning electron microscopy (SEM)

Scanning electron microscopy (SEM) is a "non-destructive" technique which "uses a focused beam of high-energy electrons" to probe the morphological features of "solid specimens" [126]. "Accelerated electrons… carry significant amounts of kinetic energy, and this energy is dissipated as a variety of signals produced by electron-sample interactions when the incident electrons are decelerated in the solid sample" [126]. "These signals include secondary electrons (that produce SEM images)," as well as "backscattered electrons," "diffracted backscattered electrons," "photons," "visible light," and "heat" [126]. In this chapter, "Sample particle size is acquired using scanning electron microscopy (SEM, Hitachi S-5000). A thin Au/Pd layer is sputter deposited on the samples to afford some electrical conductivity to the material prior to SEM imaging" [99].

2.3.3. Brunauer-Emmett-Teller (BET) surface area characterization

Assessment of the porous properties of MOFs is crucial for post-synthetic functionalization and attendant gaseous analyte adsorption. "During the process of physical adsorption, at very low relative pressure, the first sites to be covered are the more energetic ones. Those sites with higher energy on a chemically pure surface reside within narrow pores where the pore walls provide overlapping potentials. On surfaces consisting of heteroatoms, such as organic solids or impure materials, there will be variations in adsorption potential depending upon the nature of the atoms of functional groups exposed at the surface" [127]. While "more energetic sites are covered first as the pressure is increased," this behavior does not suggest "that no adsorption occurs on sites of lower potential," but instead "implies that the average residence time of a physically adsorbed molecule is longer on the higher-energy sites" [127]. When "the adsorbate pressure is allowed to increase, the surface becomes progressively coated and the probability increases that a gas molecule will strike and be adsorbed on a previously bound molecule" [127]. Therefore, "prior to complete surface coverage the formation of second and higher adsorbed layers will commence" [127].

The Brunaeur-Emmett-Teller (BET) theory describes multilayer adsorption and assumes that "where the surface is covered with only one layer of adsorbate, an equilibrium exists between that layer and the vapor; where two layers are adsorbed, the upper layer is in equilibrium with the vapor, and so forth" [127]. For "second and higher layers," the BET theory assumes that **A** ("probability of a molecule's being adsorbed upon collision with the surface"), **ν** ("vibrational frequency of the adsorbate normal to the surface when adsorbed"), and **E** (energy of adsorption) are constant [128]. This theory also assumes that "second and higher layers are all equivalent to the liquid state" [127]. Here, the energy of adsorption, **E,** is transformed into the heat of liquefaction, **L**, for second and higher layers [127].

In determining the BET surface area, equilibria established between the first and second layer (and the second and higher layers) generates the BET constant, C, shown in **Equation 2.5** [127]:

$$C = \frac{A_1 \, v_2}{A_2 v_1} e^{\frac{E_1 - L}{RT}} \qquad \textbf{(Eq. 2.5)}$$

Where:
C is the BET constant,
A_1 is the probability of molecular adsorption upon collision with the first layer,
A_2 is the probability of molecular adsorption upon collision with the second layer,
$\boldsymbol{v_1}$ is the vibrational frequency of the adsorbate normal to the surface of the first layer,
$\boldsymbol{v_2}$ is the vibrational frequency of the adsorbate normal to the surface of the first layer,
E_1 is the heat of adsorption onto the first layer,
L is the heat of liquefaction (for second and higher layers),
R is the gas constant,
and T is the temperature.

Surface area determination is accomplished through the BET equation, shown as **Equation 2.6** [127]:

$$\frac{1}{W\left[\frac{P_0}{P}-1\right]} = \frac{1}{W_m C} + \frac{C-1}{W_m C} \quad \textbf{(Eq. 2.6)}$$

Where:
C is the BET constant,
P/P_0 is the relative pressure,
W is the weight adsorbed,
and W_m is the weight adsorbed in a complete monolayer. [all punctuation modified to be consistent with previous equation.]

A plot of $1/W[P_0/P-1]$ vs. P/P_0 will produce a straight line typically for $0.05 \leq P/P_0 \leq 0.3$ [128]. W_m and C can be determined from the slope, *s*, and the y-intercept, *I*, of **Equation 2.6** (as shown in **Equation 2.7** and **Equation 2.8**) [127].

$$W_m = \frac{1}{s+i} \quad \textbf{(Eq. 2.7)}$$

$$C = \frac{s}{i} + 1 \quad \textbf{(Eq. 2.8)}$$

With W_m known, the BET surface area (S_{BET}) can be calculated from **Equation 2.9** [127]:

$$S_{BET} = \frac{W_m \bar{N} A_x}{\bar{M} m} \quad \textbf{(Eq. 2.9)}$$

Where:
W_m is the weight adsorbed in a complete monolayer,
N is Avogadro's number,
A_x is the cross-sectional area of the adsorbate,
M is the molecular weight of the adsorbate,
and m is the sample mass.

When determining S_{BET}, the value of "C" must be positive. As shown in **Equation 2.5**, the C value mathematically cannot be less than zero because of the exponential difference between the energy of adsorption of the first layer and the heat of liquefaction (thus possessing physical significance) [127]. For microporous materials, the range of P/P_0 may need to be adjusted to P/P_0 values less than 0.05 to attain a positive C value from the linear plot [127].

In this chapter, the BET measurement is as established in Davey et al. [99]. After the partial activation steps described in earlier, "the washed ZIF-8 crystals are dried at 60 °C on a hot plate

overnight. Then, the ZIF-8 crystals are recovered, placed in an oven, and heated at 110 °C (in air) for 24 h. Nitrogen adsorption isotherms are measured at 77 K using Tristar II 3020 volumetric adsorption analyzers manufactured by Micromeritics (Norcross, GA). Before adsorption measurements, the samples are out-gassed under vacuum for 24 h at 150 °C. The specific surface area of the samples is calculated using the Brunauer–Emmett–Teller (BET) method within the relative pressure range of 0.01 to 0.95 (p/p_0)" [99].

2.3.4. Ex-situ ultraviolet-visible (UV-Vis) diffuse reflectance spectroscopy

Ultraviolet-visible (UV-Vis) spectroscopy is an analytical technique that probes "electronic excitations between the energy levels that correspond to the molecular orbitals of… systems" between ~200 and 800 nm [128]. The "lowest energy transition" involves electronic transitions from the "highest occupied molecular orbital (HOMO" in the ground state to the "lowest unoccupied molecular orbital (LUMO)" in an excited state [128]. As illustrated in a previous section, the HOMO-LUMO distance corresponds to the degree of conjugation in the system [115-116, 128]. These HOMO-LUMO distances, then, for conjugated systems correspond to different wavelengths which could be absorbed (or reflected) in the visible region, permitting the perception of color [115-116, 128].

To productively investigate the color change of dye- and amine-loaded ZIF-8-based sensors when exposed to different levels of indoor carbon dioxide, the interactions between radiation and sample must be properly understood. When radiation strikes "smooth, polished surfaces like mirrors," *specular reflection* occurs in which "the angle of reflection [is] equal to the angle of incidence" [129]. However, for "dull surfaces textured like powders" exhibit *diffuse reflection*, where "the angle of reflection is independent of the angle of incidence" [129]. Diffuse reflection involves "a combination of reflection, refraction, and… (scattering) of impinging light," as well as absorption [129]. Therefore, such samples exhibiting this behavior are "simultaneous scatterers and absorbers of electromagnetic radiation" [129]. These differences between specular reflection and diffuse reflection are displayed in **Figure 2.8** [129].

Such complicated behavior of diffuse reflectors is characteristically represented by two-parameter models involving absorbance and scattering coefficients [129]. Throughout this dissertation, the Kubelka-Munk transform, F(R), is used to elucidate how UV-Vis radiation interacts with colorimetric gas sensors before and during controlled gas delivery [99, 129-130]. The Kubelka-Munk model approximates "the radiation field" as two fluxes: (1) I_{+}, traveling from the "illuminated sample surface" and (2) I_{-}, "traveling toward the illuminated surface" [130]. The background contributes a reflectance, R_g [130]. This theory is modeled in **Figure 2.9** [130].

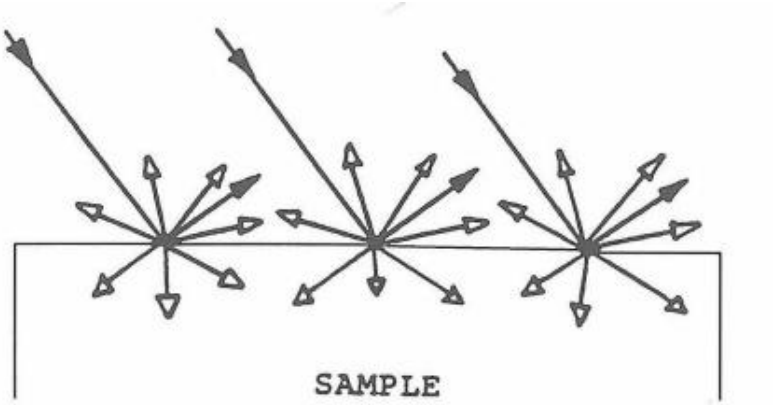

Fig. 2.8. Specular reflection (shaded arrows) and diffuse reflection (unshaded arrows). Acquired from Blitz (1998). [129].

"As radiation travels from the surface, its intensity is decreased by scattering and absorption processes, both assumed to be proportional to the thickness of the medium traversed. This is partially offset by scattering from the other beam," which produces **Equation 2.10** [130]:

$$dI_+ = -(S+K)I_+dx + SI_-dx \qquad \textbf{(Eq. 2.10)}$$

Where:
S is the scattering coefficient and K is the absorption coefficient.

A similar equation can be written for the flux traveling toward the illuminated surface, as expressed by **Equation 2.11** [130]:

$$dI_- = (S+K)I_-dx - SI_+dx \qquad \textbf{(Eq. 2.11)}$$

If the diffuse reflectance, R, is described as shown in **Equation 2.12** [130]:

$$R = \frac{I_-}{I_+} \qquad \textbf{(Eq. 2.12)}$$

Then a differential equation, dR/dx (shown as **Equation 2.13**), can be written such at some reflectance, R_∞, "of a layer which is so thick that further increase in thickness does not alter the reflectance" [130]:

$$\frac{dR}{dx} = S\left({R_\infty}^2 - 2R_\infty\left(\frac{K+S}{S}\right) + 1\right) = 0 \qquad \textbf{(Eq. 2.13)}$$

Through rearrangement, the Kubelka Munk, F(R), transform is achieved, as shown in **Equation 2.14** [130]:

$$F(R) = \frac{(1-R_\infty)^2}{2R_\infty} = \frac{K}{S} \quad \textbf{(Eq. 2.14)}$$

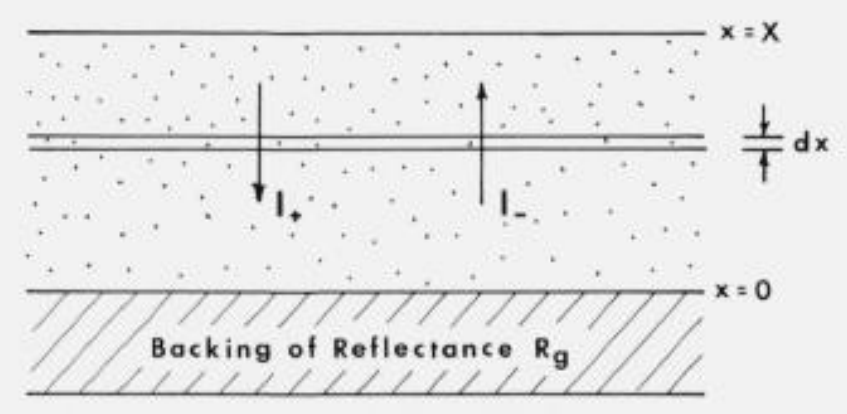

Fig. 2.9. Model of the Kubelka-Munk theory. Acquired from Hecht (1976). [130].

The gas dosing spectroscopic process works as illustrated in Davey et al. [99]. "Quantitative assessment of colorimetric CO_2 sensing is accomplished through ex-situ ultraviolet-visible diffuse reflectance spectroscopy with a Cary 5000 (Instrument No. 5.2) spectrophotometer at a scan rate of 600 nm/min. Colorimetric sensing experiments using UV-vis spectroscopy are conducted as follows. Cellulose filter paper (VWR North American) is first cut into a 0.7 cm x 0.7 cm square, affixed to a piece of double-sided black tape of same size, placed inside the UV-vis sample enclosure, and used as a blank in the UV-vis spectrophotometer. Then, another cellulose filter paper of the same size is cut and 15 μl of PSP-ED/ZIF-8 solution is drop-cast on it. After 120 s sitting in ambient environment, most of the methanol evaporates. This coated paper is similarly placed in the spectrophotometer and a 'Pre-CO_2 exposure' plot of reflectance (% R) vs wavelength (nm) is recorded" [99].

"After this run, the sample enclosure is partially opened and placed inside a specifically designed plexiglass enclosure (9 cm x 7.4 cm x 3.6 cm). Colorimetric CO_2 uptake in variable humidity is achieved by connecting the enclosure to a gas manifold [**Figure 2.10]**, which allows computer-controlled delivery of CO_2 and relative humidity via mass flow controllers (Bronkhorst) set by LabView software. A cylinder of 22,000 ppm CO_2 balanced in nitrogen is used (Praxair). Purge and balance streams are provided by passing house air through pressure swing adsorption dryers to remove humidity and an activated carbon scrubber to eliminate contaminants. Different humidity levels are created via a bubbler and controlled by the same feedback calibration system set by the LabView program. A wireless GasLab Plus CM-501 NDIR sensor is integrated in the apparatus to calibrate the achieved CO_2 and humidity levels set in LabView (as shown in [**Figure 2.11**]. For the measurements reported here, the total gas flow rate is kept constant at 300 standard cubic centimeters per minute (sccm) and the flow stream temperatures are measured at room temperature (22.0 ± 0.5 °C)" [99].

"For a given trial, the system is first purged with dry air until < 500 ppm CO_2 and the desired humidity are achieved. Then, the sample is exposed to the desired CO_2 concentration while the NDIR sensor logs the data until steady state is reached. The sample enclosure is then placed back in the spectrometer and UV-vis spectra are collected. For each trial, the % R data are converted to F(R) values (using [**Equation 2.14**]) and plotted**.** In typical absorbance spectra, phenolsulfonpthalein exhibits a color change from purple (λ_{max} = 570 nm) in basic environment to yellow (λ_{max} = 443 nm) in acidic environments [117-118]. For each CO_2 exposure (dry or humid), the ratios of the F(R) values at 443 and 570 nm are computed and plotted against CO_2 concentration (ppm). For each CO_2 exposure, at least two trials are averaged, and the standard deviation is depicted as error bars" [99].

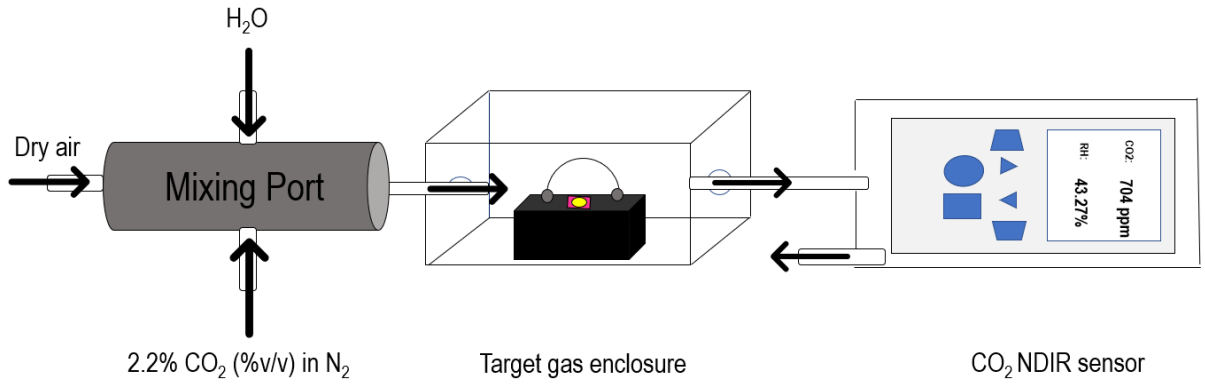

Fig. 2.10. "Gas manifold for ex-situ colorimetric CO_2 experiments. Mass flow controllers adjust flow rates of gases to be mixed, which are then directed into the enclosure where the PSP-ED/ZIF-8 sample is housed within a partially unscrewed UV-vis sample holder. The gas stream is fed into a NDIR sensor kept inside of a plastic enclosure, which reports the CO_2 concentration (ppm) and relative humidity (%)." Acquired from Davey et al. (2021). [99].

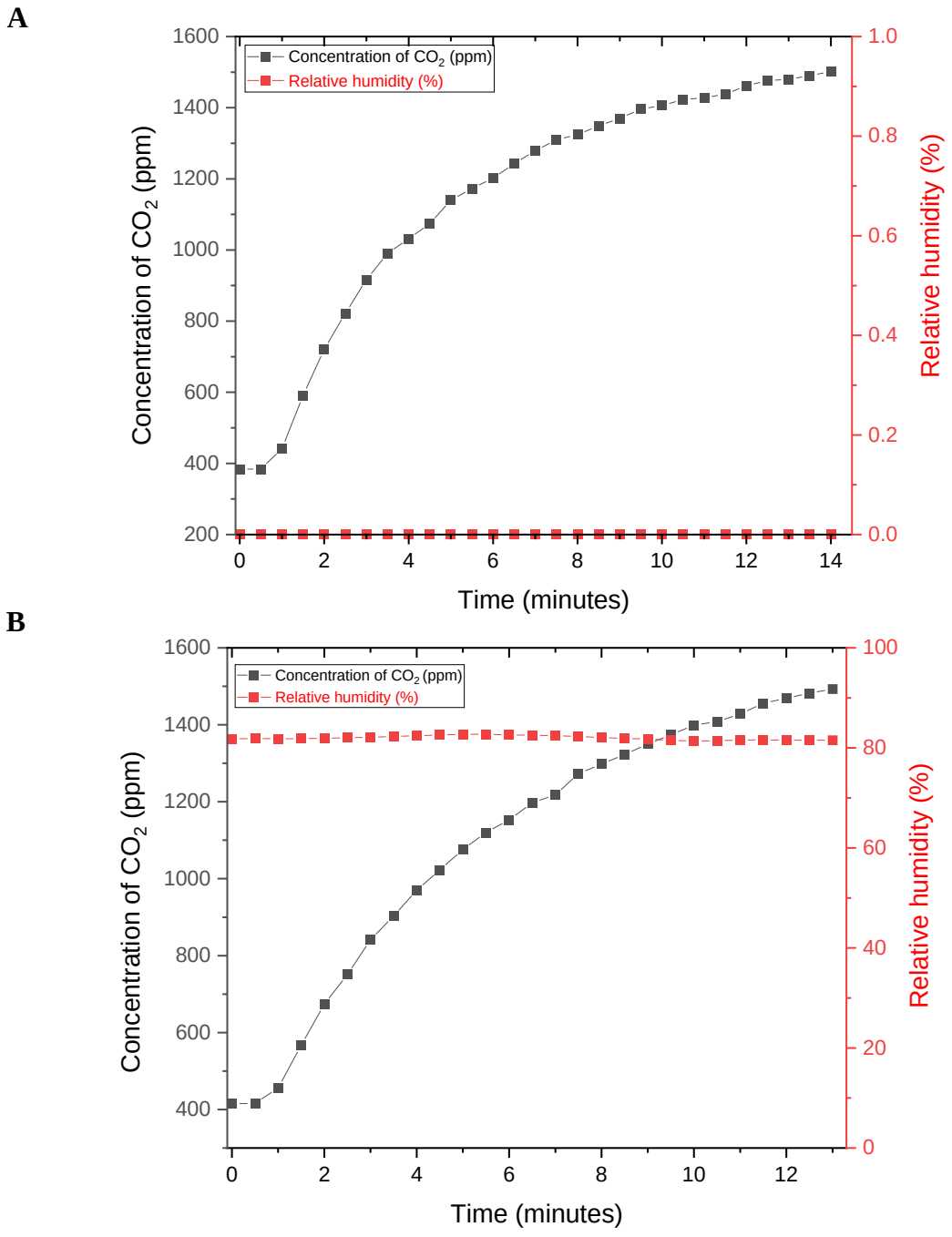

Fig. 2.11. "Sample CO_2 NDIR sensor calibrations for **(A)** 1,500 ppm CO_2, [0% RH] and **(B)** 1,500 ppm CO_2, 80% RH." Acquired from Davey et al. (2021). [99].

2.3.5. Colorimetric imaging through direct exposure assays

Colorimetric imaging is performed as explained in Davey et al. [99]. "Optical images of the samples under various environments are also obtained using the direct exposure technique (all exposures at 300 sccm). For direct exposure measurements, colorimetric ZIF-8 sensors are drop-cast on cellulose filter paper and allowed to dry for 120 s in ambient environment. Then, a video (using a Google Pixel smartphone) is recorded with applied CO_2 and relative humidity (for 10 s). After 10 s, the CO_2 atmosphere is removed, and the sensor recovers over 15 s intervals before subsequent exposure. Background CO_2 and relative humidity are logged with the GasLab Plus CM-501 CO_2 NDIR sensor" [99].

2.4 Discussion

The discussion in this chapter is entirely adapted from Davey et al. [99].

2.4.1. Material characterization

"[**Figure 2.12**] displays the XRD patterns obtained on the as-synthesized pristine ZIF-8, the PSP-ED/ZIF-8, as well as the simulated ZIF-8 (refcode: VELVOY) [131]. The major characteristic diffraction peaks at $2\theta = 7.3$, 10.4, 12.6, 14.6, 16.4, 17.9, 22.0, 24.4, and 26.6° associated with the (011), (002), (112), (022), (013), (222), (114), (233), and (134) planes are observed [132]. These results are consistent with prior reports of the pristine MOF developed in methanol at room temperature, indicating formation of the expected sodalite structure [132]. The PSP-ED/ZIF-8 sensor stability is assessed using XRD [**Figure 2.13**]. Over a 4-week timespan (at room temperature), the bulk PSP-ED/ZIF-8 material retains its crystallinity in ambient environment, demonstrating no loss of the structural integrity of ZIF-8 when mixed with phenolsulfonpthalein and ethylenediamine in methanol. MOF structural resistance to environmental factors, such as moisture and basicity, is imperative toward feasible use under various conditions [133]. In accordance with the Pearson acid-base concept, the strength of the soft ligand (imidazole) and soft metal (Zn^{2+}) interaction offers ZIF-8 a high chemical stability [134]" [99].

"Representative SEM images of pristine ZIF-8 (washed) and PSP-ED/ZIF-8 are shown in [**Figure 2.14]**. With the MOF precursor molar ratio used (metal: linker: solvent – 1:3.62:847) at room temperature in methanol, ZIF-8 nanocrystals (consistent in size with reported values in the literature) are obtained [135]. For the activated pristine ZIF-8, the BET surface area (calculated from the nitrogen isotherm in **[Figure 2.15]**) is measured to be 1,485 m^2/g, which is likewise in agreement with previously reported values [136-137]" [99].

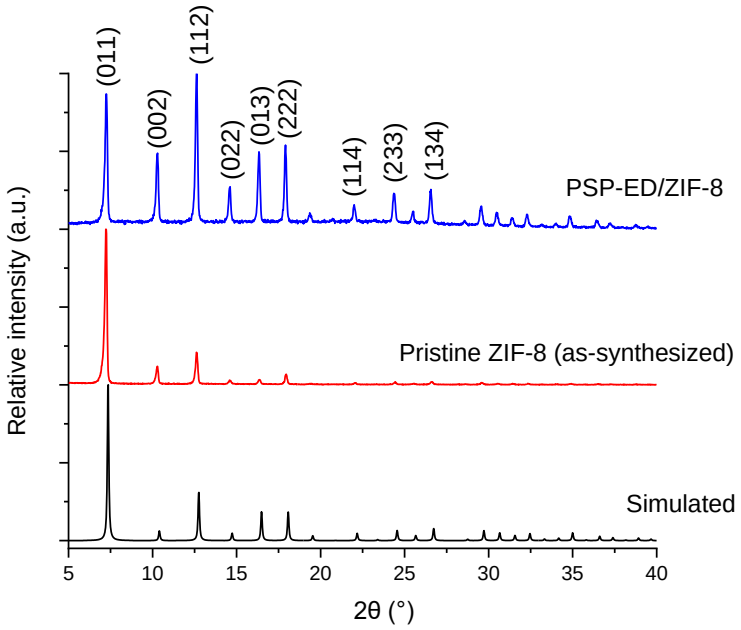

Fig. 2.12. "Powder X-ray diffraction patterns (Cu *K*-α radiation, λ = 1.54 Å)." Acquired from Davey et al. (2021). [99].

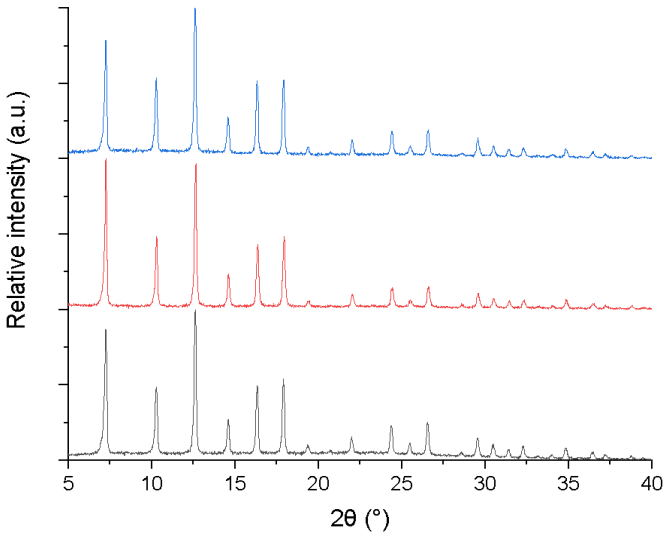

Fig. 2.13. "Effect of shelf-life on PSP-ED/ZIF-8 structure: PXRD patterns for fresh sensor (black); deposited sensor after two weeks (red); and deposited sensor after four weeks (blue)." Acquired from Davey et al. (2021). [99].

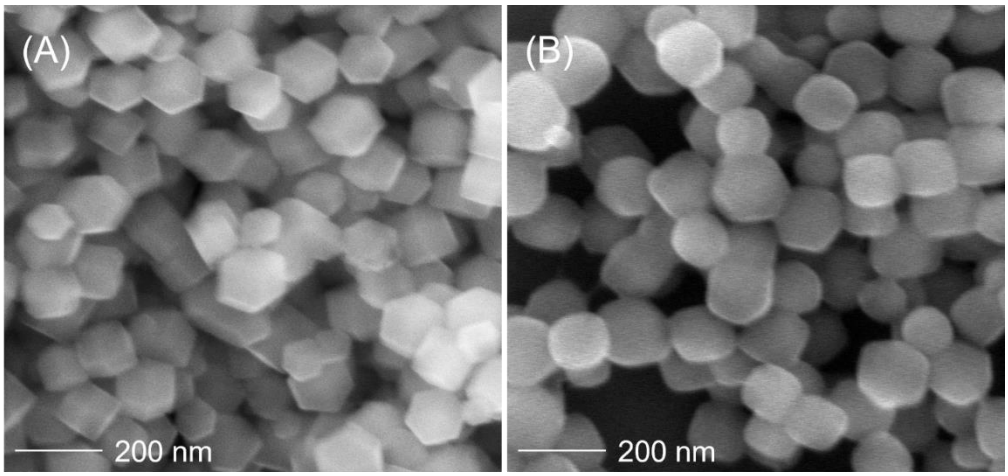

Fig. 2.14. "SEM images for **(A)** washed pristine ZIF-8 and **(B)** PSP-ED/ZIF-8 (2% ED). Size bar = 200 nm." Acquired from Davey et al. (2021). [99].

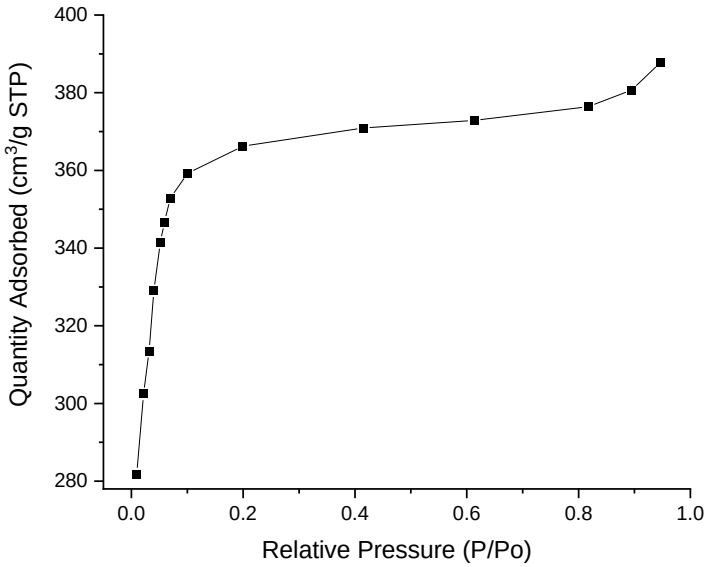

Fig. 2.15. "Nitrogen adsorption isotherm (77 K) of activated ZIF-8." Acquired from Davey et al. (2021). [99].

2.4.2. Colorimetric analyses in dry environment

"Representative colorimetric images of fresh PSP-ED/ZIF-8 exposed to CO_2 (dry) using the direct-exposure technique are shown in [**Figure 2.16**]. With increased CO_2 exposure, the drop-cast PSP-ED/ZIF-8 (initially purple) demonstrates an obvious color shift to higher intensities of yellow. This colorimetric shift is rendered possible through collaboration of phenolsulfonpthalein, ethylenediamine, and ZIF-8. To highlight the critical role of all three components, the colorimetric responses to just phenolsulfonpthalein, phenolsulfonpthalein/ethylenediamine, and phenolsulfonpthalein/ZIF-8 materials are compared to PSP-ED/ZIF-8. As can be seen in [**Figure 2.16A**], all three components — ZIF-8, ethylenediamine, and phenolsulfonpthalein— are necessary to achieve a visible response. Without any of these components, the sensors exhibit no visible response to even high levels of CO_2. As observed in [**Figure 2.16B]**, the degree of yellow achieved intensifies as the CO_2 concentration exposed increases from 700 to 7,500 ppm," indicating an increased colorimetric response with rising dry CO_2 levels [99].

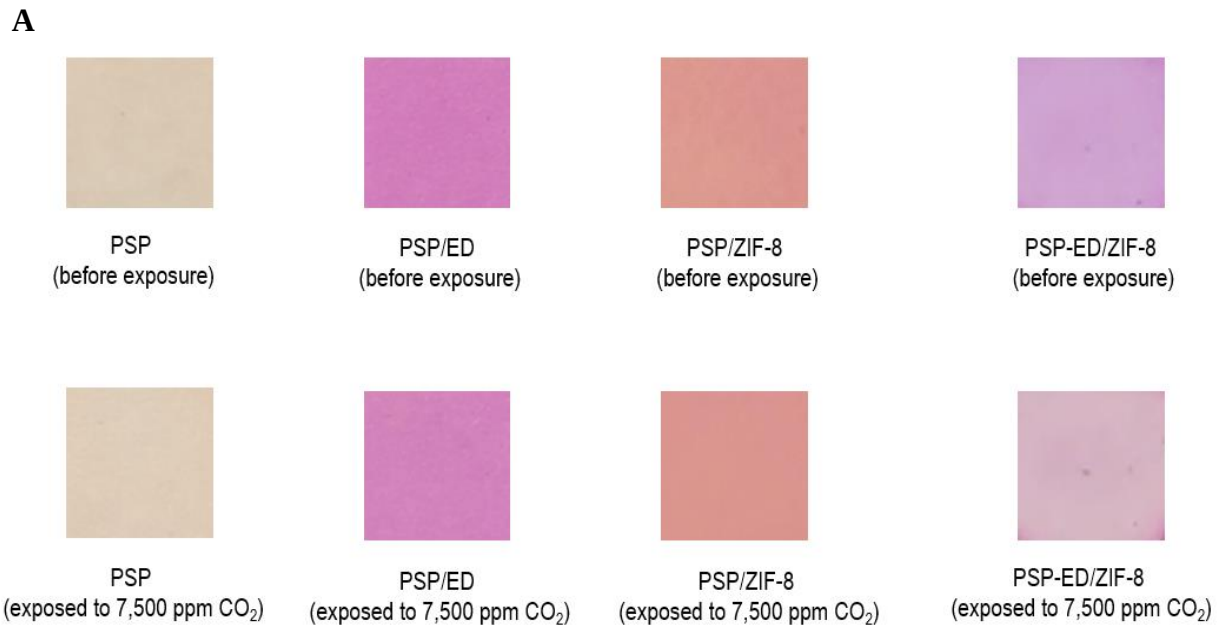

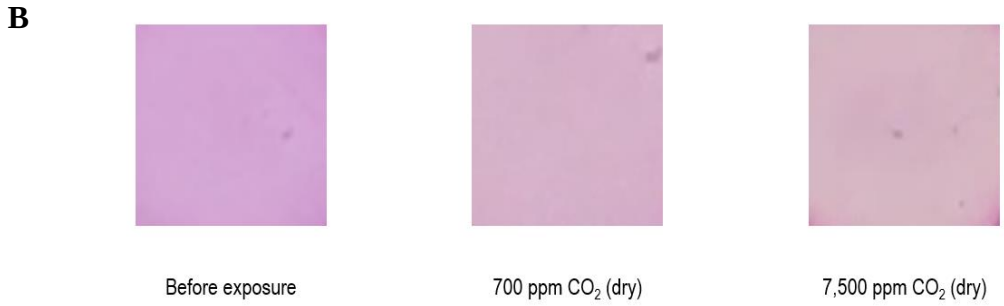

Fig. 2.16. "(A) Effects of various components in colorimetric response to 7,500 ppm CO_2. First column: 15 µl of a methanolic 0.5 mg/ml phenolsulfonpthalein solution drop-cast on cellulose filter paper. Second column: 15 µl of a methanolic 0.5 mg/ml phenolsulfonpthalein /ethylenediamine solution (2% ED, %v/v) drop-cast on cellulose filter paper. Third column: 15 µl of an 80 mg/ml ZIF-8 solution (prepared from a methanolic 0.5 mg/ml phenolsulfonpthalein solution) drop-cast on cellulose filter paper. Fourth column: 15 µl of PSP-ED/ZIF-8 drop-cast on cellulose filter paper. **(B)** Colorimetric response of PSP-ED/ZIF-8 before CO_2 is applied, when 700 ppm CO_2 is applied, and when 7,500 ppm CO_2 is applied. All under dry conditions." Acquired from Davey et al. (2021). [99].

"For the low partial pressures of CO_2 involved in this study, the visible change in colorimetric response to variable CO_2 concentrations can be difficult to qualitatively distinguish by human eye. In a similar manner to published work involving phenolsulfonpthalein absorbance spectra in cell culture media [138], plots of the 443/570 nm F(R) ratios from the UV-vis data are developed for each sensor at a specific humidity to draw quantifiable differences. First, FI vs. wavelength (nm) plots are collected (shown in [**Figure 2.17**]. With increasing the concentration of CO_2, the exposed sensor becomes more yellow and the F(R) value at 570 nm decreases.

"Ratiometric profiles from ex-situ diffuse reflectance UV-vis measurements are shown in [**Figure 2.18**] for the PSP-ED/ZIF-8 sensor. For this sensor, a broad range of target concentrations (700 – 7,500 ppm CO_2) is tested. With increasing CO_2 concentration, the colorimetric ratios (red symbols) noticeably rise from 0.283 to 0.701 ratiometric units, and the corresponding colorimetric CO_2 response visibly intensifies from 700 to 7,500 ppm CO_2 exposures under 0% relative humidity" [99].

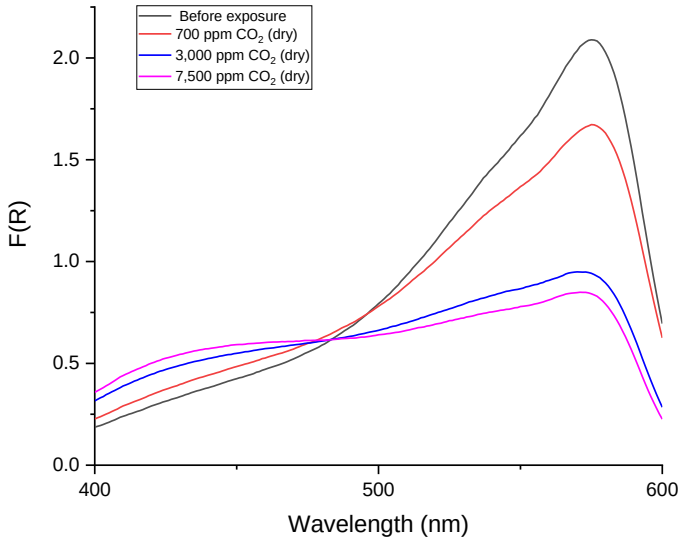

Fig. 2.17. "F(R) vs wavelength (nm) profiles with PSP-ED/ZIF-8 in variable dry CO_2 environment." Black: Before controlled CO_2 delivery. Red: 700 ppm CO_2. Blue: 3,000 ppm CO_2. Fuchsia: 7,500 ppm CO_2. Acquired from Davey et al. (2021). [99].

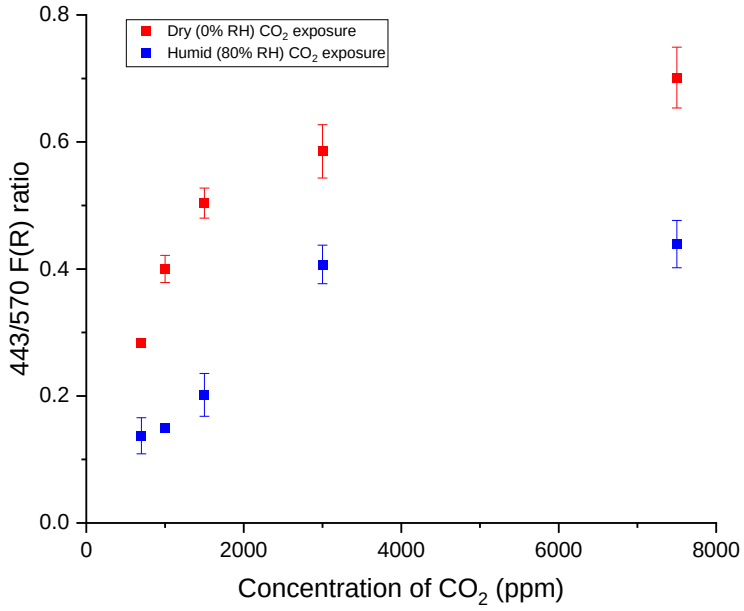

Fig. 2.18. "UV-vis ratiometric profiles (700-7,500 ppm CO_2) of PSP-ED/ZIF-8 in variable humidity." Red: 0% RH. Blue: 80% RH. Acquired from Davey et al. (2021). [99]. Error bars are standard deviation values.

"The observed colorimetric behavior is consistent with proposed reactions between ethylenediamine, CO_2, and other bases. In previous work, ethylenediamine has been grafted onto ZIF-8 via post-synthetic modification to provide basic sites toward an enhanced, solid-state CO_2 adsorption [139]. For the reported colorimetric analyte studies, the observed CO_2 response (in methanol) is proposed to occur via a two-step zwitterion mechanism [140-145], whereby (in this instance) CO_2 is adsorbed on ZIF-8 to react with the other colorimetric sensor components. In aqueous and nonaqueous solvents, ethylenediamine and CO_2 react **[Equation 2.15]** to form a 1°,3°-zwitterion intermediate, RH_2N^+—COO^-:

$$CO_2 + RNH_2 \leftrightarrow RN^+H_2CO_2^- \quad \textbf{(Eq. 2.15)}$$

"The 1°,3°-zwitterion is then deprotonated [**Equation 2.16**] by a base, B, which could be unreacted ethylenediamine, H_2O, solvent molecules, or other species in the system [140-145]. When phenolsulfonpthalein (pKa: 7.9) participates as the base, the deprotonation step shifts the pH from above 8.2 to below 6.8 and induces a colorimetric response from fuchsia to yellow [146].

$$RN^+H_2CO_2^- + B \leftrightarrow RNHCO_2^- + BH^+ \quad \textbf{(Eq. 2.16)}$$

"Repeat exposures at 700, 3,000, and 7,500 ppm CO_2 (dry) are depicted in [**Figure 2.19]**. The colorimetric CO_2 response occurs within seconds as the CO_2 concentrations are repeatedly introduced and removed. However, partial recovery is obtained with each sensor, as the final color after a third dry CO_2 exposure is modestly more yellow than that of the fresh sensor prior to dosage. While some solid-state MOF sensors demonstrate reversible CO_2 detection [147], amine-based liquid gas sensors can suffer from sluggish kinetics [93]. As shown in [**Equation 2.16]**, the carbamates formed upon zwitterionic deprotonation in protic solvent are thermodynamically stable, requiring thermal regeneration processes to reuse the sensor [93]. Thus, the sensor presented here is envisioned as a single-use sensor for colorimetric CO_2 sensing, which is commensurate with modern acid-base commercialized colorimetric sensors implemented in hospital care [148]" [99].

"As shown in [**Figure 2.16**]**,** the combined interaction of phenolsulfonpthalein, ethylenediamine, and ZIF-8 with CO_2 facilitates colorimetric gas detection. Based on the BET measurements with the pristine MOF, ZIF-8 is expected to provide a high surface area for CO_2 adsorption, as well as accommodate both phenolsulfonpthalein and ethylenediamine for the two-step zwitterion reaction. Amine scrubbers (loaded with aqueous alkanolamines) are typically employed in CO_2 capture, whereby CO_2 absorption can be represented via film theory: CO_2 first diffuses from the bulk gas phase to the gas-liquid interface, then diffuses into the bulk liquid phase, and finally reacts with the amine via the zwitterion mechanism [149-150]. However, in the absence of ZIF-8, the cellulose filter paper absorbs methanol, phenolsulfonpthalein, and ethylenediamine, preventing a finite layer with enough thickness to perform the physical and chemical CO_2 absorption steps associated with amine chemistry. Finally, the absence of ethylenediamine (with either

phenolsulfonpthalein dissolved in methanol or phenolsulfonpthalein and ZIF-8 mixed in methanol) precludes the formation of the zwitterion, which is necessary for deprotonation by the dye. Thus, it is apparent that the cooperative chemistry of ZIF-8, phenolsulfonpthalein, and ethylenediamine generate a color change upon CO_2 adsorption" [99].

Fig. 2.19. "Effect of repeated exposure of PSP-ED/ZIF-8 to **(A)** 700 ppm CO_2, **(B)** 3,000 ppm CO_2 and **(C)** 7,500 ppm CO_2 in dry atmosphere." Acquired from Davey et al. (2021). [99].

"Despite its decades of implementation, however, the validity of the zwitterion mechanism remains contested in the literature [151]. Ben Said et al. [152] performed density functional theory calculations that associated the development of the 1°,3°-zwitterion with high activation energy barriers and concluded this mechanism improbable. In addition, da Silva and Svendsen [153] used Hartree-Fock computational methods to study the mechanisms for reaction between CO_2 and aqueous alkanolamines. Their *ab initio* results suggested that a 1°,3°-zwitterion with a significant lifetime was unlikely [153]. Several authors have instead raised the single-step termolecular mechanism [151, 153-155] as an alternative reactive pathway, whereby an amine species reacts with one molecule of CO_2 and one molecule of base, B, according to [**Equation 2.17**]. The termolecular reaction mechanism has been shown consistent with the reaction kinetics of CO_2 and several amines, such as monoethanolamine (MEA), aminoethylethanolamine, and diethylenetriamine [155].

$$CO_2 + RNH_2 \cdots B \leftrightarrow RNHCO_2^- + BH^+ \qquad \textbf{(Eq. 2.17)}$$

"Formation of the 1°,3°-zwitterion, however, has been supported in some other reports. Xie et al. [156] simulated an aqueous CO_2-MEA system using a conductor-like polarizable continuum model and *ab initio* quantum mechanics/molecular mechanics. In contrast with prior authors, they posit that a two-step mechanism with a 1°,3°-zwitterion intermediate is a favorable reaction path [156]. Given the ongoing debate in the literature, it is difficult to precisely ascertain the reactive chemistry between adsorbed CO_2 and ED. However, due to its widespread use in aqueous and nonaqueous CO_2-amine systems, the zwitterion mechanism is situated in this work" [99].

2.4.3. Colorimetric analyses in humid environment

"The effect of ambient humidity on the colorimetric response of PSP-ED/ZIF-8 is also investigated. Representative colorimetric images for PSP-ED/ZIF-8 exposed 1,500 ppm CO_2 at various humidity are provided in [**Figure 2.20**]**.** While under dry conditions, the sensor responds quickly and obviously, the colorimetric sensor exhibits a suppressed response to CO_2 with incremented humidity" [99].

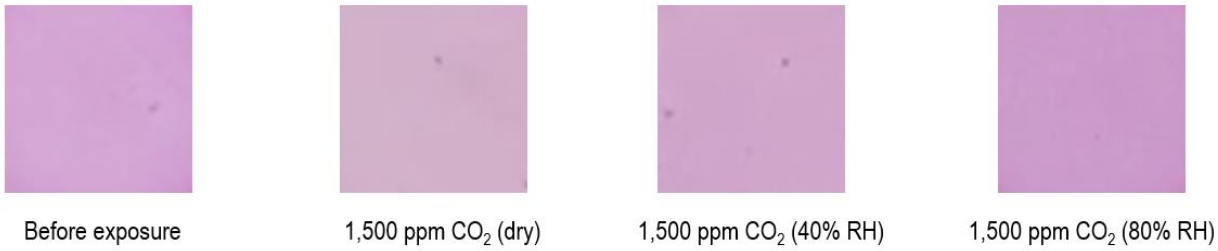

Fig. 2.20. "Fresh exposure of PSP-ED/ZIF-8 (2% ED) to 1,500 ppm CO_2 in**(A)** dry environment; **(B)** 40% RH and **(C)** 80% RH." Acquired from Davey et al. (2021). [99].

"As shown in [**Figure 2.18]**, the 443/570 nm F(R) ratios between 700 and 7,500 ppm CO_2 "reflect weaker colorimetric CO_2 responses upon 80% RH exposure" [99]. The exact mechanism of water interference in the colorimetric CO_2 sensing dynamics remains unclear. Differences in chemisorptive behavior in dry and humid environment have been observed in MOF studies. Flaig et al. [157] used solid-state ^{13}C cross-polarization magic angle spinning nuclear magnetic resonance spectroscopy to characterize CO_2 chemisorption in a diamine-functionalized IR-MOF-74-III. In dry environment, carbamic acid formation is observed from one amine reacting with CO_2 [157]. However, humidified (95% RH) conditions converted CO_2 into ammonium carbamates upon reaction with two amines [157].

"Under humid conditions, as seen with diamine-functionalized-IR-MOF-III, it is possible that the reaction stoichiometry of the colorimetric CO_2 sensing mechanism has altered toward a reduced CO_2 capacity. Assuming a pseudo steady-state hypothesis on the zwitterion intermediate concentration, the rate of reaction between CO_2 and primary amines (such as ethylenediamine) in aqueous (or nonaqueous) solvents can be approximated by **Equation 2.18** [158]

$$R_{CO_2} = \frac{-k_2\{CO_2][RNH_2]}{\frac{k_{-1}}{\sum k_B[B]}+1} \quad \textbf{(Eq. 2.18)}$$

where k_2 is the forward rate of reaction of CO_2 and ethylenediamine (**Equation 2.15**), k_{-1} is reverse rate of reaction of CO_2 and ED (**Equation 2.15**), and $\Sigma k_B[B]$ is the summation of bases present in the system eligible to deprotonate the zwitterion (**Equation 2.16**) [158].

"Under the first asymptotic limit, $\frac{k_{-1}}{\sum k_B[B]} << 1$ and deprotonation occurs much more rapidly compared to the reverse reaction in [**Equation 2.16**] [158-159]. The simplified rate law is first order with respect to CO_2 and primary amine, which has been found experimentally for aqueous CO_2-MEA systems at 303K [158-161] and CO_2-ED systems in methanol at 303K [142]. At the other asymptotic limit, $\frac{k_{-1}}{\sum k_B[B]} >> 1$ [158-159]. When a primary amine (such as ethylenediamine) contributes most to zwitterion deprotonation, [**Equation 2.18**] becomes second-order with respect to the amine [155-156]. The second asymptotic limit recovers the termolecular kinetics associated with [**Equation 2.17**], which Aboudheir et al. [162] showed for high CO_2-loaded (0.1-0.49 mol/mol), concentrated (3 to 9 M) aqueous MEA systems between 293 and 333 K" [99].

"Between these asymptotic limits, fractional reaction orders can be observed, as shown experimentally with CO_2-ED systems in pure and aqueous ethylene glycol solutions [142]. However, while such stoichiometric changes have been observed in amine-CO_2 systems, it is uncertain how the presence of ZIF-8 and phenolsulfonpthalein alters the reaction kinetics. Toward elucidation of the mechanistic colorimetric sensing mechanism between CO_2, ZIF-8, phenolsulfonpthalein, ethylenediamine, and potential interferants (such as H_2O), kinetic studies are required in methanolic solvent, which future studies will aim to provide.

"Despite the characteristic water resistance of ZIF-8 from the methyl groups associated with its ligands and coordinatively saturated Zn^{2+} sites [163-164], ZIFs can show favorable H_2O adsorption isotherms through incorporation of hydrophilic moieties. Notably, ZIF-90 and SIM-1–display significant H_2O adsorption at 298 K compared to ZIF-8 due to the hydrophilic functional groups associated with their linkers, imidazole-2-carboxaldehyde and 4-methylimidazole-5-carbaldehyde [165]. In other work, amine-functionalized solid-state ZIF-8 (from toluene reflux) was shown to exhibit a 1-2% suppression of CO_2 adsorption upon exposure to 10% RH [166]. In this context, we suspect that hydrophilic interactions between ethylenediamine and H_2O molecules could promote H_2O adsorption [167] and, under humid environment, disrupt the colorimetric CO_2 adsorption achieved in dry environment.

"Alongside hydrogen bonding interactions between ethylenediamine and H_2O, the participation of H_2O in the zwitterion mechanism is another possible source of interference in the colorimetric CO_2 sensing. When hydrophilic ethylenediamine molecules are exposed to humid CO_2, the attracted H_2O molecules can engage in the second step of the zwitterion mechanism and deprotonate the intermediate species [167]. The presence of hydrophilic ethylenediamine groups, then, could

promote water adsorption, which subsequently introduces competition with phenolsulfonpthalein for deprotonation of the zwitterion and affects the apparent color [167].

"Humid interference remains a challenge in colorimetric analyte detection using various materials [168-169]. Because humidity can disrupt colorimetric sensing through physical adsorption or chemical interactions, corrective measures can be difficult to precisely accomplish [94]. Toward addressing the effects of humidity on sensing performance, desiccants have been employed, as well as water-insoluble dyes compatible with hydrophobic substrates (such as polyvinylidene difluoride) [169]. The chemical tunability of MOFs can also be manipulated to enhance hydrophobic character. Using a post-synthetic shell-ligand exchange reaction (SLER), Liu et al. [170] substituted the outermost shell of ZIF-8 particles with 5,6-dimethylbenzimidazole and achieved an improved water-resistance and water stability. Thus, we remain optimistic in achieving a MOF colorimetric sensor with water-repelling attributes suitable for accurate detection of indoor chemical species" [99].

2.5 Summary

In this chapter, I "have designed and characterized a simple, chemically-stable, methanolic MOF-based colorimetric sensor toward detection of low CO_2 partial pressures of interest in indoor air quality monitoring. Colorimetric images…and [*ex-situ*] UV-vis spectroscopic studies show that PSP-ED/ZIF-8 is sensitive to CO_2 concentrations typical of indoor air in dry environment, with a lower limit of detection below 1,000 ppm CO_2.

"Despite an excellent response to CO_2 in dry environment, PSP-ED/ZIF-8 suffers in the presence of humidity. Both qualitative colorimetric images and quantitative UV-vis ratiometric profiles indicate colorimetric reduction upon exposure to humid CO_2. Here, the hydrophilic nature of ethylenediamine is expected to facilitate H_2O adsorption onto ZIF-8 and thus interfere with the visible CO_2 colorimetric detection otherwise achieved in dry environment. Competition between phenolsulfonpthalein and H_2O for zwitterion deprotonation is also considered as a possible source of suppression of the colorimetric CO_2 response. However, the nature of water interference remains unknown and necessitates the pursuit of kinetic studies to clarify the colorimetric CO_2 sensing mechanism.

"The ZIF-8 colorimetric sensor offers a simple detection of CO_2 via incorporation of reactions between ethylenediamine, phenolsulfonpthalein, and CO_2. Through integration of water-resistant functionalities, the MOF gas sensor will be enhanced to develop a competitive colorimetric device robust to the variable humidity characteristic of indoor air environment" [99].

In Chapter 3, "Enhanced ZIF-8-Enabled Colorimetric Indoor Carbon Dioxide Sensing through Dye-Precursor Synthesis," a second-generation indoor gas sensor is developed and characterized to improve upon some of the limitations of the first-generation indoor gas sensor, PSP-ED/ZIF-8.

Chapter 2: Developing the Prototype: An Amine-Functionalized Zeolitic Imidazolate Framework -8 (ZIF-8)-Based Colorimetric Indoor Carbon Dioxide Sensor

2.6 Acknowledgements of co-authors from published work.

Chapter 2 consists of intellectual contributions from the co-authors from Davey, A.K.; Gao, X.; Xia, Y.; Li, Z.; Dods, M.N.; Delacruz, S.; Pan, A.; Swamy, S.; Gardner, D.W.; Carraro, C.; and Maboudian, R. "Amine-functionalized metal-organic framework ZIF-8 toward colorimetric CO_2 sensing in indoor air environment." *Sensors and Actuators B: Chemical*, **2021**, 130313. DOI: https://doi.org/10.1016/j.snb.2021.130313 [99]. I would like to thank all the co-authors: Xiang Gao, Yong Xia, Zhou Li, Matthew N. Dods, Steven Delacruz, Aifei Pan, Sanket Swamy, David Gardner, Carlo Carraro, and Roya Maboudian.

Resources from supporting institutions are also included:

"The authors gratefully acknowledge the support of the National Science Foundation in the form of a Graduate Research Fellowship (A.K.D.) and grant # 1903188, as well as the Bakar Fellows Program. Work at the Molecular Foundry was supported by the Office of Science, Office of Basic Energy Sciences, of the U.S. Department of Energy under Contract No. DE-AC02-05CH11231. The contributions of M.N.D. were supported by the U.S. Department of Energy, Office of Science, Office of Basic Energy Sciences under award DE-SC0019992. The authors also thank Dr. Guangwei Min of the Electron Microscopy Laboratory (EML) at the University of California, Berkeley for advice and assistance in SEM sample preparation and image collection" [99].

Chapter 3: Enhanced ZIF-8-Enabled Colorimetric Indoor Carbon Dioxide Sensing through Dye-Precursor Synthesis

This chapter is entirely adapted from Davey et al., "Enhanced ZIF-8 enabled colorimetric CO_2 sensing through dye-precursor synthesis." *Sensors and Actuators B: Chemical*, **2023**, 374, 132783. DOI: https://doi.org/10.1016/j.snb.2022.132783 [123]. The objective of this chapter is to present a second-generation indoor CO_2 sensor, ED/PSP:ZIF-8, which exhibits an improved colorimetric CO_2 response across humidity compared to the first-generation indoor CO_2 sensor, PSP-ED/ZIF-8. Novel characterization techniques are implemented to ascertain this enhanced performance, as well as to speculate changes in phenol red incorporation underlying the nature of the improved colorimetric gas response.

3.1 Introduction to extraprecursor MOF crystallization

Multiple research endeavors have been pursued to investigate the effects of "reagent concentrations," "solvent," "time," "temperature," and "heating method" on "changes in MOF composition, structure, and/or crystal morphology" [171]. ZIF-8 particle formation involves "polymerization and nucleation," in which Zn^{2+} cations and 2-mIm$^-$ anions react to form "individual ZIF-8 units" [106]. ZIF-8 units act "as the basic building block for the formation of ZIF-8 crystals" [106]. **Equation 3.1** shows the rate law associated with **Equation 2.1**, which is the chemical equation for ZIF-8 unit formation [106]

$$Rate = k_1[Zn^{2+}][2mIm^-]^2 \qquad \textbf{(Eq. 3.1)}$$

Where:
k_1 is the rate constant,
$[Zn^{2+}]$ is the concentration of zinc cations (from the metal precursor),
and [2mIm$^-$] is the concentration of 2-methylimidazolate anions (from the ligand precursor).

When ZIF-8 unit formation increases, "the reaction mixture becomes thermodynamically unstable due to the supersaturation of ZIF8 units" [106]. In response, "the system minimizes the Gibbs free volume energy by forming ZIF-8 nuclei via nucleation process" shown in **Equation 3.2** [106].

$$\Delta G_v = -\frac{kT}{\Omega}\ln\left(\frac{C}{C_0}\right) = -\frac{kT}{\Omega}\ln(1+\sigma) \qquad \textbf{(Eq. 3.2)}$$

Where:
ΔG_v is the Gibbs free energy per unit volume,
k is the Boltzmann constant,
T is temperature
Ω is the atomic volume,
C is the concentration of the solute,
C_0 is the equilibrium solute concentration,
and σ is the supersaturation [106].

From here, "ZIF-8 nuclei then either proceed to grow into larger ZIF-8 particles or dissolve back into the precursor solution depending on whether the ZIF-8 nuclei size exceeds the critical size of ZIF-8," where "[the] critical size represents the smallest possible size that can be achieved by a stable nucleus" (as shown in **Equation 3.3**) [106]:

$$r^* = -\frac{2\Upsilon}{\Delta G_v} \quad \textbf{(Eq. 3.3)}$$

Where:
r* is the critical size,
and γ is the "surface energy of the solid phase" [106].

Beh et al. [106] illustrated the role of an increased Zn^{2+} concentration (with a fixed 2-mIm$^-$ concentration) on MOF crystallization through **Equation 3.1**, **Equation 3.2**, and **Equation 3.3**. At higher Zn^{2+} concentration, **Equation 3.2** and **Equation 3.3** suggest a higher supersaturation and a smaller ΔG_v, which results in a "smaller ZIF-8- critical size" and "the subsequent growth of the smaller ZIF-8 nuclei" [106]. Beh et al. [106] also demonstrated that ZIF-8 particles from larger Zn/2-mIm$^-$ molar ratios (greater than 1:2.7) could not be harvested (no yield) because "most of the ZIF-8 nuclei formed did not manage to grow beyond the critical size thus were unstable and dissolved back into the precursor solution," as according to **Equation 3.3**. This study exhibited the role of controlled metal-linker precursor ratio on ZIF-8 crystallization through thermodynamic assessments, which can be used to inform more complicated ZIF-8 syntheses involving extraprecursor compounds.

Carpenter et al. [172] investigated the *in-situ* incorporation of proteins—bovine serum albumin (BSA) and fluorescein isothiocyanate-tagged BSA (FITC-BSA)—into ZIF-8 reaction mixtures to form protein@MOFs. Their work demonstrated a gradual reduction in ZIF-8 crystal size with increased BSA concentration (0.625, 1.25, and 2.5 mg/ml) in Milli-Q water [172]. Moreover, X-ray diffraction and fluorescence microscopy confirmed that while BSA@ZIF-8 produced nearly exclusively crystalline phases, FITC-BSA@ZIF-8 products consisted of both amorphous and crystalline phases, which suggests "that nucleation from the amorphous phase is inhibited by FITC-BSA" [172]. In a separate study, Mazlan et al. [173] studied how the presence of oxygen-containing functional groups from graphene oxide (GO) nanosheets affect nucleation and growth to "form oriented MOF structures, favoring uniform crystal and pore structures." Here, researchers also demonstrate that the "GO loading also affected the type of oxygen functional group that interacts with the parental crystalline structure" through MOF metal-binding sites [173]. For example, while low and moderate GO loadings led to MOF interactions with epoxy groups on the basal plane, high GO content led to "the binding of metal sites to carboxylic groups can become the dominant interaction" [173].

In the previous chapter, the first-generation sensor, PSP-ED/ZIF-8, exhibited a visible (but not incredibly intense) colorimetric indoor CO_2 response at low humidity [99]. With increased humidity, this already modest gas response largely dwindled [99]. In the next section, a novel colorimetric indoor carbon dioxide sensor is developed through the direct integration of phenol

red (PSP) molecules into the ZIF-8 methanolic precursor solutions [123]. This process, termed *dye-precursor synthesis* [123], is used against the first-generation synthesis approach to characterize sensor performance across humidity and volatile organic compound environments [123].

3.2 Formation of ED/PSP:ZIF-8

The synthesis of PSP-ED/ZIF-8 (used for comparative analysis) follows the exact recipe described in Chapter 2 [99, 123]. Here, the formation of the second-generation colorimetric indoor CO_2 sensor, ED/PSP:ZIF-8, is the exact procedure from Davey et al. [123].

"For the synthesis of ED/PSP:ZIF-8, 2.08 g of zinc nitrate hexahydrate ($Zn(NO_3)_2 \cdot 6H_2O$; Fischer Scientific) and 2.08 g of 2-methylimidazole (Hmim, 99%, Sigma-Aldrich) are dissolved in 120 ml of methanol (Fischer Chemical) in separate beakers through prolonged sonication (Crest Ultrasonics)**.** Then, 60 mg of phenol red are added to the zinc precursor solution and 60 mg of phenol red are added to the imidazolate precursor solution. After sonicating these solutions, the phenol red/imidazolate precursor solution is poured into the phenol red/zinc precursor solution and allowed to react at room temperature for 48 h (with no stirring). The resulting crystals, termed PSP:ZIF-8, are separated from the methanolic supernatant through slowly pouring into a disposable scintillation vial (Trident technology (Jiangsu) Co., Ltd.). Then, a 2% ethylenediamine (99%, Sigma-Aldrich) solution (% v/v) in methanol is produced by adding 100 µl of ethylenediamine to 4.9 ml of methanol. This solution is then blended with the PSP:ZIF-8 crystals to form an 80 mg PSP:ZIF-8/ml solvent mixture" [123]. The different steps of ED/PSP:ZIF-8 synthesis are shown in **Figure 3.1** [123].

Fig. 3.1 Synthesis of the second-generation indoor colorimetric CO_2 sensor, ED/PSP:ZIF-8. Adapted from Davey et al. [123].

3.3 Experimental Characterization Techniques

3.3.1 Renewed characterization techniques

The same PXRD technique illustrated in Chapter 2 is implemented for this study.

3.3.2 Scanning electron microscopy (SEM)

SEM data collection proceeds as described in Davey et al. [123]. "Morphological information about the synthesized materials is acquired using scanning electron microscopy, SEM (Zeiss Gemini Ultra55 Field Emission SEM) at an operating voltage of 5 kV. Samples are drop-cast on silicon chips, and sputter coated with Au (10.0 nm) for 7-min to provide appreciable electrical conductivity prior to collecting SEM imaging data" [123].

3.3.3 Transmission electron microscopy (TEM)

Transmission electron microscopy (TEM) uses "the emission of electron beams as the fundamental basis of its operation… for the analysis and visualization of samples presented within ranges of… (1 micrometer) and… (1 nanometer)" [174]. This technique is based on **Equation 3.4**, which is based on de Broglie's "principle of the wave-like nature of matter" [175]:

$$\lambda = \frac{h}{p} \qquad \textbf{(Eq. 3.4)}$$

Where: λ is the "associated wavelength,"
h is Planck's constant,
and *p* "is the magnitude of the particle momentum **p**" [175].

When an electron traveling through a large potential difference, V, is accelerated to a velocity, v, the electron approaches the velocity, *c*, of light in a vacuum (such that relativistic effects must be considered) [175]. The relativistic change of the electron mass, *m*, related to the velocity, v, can be expressed as a function of the rest mass, m_0, as shown in **Equation 3.5** [175].

$$m = \frac{m_0}{1-\frac{v^2}{c^2}} \qquad \textbf{(Eq. 3.5)}$$

In traveling through the potential difference, V, the change in energy of the electron can be determined from **Equation 3.6** [175]:

$$mc^2 = m_0c^2 + eV \qquad \textbf{(Eq. 3.6)}$$

In combining **Equation 3.5** and **Equation 3.6**, the momentum, *p*, can be determined through **Equation 3.7** [175]:

$$p = mv = [2eVm_0 + \left(\frac{eV}{c}\right)^2]^{1/2} \qquad \textbf{(Eq. 3.7)}$$

From **Equation 3.8**, the wavelength of the electrons is a function of the potential difference (which is the accelerating voltage of the system) [175]:

$$\lambda = \frac{h}{p} = h[2eVm_0 + \left(\frac{eV}{c}\right)^2]^{-1/2} \quad \textbf{(Eq. 3.8)}$$

TEM data collection are in accordance with the protocol from Davey et al. [123]. "ZIF-8-based sensors are dispersed in isopropyl alcohol by bath sonication for 15 minutes and drop-cast onto copper/lacey carbon grids for transmission electron microscopy (TEM) imaging. TEM imaging is carried out on a JEOL-2010 microscope operated at 80 keV. Particle size distributions are completed using Fiji imaging software" [123].

3.3.4 Fourier transform infrared (FTIR) spectroscopy

Fourier transform infrared (FTIR) spectroscopy is an analytical technique used to probe the molecular structure of compounds through the generation of an infrared spectrum [176]. Through the harmonic oscillator first approximation (consistent with Hooke's law), the frequency of the absorbed infrared radiation, ν, is related to the reduced mass, μ, and the stiffness of the spring, k, as shown in **Equation 3.9** [176]:

$$\nu = (\frac{1}{2\pi c})\sqrt{\frac{k}{\mu}} \quad \textbf{(Eq. 3.9)}$$

FTIR data collection are in accordance with the protocol from Davey et al. [123]. "Fourier transform infrared (FTIR) transmittance data are collected (spectral range: 4000 to 400 cm^{-1}; resolution: 4 cm^{-1}) using a Bruker Vertex80 FTIR instrument" [123].

3.3.5 Brunaeur-Emmett-Teller (BET) surface area characterization

BET experimental protocols are consistent with Davey et al. [123]. "Brunaeur-Emmett-Teller (BET) surface analysis and pore size distribution measurements (N_2 at 77 K) are accomplished using a Micromeritics Gemini VII Surface Area and Porosity instrument. Prior to BET measurements, 80 mg/ml solutions of ZIF-8-based samples are centrifuged, separated from the supernatant, and dried at room temperature (21.5 ± 0.3 °C at 49.8 ± 1% RH). The resulting powders are then degassed at 150 °C overnight using a Micromeritics VacPrep 061 Sample Degas System" [123].

3.3.6 In-situ ultraviolet-visible (UV-Vis) diffuse reflectance spectroscopy

In replacement of the *ex-situ* UV-Vis technique implemented in Chapter 2, this chapter uses an *in-situ* technique in which UV-Vis measurements are collected in the presence of gas. Measurements are collected as described in Davey et al. [123].

"*In-situ* ultraviolet-visible diffuse reflectance spectroscopy with an Evolution 300 UV-Vis (Thermo Scientific) spectrophotometer (spectral range: 400 to 600 nm; bandwidth: 1.0 nm; scan

speed: 60 nm/min) is used to quantify the color change upon controlled exposure to CO_2. Sample deposition onto cellulose filter paper (VWR North American) and insertion into the spectrophotometer closely follows the procedure reported in the prior work [24]. Specifically, a 0.7 cm x 0.7 cm piece of cellulose filter paper is attached to the UV-Vis sample enclosure via double-sided carbon black tape (Ted Pella, Inc.), inserted into the UV-Vis chamber, and used as a reflectance (% R) background [24]. Then, 20 ul of PSP-ED/ZIF-8 or ED/PSP:ZIF-8 is drop-cast on another piece of 0.7 cm x 0.7 cm cellulose filter paper, dried for 120 s, and placed into the UV-Vis spectrophotometer for *in-situ* target gas exposure.

"The *in-situ* UV-Vis measurements under controlled CO_2 exposures proceed as illustrated in **[Figure 3.2].** A CO_2 cylinder (Airgas; 0.995 mol% CO_2 in N_2), dry air cylinder (Praxair; 79 mol% N_2; 21 mol% O_2), and acetone cylinder (Airgas; 0.1001 mol% $(CH_3)_2CO$ in N_2) are attached to a gas line. To achieve the desired CO_2 levels, the gas valves (shown in red) are opened and needle valves particular to the inlet CO_2 and dry air flows are adjusted to attain desired flowrates (plotted in [**Figure 3.3]**. Once the gases are mixed, they are channeled through either (a) a continuous stream that maintains dry conditions (indicated in **[Figure 3.2]** with a downward yellow arrow) or (b) a bubbler to adjust the relative humidity (indicated in **[Figure 3.2]** with an upward blue arrow). The resulting mixture is fed into the UV-Vis chamber until steady-state is reached after about 7 min [**Figure 3.4]**. The total gas flow rate (set at 300 ml/min) composed of a given concentration of CO_2 and air flow rates is measured using an Agilent Technologies ADM2000 Universal Gas Flowmeter. As shown in **[Figure 3.2]**, each CO_2 concentration (and corresponding humidity value) is calibrated with a wireless GasLab Plus CM-501 NDIR sensor (contained within a sealed plastic vessel). Dry and humid conditions are taken to be 0.133 ± 0.8% RH and 45.4 ± 3% RH, respectively, at 23.5 ± 1 ºC" [123].

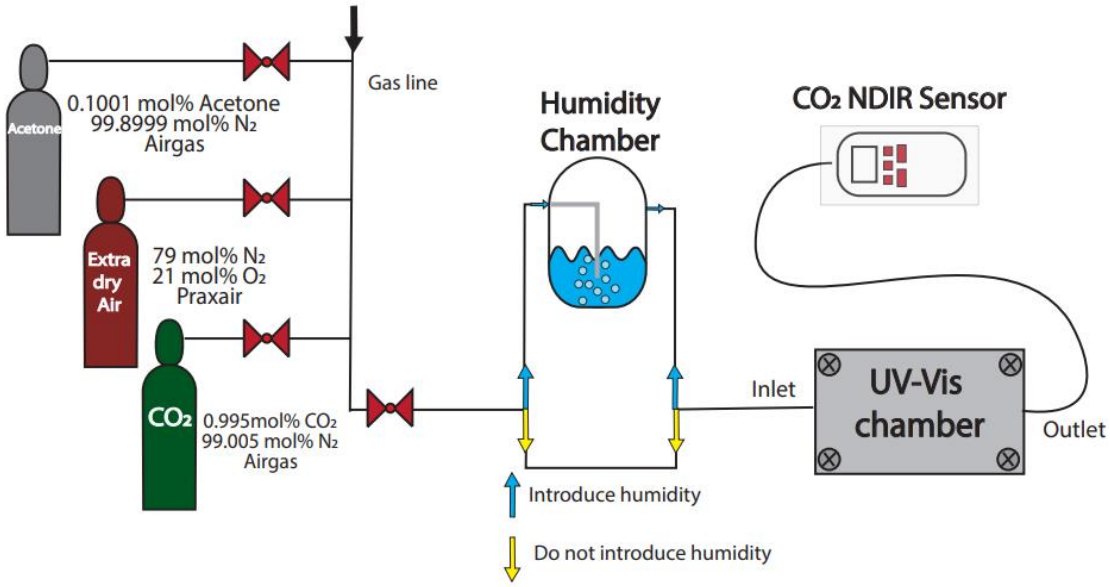

Fig. 3.2 "Operation of the *in-situ* UV-Vis diffuse reflectance spectroscopy." Acquired from Davey et al. [123].

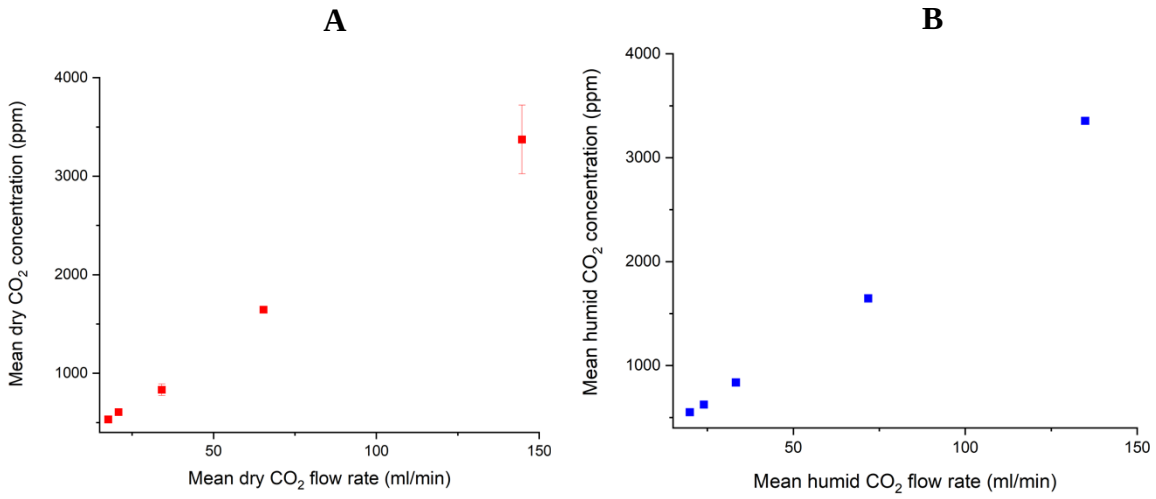

Fig. 3.3 "Mean CO_2 concentrations (ppm) versus mean CO_2 flow rates under **(A)** dry conditions (0.133 ± 0.8% RH) and **(B)** humid conditions (45.4 ± 3% RH) at room temperature (23.5 ± 1 °C)." Acquired from Davey et al. [123]. Error bars are standard deviation values.

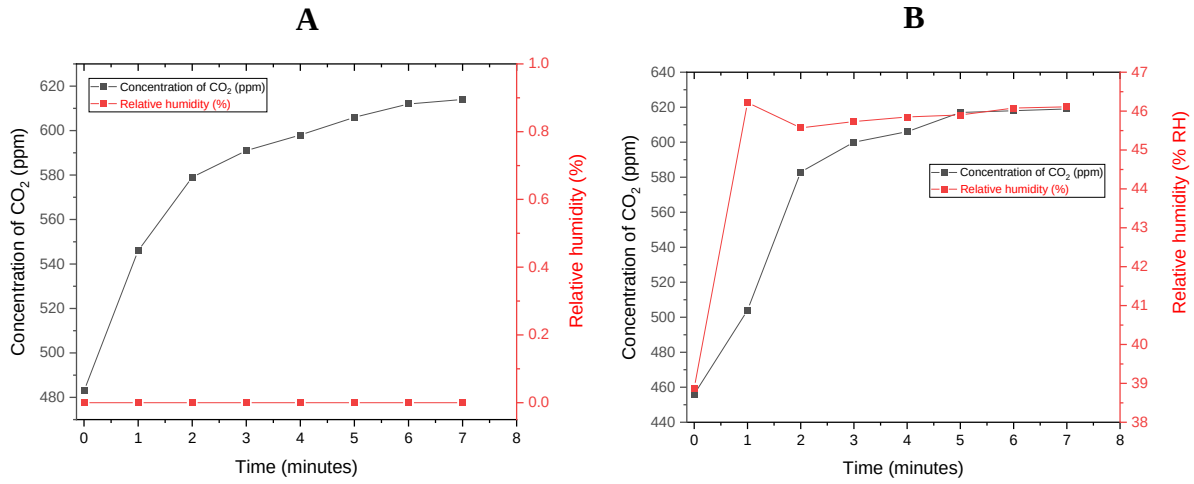

Fig. 3.4 "Representative time evolution of CO_2 (at ~620 ppm) and RH in **(A)** dry environment and **(B)** humid environment." Acquired from Davey et al. [123].

"Once the sensor-coated filter paper is placed inside the UV-Vis spectrophotometer, the sensor is exposed to a specific CO_2 concentration and humidity using the methods described above [99]. After steady-state is reached, a reflectance (% R) vs. wavelength (nm) profile is collected [99]. Each diffuse reflectance value is then converted into a Kubelka-Munk value, F(R) (shown as **Eq. 2.14**), consisting of the absorption coefficient (K) and scattering coefficient (S) [99]. In the diffuse reflectance UV-Vis spectra, phenol red changes color from violet (λ_{max} ~ 570 nm) under basic conditions to yellow (λ_{max} ~ 443 nm) under acidic conditions. For each CO_2 exposure, the ratios of the respective 443 and 570 nm F(R) values are depicted as scatter plots as a function of CO_2 concentration (ppm) [99].

"Toward probing the long-term gas sensing performance and sensor stability in variable humidity, additional *in-situ* UV-Vis spectra are collected in which sensors (25 μl drop-cast on cellulose filter paper) are exposed to 3500 ± 300 ppm CO_2 (total gas flow rate: 300 ml/min). All trials are collected at room temperature (23.0 ± 0.8 ºC) and in dry (0% RH) and humid (82.0 ± 5% RH) environments. Colorimetric 443/570 nm F(R) ratios are tabulated for up to 120 min of exposure to CO_2. After that, the sensor is exposed to 300 ml/min dry air for 20 min. Subsequently, the dry air is turned off for an additional 20 min. At this time, another "0-min" spectrum is obtained, and the sensor is exposed to 3500 ppm CO_2 again at different times for 120 min. For this experiment, three cycles are collected (in dry and humid environment). Following multiple hours of repeated in-situ UV-Vis spectroscopic measurements, ZIF-8 stability on cellulose filter paper is analyzed using FTIR spectroscopy.

"To evaluate the effect of VOCs on colorimetric CO_2 sensing, the same *in-situ* UV-Vis dosing experiments (described in **[Figure 3.2]**) are performed using acetone (Airgas; 0.1001 mol% $(CH_3)_2CO$ in N_2). Given the emergence of nasal, throat, and optic irritation from acetone exposure, the U.S. National Institute for Occupational Safety and Health (NIOSH) recommended exposure limit/time weight average (REL/TWA) for this gas is 250 ppm [177]. In this study, the acetone concentration up to 314 ppm is probed. The acetone flow rate is varied while maintaining a set CO_2 concentration (in 450 to 3600 ppm range) and a total gas flow rate of 350 ml/min. [**Equation 3.10]** demonstrates how these selected acetone flow rates are converted to respective concentrations in ppm.

$$[Ac]_{UV-Vis} = \frac{[Ac]_{cylinder} * Ac_{flowrate}}{TG_{flowrate}} \quad \textbf{(Eq. 3.10)}$$

where:
$[Ac]_{UV\text{-}Vis}$ = concentration of acetone in the *in-situ* UV-Vis chamber (ppm)
$[Ac]_{cylinder}$ = concentration of acetone in the cylinder (1000 ppm).
$Ac_{flowrate}$ = flow rate of acetone/nitrogen stream (ml/min).
$TG_{flowrate}$ = total gas flow rate entering the UV-Vis chamber (350 ml/min)" [123].

3.3.7 Colorimetric imaging and red-, green, blue (RGB) color decomposition

Colorimetric assays are collected as described in Davey et al. [123]. "In addition to the *in-situ* UV-Vis spectroscopic technique, optical images of both sensors (in variable CO_2 and humid environments) are obtained and then read into a MATLAB script for subsequent analysis. First, 20 µl of the sensing solutions are drop-cast on cellulose filter paper and allowed to dry in ambient air (453 ± 2 ppm CO_2; 40.6 ± 2% RH; 27.7 ± 0.7 °C) for 120 s [99]. The same LabView-controlled gas manifold system described in prior work is used for qualitative color change studies, consisting of house air, an evaporator system, pressure swing adsorption dryers, mass flow controllers (Bronkhorst), and target gases [24]. A cylinder of 50,380 ppm CO_2 balanced in nitrogen (Praxair) is used for colorimetric imaging [99]. Toward qualitatively assessing the role of select VOCs on the observed color change (in dry conditions), a 978 ppm ethanol cylinder (Praxair; balanced in nitrogen) and 400 ppm acetone (Praxair; balanced in nitrogen) cylinder are used. Similar to the human health symptoms borne from acetone exposure [177], ethanol is associated with nasal and optic irritation, resulting in a NIOSH REL/TWA of 1000 ppm [178]. For these colorimetric imaging assays, the total gas flow rate is kept constant at 300 standard cubic centimeters per minute (sccm) and the corresponding humidity values are measured at ambient temperature (27.7 ± 0.7 °C). Select CO_2 and humidity levels are validated using a wireless GasLab Plus CM-501 NDIR sensor [99].

MATLAB-generated red-, green-, and blue (RGB) distributions also are collected as described in Davey et al. [123]. "For a given CO_2 concentration and humidity (or VOC exposure), each sensor is directly exposed for 20 s. Progressive color changes are recorded using a Google Pixel 4 XL smartphone [24]. From these videos, 'Before controlled exposure' and 'Exposed' images are prepared and downloaded into a MATLAB script as 1.7" x 1.7" squares [99]. Color output is produced as a 162 x 162-pixel red-green-blue (RGB) distribution [99]. RGB values are obtained with the Y-axis held constant at pixel 81, with the X-axis sweeping from pixels 60 to 100 [99]" [123]. **Figure 3.5** shows the MATLAB script and output for colorimetric imaging.

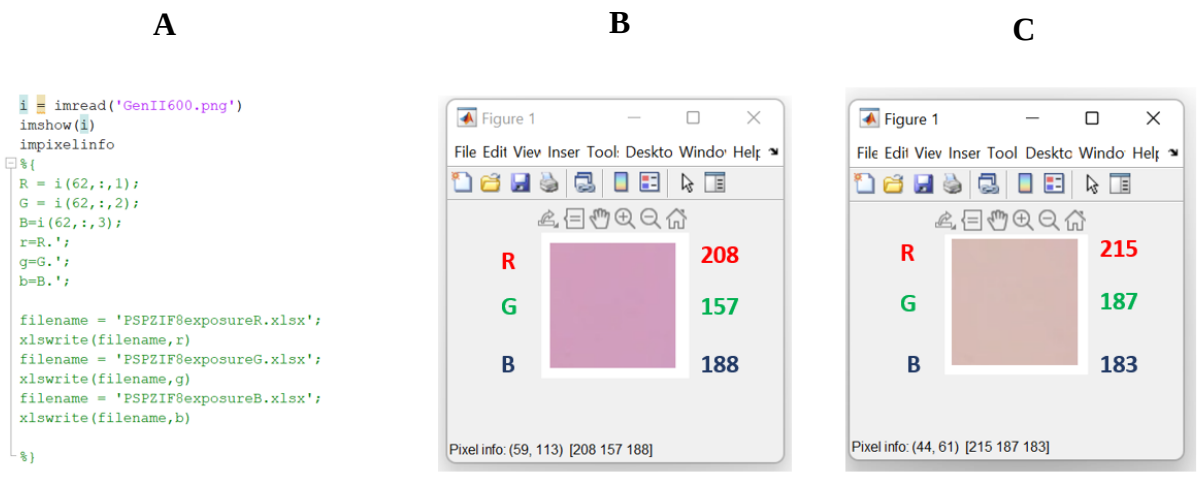

Fig. 3.5 **(A)** MATLAB script for RGB image distribution; **(B)** RGB image distribution (before controlled gas exposure); and **(C)** RGB image distribution (during controlled gas exposure).

3.4 Discussion

3.4.1 Materials characterization

Structural analysis is consistent with data from Davey et al. [123]. "[**Figure 3.6**] shows the collected PXRD patterns from the simulated pristine ZIF-8 (refcode: VELVOY) [131], synthesized pristine ZIF-8, PSP-ED post synthetically added to ZIF-8 (PSP-ED/ZIF-8), PSP added to ZIF-8 precursor solution (PSP:ZIF-8), and ED added to PSP:ZIF-8 (ED/PSP:ZIF-8). In all samples, the diffraction peaks are consistent with the expected sodalite structure of ZIF-8 reported in the literature [99, 179]. However, small peak shifts are observed with the PSP:ZIF-8 and ED/PSP:ZIF-8 materials compared to the pristine ZIF-8 and PSP-ED/ZIF-8 materials. Computational methods examining the structure and stability of ZIF-8 suggest that this observation could be ascribed to emergent defects within the lattice [180], such as from linker vacancies and dangling linkers, which could result in strain of the ZIF-8 lattice when synthesized with PSP. Moreover, the addition of ethylenediamine to form PSP-ED/ZIF-8 and ED/PSP:ZIF-8 produces a change in relative XRD peak intensities compared to those of pristine ZIF-8 and PSP:ZIF-8. As has been observed with metal-organic frameworks loaded with C_{60} fullerenes [181] and with adsorbed benzene [182], the changes in relative XRD peak intensities between the first- and second-generation sensors may be attributed to the changes in electron density along crystallographic planes upon ethylenediamine incorporation onto the MOF.

"SEM images of pristine ZIF-8, PSP-ED/ZIF-8, PSP:ZIF-8, and ED/PSP:ZIF-8 are depicted in [**Figure 3.7**]. For the pristine ZIF-8 and PSP-ED/ZIF-8, ~100 nm nanocrystals are obtained, which is in agreement with reported room temperature methanolic ZIF-8 synthesis with similar metal : linker : precursor molar ratios [99, 135]. Upon incorporation of phenol red into the ZIF-8 precursor mixture, however, the PSP:ZIF-8 (and ED/PSP:ZIF-8) formed are nearly significantly larger in size (~400 nm). In addition to the role of the modified duration of MOF synthesis [183], the change in reaction solution composition (with phenol red now mixed with ZIF-8 precursors in methanol) may result in a ZIF-8 growth favoring larger crystals [171]. TEM images for PSP-ED/ZIF-8 and ED/PSP:ZIF-8 are shown in [**Figure 3.8**]. Whereas the average particle size for PSP-ED/ZIF-8 is 0.111 $\pm$ 0.03 μm, the ED/PSP:ZIF-8 particles are 0.425 $\pm$ 0.07 μm.

"FTIR transmittance spectra for the gas sensing materials and their constituents are shown in **[Figure 3.9].** As listed in [**Table 3.1**], the observed 421 cm^{-1} vibrational band in pristine ZIF-8, PSP-ED/ZIF-8, PSP:ZIF-8, and ED/PSP:ZIF-8 is associated with the Zn-N stretch of the ZIF-8. In addition, the bands at 2931 and 3135 cm^{-1}-observed in PSP-ED/ZIF-8 and ED/PSP:ZIF-8 samples are ascribed to the aliphatic and aromatic C-H stretches of the imidazolate ligand, respectively [171, 184-185]. The broad band positioned at 3310 cm^{-1} is assigned to an -OH stretching mode from the methanol solvent [186]. Finally, the bands observed at 3280 and 3355 cm^{-1} are attributed to N-H stretching modes of ethylenediamine [186-187]. Consistent with the PXRD patterns, these FTIR spectra confirm the formation of ZIF-8, as well as its chemical stability in the presence of phenol red and ethylenediamine for both sensors, PSP-ED/ZIF-8 and ED/PSP:ZIF-8. Moreover, as evidenced via the preserved Zn-N 421 cm^{-1} mode shown in [**Figure**

3.10], both PSP-ED/ZIF-8 and ED/PSP:ZIF-8 remain stable in basic environment over multiple weeks. This chemical stability of ZIF-8 in basic environment is attributed to the linkage of soft imidazolate anions with soft Zn^{2+} cations, which hard-soft acid-base theory predicts an excellent metal-ligand bond strength toward good metal-organic framework stability [99, 188]" [123].

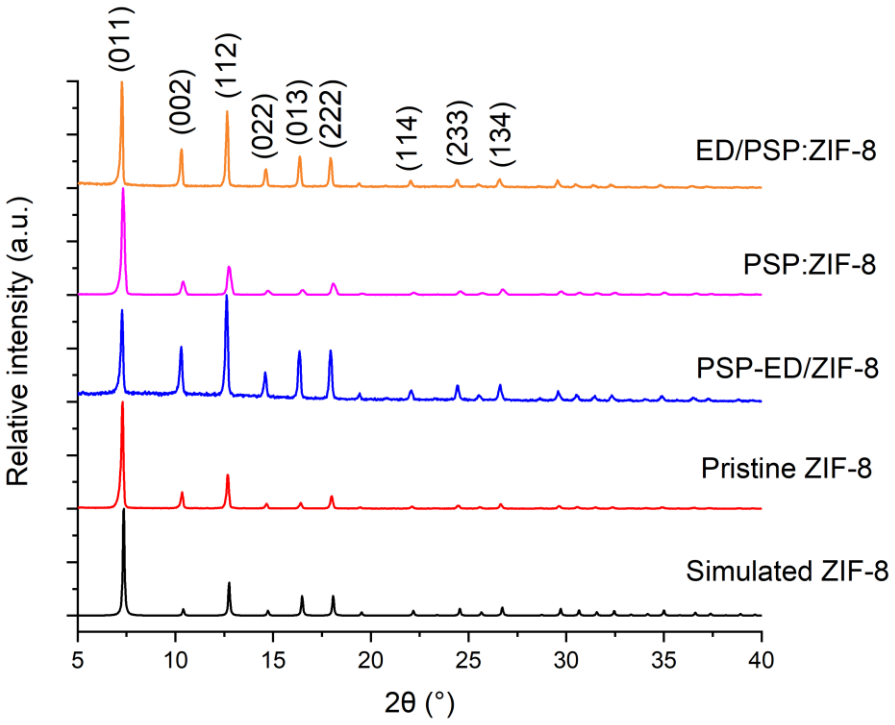

Fig. 3.6 Powder X-ray diffraction patterns (Cu *K*-α radiation, λ = 1.54 Å) of simulated ZIF-8 (VELVOY)- black, pristine ZIF-8-red, PSP-ED/ZIF-8-blue, PSP:ZIF-8-magenta, and ED/PSP:ZIF-8-orange. Acquired from Davey et al. [123].

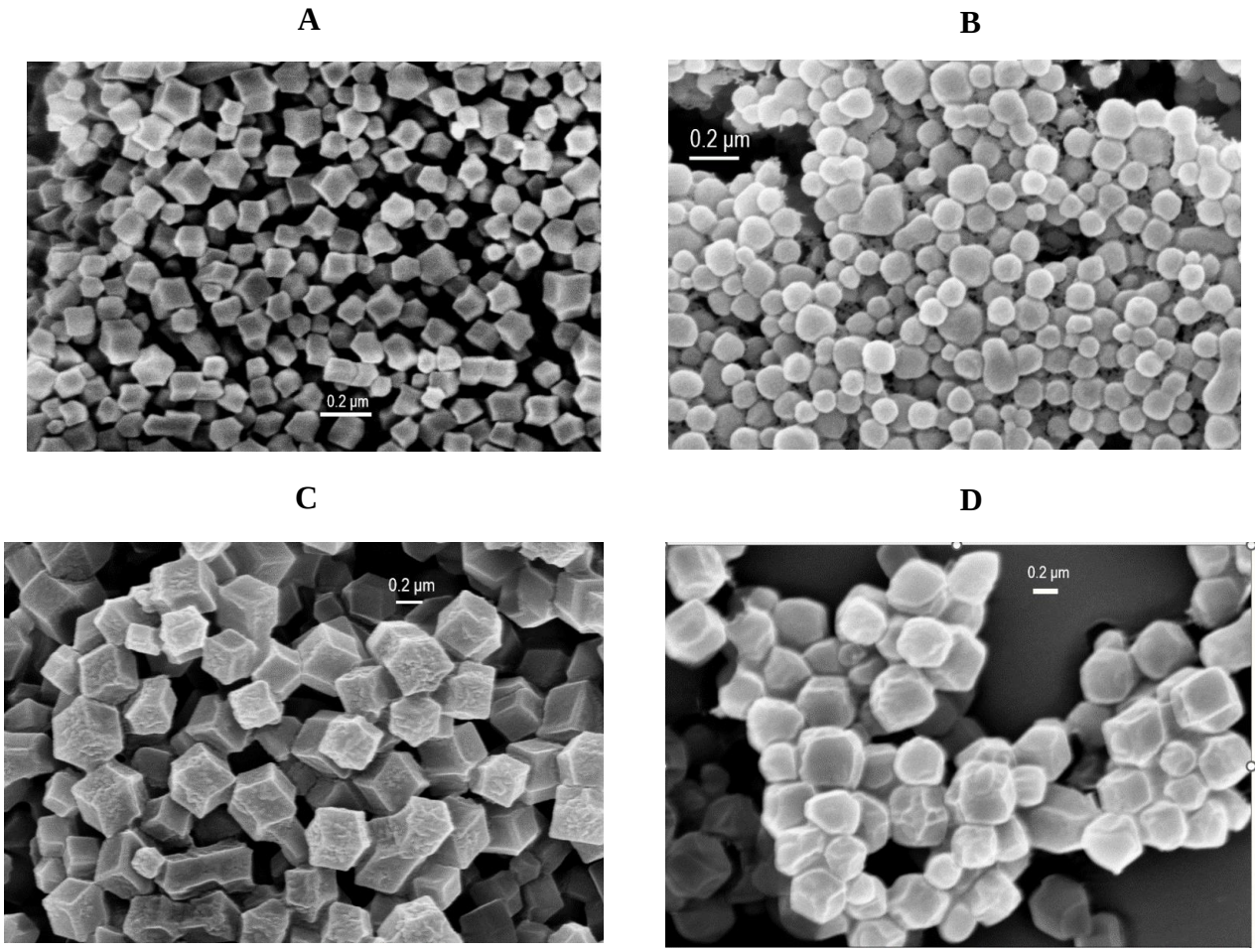

Fig. 3.7 "SEM images for **(A)** Pristine ZIF-8, **(B)** PSP-ED/ZIF-8, **(C)** PSP:ZIF-8, and **(D)** ED/PSP:ZIF-8. Size bar: 0.2 um." Acquired from Davey et al. [123].

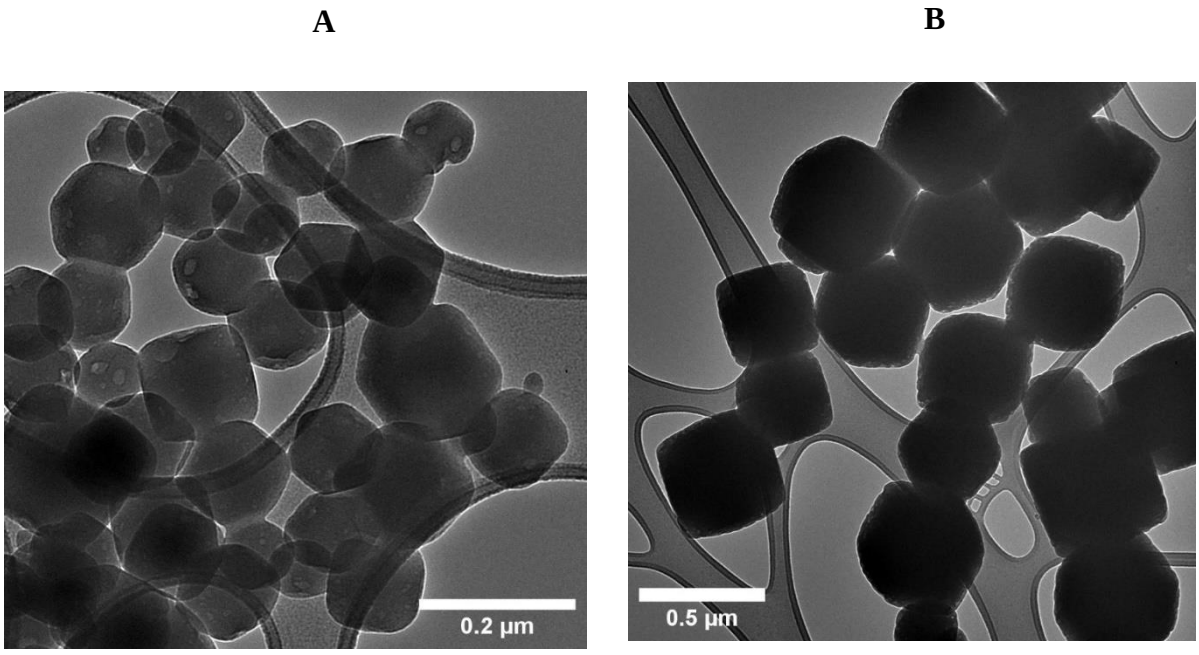

Fig. 3.8 "TEM images for **(A)** PSP-ED/ZIF-8 (size bar: 0.2 um) and **(B)** ED/PSP:ZIF-8 (size bar: 0.5 um)." Acquired from Davey et al. [123].

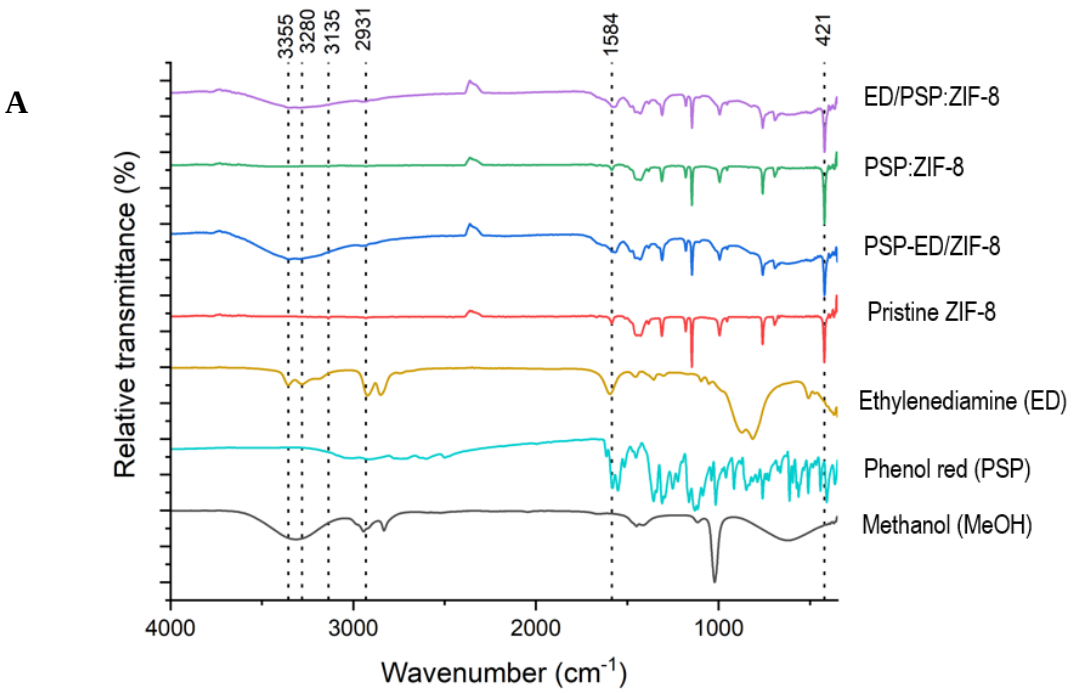

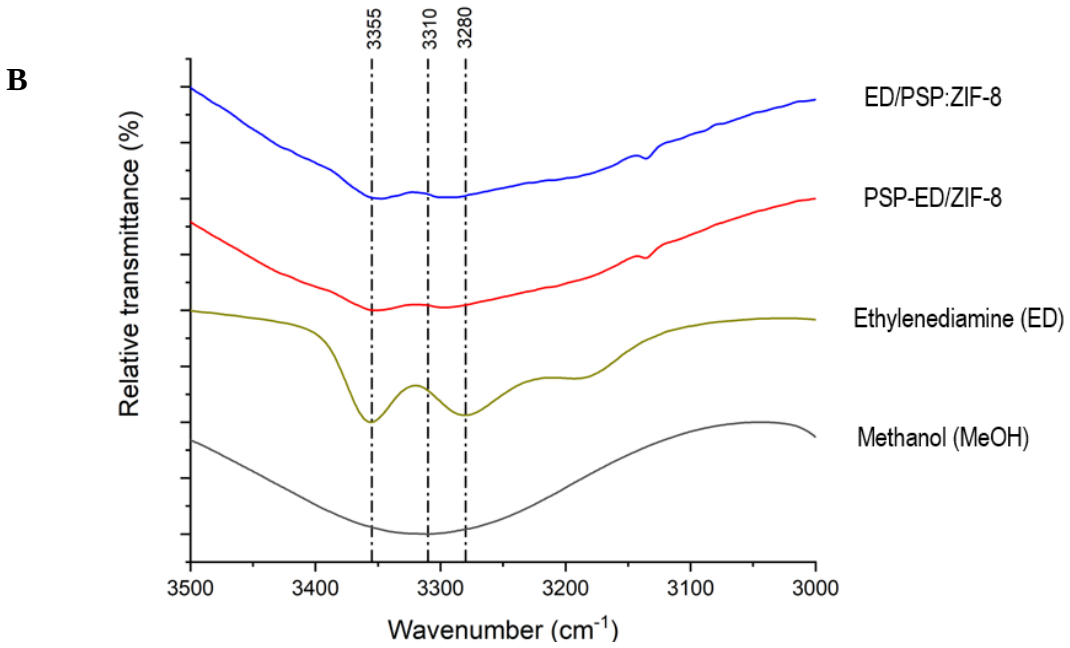

Fig. 3.9 "**[A]** Relative Fourier transform infrared (FTIR) transmittance values (%) versus wavenumber (cm^{-1}) for various colorimetric sensor components of the first-generation (PSP-ED/ZIF-8) and second-generation (ED/PSP:ZIF-8) materials. **[B]** Relative Fourier transform infrared (FTIR) transmittance values (%) versus wavenumber (cm^{-1}) from 3500 to 3000 cm^{-1} for the first-generation (PSP-ED/ZIF-8) and second-generation (ED/PSP:ZIF-8) materials as well as ethylenediamine and methanol." Acquired from Davey et al. [123].

Table 3.1. FTIR vibrational bands and corresponding molecular vibration assignments. Acquired from Davey et al. [123].

Vibrational band (cm^{-1})	**Assignment**
421	Zn-N stretch from ZIF-8 coordination bond.
1584	C=N stretch from imidazolate ligand.
2931	Aliphatic C-H stretch (imidazolate)
3135	Aromatic C-H stretch (imidazolate)
3280	N-H stretch from ethylenediamine
3310	O-H stretch from methanol.
3355	N-H stretch from ethylenediamine.

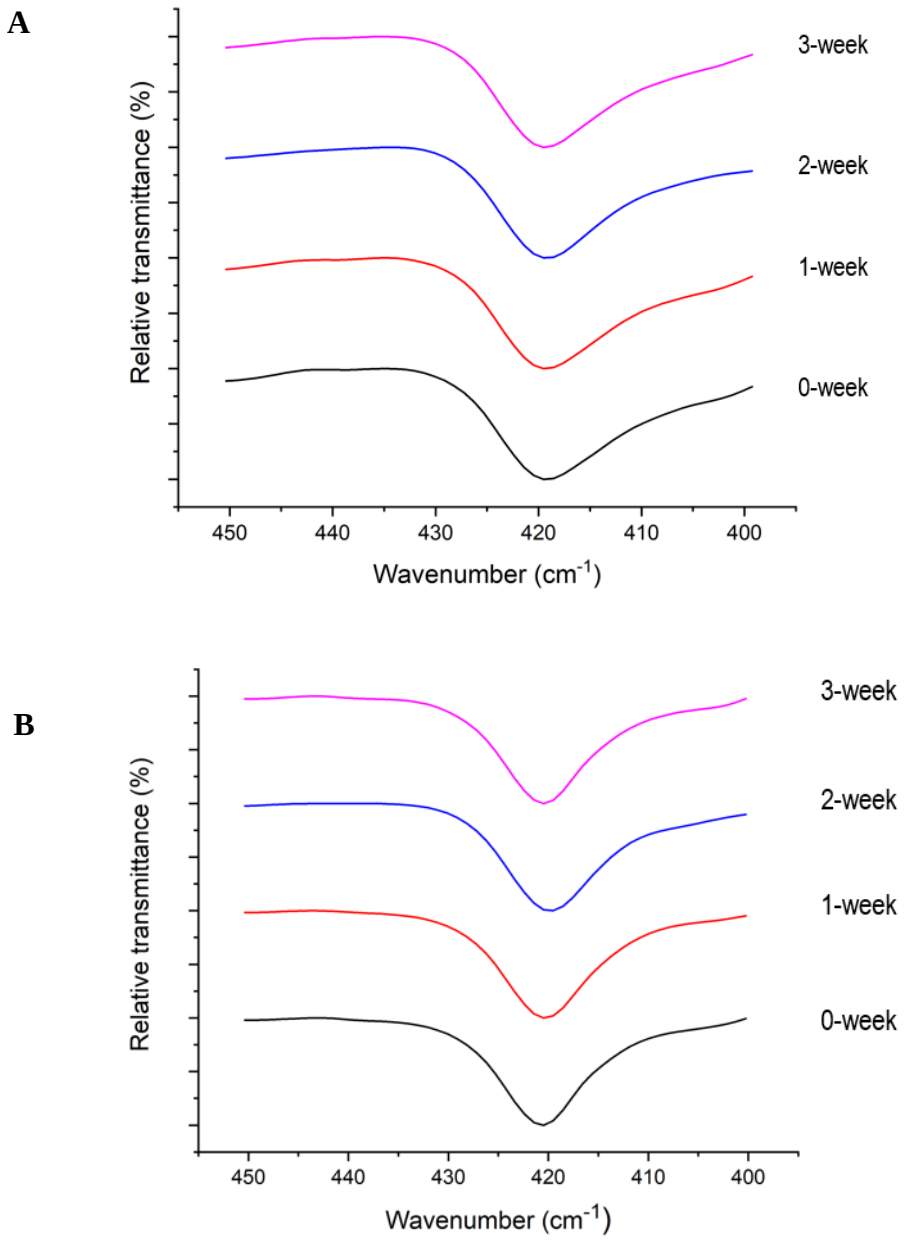

Fig. 3.10 "FTIR spectra of **(A)** PSP-ED/ZIF-8 and **(B)** ED/PSP:ZIF-8 at 0-week (black), 1-week (red), 2-week (blue), and 3-week (magenta)." Acquired from Davey et al. [123].

3.4.2 Colorimetric analyses in dry environment

"The colorimetric gas studies performed at low humidity are acquired from Davey et al. [123]. Colorimetric responses of PSP-ED/ZIF-8 and ED/PSP:ZIF-8 exposed to 300 sccm dry CO_2 are

displayed in [**Figure 3.11**]. With increasing CO_2 levels, both sensors exhibit an increased yellow intensity. However, compared to the modest responses of the first-generation PSP-ED/ZIF-8 material at 600 ppm CO_2 and above, those of the second-generation ED/PSP:ZIF-8 material indicate a stronger yellow color. Mean RGB intensities for these exposures are provided in [**Tables 3.2** and **3.3**] for PSP/ED-ZIF-8 and ED/PSP:ZIF-8, respectively. For the first-generation PSP/ED-ZIF-8 sensor, the average G-values increase and the average B-values decrease with increasing dry CO_2 exposure, demonstrating a stronger fuchsia-to-yellow colorimetric transition. For the second-generation ED/PSP:ZIF-8 material, the mean R-values and mean G-values both increase with rising dry CO_2 exposures. In alignment with the colorimetric assays depicted in [**Figure 3.11**], the mean R- and G-values for the new ED/PSP:ZIF-8 material exposed to 600 ppm CO_2 and above, respectively, are significantly larger than those for the PSP-ED/ZIF-8 material, indicating a stronger color response.

"Transient and repeated exposures to 2500 ppm CO_2 are displayed in [**Figure 3.12**]**.** Similar to the results of **[Figure 3.11**], the ED/PSP:ZIF-8 exhibits a vibrant yellow color compared to that of PSP-ED/ZIF-8, indicating a stronger colorimetric gas response. Both sensors respond to CO_2 within 1 s, and achieve a full color change within 20 to 30 s. The quick response times, as well as sensitivity to < 1000 ppm dry CO_2 displayed in [**Figure 3.11**], are consistent with reported ambient colorimetric CO_2 detection using dye- and tertiary amino alcohol-loaded porous adsorbents [19]. However, whereas the latter sensors are reversible [19], PSP-ED/ZIF-8 and ED/PSP:ZIF-8 only partially recover upon CO_2 removal (as shown in [**Figures 3.12-C** and **S4-D**] and sustain a residual yellow tinge compared to their pre-exposed states" [123].

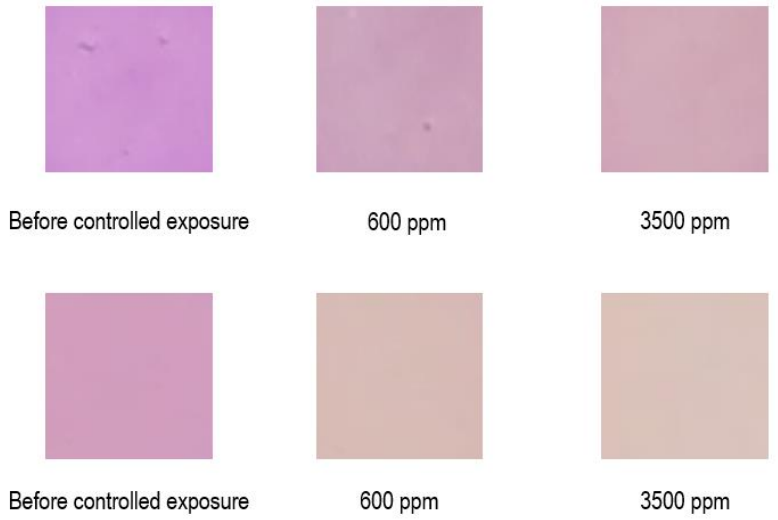

Fig. 3.11 "Colorimetric images of sensors before controlled exposure under 0% relative humidity, exposed to 600 ppm CO_2, and 3500 ppm CO_2**. Top row**: PSP-ED/ZIF-8 (first-generation sensor). **Bottom row**: ED/PSP:ZIF-8 (second-generation sensor). Images are taken after 30 s of exposure." Acquired from Davey et al. [123].

Table 3.2 "Mean RGB values for PSP-ED/ZIF-8 exposed to dry CO_2." Acquired from Davey et al. [123].

Exposure	Mean R-value	Mean G-value	Mean B-value
Before exposure	205 ± 0.7	145 ± 2.0	209 ± 1.0
600 ppm CO_2	203 ± 1.0	163 ± 1.0	187 ± 2.0
3500 ppm CO_2	209 ± 1.0	169 ± 1.0	183 ± 1.0

Table 3.3 "Mean RGB values for ED/PSP:ZIF-8 exposed to dry CO_2." Acquired from Davey et al. [123].

Exposure	Mean R-value	Mean G-value	Mean B-value
Before exposure	209 ± 0.7	158 ± 0.7	191 ± 1.0
600 ppm CO_2	215 ± 0.3	188 ± 0.8	182 ± 0.9
3500 ppm CO_2	218 ± 0.5	194 ± 0.3	187 ± 1.0

"In addition to the color-based assays, quantitative results from the *in-situ* UV-Vis spectra for various CO_2 exposures are presented in [**Figure 3.13**]. As the CO_2 level increases from 540 to 3350 ppm, the 443 nm F(R) peak intensity rises relative to that at 570 nm for the PSP-ED/ZIF-8 material. However, for the new ED/PSP:ZIF-8 material, the 570 nm F(R) peak decreases relative to the 443 nm F(R) peak with increasing CO_2 levels. Colorimetric ratios of the 443 and 570 nm F(R) values versus CO_2 level (in ppm) are shown in [**Figure 3.14**]. For both sensors, the ratios expectedly increase with rising CO_2 concentrations as the fuchsia-to-yellow color transition intensifies. However, as anticipated from the imaged exposures and RGB color distributions, the 443/570 nm F(R) ratios for the ED/PSP:ZIF-8 material are much larger than those of the PSP-ED/ZIF-8 material, similarly revealing a stronger colorimetric response to CO_2 in dry environment" [123].

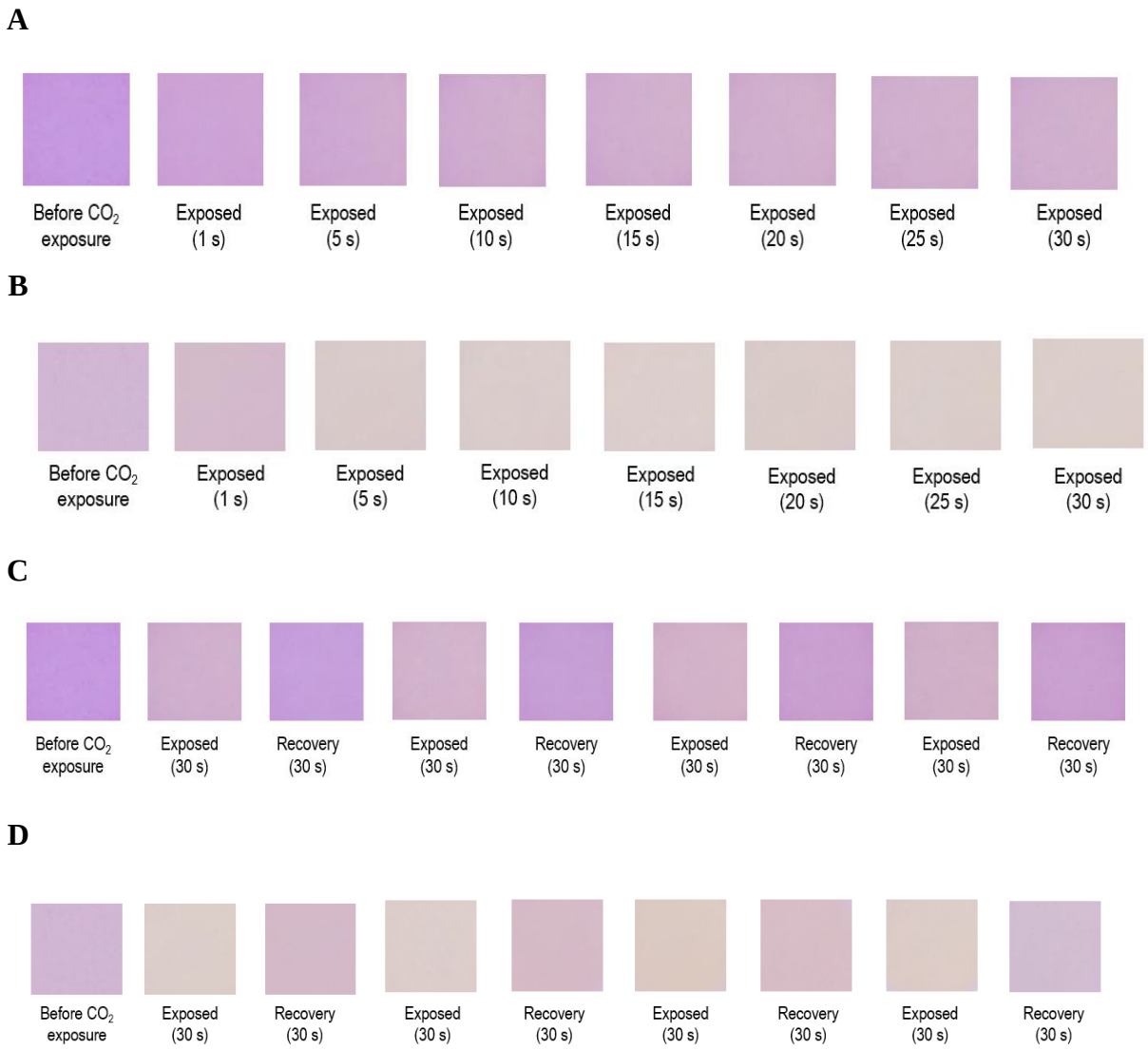

Fig. 3.12 "Colorimetric response time and recovery upon exposure to 2500 ppm CO_2 in dry environment (0% RH at 24.7 ± 0.4 ºC). Total flow: 300 sccm. **(A)** Progression of the color change of PSP-ED/ZIF-8 over 30 s. **(B)** Progression of the color change of ED/PSP:ZIF-8 over 30 s. **(C)** Repeat exposure of PSP-ED/ZIF-8 to dry CO_2. **(D)** Repeat exposure of ED/PSP:ZIF-8 to dry CO_2." Acquired from Davey et al. [123].

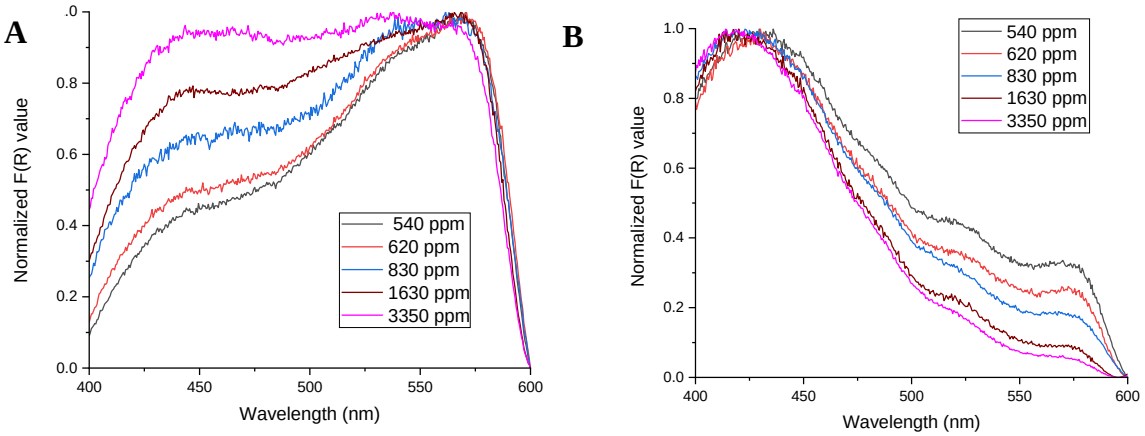

Fig. 3.13 "Normalized F(R) values versus wavelength (nm) for dry CO_2 exposures. 540 ppm (black); 620 ppm CO_2 (red); 830 ppm (blue); 1630 ppm (wine); and 3350 ppm (magenta). **(A)** PSP-ED/ZIF-8 (first-generation sensor). **(B)** ED/PSP:ZIF-8 (second-generation sensor)" [123]. Acquired from Davey et al. [123].

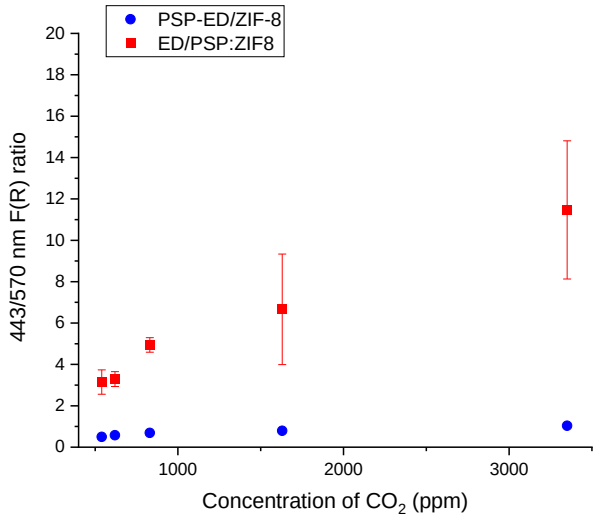

Fig. 3.14 "443/570 nm F(R) ratios for PSP-ED/ZIF-8 (blue) and ED/PSP:ZIF-8 (red) as a function of dry CO_2 exposure (in ppm). Standard deviation values are plotted as error bars which are smaller than the symbol size for PSP-ED/ZIF-8 sensor. For the ED/PSP:ZIF-8 material, the larger error bars observed at higher CO_2 concentrations are attributed to the high reflectance values achieved with increasing CO_2 levels (87% and up) as the sensor becomes more yellow" [123]. Acquired from Davey et al. [123].

3.4.3 Colorimetric analyses in humid environment

"Colorimetric profiles of PSP-ED/ZIF-8 and ED/PSP:ZIF-8 exposed to 1500 ppm CO_2 in 0%, 40%, and 80% relative humidity are depicted in [**Figure 3.15**]. With increasing humidity, while the first-generation sensor scarcely provides a colorimetric CO_2 response at 40% RH and above, the second-generation sensor still exhibits a visible fuchsia-to-yellow transition compared to its "Before controlled exposure" at higher humidity. The effect of humidity on the colorimetric sensitivity to CO_2 is also portrayed in [**Tables 3.4** and **3.5**]. For the PSP-ED/ZIF-8 material, the R- and G-values both decrease with increasing humidity, with a significantly larger drop observed in the G-values. The ED/PSP:ZIF-8 material also exhibits reduced R- and G-values with increased humidity; however, these R- and G-values are markedly more intense than those of the PSP-ED/ZIF-8 sensor at the same CO_2 concentration and humidity. Similarly, the B-values in dry and humid CO_2 conditions for the second-generation sensor are smaller than those for the first-generation sensor, indicating a stronger fuchsia-to-yellow color change" [123].

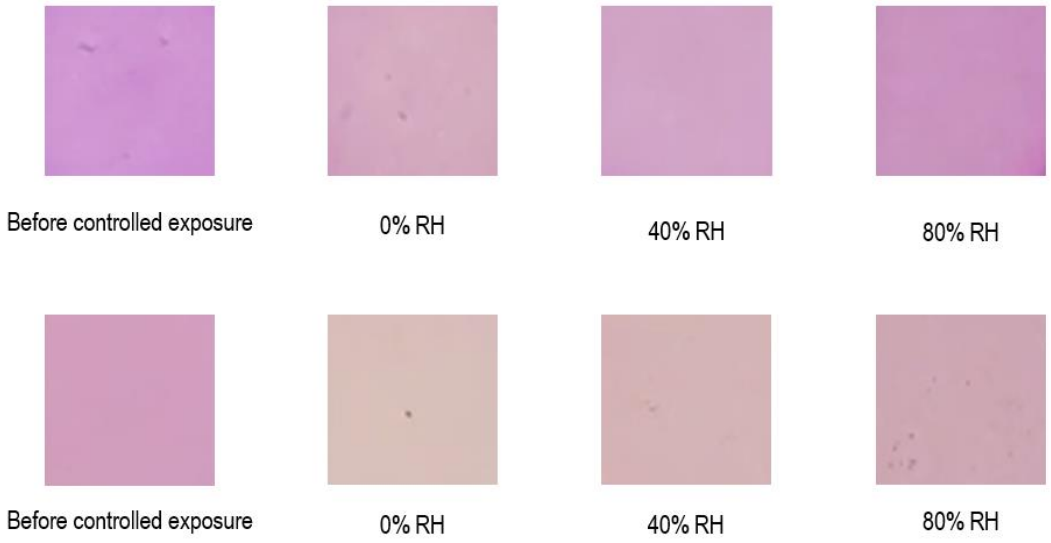

Fig. 3.15 "Colorimetric images of sensors before controlled exposure, exposed to 600 ppm CO_2, under varied relative humidity. Top row: PSP-ED/ZIF-8 (first-generation sensor). Bottom row: ED/PSP:ZIF-8 (second-generation sensor). Images are taken after 30 s of exposure." Acquired from Davey et. al [123].

Table 3.4 "Mean RGB values for PSP-ED/ZIF-8 exposed to 1500 ppm CO_2 in variable humidity" [123]. Acquired from Davey et. al [123].

Relative humidity (%)	Mean R-value	Mean G-value	Mean B-value
0	213 ± 2	171 ± 1	192 ± 1
40	208 ± 1	164 ± 1	196 ± 1
80	203 ± 1	148 ± 1	191 ± 1

Table 3.5 "Mean RGB values for ED/PSP:ZIF-8 exposed to 1500 ppm CO_2 in variable humidity" [123]. Acquired from Davey et. al [123].

Relative humidity (%)	Mean R-value	Mean G-value	Mean B-value
0	216.0 ± 0.5	192.0 ± 0.7	186.0 ± 0.3
40	212.0 ± 0.4	180.0 ± 0.5	181.0 ± 0.5
80	205.0 ± 0.3	168.0 ± 0.5	178.0 ± 0.5

"Transient and repeated colorimetric imaging assays for PSP-ED/ZIF-8 and ED/PSP:ZIF-8 exposed to 2500 ppm CO_2 in 35% and 60% RH are shown in [**Figures 3.16** and **3.17**], respectively. Similar to their dry exposures, both sensors respond to humid CO_2 within seconds. However, with increased humidity, the colorimetric gas response is suppressed in both sensors (with that of ED/PSP:ZIF-8 outperforming that of PSP-ED/ZIF-8 at both moderate and elevated humidity). Finally, neither sensor completely recovers upon release from humid CO_2 environment, maintaining a slightly different color from its original state following four cycles of humid gas exposure" [123].

"Normalized F(R) profiles versus wavelength (in nm) are plotted in [**Figure 3.18**] as a function of CO_2 concentration under RH of 45.4 ± 3%. As the CO_2 exposures rise from 540 to 3350 ppm, the 443 nm F(R) peak intensity increases relative to that of the 570 nm F(R) peak for both first- and second-generation materials. [**Figure 3.19**] depicts these ratios as a function of humid CO_2 level. At any humid CO_2 concentration in this span, the colorimetric response is enhanced for the second-generation ED/PSP:ZIF-8 material relative to the first-generation PSP/ED-ZIF-8 material, with a sharp increase in the yellow intensity at higher CO_2 exposures. However, compared to colorimetric ratios achieved from the dry gas exposures displayed in **[Figure 3.13]**, the 443/570 nm F(R) ratios in humid environment are smaller for both first- and second-generation sensors, establishing water as a sustained interferant in the colorimetric gas sensing mechanism [24]" [123].

Fig. 3.16 "Colorimetric response time and recovery upon exposure to 2500 ppm CO_2 in humid environment (34.6 ± 3 % RH at 24.7 ± 0.4 °C). Total flow: 300 sccm. (A) Progression of the color change of PSP-ED/ZIF-8 over 30 s. (B) Progression of the color change of ED/PSP:ZIF-8 over 30 s. (C) Repeat exposure of PSP-ED/ZIF-8 to humid CO_2. (D) Repeat exposure of ED/PSP:ZIF-8 to humid CO_2." Acquired from Davey et al. [123].

Fig. 3.17 "Colorimetric response time and recovery upon exposure to 2500 ppm CO_2 in humid environment (58.8 ± 3 % RH at 24.7 ± 0.4 °C). Total flow: 300 sccm. **(A)** Progression of the color change of PSP-ED/ZIF-8 over 30 s. **(B)** Progression of the color change of ED/PSP:ZIF-8 over 30 s. **(C)** Repeat exposure of PSP-ED/ZIF-8 to humid CO_2. **(D)** Repeat exposure of ED/PSP:ZIF-8 to humid CO_2." Acquired from Davey et al. [123].

"Cyclic *in-situ* UV-Vis measurements of PSP-ED/ZIF-8 and ED/PSP:ZIF-8 exposed to 3500 ppm CO_2 (in 0 and 80% RH, respectively) are tabulated in [**Tables 3.6, 3.7, 3.8, and 3.9]**. As observed qualitatively from the colorimetric imaging assays, neither sensor fully recovers the 443/570 nm F(R) ratio ascribed to its pre-exposed state. The irreversible nature of both sensors upon gas exposure (across humidity) is largely attributed to the gradual evaporation of methanol upon deposition onto cellulose filter paper, which prevents either sensor from fully recovering its original color [24]. As shown in [**Table 3.6]**, PSP-ED/ZIF-8 maintains achieves similar quantitative color change responses to dry CO_2 in the first and second cycle. However, the colorimetric response comparatively decreases upon the third cycle. While PSP-ED/ZIF-8 exhibits a stronger quantitative color change to dry CO_2 (as evidenced in [**Table 3.7]**), the colorimetric response noticeably decreases with increased cycles. Upon prolonged exposure to humid CO_2 (in [**Table 3.8]**), PSP-ED/ZIF-8 exhibits an increase in its 443/570 nm F(R) ratio from the first to the second cycle, with a small increase from the second cycle to the third cycle. Finally, as depicted in [**Table 3.9]**, the ED/PSP:ZIF-8 similarly shows an increase in 443/570 nm F(R) ratios with increased cycling in humidity" [123].

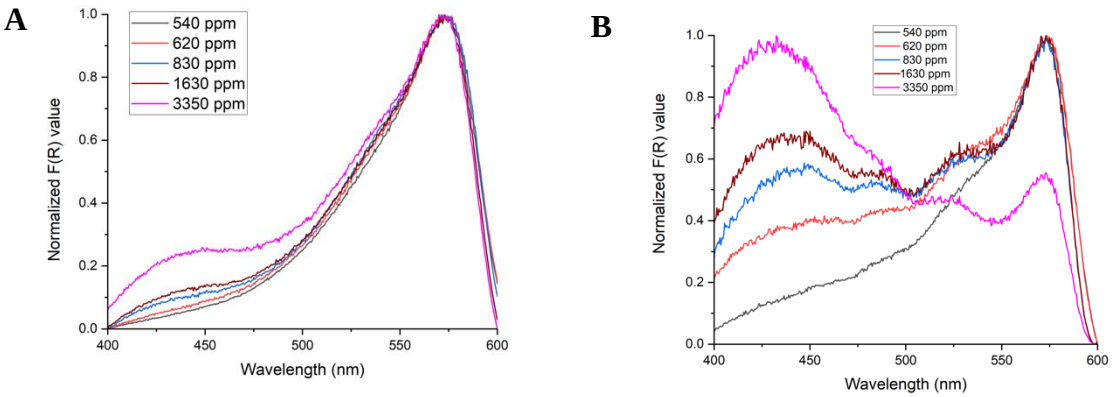

Fig. 3.18 "Normalized F(R) values versus wavelength (nm) for humid CO_2 exposures (RH: 45.4 ± 3%). 540 ppm (black); 620 ppm CO_2 (red); 830 ppm (blue); 1630 ppm (wine); and 3350 ppm (magenta). **(A)** PSP-ED/ZIF-8 (first-generation sensor). **(B)** ED/PSP:ZIF-8 (second-generation sensor)." Acquired from Davey et al. [123].

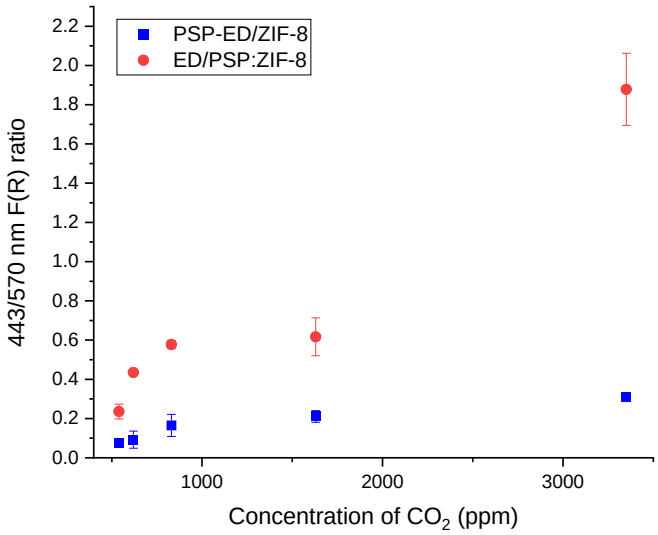

Fig. 3.19 "443/570 nm F(R) ratios for PSP-ED/ZIF-8 (blue) and ED/PSP:ZIF-8 (red) as function of CO_2 concentration (in ppm) under relative humidity of 45.4 ± 3%. Standard deviation values are plotted as error bars." Acquired from Davey et al. [123].

Table 3.6. "443/570 nm F(R) ratios of PSP-ED/ZIF-8 exposed to three cycles of 3500 ppm CO_2 (0% RH at 23.0 ± 0.8 °C). Total gas flow rate: 300 ml/min." Acquired from Davey et al. [123].

Time (minutes)	Cycle 1	Cycle 2	Cycle 3
0	**0.163**	**0.782**	**0.640**
1	0.761	0.849	0.767
5	0.808	0.871	0.789
10	0.833	0.863	0.789
20	0.864	0.888	0.808
30	0.869	0.890	0.814
45	0.900	0.902	0.835
60	0.897	0.905	0.834
90	0.917	0.919	0.847
120	0.941	0.912	0.844

Table 3.7. **"**443/570 nm F(R) ratios of ED/PSP:ZIF-8 exposed to three cycles of 3500 ppm CO_2 (0% RH at 23.0 ± 0.8 °C). Total gas flow rate: 300 ml/min." Acquired from Davey et al. [123].

Time (minutes)	Cycle 1	Cycle 2	Cycle 3
0	**0.950**	**2.53**	**2.16**
1	5.45	3.00	2.55
5	5.54	3.07	2.66
10	5.80	3.12	2.67
20	6.40	3.24	2.75
30	6.15	3.14	2.52
45	6.22	2.94	2.65
60	6.01	3.12	2.54
90	5.19	2.84	2.57
120	5.41	2.73	2.52

Table 3.8. "443/570 nm F(R) ratios of PSP-ED/ZIF-8 exposed to three cycles of 3500 ppm CO_2 (82.0 ± 5% RH at 23.0 ± 0.8 °C). Total gas flow rate: 300 ml/min." Acquired from Davey et al. [123].

Time (minutes)	Cycle 1	Cycle 2	Cycle 3
0	**0.241**	**0.473**	**0.652**
1	0.347	0.406	0.435
5	0.328	0.412	0.445
10	0.334	0.400	0.439
20	0.341	0.410	0.428
30	0.350	0.399	0.428
45	0.324	0.394	0.395
60	0.230	0.403	0.428
90	0.133	0.408	0.431
120	0.124	0.397	0.430

Table 3.9 "443/570 nm F(R) ratios of ED/PSP:ZIF-8 exposed to three cycles of 3500 ppm CO_2 (82.0 ± 5% RH at 23.0 ± 0.8 °C). Total gas flow rate: 300 ml/min." Acquired from Davey et al. [123].

Time (minutes)	Cycle 1	Cycle 2	Cycle 3
0	**0.247**	**0.573**	**0.833**
1	0.474	0.569	0.798
5	0.464	0.582	0.819
10	0.471	0.596	0.765
20	0.515	0.593	0.749
30	0.533	0.576	0.732
45	0.589	0.623	0.696
60	0.563	0.641	0.767
90	0.568	0.637	0.789
120	0.551	0.607	0.804

"Following cyclic exposure to both dry and humid gas conditions, both sensors are scanned via FTIR spectroscopy to probe the stability of ZIF-8. Recent studies in the literature have illustrated how the structural integrity of ZIF-8 is compromised when submerged in pure water under specific mass ratios and ambient conditions for 24 h [48]. ZIF-8 hydrolysis has similarly been reported in water at higher temperatures [49]. In addition to structural degradation from prolonged immersion in water, ZIF-8 has also been shown to be vulnerable to structural degradation under prolonged exposure to acidic gases (such as CO_2) at elevated humidity [50]. [**Figure 3.20]** shows FTIR spectra of recovered PSP-ED/ZIF-8 and ED/PSP:ZIF-8 samples following cyclic exposure to dry and humid CO_2. The preserved 421 cm^{-1} Zn-N stretch in both the first- and second-generation sensors subsequent gas exposure indicates the stability of ZIF-8 to prolonged dry and humid CO_2 exposure. Compared to prior studies on ZIF-8 degradation, it is possible that the dilute CO_2 atmospheres exposed (resembling indoor air conditions), as well as the length of time exposed and mass of sensor deposited on the cellulose filter paper, do not readily induce a measurable collapse of the crystalline MOF network" [123].

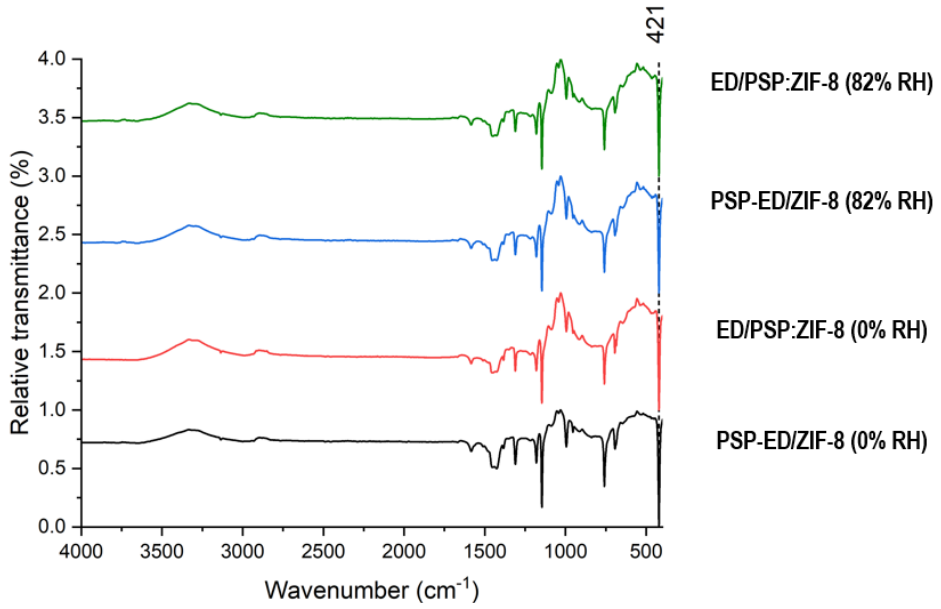

Fig. 3.20 "FTIR spectra of gas sensors after cyclic *in-situ* UV-Vis gas measurements **(A)** PSP-ED/ZIF-8 (0% RH); **(B)** ED/PSP:ZIF-8 (0% RH); **(C)** PSP-ED/ZIF-8 (82% RH); and **(D)** ED/PSP:ZIF-8 (82% RH). Blank cellulose filter paper is used as the background." Acquired from Davey et. al [123].

3.4.4 Sensors' responses to volatile organic compounds (VOCs)

"To assess the role of other airborne pollutants (such as VOCs) as possible interferants in the colorimetric CO_2 sensing mechanism, colorimetric assays and *in-situ* UV-Vis spectra are collected in response to acetone and ethanol. [**Figure 3.21**] shows colorimetric images of the PSP-ED/ZIF-8 and ED/PSP:ZIF-8 materials exposed to dry house air (458 ± 3 ppm CO_2), as well as dry house air mixed with 200 ppm ethanol and 200 ppm acetone. Compared to humid CO_2 exposures, the presence of these select VOCs demonstrates a relatively negligible effect on the observed color change achieved in dry atmosphere. In addition to the colorimetric imaging results, [**Figure 3.22**] demonstrates the results of *in-situ* UV-Vis experiments with CO_2 (450-3600 ppm) mixed with dry air and acetone (0, 20, and 314 ppm) at a total gas flow rate of 350 ml/min. Unlike the spectra observed in a humid atmosphere, both sensors exhibit a high selectivity to CO_2 with rising acetone levels, with the ED/PSP:ZIF-8 material displaying a significantly stronger color change than the PSP-ED/ZIF-8 material" [123].

Fig. 3.21 "Colorimetric exposure to dry house air, dry house air mixed with 200 ppm ethanol, and dry house air mixed with 200 ppm acetone. **Row A:** PSP-ED/ZIF-8 (first-generation material). **Row B:** ED/PSP:ZIF-8 (second-generation material). Dry house air is 458 ± 3 ppm CO_2." Acquired from Davey et al. [123].

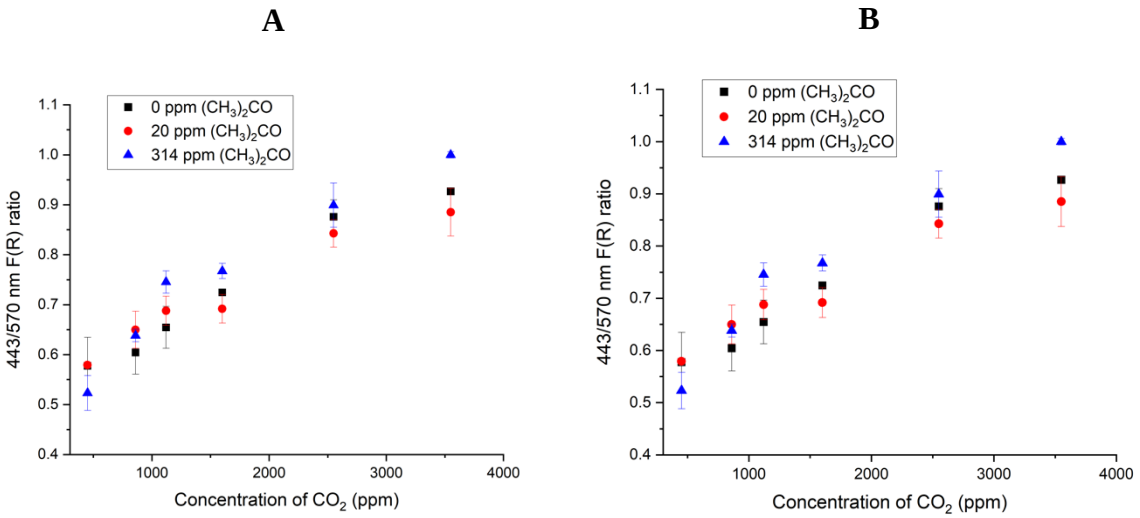

Fig. 3.22 "443/570 nm F(R) ratios obtained from *in-situ* UV-Vis spectra of **(A)** PSP-ED/ZIF-8 and **(B)** ED/PSP:ZIF-8 vs. CO_2 concentration in presence of 0, 20, and 314 ppm of acetone. Total gas flowrate: 350 ml/min." Acquired from Davey et al. [123]. Error bars are standard deviation values.

3.4.5 Hypotheses of apparent differences between the sensors

This section is obtained from Davey et al. [123]. "To understand the colorimetric CO_2 sensing behavior observed in dry and humid conditions, as well as in the presence of select VOCs, the zwitterion mechanism is described in this section. In the previous work [99, 140-145], the zwitterion mechanism (characteristically used to evaluate the reaction chemistries involving CO_2 absorbed into aqueous primary and secondary amine solutions) was proposed to comprehend the color change dynamics involving ZIF-8, phenol red, and ethylenediamine in response to CO_2 and humidity in methanolic solvent [99, 140-145]. Once adsorbed by ZIF-8, CO_2 is posited to first react with ethylenediamine (shown in [**Equation 2.15]** as RNH_2) to produce a zwitterion species [99, 140-145]. Upon formation of the zwitterion, the second step of the reaction [shown as **Equation 2.16**] ensues in which a base in the system, B, deprotonates the zwitterion to form a protonated species and carbamate species [99, 140-145]" [123].

"At low humidity, the pH indicator, phenol red, is expected to function as the primary base and abstract the proton from the zwitterion species, thus modifying its conjugation and triggering a clear fuchsia-to-yellow color transition dependent on CO_2 concentration [99]. However, in humid conditions, water can participate in [**Equation 2.16**] as a free base to deprotonate the zwitterion [99]. Thus, it is hypothesized that adsorbed phenol red molecules might compete with water for access to the proton of the zwitterion, resulting in colorimetric suppression with increased humidity [99]. In addition, the intrinsic hydrophilicity of ethylenediamine could promote water adsorption to the detriment of CO_2 adsorption, inhibiting formation of the zwitterion and thus disrupting the colorimetric gas response accomplished in dry environment [99]" [123].

"Related to the cyclic *in-situ* UV-Vis results shown in [**Tables 3.6** and **3.7**], it is possible that the reduced colorimetric gas response observed with increased cycling can be ascribed to both the transient loss of methanol and formation of stable carbamates, which both age the sensor and limit the regeneration of ethylenediamine for subsequent CO_2 chemisorption [99]. However, as observed in [**Tables 3.8** and **3.9**], it is possible that the dry air purge streams between cycles disrupt hydrogen bonding interactions between ethylenediamine and water in a humid gas environment, freeing more ethylenediamine molecules for subsequent CO_2 chemisorption and generating higher 443/570 nm F(R) ratios [189]. In contrast with these colorimetric studies using dye- and amine-modified ZIF-8 species, other amine-based systems exhibit an increased sensitivity to indoor levels of CO_2 in humid environment [190]. For example, a polymer blend of poly(ethylene oxide) and poly(ethyleneimine) coated onto a resonant mass sensor was proposed to demonstrate an enhanced indoor CO_2 detection in humid environment due to the availability of water molecules to convert carbamate species into stable bicarbonates, which provides free amines to bind additional CO_2 [190]. Given these differences, it is imperative to establish the specific interaction between ethylenediamine and water in these ZIF-8-based sensors, as well as possible competition between water and phenol red in the zwitterion deprotonation step during humid gas delivery [99]. However, with respect to mixed CO_2/VOC studies reported in [**Figures. 3.21** and **3.22**], it is possible that neither acetone nor ethanol disturbs the chemisorptive interaction between CO_2 and ethylenediamine, nor functions as a competitive base for adsorbed phenol red species [99]" [123].

"To understand the enhanced response to CO_2 observed in the second generation (ED/PSP:ZIF-8) sensor, the nature of phenol red and ethylenediamine adsorption onto ZIF-8 need to be evaluated between both sensors. While both sensors incorporate ethylenediamine through post-synthetic mixing with the MOF, the ED/PSP:ZIF-8 material involves the direct inclusion of phenol red into the ZIF-8 precursor broth, which results in the formation of nanocrystals more than triple the size of the pristine ZIF-8. In addition to understanding the role of synthetic phenol red mixing on ZIF-8 growth [171], the location of phenol red with respect to ZIF-8 between both sensors must be established. The structural flexibility of ZIF-8—associated with the "gate-opening" phenomenon describing a rotational swing of the imidazolate linkers to expand the 6-member ring pore aperture beyond its nominal 3.4 Å size—has been observed with penetrating liquids at high-pressure [191], as well as both computational and experimental studies involving the adsorption of gases with kinetic diameters exceeding 3.4 Å [192-193]. However, the ambient-pressure, room-temperature mixing of phenol red molecules with pristine ZIF-8 nanoparticles in methanol that produces the first-generation sensor is not anticipated to result in phenol red penetration through the ZIF-8 nominal pore aperture via the gate-opening phenomenon. Rather, it is expected that phenol red remains adsorbed on the external surface of the ZIF-8 adsorbent. However, in the case of the second-generation sensor, it is hypothesized that phenol red molecules, mixed with the ZIF-8 ligand and metal precursor solution in methanol, might become incorporated within the 11.6 Å pore cavities as ZIF-8 grows [109-110]. Prior studies on ZIF-8 have attributed preferential gas adsorption sites with regions proximate to the imidazolate linkers [111, 194]. Given how ZIF-8 crystals grow in a phenol red-incorporated methanolic MOF precursor solution in the second-generation sensing approach, it is possible that dye molecules are well-distributed throughout the MOF and more proximate to CO_2-affinative regions of the linker than the first-generation sensor,

triggering stronger colorimetric gas responses across humidity [111, 194]. To test this hypothesis on comparative phenol red location on ZIF-8 between both sensors, the following set of experiments are conducted" [123].

"[**Figure 3.23**] shows the PSP-ED/ZIF-8 and ED/PSP:ZIF-8 materials after successive washes in methanol. Whereas the PSP-ED/ZIF-8 sensor becomes much lighter with increased washes, the ED/PSP:ZIF-8 sensor does not. The structural integrity of ZIF-8 is maintained upon washing, as displayed from the sustained 421 cm^{-1} Zn-N stretches shown in [**Figure 3.24-A**]**.** With increased washes, the 1028 cm^{-1} C-O stretch associated with methanol emerges for both sensors [184, 186]. Though the ZIF-8 structure is maintained, ethylenediamine is lost with successive washes. [**Figures 3.24-B** and **3.24-C**] show the disappearance of the 3280 and 3355 N-H stretches associated with ethylenediamine upon washing, which suggests that ethylenediamine is adsorbed to the external surface of the ZIF-8 adsorbent [187].

"Toward estimating phenol red adsorption onto ZIF-8 between both materials, three samples (each) of PSP-ED/ZIF-8 and ED/PSP:ZIF-8 are (i) centrifuged, (ii) separated from their supernatant, (iii) rinsed with methanol for 60-min (in a sonication bath), (iv) centrifuged again, (v) separated again from their supernatant, and (vi) blended with methanol, a 2% ethylenediamine (by volume) methanolic solution, or a 0.5 mg/ml solution of phenol red dissolved in a 2% ethylenediamine (by volume) methanolic solution. [**Figure 3.25**] shows the response of these washed sensors to 800 ppm CO_2 (in dry conditions). When re-mixed with only methanol, neither sensor responds to CO_2. However, when re-mixed with ethylenediamine in methanol, the washed second-generation ED/PSP:ZIF-8 material demonstrates a strong fuchsia-to-yellow color change. On the other hand, the first-generation PSP-ED/ZIF-8 material turns white-yellow and shows minimal response to CO_2. When re-mixed with phenol red and ethylenediamine in methanol, though, the original PSP/ED-ZIF-8 material demonstrates a CO_2 response similar to that of its unwashed, fresh state. In other words, whereas the rinsed ED/PSP:ZIF-8 material only requires ethylenediamine (in methanol) to recover its colorimetric sensitivity to CO_2, the rinsed PSP-ED/ZIF-8 material requires *both* phenol red and ethylenediamine (in methanol). *These results support that ethylenediamine is bound to the external MOF surface for both sensors, whereas phenol red is incorporated within the internal surfaces of ZIF-8 in the second-generation sensor but on the external surface of ZIF-8 for the first-generation sensor*" [123].

"To further test the location of phenol red within ZIF-8 between the two sensors, an 80 mg/ml ZIF-8 solution is prepared by blending ZIF-8 with a 0.5 mg/ml phenol red solution (in methanol). Similar to the processes described above, this material—termed PSP/ZIF-8—is washed several times in methanol (for 30-min). The same process is performed using an 80 mg/ml PSP:ZIF-8 solution (in methanol). [**Figure 3.26**] shows how the PSP/ZIF-8 material becomes lighter with successive washes, transitioning from orange to light pink. In contrast, as shown in [**Figure 3.27**], the PSP:ZIF-8 material does not exhibit such a large color change with continued washing. Upon washing several times, the PSP/ZIF-8 and PSP:ZIF-8 materials are placed into the UV-Vis spectrophotometer and the reflectance (%R) at 570 nm is evaluated. As displayed in [**Table 3.10**], the rinsed PSP/ZIF-8 material exhibits large increases in 570 nm reflectance values upon successive washes, suggesting loss of phenol red. However, the PSP:ZIF-8 material does not

demonstrate such pronounced changes in its 570 nm reflectance value with continued washing, implying the retention of phenol red molecules and their incorporation within the internal surfaces of MOF" [123].

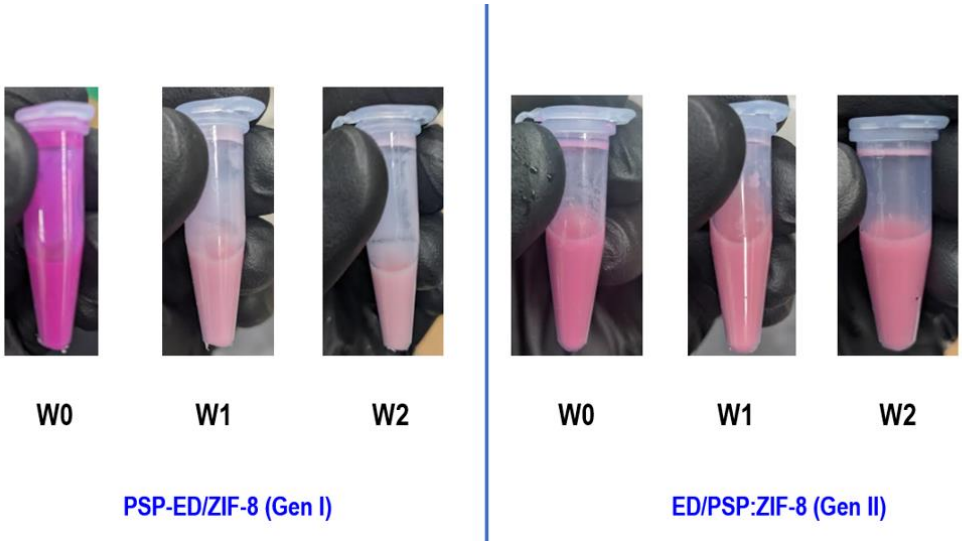

Fig. 3.23 "Optical images of PSP-ED/ZIF-8 **(left)** and ED/PSP:ZIF-8 **(right)** after successive washes in methanol. For the first-generation material, an 80 mg/ml ZIF-8 solution of PSP-ED/ZIF-8 is centrifuged at 12,000 rpm for 5-min. After the supernatant is removed, pure methanol is added to the pellet to form another 80 mg/ml ZIF-8 solution. This solution is sonicated for 30-min, and then centrifuged again at 12,000 rpm for 5-min. Then, upon removal of the supernatant, pure methanol is added again to the pellet to form an 80 mg/ml ZIF-8 solution, which is sonicated for another 30-min, centrifuged at 12,000 rpm for 5-min, removed from its supernatant, and mixed again with methanol to form a final 80 mg/ml ZIF-8 solution. In total, the PSP-ED/ZIF-8 is washed twice. For the second-generation material, an 80 mg/ml PSP:ZIF-8 solution of ED/PSP:ZIF-8 is centrifuged at 12,000 rpm for 5-min. After the supernatant is removed, pure methanol is added to the pellet to form another 80 mg/ml PSP:ZIF-8 solution. This solution is sonicated for 30-min, and then centrifuged again at 12,000 rpm for 5-min. Then, upon removal of the supernatant, pure methanol is added again to the pellet to form an 80 mg/ml PSP:ZIF-8 solution, which is sonicated for another 30-min, centrifuged at 12,000 rpm for 5-min, removed from its supernatant, and mixed again with methanol to form a final 80 mg/ml PSP:ZIF-8 solution. In total, the ED/PSP:ZIF-8 is washed twice" [123]. Acquired from Davey et al. [123].

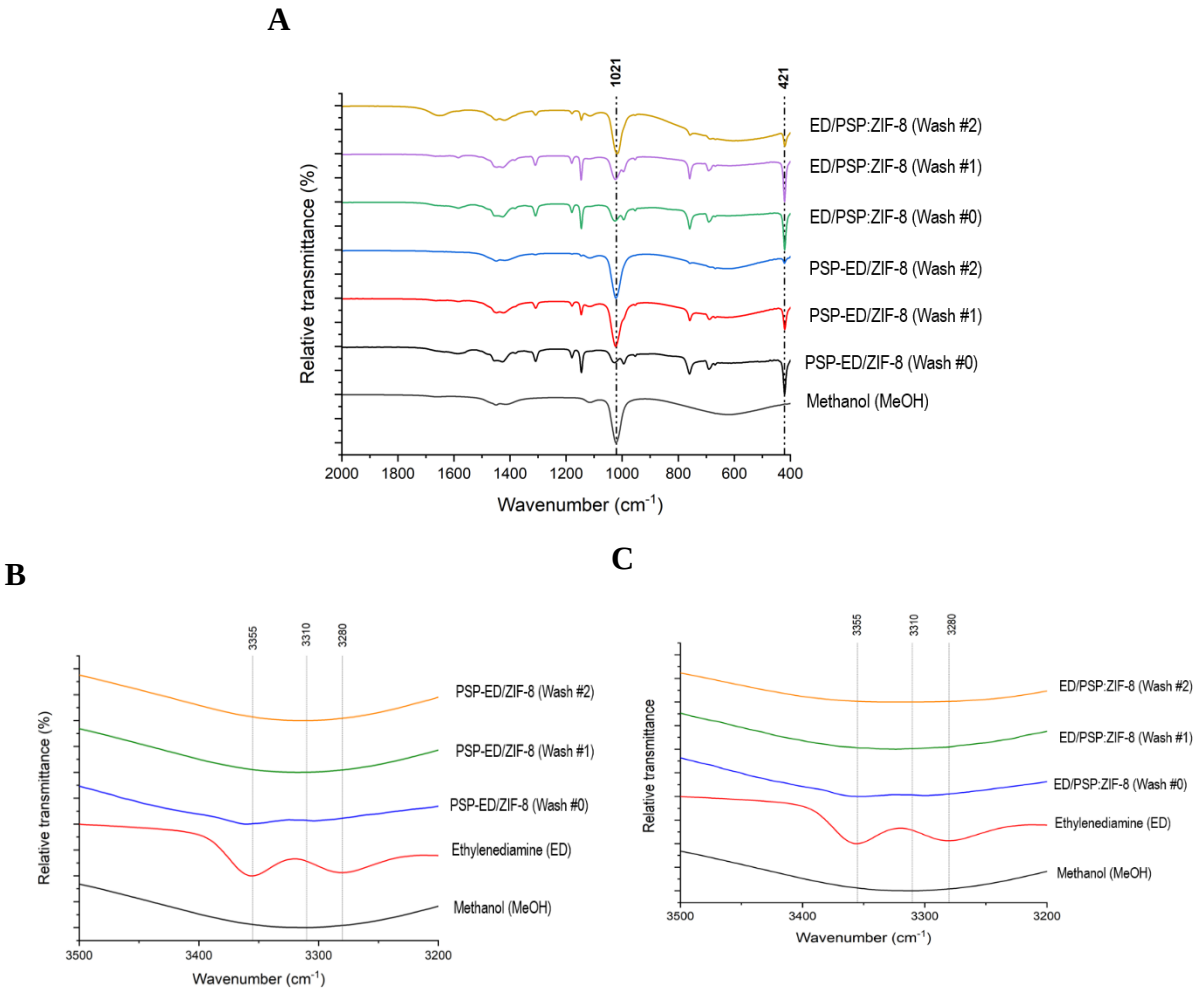

Fig. 3.24 "Effect of successive washing in methanol on the FTIR spectra of ZIF-8-based colorimetric CO_2 sensors. **(A)** PSP-ED/ZIF-8 and ED/PSP:ZIF-8 (ZIF-8 region). **(B)** PSP-ED/ZIF-8 (ethylenediamine and methanol region). **(C)** ED/PSP:ZIF-8 (ethylenediamine and methanol region)" [123]. Acquired from Davey et al. [123].

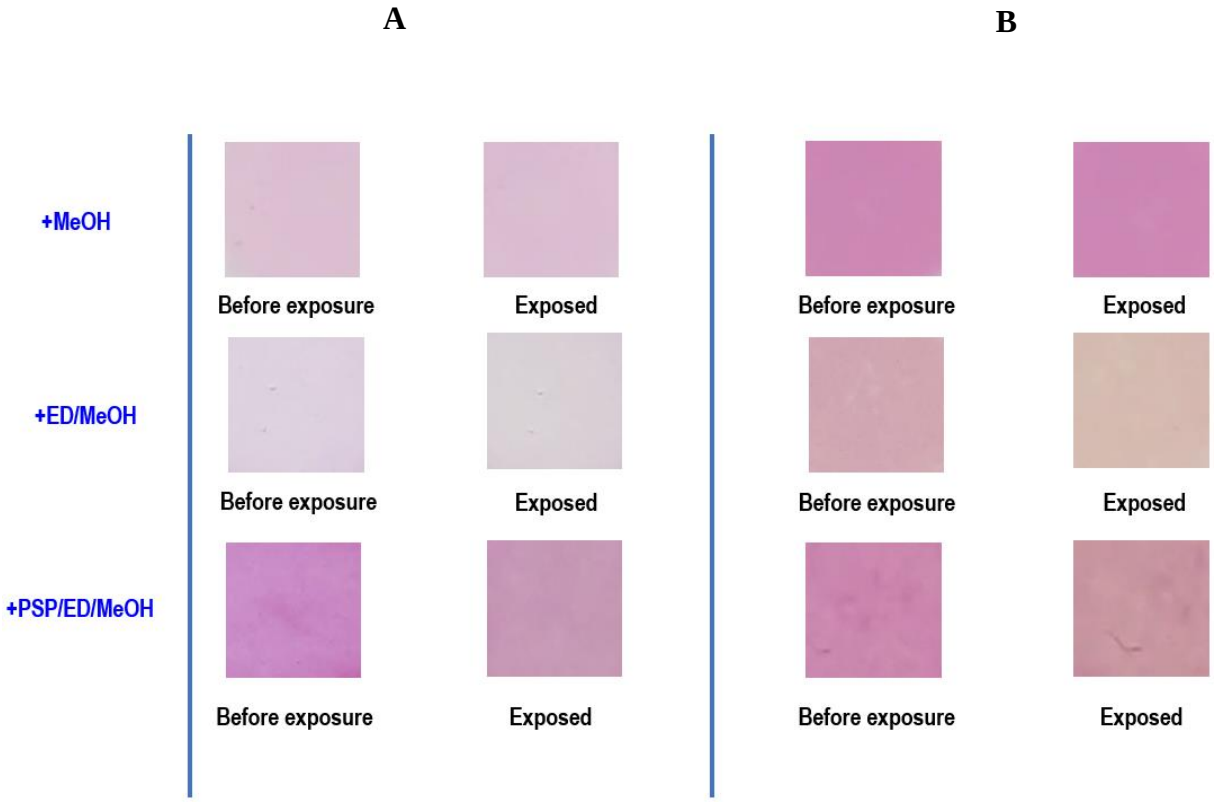

Fig. 3.25 "Colorimetric exposure of washed sensors to 800 ppm CO_2 (dry). **Column one (A):** PSP-ED/ZIF-8-based materials (Gen I). **Column two (B):** ED/PSP:ZIF-8-based materials (Gen II). **First row:** Washed, mixed with methanol. **Second row:** Washed, mixed with a 2% ethylenediamine (%v/v) methanolic solution. **Third row:** Washed, mixed with a 0.5 mg/ml phenol red solution (dissolved in a 2% ethylenediamine, %v/v, methanolic solution). In this washed experiment, three centrifuge tubes with 80 mg/ml ZIF-8 solution of PSP-ED/ZIF-8 (each) and three centrifuge tubes with 80 mg/ml PSP:ZIF-8 solution of ED/PSP:ZIF-8 (each) are centrifuged at 12,000 rpm for 5-min. After the supernatant is removed, pure methanol is added to each pellet to form another 80 mg/ml solution. These solutions are sonicated for 60-min, and then centrifuged again at 12,000 rpm for 5-min. Upon removal of the supernatant, six distinct solutions are formed: (1) to the first centrifuge tube, pure methanol is added to form an 80 mg/ml ZIF-8 solution; (2) to the second centrifuge tube, a 2% ethylenediamine (% v/v) methanolic solution is added to form an 80 mg/ml ZIF-8 solution; (3) to the third centrifuge tube, a 0.5 mg/ml phenol red solution (dissolved in a 2% ethylenediamine, %v/v, in methanol) is added to form a final 80 mg/ml ZIF-8 solution; (4) to the fourth centrifuge tube, pure methanol is added to form an 80 mg/ml PSP:ZIF-8 solution; (5) to the fifth centrifuge tube, a 2% ethylenediamine (% v/v) methanolic solution is added to form an 80 mg/ml PSP:ZIF-8 solution; and (c) to the sixth centrifuge tube, a 0.5 mg/ml phenol red solution (dissolved in a 2% ethylenediamine, %v/v, in methanol) is added to form a final 80 mg/ml PSP:ZIF-8 solution" [123]. Acquired from Davey et al. [123].

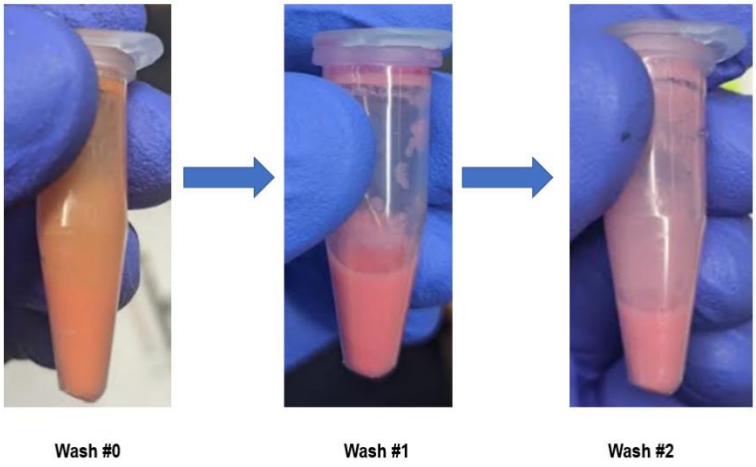

Fig. 3.26 "Optical images of PSP/ZIF-8 after successive washes. Similar to the first washed experiment with PSP-ED/ZIF-8, the experiment begins with forming an 80 mg/ml solution of PSP/ZIF-8, in which ZIF-8 is dissolved in a 0.5 mg/ml phenol red solution (in methanol). Then, this solution is centrifuged at 12,000 rpm for 5-min. After the supernatant is removed, pure methanol is added to the pellet to form another 80 mg/ml ZIF-8 solution. This solution is sonicated for 30-min, and then centrifuged again at 12,000 rpm for 5-min. Then, upon removal of the supernatant, pure methanol is added again to the pellet to form an 80 mg/ml ZIF-8 solution, which is sonicated for another 30-min, centrifuged at 12,000 rpm for 5-min, removed from its supernatant, and mixed again with methanol to form a final 80 mg/ml ZIF-8 solution. In total, the PSP/ZIF-8 is washed twice." Acquired from Davey et al. [123].

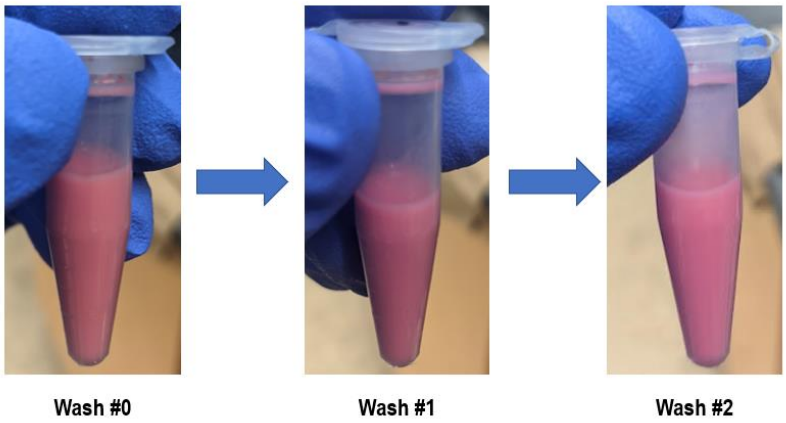

Fig. 3.27 "Optical images of PSP:ZIF-8 after successive washes. Similar to the first washed experiment with ED/PSP:ZIF-8, the experiment begins with forming an 80 mg/ml solution of PSP:ZIF-8, in which PSP:ZIF-8 (as-synthesized) is dissolved in methanol. Then, this solution is centrifuged at 12,000 rpm for 5-min. After the supernatant is removed, pure methanol is added to the pellet to form another 80 mg/ml PSP:ZIF-8 solution. This solution is sonicated for 30-min, and then centrifuged again at 12,000 rpm for 5-min. Then, upon removal of the supernatant, pure methanol is added again to the pellet to form an 80 mg/ml PSP:ZIF-8 solution, which is sonicated for another 30-min, centrifuged at 12,000 rpm for 5-min, removed from its supernatant, and mixed again with methanol to form a final 80 mg/ml PSP:ZIF-8 solution. In total, the PSP:ZIF-8 is washed twice." Acquired from Davey et al. [123].

Table 3.10 "Reflectance value at 570 nm (% R) as a function of number of washes for the PSP/ZIF-8 material (based on the Gen I sensor) and PSP:ZIF-8 material (based on the Gen II sensor)" [123]. Acquired from Davey et al. [123].

# of washes	Reflectance value at 570 nm for PSP/ZIF-8 (%)	Reflectance value at 570 nm for PSP:ZIF-8 (%)
0	55.7 ± 5	55.5 ± 2
1	63.0 ± 9	53.7 ± 5
2	71.4 ± 9	50.1 ± 3

"Comparative surface area and micropore volume are shown for pristine ZIF-8 and PSP:ZIF-8 in **[Table 3.11**]**.** The reported BET surface area and micropore volume of pristine ZIF-8 are consistent with those in the literature [26, 60-61]. BET surface area plots for the respective materials are displayed in [**Figure 3.28**]**.** Relative to pristine ZIF-8, the formation of PSP:ZIF-8 results in crystals with a reduced BET surface area, Langmuir surface area, and micropore surface area, which could be ascribed to the incorporation of phenol red molecules into the micropores of ZIF-8" [123]. [**Table 3.12]** reveals that the ED/PSP:ZIF-8 material has a greater surface area than PSP-ED/ZIF-8, which could be due to how ethylenediamine differently volatilizes from the surface of ZIF-8 given where phenol red is located on the MOF. "As shown in [**Fig. 3.29**], the two micropores near 10 Å and 12 Å of PSP-ED/ZIF-8 and ED/PSP:ZIF-8 are consistent with reported ZIF-8 micropore widths [62-63]" [123]. The absence of major changes to the pore dimensions imply that the "gate-swing" phenomenon is not observed here and that the nominal pore aperture is not significantly altered [191-193]. Finally, as shown in [**Table 3.13**]**,** "the significant reduction of external surface area between the Pristine ZIF-8 and PSP-ED/ZIF-8 could be assigned to the binding of phenol red to the external surface of ZIF-8 in this synthetic approach (rather than within the internal pores)" [123].

Table 3.11 "BET surface area, Langmuir surface area, Dubinin-Astakhov micropore surface area, and Horvath-Kawazoe maximum pore volume for Pristine ZIF-8 and PSP:ZIF-8" [123]. Adapted from Davey et al. [123].

Material	**BET surface area (m^2/g)**	**Langmuir surface area (m^2/g)**	**Dubinin-Astakhov micropore surface area (m^2/g)**	**Horvath-Kawazoe maximum pore volume at p/p° = 0.981 (cm^3/g)**
Pristine ZIF-8	1744.2	1933.0	1710.5	0.72
PSP:ZIF-8	1710.0	1794.6	1693.1	0.64

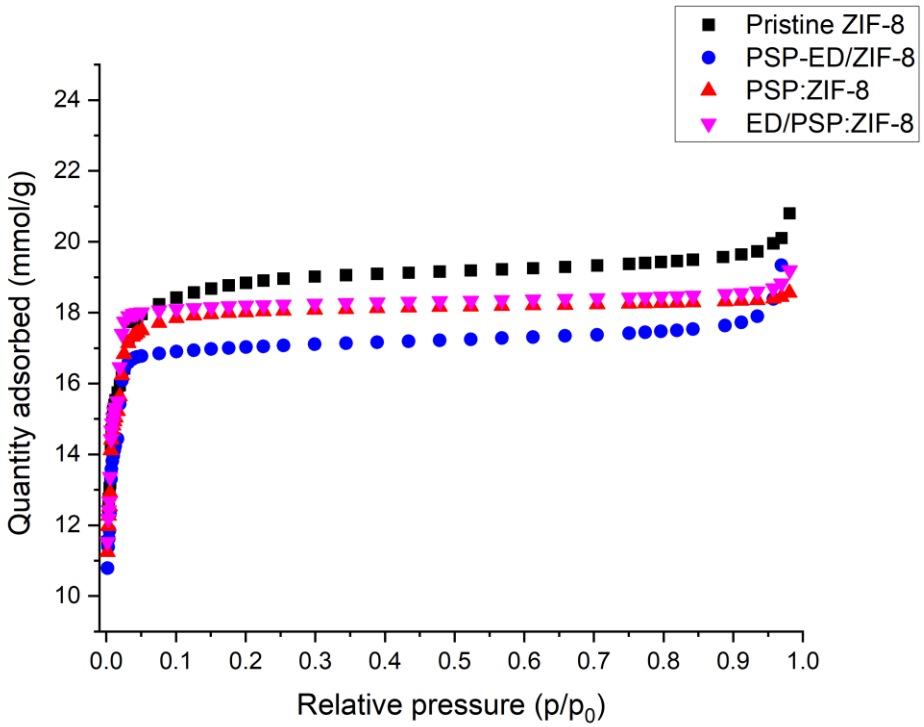

Fig. 3.28 Plot of Quantity adsorbed (mmol/g) vs. relative pressure (p/p_0). Pristine ZIF-8: black. PSP/ED-ZIF-8: blue. PSP:ZIF-8: red. ED/PSP:ZIF-8: magenta. Adapted from Davey et al. [123].

Table 3.12 BET surface area for PSP-ED/ZIF-8 and ED/PSP:ZIF-8. Adapted from Davey et al. [123].

Material	BET surface area (m^2/g)
PSP-ED/ZIF-8	1657.5
ED/PSP:ZIF-8	1732.2

Table 3.13 "T-plot external surface area of Pristine ZIF-8, PSP-ED/ZIF-8, PSP:ZIF-8, and ED/PSP:ZIF-8" [123]. Acquired from Davey et al. [123].

Material	t-plot external surface area (m^2/g)
Pristine ZIF-8	177.4
PSP-ED/ZIF-8	58.5
PSP:ZIF-8	66.4
ED/PSP:ZIF-8	43.4

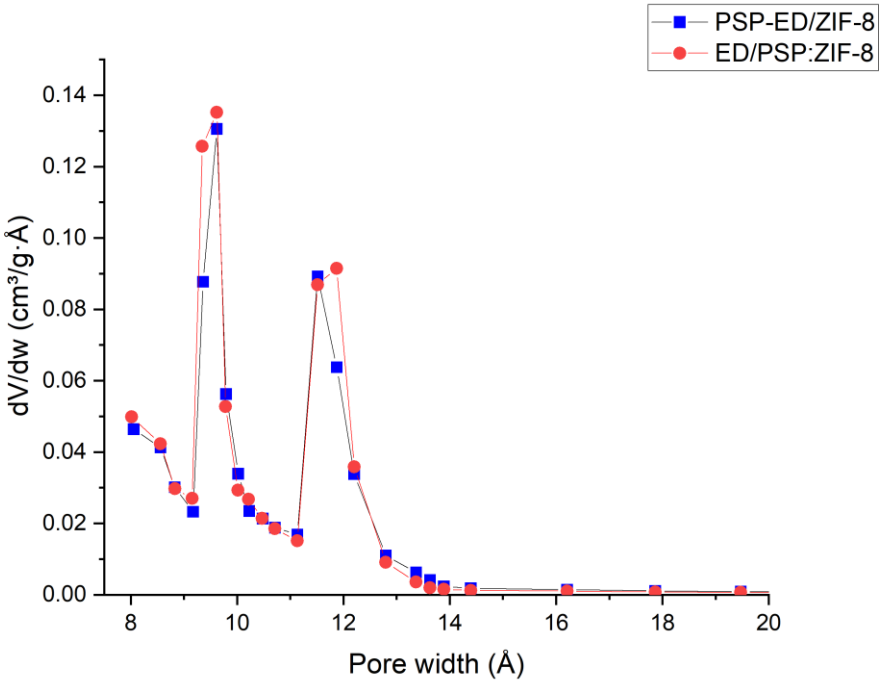

Fig. 3.29 "Differential pore volume distributions of PSP-ED/ZIF-8 (blue) and ED/PSP:ZIF-8 (red)" [123]. Acquired from Davey et al. [123].

"To expand on these experiments, the nature of interactions that inform phenol red and ethylenediamine adsorption onto ZIF-8 [195-198] will need to be studied in the future. Several spectroscopies, including second harmonic scattering techniques [199-202], nuclear magnetic resonance, X-ray-based, and vibrational techniques, will be pursued to elucidate the complex reaction mechanism involving ZIF-8, phenol red, ethylenediamine, CO_2, and humidity in methanol [147, 203-204]. Through these experiments, the reaction products of the colorimetric gas sensing can be established, as well as the role of water as an interferant" [123].

3.5 Summary

"In this work, [I] successfully synthesized a second-generation, ZIF-8-based colorimetric CO_2 sensor from the direct mixing of the pH indicator, phenol red, with ZIF-8 precursors in a room temperature methanolic solvent. While PXRD patterns and FTIR spectra confirmed the chemical stability of this new sensor, ED/PSP:ZIF-8, MATLAB-generated RGB distributions and *in-situ* UV-Vis spectroscopy demonstrated an improved colorimetric CO_2 response in variable humidity and in presence of acetone and ethanol interferents, compared to that of the first-generation sensor, PSP-ED/ZIF-8. Additional experiments suggested that in the ED/PSP:ZIF-8 sensor, phenol red molecules were most likely incorporated in the interior of ZIF-8, while they resided on its external

surface in the first-generation sensor, PSP-ED/ZIF-8. Future work will employ both vibrational and X-ray spectroscopies to understand colorimetric sensing differences between both PSP-ED/ZIF-8 and ED/PSP:ZIF-8, with emphasis on identifying differences in phenol red adsorption onto ZIF-8 and the role of water as an inhibitor for colorimetric gas sensing" [123].

In Chapter 4, "Spectroscopic Differentiation of Dye- and Amine-Modified Metal-Organic Framework-Based Colorimetric Gas Sensors for Indoor Chemical Species Detection," I will use an array of spectroscopic techniques, (as well as elemental analysis), to (i) investigate fundamental differences in the first- and second-generation sensors related to phenol red adsorption onto ZIF-8 and (ii) ascertain the role of ethylenediamine on phenol red adsorption onto ZIF-8 toward colorimetric indoor analyte monitoring.

3.6 Acknowledgements of co-authors from published work

Chapter 3 consists of intellectual contributions from the co-authors from **Davey, A.K.;** Li, Z.; Lefton, N.; Leonhardt, B.; Pourghaderi, A.; McElhany, S.; Popple, D.; Dai, C.; Kahn, S.; Dods, M.N.; Zettl, A.; Carraro, C.; and Maboudian R. "Enhanced ZIF-8 enabled colorimetric CO_2 sensing through dye-precursor synthesis." *Sensors and Actuators B: Chemical*, **2023**, 374, 132783. DOI: https://doi.org/10.1016/j.snb.2022.132783 [123]. I would like to thank all the co-authors: Zhou Li, Natalie Lefton, Branden Leonhardt, Alireza Pourghaderi, Stuart McElhany, Derek Popple, Chunhui Dai, Salman Kahn, Matthew N. Dods, Alex Zettl, Carlo Carraro, and Roya Maboudian.

Resources from supporting institutions are also included:

"The authors gratefully acknowledge the support of the National Science Foundation in the form of a Graduate Research Fellowship (A.K.D.) and grant # 1903188, as well as the Bakar Fellows Program. The contributions of M.N.D. were supported by the U.S. Department of Energy, Office of Science, Office of Basic Energy Sciences under award DE-SC0019992. The authors also acknowledge the Lawrence-Berkeley National Laboratory Catalysis Facility and Dr. Chithra Asokan for assistance with FTIR measurements. The gas sensing measurements were supported by the Director, Office of Science, Office of Basic Energy Sciences, Materials Sciences and Engineering Division, of the US Department of Energy under contract no. DE-AC02-05-CH11231, within the Nanomachines Program (KC1203). Transmission electron microscopy was also supported *by the U.S. Department of Energy, Office of Science, Office of Basic Energy Sciences, Materials Sciences and Engineering Division, under Contract No. DE-AC02-05-CH11231 within the van der Waals Heterostructures Program (KCWF16). Work at the Molecular Foundry was supported by the Office of Science, Office of Basic Energy Sciences, of the U.S. Department of Energy under Contract No. DE-AC02-05CH11231"* [123].

Chapter 4: Spectroscopic Differentiation of Dye- and Amine-Modified Metal-Organic Framework-Based Colorimetric Gas Sensors for Indoor Chemical Species Detection

The nature of this chapter involves (i) clarifying the interplay of ZIF-8, phenol red, and ethylenediamine in the colorimetric indoor carbon dioxide sensing mechanism among the first- and second-generation indoor gas sensors; (ii) determining whether ethylenediamine modulates intermolecular forces associated with phenol red adsorption onto ZIF-8; and (iii) introducing advanced techniques for future analysis of ZIF-8, phenol red, and ethylenediamine systems.

4.1 Introduction to dye- and amine-loaded system mechanistic studies

4.1.1 Introduction to dye/MOF UV-Vis and FTIR spectroscopic adsorption assessment

Understanding the nature of halochromic compound (or dye) adsorption onto MOFs is imperative for various applications. Beyond the colorimetric gas sensing implemented in this work, dye and MOF interactions are largely used in contaminated water treatment [205]. Highly-toxic synthetic dyes are discharged into water systems "from various industries, such as rubber, printing, leather, plastic" and "textiles" [206]. Such aqueous dye accumulation has deleterious impacts on "aquatics and human life," associated with dermal, nervous, kidney, and reproductive harms on human health [206].

To deploy effective adsorbents toward the treatment of water systems beset by toxic organic species, intermolecular forces between dyes and MOF systems must be established. In addition to the molecular structure and size of the dye, adsorption involves various mechanisms, such as electrostatic interactions, π-π stacking, hydrogen bonding, and hydrophobic interactions [206]. In a conventional dye/MOF study, a solid MOF of known mass is dispersed in a solvent of known volume and concentration of dye [66]. After stirring this solution at a known temperature for a controlled time, the dye/MOF solutions are centrifuged, and then the equilibrium concentration of the supernatant solution is measured using a linear Absorbance vs. Concentration calibration (in accordance with the Beer-Lambert law) through UV-Vis spectroscopy [197]. This process is expressed in **Equation 4.1** [197]:

$$q_E = \frac{(C_0 - C_E)V}{m_{MOF}} \quad \textbf{(Eq. 4.1)}$$

Where:
q_E is the equilibrium adsorption of dye onto the MOF (mg dye/g MOF),
C_0 is the initial concentration of the dye (mg dye/L solvent),
C_E is the equilibrium concentration of the dye (mg dye/L solvent),
V is the volume of the solvent used (L solvent),

and m_{MOF} is the mass of the MOF (g MOF) [197].

At various initial concentrations of a chosen dye, C_0, various equilibrium concentrations of dye, C_E, can be calculated from Beer-Lambert law calibrations through UV-Vis spectroscopic experiments. Thus, various equilibrium adsorption values, q_E, can be computed [197]. Different relationships between q_E and C_E can be obtained to explicate the adsorption thermodynamics of dyes onto select MOFs [207]. **Equation 4.2** demonstrates the *Langmuir adsorption isotherm model* [207], which assumes molecular adsorption occurs "at specific homogenous sites within the adsorbent surface" through monolayer coverage [208]:

$$\frac{C_E}{q_E} = \frac{1}{Q_M K_L} + \frac{C_E}{Q_M} \quad \textbf{(Eq. 4.2)}$$

Where:
q_E is the equilibrium adsorption of dye onto the MOF (mg dye/g MOF),
C_E is the equilibrium concentration of the dye (mg dye/L solvent),
Q_m is the "maximum adsorption capacity" (mg dye/g MOF),
and K_L is the "affinity constant…related to the adsorption binding energy" (L solvent/mg dye) [208].

Another dye/MOF adsorption scheme is the *Freundlich adsorption isotherm model* [207], which "is an empirical equation assuming that the adsorption take[s] place on a heterogeneous surface through a multilayer adsorption mechanism" [208]. The Freundlich adsorption isotherm model is depicted in **Equation 4.3** [208]:

$$\ln(q_E) = \ln(K_F) + \left(\frac{1}{n}\right) \ln(C_E) \quad \textbf{(Eq. 4.3)}$$

Where:
q_E is the equilibrium adsorption of dye onto the MOF (mg dye/g MOF),
C_E is the equilibrium concentration of the dye (mg dye/L solvent),
K_F is the Freundlich adsorption constant,
and n "represents the strength of the driving force of adsorption" [208].

In prior literature, **Equation 4.2** and **Equation 4.3** have been plotted and the relative R^2 values have been used to determine the probable pathway through which dyes adsorb to MOFs [208]. Through such calculations, Noor et al. showed that ZIF-8 (and other ZIFs) adsorbed cationic and anionic dyes (such as methyl orange, methylene blue, and crystal violet) through a Langmuirian thermodynamic process [208]. Moreover, this research associated charged dye/ZIF adsorption with electrostatic interactions and π-π stacking [208]. In a separate study, Nanthamathee and Dechatiwongse demonstrated the adsorption of the neutral dye, phenol red, onto zirconium-based MOFs (such as UiO-66-X, where X=H, NH_2, NO_2) occurred through a Freundlich adsorption pathway [197]. Moreover, observed shifts of N-H and N-O stretching modes of the zirconium-based MOFs (upon adsorption of phenol red) in this work implied specific interactions of functional groups on the MOFs with phenol red [197].

Chapter 4: Spectroscopic Differentiation of Dye- and Amine-Modified Metal-Organic Framework-Based Colorimetric Gas Sensors for Indoor Chemical Species Detection

In this chapter, the adsorption of phenol red onto ZIF-8 (0 – 20 mg/ml phenol red in methanolic solutions) will be investigated through both UV-Vis and FTIR spectroscopic tools. Through these techniques, the nature of how ethylenediamine (as a basic species) informs the intermolecular forces between phenol red and ZIF-8 will be assessed (with a goal of using such insights to synthesize color-based inorganic chemical sensors more meticulously for indoor gas detection).

4.1.2 Introduction to carbon, hydrogen, nitrogen, and sulfur (CHNS) elemental analysis

Carbon, hydrogen, nitrogen, and sulfur (CHNS) elemental analysis provides a rapid technique through which to probe how much dye has been adsorbed by a MOF [209]. Through combustion (with temperatures ~1,000 °C), "carbon is converted to carbon dioxide; hydrogen to water; nitrogen to nitrogen gas/oxides of nitrogen," and sulfur to sulfur dioxide [209]. These combustion products are drawn from the combustion chamber "by inert carrier gas such as helium and passed over heated… high purity copper," which "remove[s] any oxygen not consumed in the initial combustion and… convert[s] any oxides of nitrogen to nitrogen gas" such that only carbon dioxide, water, nitrogen, and sulfur dioxide remain [209]. Finally, these gases are separated through gas chromatography and quantified via "thermal conductivity detection," which "requires calibrations for each element by using high purity 'micro-analytical standard' compounds such as… benzoic acid" [209].

In this chapter, CHNS elemental analysis is used to quantify (i) how much phenol red adsorbs to ZIF-8 between the first- and second-generation sensor synthesis schemes (0 to 5 mg/ml phenol red in methanol) and (ii) how much phenol red adsorbs to pristine ZIF-8 in the presence and absence of ethylenediamine (0 to 20 mg/ml phenol red in methanol-based solvent). Through such quantitative capabilities, CHNS elemental analysis is argued to be a complementary technique with respect to more complicated spectroscopic characterization methods described in Chapter 4.4.

4.2 Elucidating the role of phenol red: MOF formation and colorimetric gas exposure

This section of Chapter 4 aims to more closely investigate the results addressed previously in Chapter 2 and Chapter 3. Namely, colorimetric indoor gas sensing between the first- and second-generation sensors will be contrasted through an assessment of the effect of how phenol red is introduced on ZIF-8 crystallinity. Elemental analysis is used to quantify differences in phenol red adsorption on the first- and second-generation colorimetric gas sensors and guide next steps for future spectroscopic research.

4.2.1 Synthesis of the sensors: liquid and solid

The methanol-based formation of PSP/ZIF-8 (associated with the first-generation sensor) and PSP:ZIF-8 (associated with the second-generation sensor) closely follows the recipes described in Chapter 2 and Chapter 3. Once pristine ZIF-8 crystals are washed three times in methanol (as described in Chapter 2), several methanolic phenol red solutions are prepared (0.3 to 5 mg/ml phenol red in methanol). Then, various PSP/ZIF-8 solutions are developed through blending 80 mg pristine ZIF-8 per ml of phenol red solution (ranging from 0.3 to 5 mg/ml). Similarly, PSP:ZIF-8 formation occurs as described via dye-precursor synthesis in Chapter 3 (with phenol red concentrations in the metal and linker ZIF-8 precursor solutions ranging from 0.3 to 5 mg/ml in methanol). For example, a "3 mg/ml" (referring to the phenol red synthetic loading) PSP:ZIF-8 (as-synthesized) solution is prepared from dissolving 2.08 g of zinc nitrate hexahydrate in 120 ml methanol and 2-methlyimidazole in 120 ml methanol. Then, 360 mg of phenol red are added to both solutions and dissolved via sonication. Finally, the phenol red/2-methlyimidazolate solution is slowly poured into the phenol red/zinc nitrate hexahydrate solution, and the reaction is allowed to proceed (unstirred) for 48 hr at room temperature. **Figure 4.1** displays different phenol red methanolic solutions, as well as the colors of metal and linker precursor solutions with increased phenol red loadings. **Figure 4.2** shows the PSP/ZIF-8 and PSP:ZIF-8 solutions used for analysis. It is noted that the PSP:ZIF-8 solutions shown in **Figure 4.2** are "as-synthesized." 160 mg/ml PSP:ZIF-8 solutions are used for PXRD, FTIR, and X-ray spectroscopic analyses.

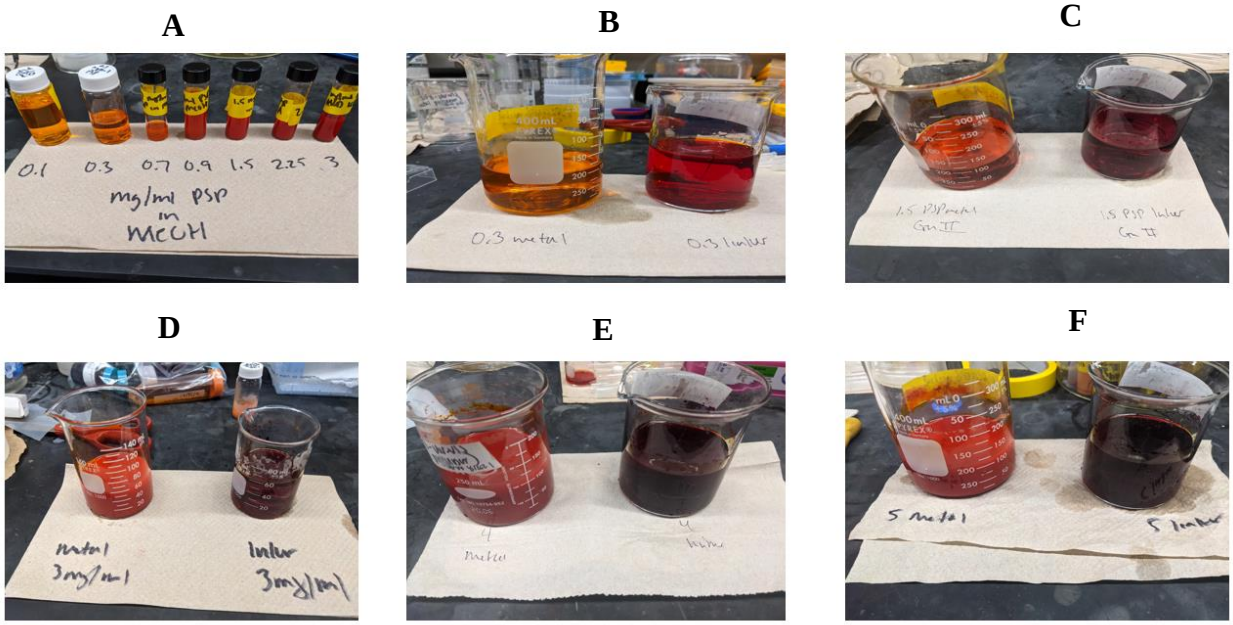

Fig. 4.1 (A) Different phenol red solutions (in methanol) used to prepare 80 mg/ml PSP/ZIF-8 solutions. Zinc nitrate hexahydrate (left) and 2-methylimidazolate (right) solutions for preparing PSP:ZIF-8 with **(B)** 0.3 mg/ml phenol red; **(C)** 1.5 mg/ml phenol red; **(D)** 3.0 mg/ml phenol red; **(E)** 4.0 mg/ml phenol red; and **(F)** 5.0 mg/ml phenol red.

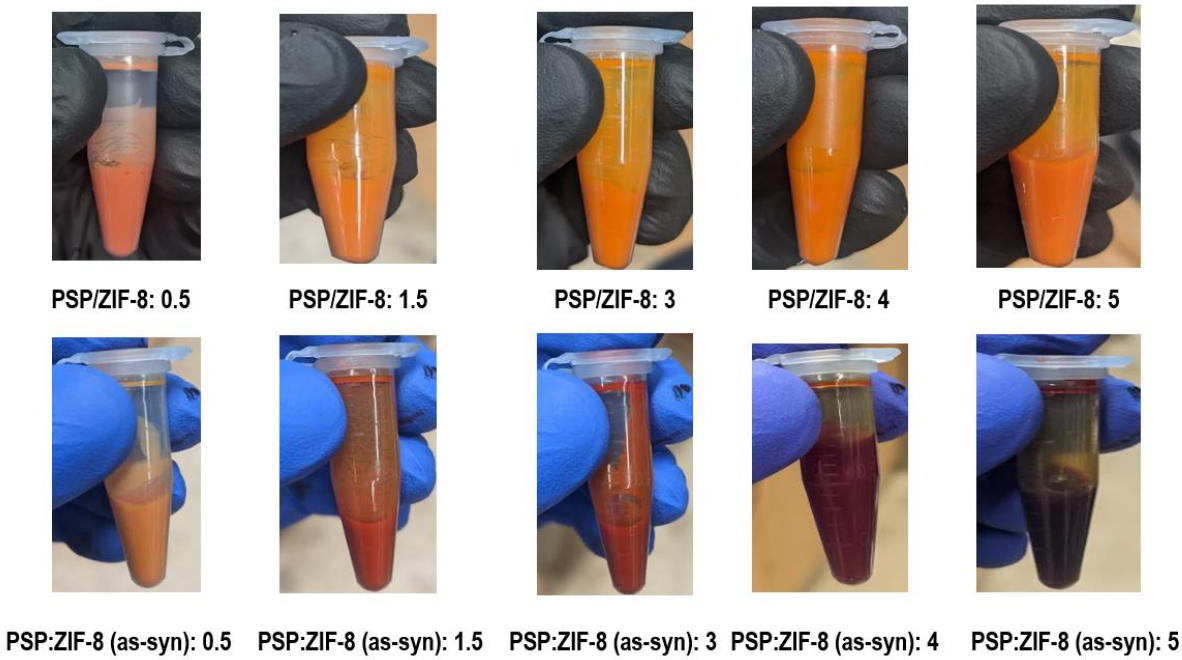

Fig. 4.2 (Top row): 80 mg/ml PSP/ZIF-8 methanolic solutions (0.5 to 5 mg/ml phenol red). **(Bottom row):** PSP:ZIF-8 methanolic solutions (0.5 to 5 mg/ml phenol red) as-synthesized (no washing).

Figure 4.3 shows the PSP-ED/ZIF-8 and ED/PSP:ZIF-8 solutions used for analysis. All PSP-ED/ZIF-8 solutions used are 80 mg ZIF-8/ml colorimetric solvent. For PXRD and FTIR spectroscopic measurements, 160 mg/ml ED/PSP:ZIF-8 solutions are developed. However, 80 mg/ml ED/PSP:ZIF-8 solutions are used for colorimetric imaging and *in-situ* UV-Vis spectroscopic gas sensing in dry CO_2 atmosphere. For these studies, a 2% ethylenediamine (% v/v) solution is used.

To prepare the solid PSP/ZIF-8 samples, pristine ZIF-8 crystals (after rinsed with methanol three times) are mixed with various phenol red methanolic solutions and stirred for 24-hr at room temperature. After 24-hr, the dye-adsorbed ZIF-8 species are separated from supernatant using an eppendorf Centrifuge 5430 R (10:00 min; 25 °C; 6,000 rpm) and allowed to dry for 24-hr at room temperature in open lab atmosphere. Similarly, the as-synthesized PSP:ZIF-8 crystals are separated from supernatant using an eppendorf Centrifuge 5430 R (10:00 min; 25 °C; 6,000 rpm) and allowed to dry for 24-hr at room temperature in open lab atmosphere. Images of PSP/ZIF-8 and PSP:ZIF-8 powders are displayed in **Figure 4.4**.

Fig. 4.3 (Top row): 80 mg/ml PSP-ED/ZIF-8 methanolic solutions (0.5 to 5 mg/ml phenol red). **(Bottom row):** 80 mg/ml ED/PSP:ZIF-8 methanolic solutions (0.5 to 5 mg/ml phenol red). Ethylenediamine loadings are 2% (%v/v) in methanol.

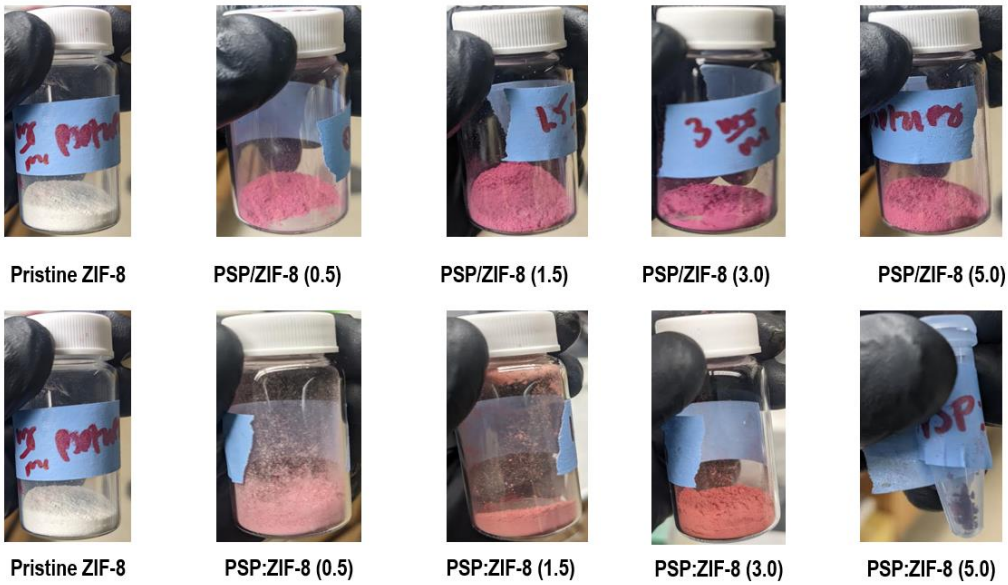

Fig. 4.4 (Top row): PSP/ZIF-8 powders. **(Bottom row):** PSP:ZIF-8 powders. Pristine ZIF-8 powders are positioned beside both PSP/ZIF-8 and PSP:ZIF-8 samples for color comparison.

4.2.2 Colorimetric assays – 3,000 ppm CO_2 in 0% RH

Colorimetric assays are collected for PSP-ED/ZIF-8 and ED/PSP:ZIF-8 materials (drop-cast on cellulose filter paper) across a range of phenol red concentrations (0.3, 0.7, 0.9, 1.5, and 3.0 mg/ml phenol red in a 2% ethylenediamine methanolic solution) in dry environment (0% RH at . **Figure 4.5** shows the colorimetric gas response to 3,000 ppm CO_2 in 0% RH for the first-generations sensor, PSP-ED/ZIF-8. With increased phenol red loadings, the "before exposure" images transition from a light fuchsia to a darker purple color. Moreover, with exposure to dry CO_2, the brightness of the yellow color change attenuates, shifting only from a darker purple to a yellow-tinged, lighter purple hue at 3 mg/ml phenol red loading in PSP-ED/ZIF-8.

Similar results are shown for ED/PSP:ZIF-8 in **Figure 4.6**. At lower phenol red loadings, the color change is immensely perceptible, achieving a stronger yellow response than achieved by PSP-ED/ZIF-8 at the same loading (0.3 mg/ml phenol red). However, with increased phenol red concentrations blended with the ZIF-8 methanolic metal and ligand precursors, the color change evolves from a strong yellow to a reddish-yellow color.

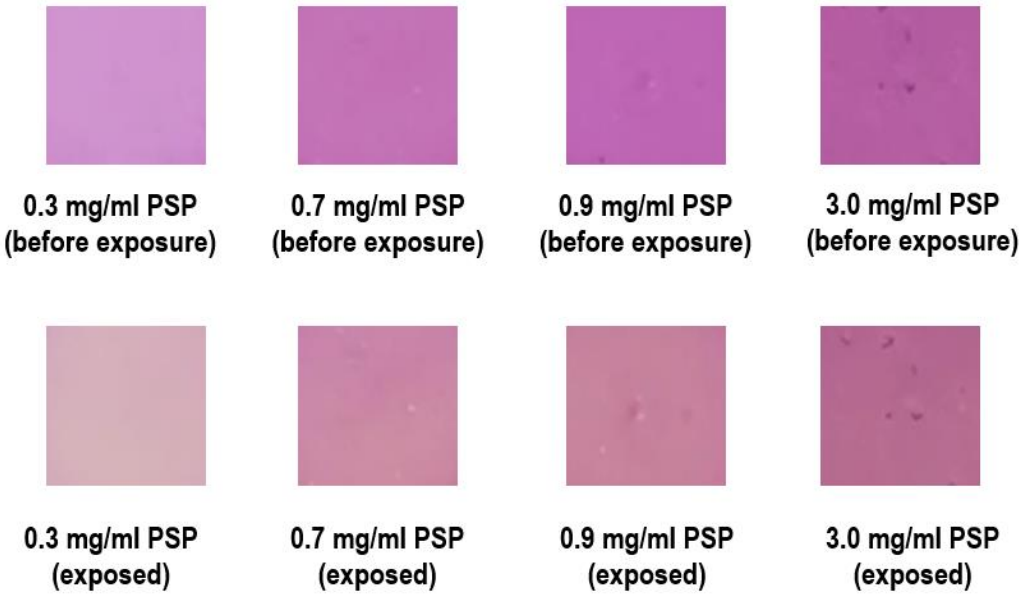

Fig. 4.5 (Top row): PSP-ED/ZIF-8 samples drop-cast on cellulose filter paper before controlled CO_2 exposure. **(Bottom row):** PSP-ED/ZIF-8 samples drop-cast on cellulose filter paper exposed to 3,000 ppm CO_2 in 0% RH.

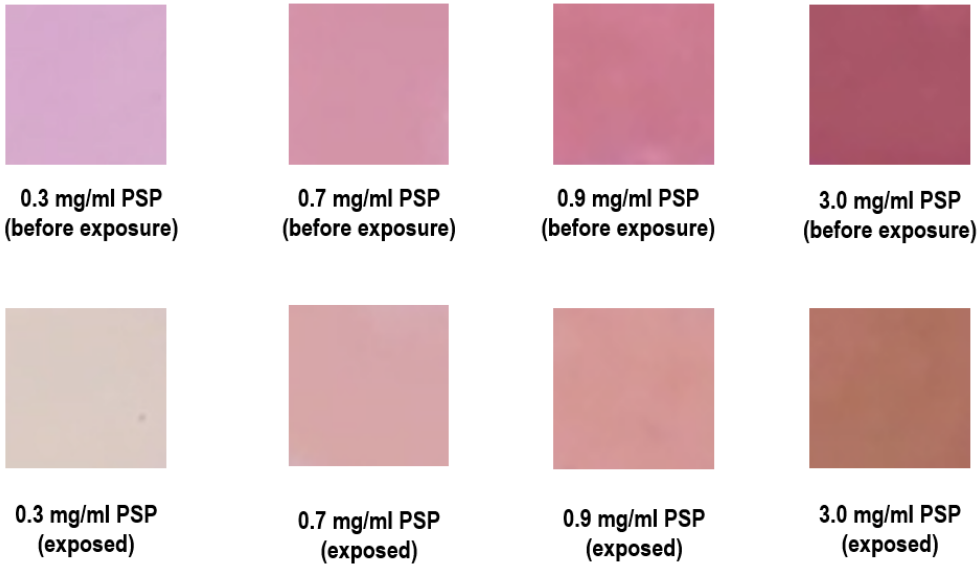

Fig. 4.6 (Top row): ED/PSP:ZIF-8 samples drop-cast on cellulose filter paper before controlled CO_2 exposure. **(Bottom row):** ED/PSP:ZIF-8 samples drop-cast on cellulose filter paper exposed to 3,000 ppm CO_2 in 0% RH.

Mean red, green, and blue (RGB) color distribution values are shown in **Table 4.1** for PSP-ED/ZIF-8 and **Table 2** for ED/PSP:ZIF-8 to compare the color changes achieved at zero humidity. With increased phenol red loadings in PSP-ED/ZIF-8, all "before exposure" values decrease (with significant decreases in the G- and B-values compared to the R-values). For each concentration of phenol red used in PSP-ED/ZIF-8, R- and G-values increase in the presence of CO_2 relative to before CO_2 exposure; the opposite trend is observed with the B-values. As with earlier studies, such results indicate a color change from the proposed zwitterion mechanism in the presence of CO_2 [140-145]. However, all RGB values decrease upon exposure to dry CO_2 with increased phenol red loadings; specifically, the G-value values are largely reduced. As described with **Figure 4.5**, these results indicate a muted color change with substantive increases in phenol red loadings onto pristine ZIF-8. Similar to the results of PSP-ED/ZIF-8, ED/PSP:ZIF-8 exhibits lowered RGB values among all "before exposure" images with increased phenol red loadings (as shown in **Table 4.2**). Moreover, compared to PSP-ED/ZIF-8, the G-values at each phenol red loading (upon exposure to dry CO_2) is higher; the R- values generally increase (upon exposure to dry CO_2) relative to those of PSP-ED/ZIF-8 below 3.0 mg/ml phenol red loaded. This observation, coupled with smaller B-values in ED/PSP:ZIF-8 at higher phenol red loadings, demonstrates a stronger color change of the second-generation sensor than the first-generation sensor even with increased phenol red loadings. Nonetheless, all RGB values for ED/PSP:ZIF-8 decrease (upon exposure to CO_2) with increased phenol red loading, resulting in the transition from the bright yellow color to the red-yellow color shown in **Figure 4.6**.

Table 4.1 Red, green, and blue (RGB) distributions for various PSP-ED/ZIF-8 sensors (0.3 – 3 mg/ml phenol red) exposed to 3,000 ppm CO_2 in 0% RH.

Concentration of phenol red (mg/ml)	Mean R-value (before)	Mean R-value (exposed)	Mean G-value (before)	Mean G-value (exposed)	Mean B-value (before)	Mean B-value (exposed)
0.3	207 ± 1	**212 ± 1**	146 ± 1	**175 ± 2**	206 ± 1	**185 ± 1**
0.7	195 ± 1	**203 ± 1**	114 ± 1	**139 ± 2**	181 ± 1	**165 ± 2**
0.9	190 ± 1	**197 ± 2**	102 ± 2	**129 ± 2**	179 ± 1	**156 ± 3**
3.0	181 ± 2	**182 ± 2**	94.4 ± 1	**107 ± 2**	162 ± 2	**144 ± 1**

Table 4.2 Red, green, and blue (RGB) distributions for various ED/PSP:ZIF-8 sensors (0.3 – 3 mg/ml phenol red) exposed to 3,000 ppm CO_2 in 0% RH.

Concentration of phenol red (mg/ml)	Mean R-value (before)	Mean R-value (exposed)	Mean G-value (before)	Mean G-value (exposed)	Mean B-value (before)	Mean B-value (exposed)
0.3	215 ± 2	**218 ± 1**	171 ± 2	**201 ± 1**	204 ± 2	**193 ± 2**
0.7	211 ± 2	**215 ± 1**	148 ± 1	**166 ± 0.4**	168 ± 2	**170 ± 1**
0.9	203 ± 2	**213 ± 2**	122 ± 2	**151 ± 3**	143 ± 3	**148 ± 3**
3.0	168 ± 1	**176 ± 2**	85.2 ± 1	**115 ± 2**	103 ± 1	**98.4 ± 3**

4.2.3 In-situ ultraviolet-visible (UV-Vis) diffuse reflectance spectroscopy and associated BET measurements

An *in-situ* UV-Vis spectroscopic technique is implemented to quantitatively compare how PSP-ED/ZIF-8 and ED/PSP:ZIF-8 perform across a range of dry CO_2 levels (675 – 7,500 ppm) and across various phenol red loadings (0.9 – 5.0 mg/ml). The experimental approach outlined in **Figure 3.2** is also used here. Mean CO_2 levels are computed using a Varian Electronic Instruments Intelligent Digital Flowmeter and plotted as a function of CO_2 flow rate in **Figure 4.7**. All calibrations are performed at 0% relative humidity and room temperature (23.6 ± 1 °C). The balance gas is dry air and the total gas flowrate is 300 ml/min.

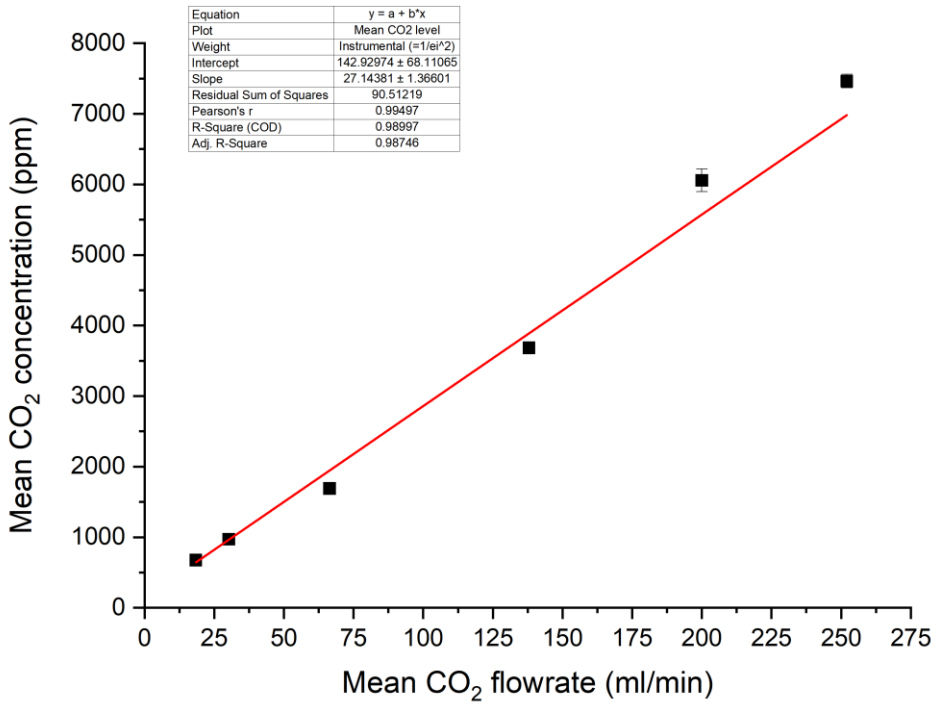

Fig. 4.7 Mean CO_2 concentration (ppm) versus mean CO_2 flowrate (ml/min) calibrations. All measurements are taken over a 10-min period at room temperature (23.6 ± 1 °C) using a Varian Electronic Instruments Intelligent Digital Flowmeter. The balance gas is dry air. Total gas flowrate: 300 ml/min. Error bars are standard deviation values.

Figure 4.8 displays the 443/570 nm F(R) ratios as a function of CO_2 concentration (in ppm) for PSP-ED/ZIF-8 and ED/PSP:ZIF-8 (0.9 – 5.0 mg/ml phenol red). For both sensors, the 443/570 nm F(R) ratios largely increase at smaller phenol red loadings. Similar to the quantitative color trends observed in Chapter 3, the ED/PSP:ZIF-8 sensor demonstrates larger 443/570 nm F(R) ratios than PSP-ED/ZIF-8 (at low phenol red loadings).

To better evaluate colorimetric behavior at intermediate gas levels, comparative UV-Vis analysis is performed at 3700 ppm CO_2. As shown in **Figure 4.9**, both PSP-ED/ZIF-8 and ED/PSP:ZIF-8 sensors generally exhibit reduced 443/570 nm F(R) ratios with increased phenol red loadings. This trend is resonant with that observed among the colorimetric images and tabulated RGB distribution data shown in **Figure 4.5**, **Figure 4.6**, **Table 4.1**, and **Table 4.2**. At higher phenol red loadings, PSP-ED/ZIF-8 exhibits a saturation of the colorimetric gas response near 0.4 ratiometric units. However, above 3 mg/ml phenol red loadings, the ED/PSP:ZIF-8 experiences a large and linear drop in the colorimetric gas response.

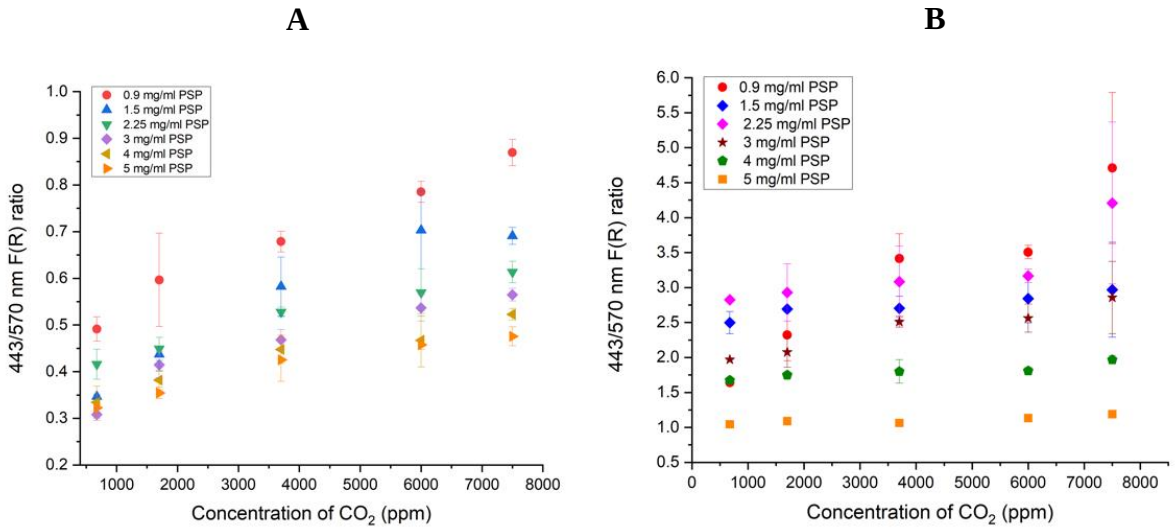

Fig. 4.8 443/570 nm ratios for **(A)** PSP-ED/ZIF-8 and **(B)** ED/PSP:ZIF-8 exposed to dry CO_2 (675 – 7,500 ppm) across a range of phenol red loadings (0.9 – 5.0 mg/ml in a 2%, %v/v, ethylenediamine solution in methanol). Error bars are standard deviation values.

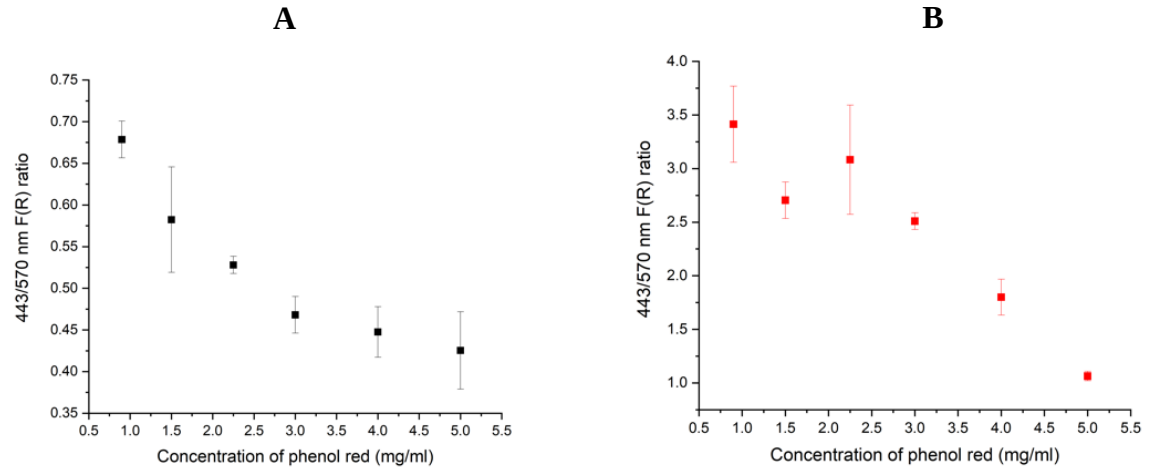

Fig. 4.9 443/570 nm ratios for **(A)** PSP-ED/ZIF-8 and **(B)** ED/PSP:ZIF-8 exposed to 3,700 ppm CO_2 (0% RH) as a function of phenol red loading (0.9, 1.5, 2.25, 3, 4, and 5 mg/ml). Error bars are standard deviation values.

Figure 4.10 shows the normalized F(R) data for PSP-ED/ZIF-8 exposed to 675, 1700, 3700, 6000, and 7500 ppm CO_2 (at 0% RH) as a function of wavelength (nm) for both 4 mg/ml phenol red and 5 mg/ml phenol red. For both phenol red loadings, there exists an obvious increase in the 443 nm F(R) value relative to the 570 nm F(R) value. However, as observed in **Figure 4.8-A** and **Figure 4.9-A**, this ratio between the 443 and 570 nm F(R) values stabilizes with increased dry CO_2 levels. However, for both 4 mg/ml phenol red and 5 mg/ml phenol red PSP-ED/ZIF-8, it is apparent that a difference in the colorimetric gas response occurs over the range of concentrations exposed.

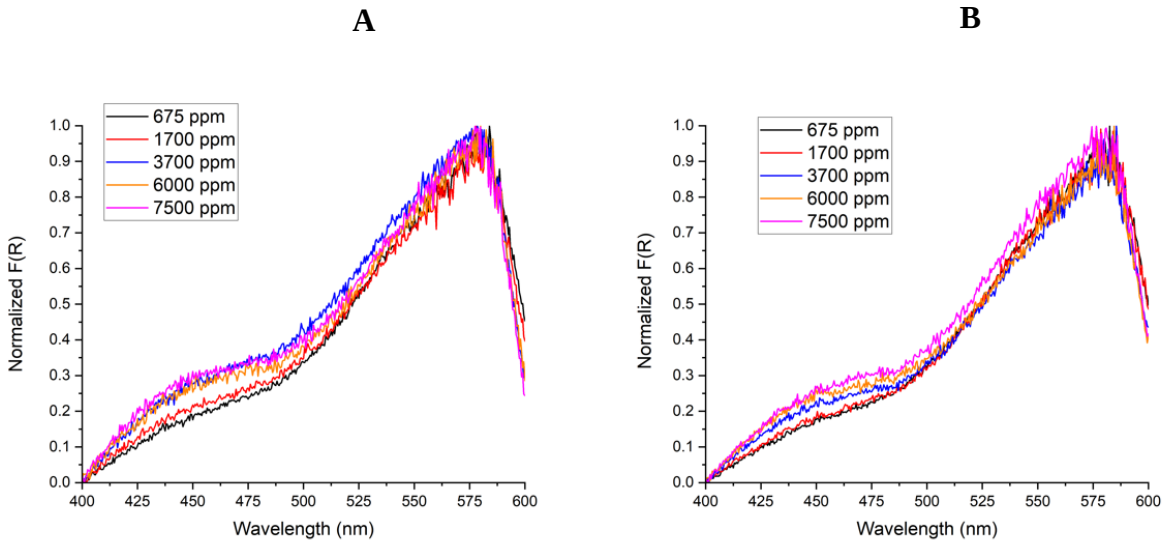

Fig. 4.10 Normalized F(R) values vs. wavelength (nm) for PSP-ED/ZIF-8 with **(A)** 4 mg/ml phenol red and **(B)** 5 mg/ml phenol red in dry CO_2 environment. **Black:** 675 ppm. **Red:** 1700 ppm. **Blue:** 3700 ppm. **Orange:** 6000 ppm. **Magenta:** 7500 ppm.

Figure 4.11 displays the normalized F(R) data for ED/PSP:ZIF-8 exposed to 675, 3700, 6000, and 7500 ppm CO_2 (at 0% RH) as a function of wavelength (nm) for both 4 mg/ml phenol red and 5 mg/ml phenol red. For the 4 mg/ml phenol red ED/PSP:ZIF-8, the 570 nm F(R) value decreases with increasing CO_2 level in a similar fashion as lower phenol red loadings. However, as shown in **Figure 4.11-B**, significant noise appears at 5 mg/ml ED/PSP:ZIF-8 for all gas levels exposed. As observed in **Figure 4.8-B**, no meaningful color change is achieved, generating a 443/570 nm F(R) ratio ~1.00 ratiometric units for all dry gas exposures.

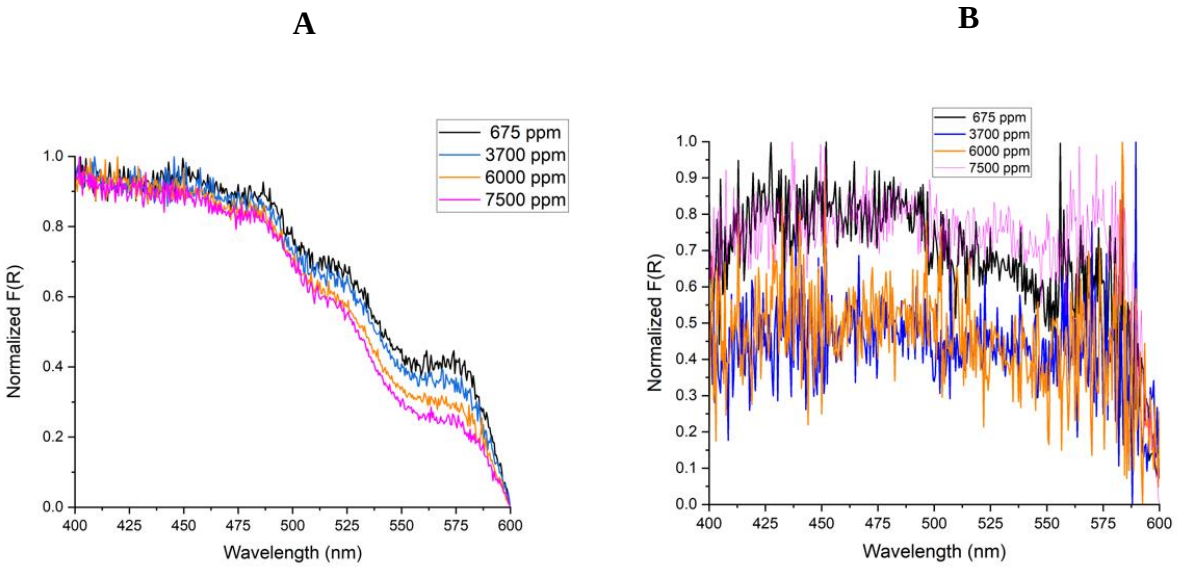

Fig. 4.11 Normalized F(R) values vs. wavelength (nm) for ED/PSP:ZIF-8 with **(A)** 4 mg/ml phenol red and **(B)** 5 mg/ml phenol red in dry CO_2 environment. **Black:** 675 ppm. **Red:** 1700 ppm. **Blue:** 3700 ppm. **Orange:** 6000 ppm. **Magenta:** 7500 ppm.

Several observations are established in this section. Firstly, the qualitative color change and quantitative *in-situ* UV-Vis diffuse reflectance spectroscopic results indicate a general reduction in color change for the first- and second-generation indoor CO_2 sensors with increased phenol red loading. **Figure 4.12** shows an initial BET isotherm for 5 mg/ml PSP/ZIF-8 using the same synthesis approach described in Section 4.2.1 and BET surface characterization protocol outlined in Section 3.3.5. (Due to low yield below the minimum mass for surface analysis, BET characterization is not completed for PSP:ZIF-8 loaded with 5 mg/ml phenol red). From this plot, a BET surface area and a Langmuir surface area of 1658.5 m^2/g and 1862.7 m^2/g, respectively, are computed. Relative to values for pristine ZIF-8 reported in **Table 3.11**, these values for PSP/ZIF-8 (5 mg/ml phenol red) are appreciably smaller. In addition, the PSP/ZIF-8 (5 mg/ml phenol red) shows a t-plot external surface area of 63.5 m^2/g, which is significantly smaller than that of pristine ZIF-8 reported in **Table 3.13**. These results could suggest that the loss of external surface area from increased phenol red loadings might remove available surface area for CO_2 adsorption, thus reducing the colorimetric response (upon addition of ethylenediamine to enable gas chemisorption). Moreover, the poor colorimetric sensing performance of ED/PSP:ZIF-8 (with 5 mg/ml phenol red) is noted in the large noise from the normalized F(R) values of the resonant UV-Vis wavelengths of phenol red. To better understand this behavior relative to that of the PSP-ED/ZIF-8 material, several structural assessments (involving FTIR spectroscopy, PXRD pattern collection, and CHNS elemental analysis) are conducted in the subsequent subsections.

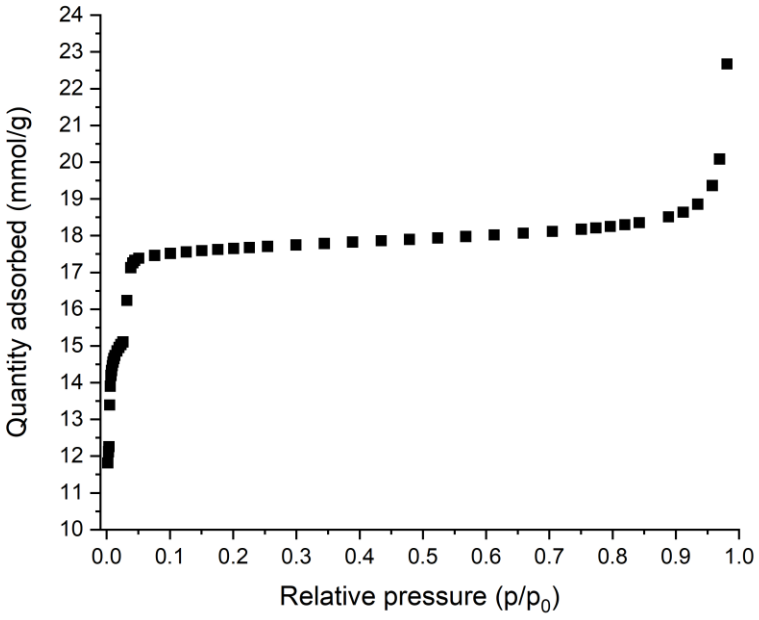

Fig. 4.12 BET isotherm for PSP/ZIF-8 (5 mg/ml phenol red). N_2 at 77K is used.

4.2.4 Fourier transform infrared (FTIR) spectra – effect of high phenol red loading

FTIR spectroscopy is performed in this subsection to compare how the phenol red/ZIF-8 adsorption approach between the first- and second-generation sensors influences the successful formation of the MOF. In this subsection, high concentrations of phenol red are used (up to 10 mg/ml phenol red in methanol) toward the assessment of the molecular structure of ZIF-8. **Figure 4.13** shows FTIR Transmittance (%) versus wavenumber (cm^{-1}) data for PSP/ZIF-8 samples produced from the liquid-phase drop-cast method illustrated in Chapter 4.2.1. (In Chapter 4.3, a different FTIR spectroscopic experiment will be discussed toward evaluating *where* phenol red may adsorb to pristine ZIF-8 with and without ethylenediamine). As evident in **Figure 4.13**, the maintenance of the 421 cm^{-1} mode associated with the stretch of the Zn-N coordination bond confirms the stability of ZIF-8 from 0 mg/ml phenol red to 10 mg/ml phenol red in PSP/ZIF-8 [123. 171, 184-185]. However, as discerned from **Figure 4.14,** the 421 cm^{-1} Zn-N coordination bond IR-active vibrational mode vanishes at PSP:ZIF-8 with 5 mg/ml phenol red loaded (and higher). Thus, ZIF-8 does not appear to crystallize in the presence of 5 mg/ml phenol red in the methanolic metal and linker precursor mixture. To advance this hypothesis, both powder X-ray diffraction (PXRD) and carbon, hydrogen, nitrogen, and sulfur (CHNS) elemental analysis are implemented.

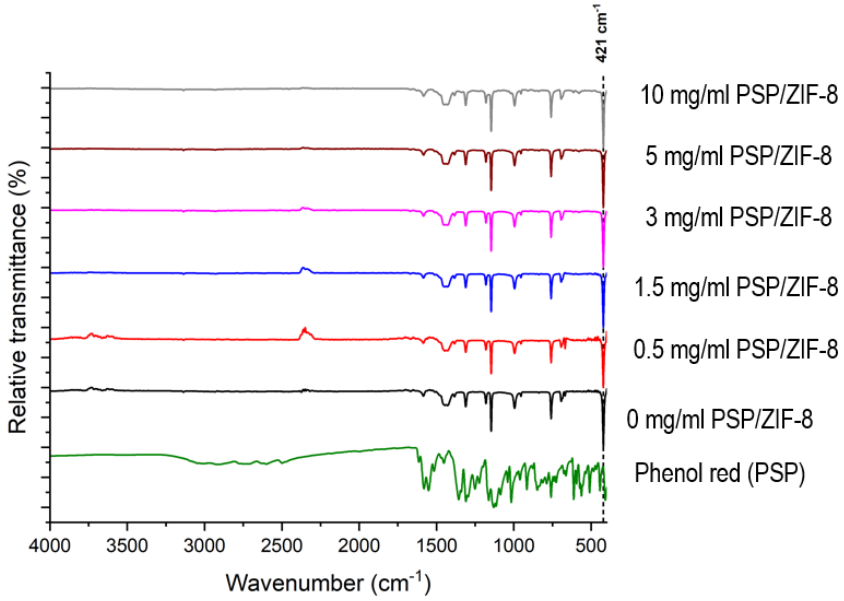

Fig. 4.13 Relative transmittance (%) vs wavenumber (cm^{-1}) for PSP/ZIF-8 (liquid drop-cast samples). Collected from a Bruker Vertex80 FTIR instrument (4000 to 400 cm^{-1}).

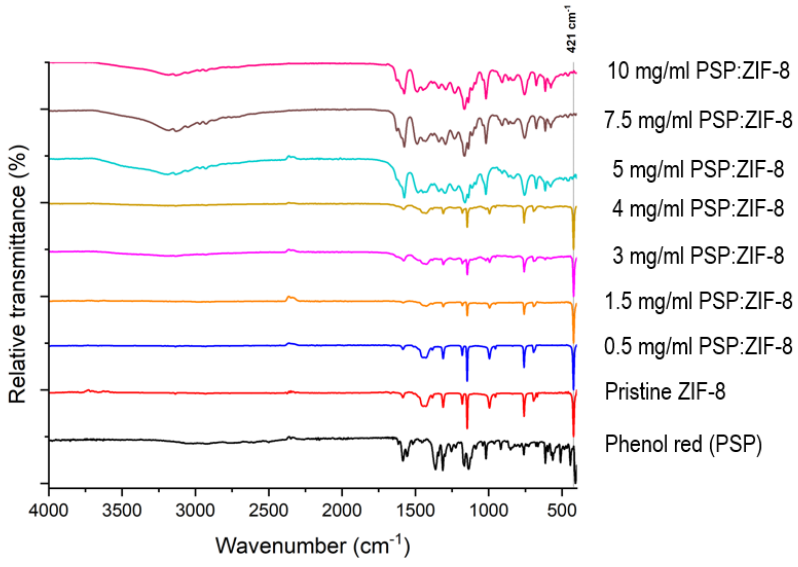

Fig. 4.14 Relative transmittance (%) vs wavenumber (cm^{-1}) for PSP:ZIF-8 (liquid drop-cast samples). Collected from a Bruker Vertex80 FTIR instrument (4000 to 400 cm^{-1}).

4.2.5 Powder X-ray diffraction (PXRD) – effect of high phenol red loading

PXRD data for PSP:ZIF-8 (0.5 – 10 mg/ml phenol red in methanol) are shown in **Figure 4.15**. These patterns are collected using a Rigaku Miniflex 6G Benchtop Powder XRD (ChexFLEX: RUA #2172; 40kV/15 mA; X-ray Source: Sealed Source Tube (Cu-Kα Radiation); scan rate: 3.0°/min; and 1D scan mode). Below 4.0 mg/ml phenol red incorporated into the ZIF-8 precursor mixtures, the major diffraction peaks associated with ZIF-8 are achieved [99, 131-132], confirming the sodalite structure of ZIF-8. However, at 5 mg/ml phenol red incorporated into PSP:ZIF-8, the diffraction peak at the (011) plane (2θ = 7.3°) demonstrates a reduced intensity, with the other diffraction peaks disappeared. Above this phenol red loading, none of the diffraction peaks associated with the sodalite structure of ZIF-8 are visible. Coupled with the FTIR spectra displayed in **Figure 4.14**, these PXRD patterns indicate the unsuccessful formation of ZIF-8 at higher phenol red concentrations.

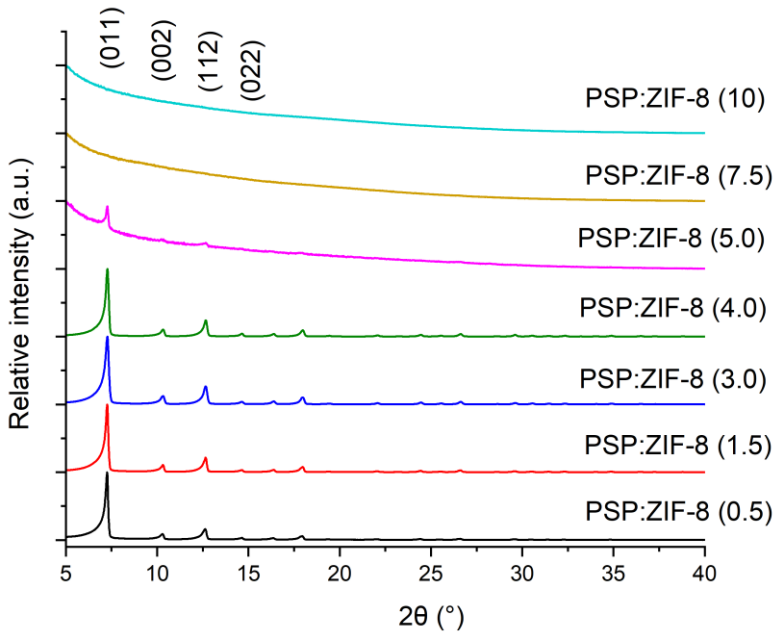

Fig. 4.15 Powder X-ray diffraction (PXRD) patterns for PSP:ZIF-8 with 0.5, 1.5, 3.0, 4.0, 5.0, 7.5, and 10 mg/ml phenol red blended with the metal and ligand precursor solutions (drop-cast on PXRD sample holders).

The apparent inhibition of ZIF-8 crystallization at higher phenol red loadings is associated with the colorimetric gas responses depicted in **Figure 4.11-B**. As established in **Figure 2.16**, the colorimetric gas sensing described in this dissertation requires the presence of the MOF as an adsorbent species to both accommodate the colorimetric components and provide adsorption sites for CO_2 [99]. Thus, the significant noise in the ED/PSP:ZIF-8 *in-situ* UV-Vis diffuse reflectance spectra (at 5 mg/ml phenol red) in **Figure 4.11-B** is ascribed to the suppression of ZIF-8 formation, which prevents observable color changes across the range of indoor gas levels.

4.2.6 Carbon, hydrogen, nitrogen, and sulfur (CHNS) elemental analysis

Despite the compromised formation of ZIF-8 at higher phenol red loadings among the second-generation sensors, the colorimetric imaging assays and *in-situ* UV-Vis diffuse reflectance spectra demonstrate stronger color changes among the ED/PSP:ZIF-8 sensors than the PSP-ED/ZIF-8 sensors at lower and intermediate phenol red loadings. To both assess the role of phenol red incorporation on the successful crystallization of ZIF-8 and the attained colorimetric gas response at low humidity, carbon, hydrogen, nitrogen, and sulfur (CHNS) elemental analysis is conducted on solid powders (from **Figure 4.4**) using a ThermoFisher Flash Smart Elemental analyzer (detection limit: 0.01%). The calculated CHNS elemental composition of ZIF-8 and phenol red is provided in **Table 4.3** [117-118, 211]. In addition, the CHNS elemental composition data for PSP/ZIF-8 and PSP:ZIF-8 samples are shown in **Table 4.4** and **Table 4.5**, respectively.

Table 4.3 CHNS elemental composition values for pristine ZIF-8 and phenol red (calculated from the molecular weight associated with the chemical structure).

Sample	C%	H%	N%	S%
Pristine ZIF-8	42.22	4.43	24.62	0
Phenol red	64.39	3.98	0	9.04

Table 4.4 CHNS elemental composition data for PSP/ZIF-8 powders (up to 5 mg/ml phenol red).

Sample	C%	H%	N%	S%
Pristine ZIF-8	41.85	4.44	23.82	0
PSP/ZIF-8 (0.5)	42.5	4.45	23.78	0
PSP/ZIF-8 (1.5)	42.19	4.41	23.55	0.07
PSP/ZIF-8 (3.0)	42.22	4.41	23.32	0.12
PSP/ZIF-8 (5.0)	42.27	4.43	23.29	0.15

Table 4.5 CHNS elemental composition data for PSP:ZIF-8 powders (up to 5 mg/ml phenol red).

Sample	C%	H%	N%	S%
Pristine ZIF-8	41.85	4.44	23.82	0
PSP:ZIF-8 (0.5)	41.78	4.46	23.91	0
PSP:ZIF-8 (1.5)	42.05	4.46	23.77	0.05
PSP:ZIF-8 (3.0)	42.14	4.41	23.28	0.10
PSP:ZIF-8 (5.0)	45.08	4.38	15.95	1.58

Upon observation of the CHNS elemental values listed in **Table 4.3**, it is apparent that while both MOF and dye species contribute carbon (C) and hydrogen (H) atoms, only ZIF-8 contributes a nitrogen (N) atom and only phenol red contributes a sulfur (S) atom. Thus, an assessment of *how much phenol red is adsorbed to ZIF-8 between both the first- and second-generation sensors is accomplished through comparisons of how the nitrogen (N) and sulfur (S) contributions evolve with increased phenol red loading*. As shown in both **Table 4.4** and **Table 4.5**, the measured CHNS composition of pristine ZIF-8 is consistent with that reported in the literature [211] and that obtained from molecular weight calculations. With increasing levels of phenol red concentrated onto ZIF-8, the carbon (C) and sulfur (S) percentages increase and the nitrogen (N) percentages decrease for both PSP/ZIF-8 and PSP:ZIF-8 powders. More specifically, below 5 mg/ml phenol red incorporated into ZIF-8, the PSP/ZIF-8 and PSP:ZIF-8 exhibit similar nitrogen (N) and sulfur (S) values, with the nitrogen (N) and sulfur (S) composition of PSP/ZIF-8 being slightly smaller and greater, respectively.

As exhibited in **Table 4.5**, the CHNS values for PSP/ZIF-8 at 5 mg/ml phenol red are immensely different from those reported for PSP:ZIF-8 at lower phenol red loadings. While the hydrogen (H) content remains consistent with that from lower phenol red loadings, the carbon (C) content increases to 45%. However, the nitrogen (N) content dwindles to 15.95%, which is significantly smaller than what is expected for solid ZIF-8 powder for this phenol red loading. Moreover, the sulfur (S) content has risen vastly to 1.58%, which is exceedingly more than expected from phenol red adsorbed to ZIF-8. These CHNS elemental composition results, combined with the PXRD patterns, FTIR spectra, and UV-Vis spectra shown earlier, substantiate the incomplete formation of ZIF-8 at higher phenol red loadings. Based on **Figure 4.14** and **Figure 4.15**, some amorphous, solid blend of the ZIF-8 reaction precursors and phenol red could form at these higher dye loadings. In reference to **Figure 4.11-B**, it is possible that CO_2 (across the range of calibrated concentrations) encounters this solid and fails to adsorb due to the absence of binding sites characteristic of ZIF-8. Thus, across these indoor gas levels, no color change is quantitatively probed via the *in-situ* diffuse reflectance UV-Vis spectra. Previous research has generated evidence that ZIF crystallization occurs "through an amorphous or medium-range order phase" that undergoes "subsequent transition(s) yielding the final crystalline product" [171]. More so, the reaction parameters, such as reaction "solution composition," can control "relative growth rates" along specific crystallographic directions in MOFs [171]. Here, the 48-hr MOF reaction period, as well as the high concentrations of phenol red developed within the ZIF-8 precursor solutions, are suspected to obstruct the successful formation of long-range order ZIF-8, resulting in the unachieved color change among ED/PSP:ZIF-8 at 5 mg/ml phenol red [171].

While an upper limit for phenol red incorporation into the colorimetric gas sensor MOF adsorbent reaction solution has been determined, differences in the location of phenol red with respect to ZIF-8 between PSP-ED/ZIF-8 and ED/PSP:ZIF-8 has yet to be elucidated. The small difference in the sulfur (%S) content in PSP/ZIF-8 and PSP:ZIF-8 (from CHNS elemental composition data shown in **Table 4.4** and **Table 4.5**) suggest that phenol location on ZIF-8 (rather than phenol red amount) is most likely to contribute to significant differences in the colorimetric response achieved in PSP-ED/ZIF-8 and ED/PSP:ZIF-8, respectively. In Chapter 4.4.2, X-ray-based spectroscopic

techniques will be introduced toward a future objective of associating phenol red/ZIF-8 adsorption to the magnitude of the color change achieved in various CO_2 environments involving humidity and VOCs. In the subsequent section, the role of ethylenediamine will be discussed in detail.

4.3 Elucidating the role of ethylenediamine: discerning phenol red/ZIF-8 intermolecular forces and determining chemisorptive CO_2 binding

The purpose of this section is to (i) ascertain the effect of ethylenediamine on phenol red/ZIF-8 adsorption thermodynamics; (ii) determine the effect of variable ethylenediamine loading on the observed colorimetric gas response in dry environment; and (iii) explicate the chemical sensing mechanism of indoor CO_2 through spectroscopic studies involving ethylenediamine as the primary amine species.

4.3.1 Synthesis of PSP/ZIF-8 and PSP-ED/ZIF-8 with high phenol red loadings: liquid and solid

The synthesis of PSP/ZIF-8 and PSP-ED/ZIF-8 (with higher loadings) follows the recipes outlined in Chapter 4.2.1. In this preparation, however, the phenol red loadings are 0, 5, 10, and 20 mg/ml (respectively) in pure methanol or a 2% ethylenediamine (%v/v) solution in methanol. **Figure 4.16** shows different solutions of phenol red dissolved in protic solvent. As observed, the solutions transition from clear to orange to light red to dark red with increased phenol red concentrations. PSP/ZIF-8 and PSP-ED/ZIF-8 methanolic samples are used to collect PXRD patterns, colorimetric images, and *in-situ* UV-Vis diffuse reflectance spectra (in the presence of indoor levels of carbon dioxide).

Fig. 4.16. Highly-loaded phenol red (PSP) solutions in pure methanol (0 to 20 mg/ml).

To prepare the phenol red-adsorbed ZIF-8 solid powders (with and without ethylenediamine), pristine ZIF-8 is stirred (100 rpm) at room temperature for 24-hr with various phenol red loadings (0 to 20 mg/ml) in pure methanol or a 2% ethylenediamine methanolic solution. This mixing process is depicted in **Figure 4.17**. Following this process, the dye-adsorbed ZIF-8 samples are dried at room temperature for 24-hr in ambient lab atmosphere. Finally, these solid samples are ground using a mortar and pestle, and then stored in separate scintillation vials (as shown in **Figure 4.18**). All solid samples are used for SEM collection, FTIR spectroscopic analysis, and CHNS elemental analysis.

A **B**

Fig. 4.17. Room-temperature equilibrium mixing of pristine ZIF-8 with **(A)** phenol red in methanol and **(B)** phenol red in a 2% ethylenediamine methanolic solution.

Fig. 4.18. (Top row): PSP/ZIF-8 powders (0% ethylenediamine in methanol). **(Bottom row):** PSP-ED/ZIF-8 (2% ethylenediamine in methanol). Concentrations are shown in mg/ml phenol red (in either methanol or ethylenediamine/methanol solution).

4.3.2 Synthesis of PSP-ED/ZIF-8 and ED/PSP:ZIF-8 with high ethylenediamine loadings

In this section, PSP-ED/ZIF-8 and ED/PSP:ZIF-8 are prepared as described in Chapter 3 (with ethylenediamine concentrations scaled up to 20%, %v/v, in methanol). Different ethylenediamine solutions (with constant phenol red loading) are shown in **Figure 4.19**. All samples are used for FTIR spectra collection and *in-situ* diffuse reflectance UV-Vis spectra collection.

Fig. 4.19. Ethylenediamine solutions (up to 20%, %v/v in methanol). Dye loadings are set constant at 0.5 mg phenol red/ml solvent.

4.3.3 Powder X-ray diffraction (PXRD): stability of ZIF-8 with large dye loadings

Figure 4.20 displays PXRD patterns for PSP/ZIF-8 and PSP-ED/ZIF-8 samples (up to 20 mg/ml phenol red in solvent). To collect these diffraction patterns, a Rigaku Miniflex 6G Benchtop Powder XRD is used (40 kV/15 mA; X-ray Source: Sealed Source Tube (Cu-Kα Radiation); scan rate: 3.0°/min; and 1D scan mode). For both samples, the major diffraction peaks of ZIF-8 are preserved, indicating excellent stability upon adsorption of large phenol red loadings. As observed in earlier chapters, the change in relative intensity upon incorporation of ethylenediamine (to form PSP-ED/ZIF-8) is ascribed to changes in electron density associated with the crystallographic directions characteristic of ZIF-8 [99, 123].

4.3.4 Scanning electron microscopy (SEM): morphological features with and without ethylenediamine of high phenol red-loaded ZIF-8

Figure 4.21 and **Figure 4.22** show SEM images for PSP/ZIF-8 powders and PSP-ED/ZIF-8, respectively (collected using the same instrument in Chapter 2) [123]. In accordance with **Figure 4.20**, as well as previous ZIF-8-based materials [99, 123], the dye-adsorbed, crystals are modestly larger than 100 nm in size and exhibit a rhombic dodecahedral shape. As observed in **Figure 4.21**, the edges of the particles became less sharp up to 20 mg/ml phenol loaded onto ZIF-8.

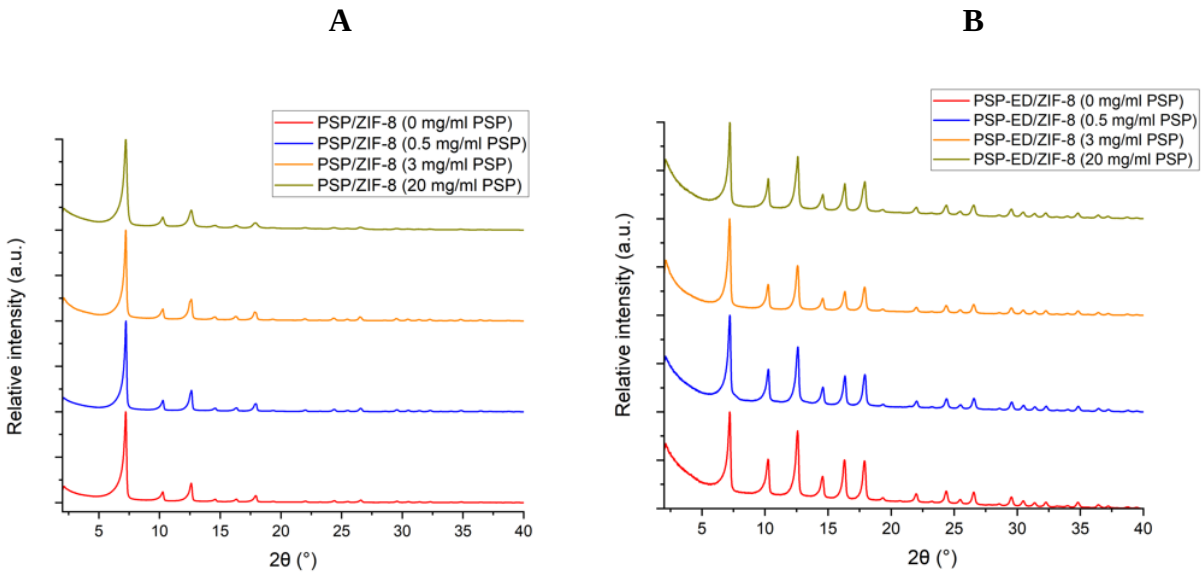

Fig. 4.20. PXRD patterns for **(A)** PSP/ZIF-8 and **(B)** PSP-ED/ZIF-8 drop-cast samples.

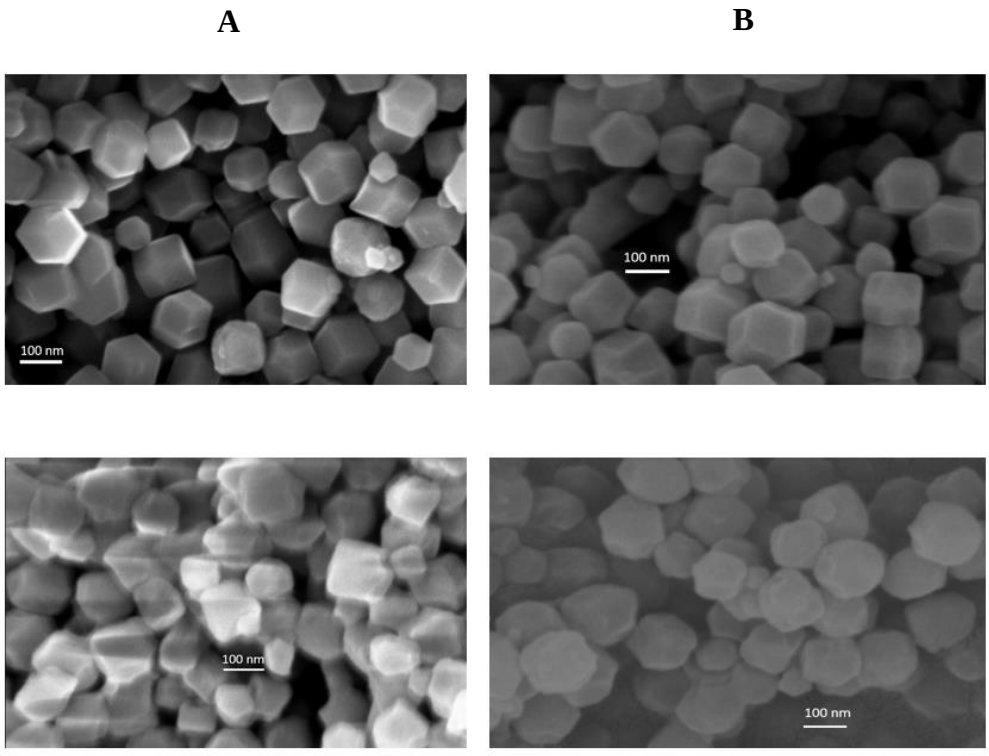

Fig. 4.21. SEM images for PSP/ZIF-8 at **(A)** 0 mg/ml phenol red, **(B)** 5 mg/ml phenol red, **(C)** 10 mg/ml phenol red, and **(D)** 20 mg/ml red. Size bar: 100 nm.

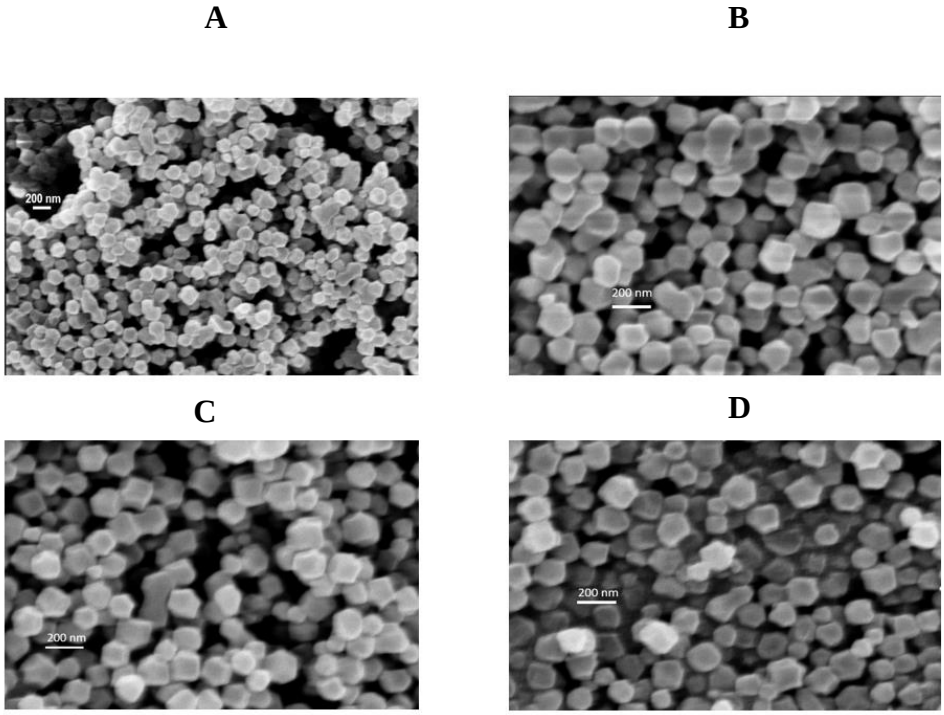

Fig. 4.22. SEM images for PSP-ED/ZIF-8 at **(A)** 0 mg/ml phenol red, **(B)** 5 mg/ml phenol red, **(C)** 10 mg/ml phenol red, and **(D)** 20 mg/ml red. Size bar: 200 nm.

4.3.5 Fourier transform infrared (FTIR) spectroscopy: the influence of ethylenediamine on phenol red adsorption

Figure 4.23 shows FTIR spectra (collected via Bruker Vertex80 spectrometer; 400 to 4,000 cm^{-1}; 100 scans) for powder PSP/ZIF-8 (0 to 20 mg/ml phenol red in methanol). **Figure 4.23-A** demonstrates that the incremented phenol red loadings do not disturb the 421 cm^{-1} Zn-N stretching mode of ZIF-8, confirming the stability of the MOF [99, 123]. Moreover, the unshifted nature of the 421 cm^{-1} IR-active mode with increased phenol red loading suggests that electrostatic interactions between acidic sites from Zn^{2+} and negatively charged species on ZIF-8 might not dominate [66, 208]. **Figure 4.23-B** displays the emergence of an IR-active mode at ~614 cm^{-1}, which is attributed to C-H bending in phenol red [210]. As shown, this IR-active mode becomes more visible with increasing the phenol red loading onto ZIF-8. **Figure 4.23-C** displays the 995 cm^{-1} =C-H in-plane bend, which remains preserved and unshifted across the dye-adsorbed samples [204]. The emergent peaks at 1018 and 1041 cm^{-1} in PSP/ZIF-8 (at 10 and 20 mg/ml phenol red, respectively) are assigned to S=O stretching from the phenol red [210]. **Figure 4.23-D** shows the =C-H in plane deformations at 1147 and 1179 cm^{-1}, the CH_2 wagging at 1311 cm^{-1}, and the CH_3 antisymmetric bend at 1384 cm^{-1} [204], which are maintained and unshifted across the PSP/ZIF-8 samples. **Figure 4.23-E** displays the 1457 cm^{-1} C=C stretch, which is also maintained and unshifted [204]. However, with increasing phenol red concentrations, the 1584 cm^{-1} C=N stretch of the imidazolate ligand clearly shifts to lower wavenumber, which could imply π-π stacking

existent between the phenol red and this region of the ZIF-8 linker [204]. Finally, **Figure 4.23-F** shows the maintained (and unshifted) C-H symmetric stretch of the methyl group on ZIF-8 across the PSP/ZIF-8 samples [204]. However, a slight shift of the 3137 cm^{-1} =C-H aromatic stretch appears with increased phenol red loading, which could potentially suggest another physisorptive interaction between phenol red and this region of ZIF-8 [204].

Figure 4.24 depicts the FTIR spectra collected for PSP-ED/ZIF-8 powders (0 to 20 mg/ml phenol red in 2% ethylenediamine, %v/v, methanolic solutions). **Figure 4.24-A** demonstrates that the incremented phenol red loadings (in alkaline environment) do not compromise the 421 cm^{-1} Zn-N stretching mode of ZIF-8, confirming the stability of the MOF [99, 123]. As observed with PSP-ED/ZIF-8, the unshifted nature of the 421 cm^{-1} IR-active mode with increased phenol red loading suggests that electrostatic interactions from the zinc metal are likely not dominant [66, 208]. **Figure 4.24-B** shows the ~614 cm^{-1} IR-active mode, which is labeled as C-H bending from phenol red [210]. **Figure 4.24-C** depicts the 995 cm^{-1} =C-H in-plane bend, which does not move across the dye-adsorbed samples [204]. The 1018 and 1041 cm^{-1} IR-active modes are assigned to S=O stretching from the phenol red [210]. **Figure 4.24-D** confirms that the =C-H in plane deformations at 1147 and 1179 cm^{-1}, the CH_2 wagging at 1311 cm^{-1}, and the CH_3 antisymmetric bend at 1384 cm^{-1} [204], are not moved from incremented phenol red loading (in methanol). **Figure 4.24-E** shows the unshifted 1457 and 1584 cm^{-1} IR-active modes, which correspond to the C=C stretch and C=N stretch, respectively [204]. Lastly, **Figure 4.24-F** shows the unshifted aliphatic C-H stretch (at 2931 cm^{-1}) and the aromatic =C-H stretch (at 3137 cm^{-1}) [204]. In addition, all PSP-ED/ZIF-8 samples possess the N-H stretches characteristic of ethylenediamine at 3280 cm^{-1} and 3360 cm^{-1} [123]. Compared to the PSP/ZIF-8 sample, the PSP-ED/ZIF-8 does not exhibit major shifts of the ZIF-8 IR-active modes characteristic of the chemical structure. It is possible that the significant loading of ethylenediamine could mute such shifts. However, to better understand the role of surface basicity (or ethylenediamine incorporation) on phenol red/ZIF-8 adsorptive chemistry, other surface characterization and elemental analysis techniques will be implemented in subsequent subsections.

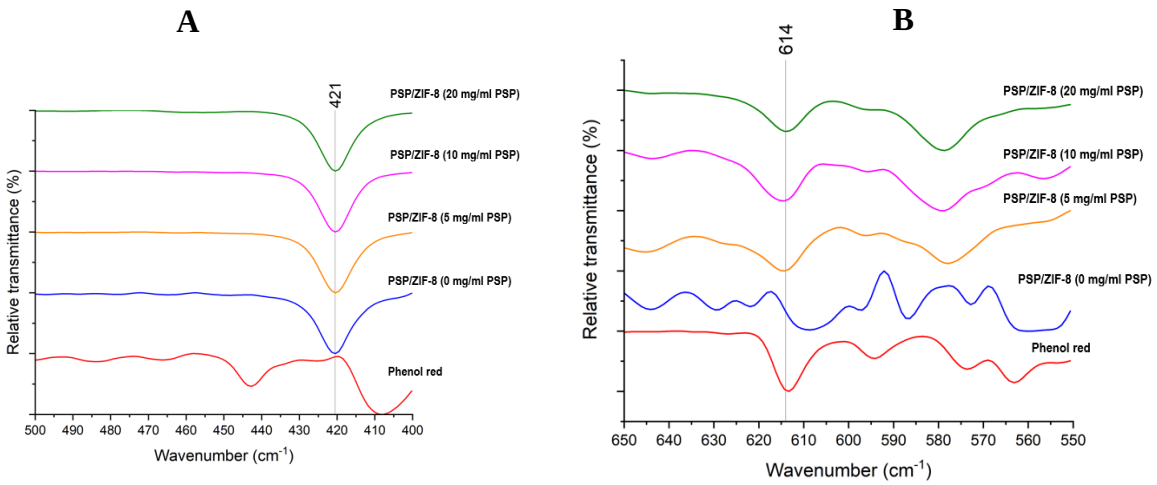

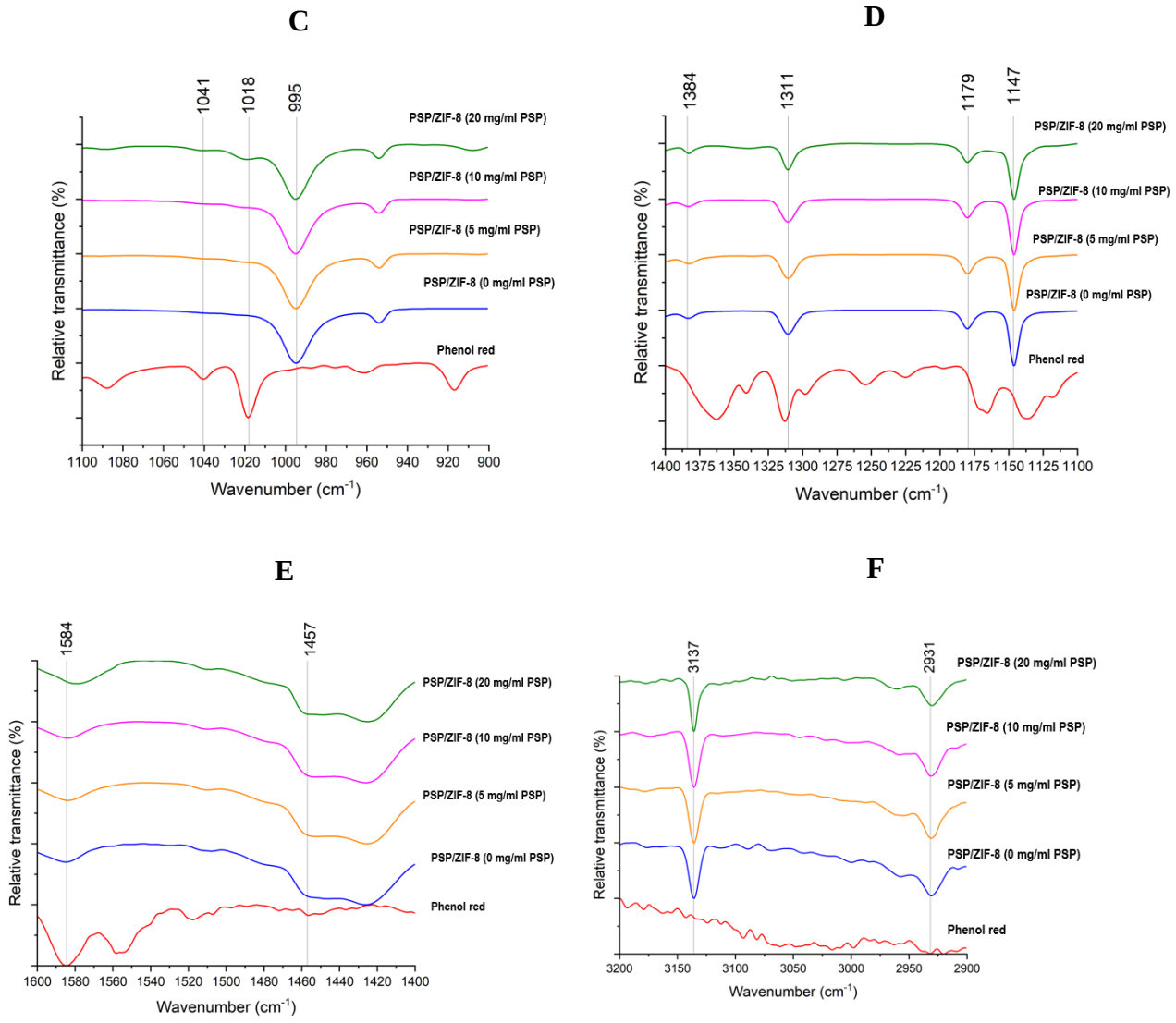

Fig. 4.23. FTIR spectra for PSP/ZIF-8. Phenol red: red. PSP/ZIF-8 (0 mg/ml phenol red): blue. PSP/ZIF-8 (5 mg/ml phenol red): orange. PSP/ZIF-8 (10 mg/ml phenol red): magenta. PSP/ZIF-8 (20 mg/ml phenol red): olive. **(A)** 500 - 400 cm^{-1}; **(B)** 850 - 650 cm^{-1}; **(C)** 1100-900 cm^{-1}; **(D)** 1400 – 1100 cm^{-1}; **(E)** 1600-1400 $cm^{=1}$; and **(F)** 3200-2900 cm^{-1}.

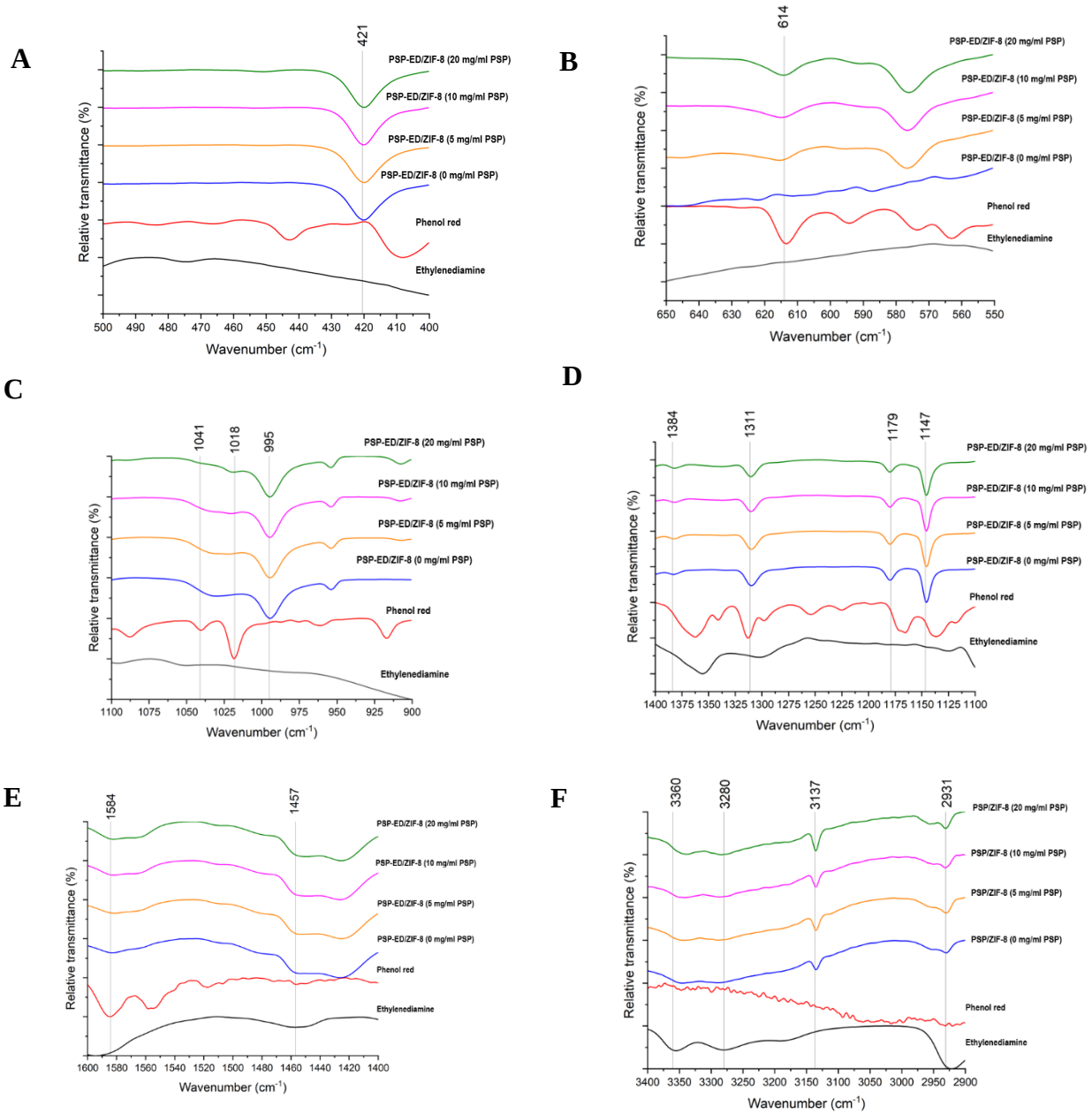

Fig. 4.24. FTIR spectra for PSP-ED/ZIF-8. Ethylenediamine: black. Phenol red: red. PSP-ED/ZIF-8 (0 mg/ml phenol red): blue. PSP-ED/ZIF-8 (5 mg/ml phenol red): orange. PSP-ED/ZIF-8 (10 mg/ml phenol red): magenta. PSP-ED/ZIF-8 (20 mg/ml phenol red): olive. **(A)** 500 - 400 cm^{-1}; **(B)** 850 - 650 cm^{-1}; **(C)** 1100-900 cm^{-1}; **(D)** 1400 – 1100 cm^{-1}; **(E)** 1600-1400 $cm^{=1}$; and **(F)** 3200-2900 cm^{-1}.

4.3.6 Fourier transform infrared (FTIR) spectroscopy: ZIF-8 stability in high basicity from controlled ethylenediamine environment

Figure 4.25 shows the FTIR spectra for ED/ZIF-8, PSP-ED/ZIF-8, and ED/PSP:ZIF-8 with increased ethylenediamine loadings (up to 20%, %v/v, in methanol). For the first- and second-generation sensors, phenol red loadings are maintained at 0.5 mg/ml in colorimetric solvent. The 421 cm^{-1} Zn-N stretch is preserved for all samples with increased ethylenediamine loadings, indicating the chemical stability of ZIF-8 in significantly basic environment.

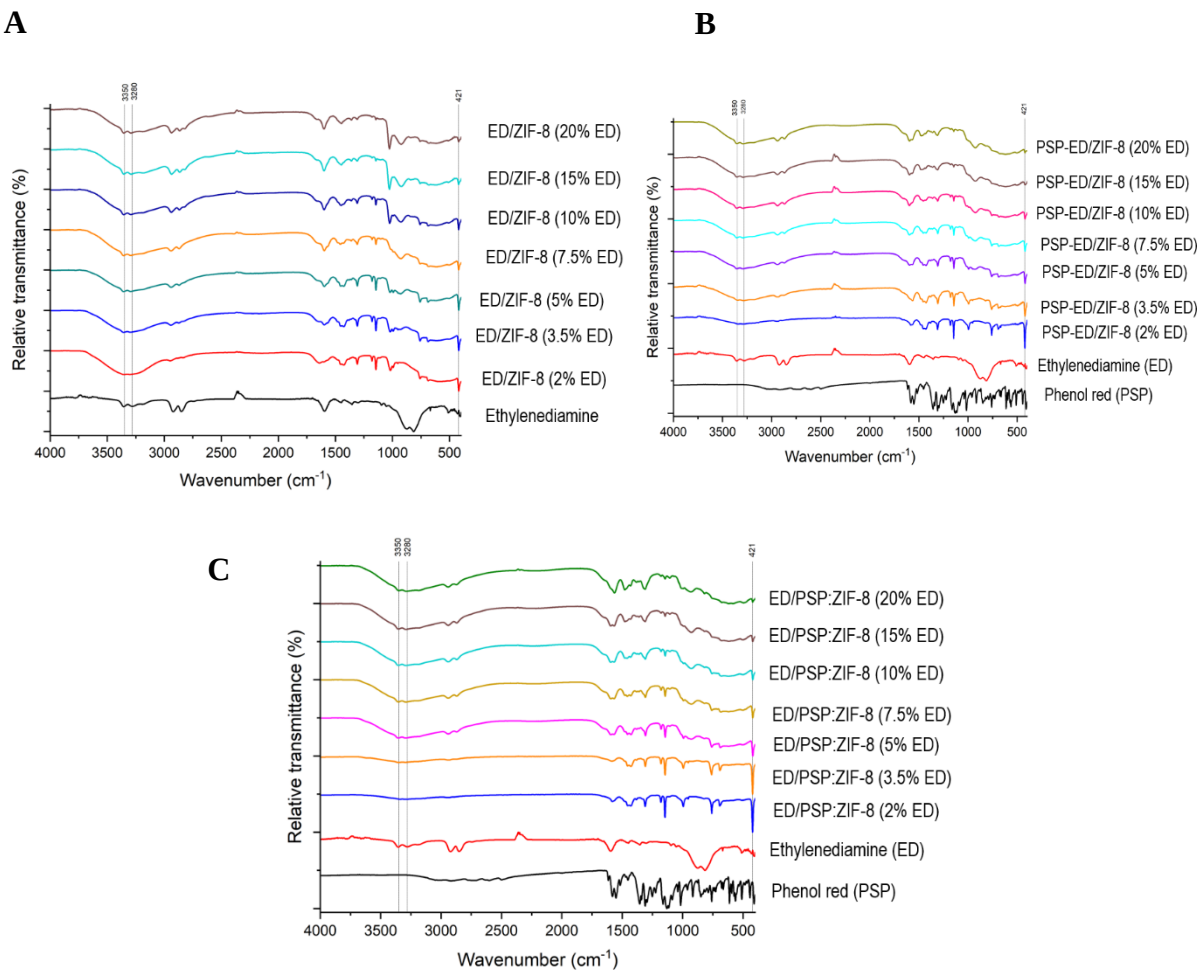

Fig. 4.25. FTIR spectra for **(A)** ED/ZIF-8, **(B)** PSP-ED/ZIF-8, and **(C)** ED/PSP:ZIF-8 with variable ethylenediamine loadings (0 to 20%, %v/v, in methanol). For the first- and second-generation sensors, phenol red concentrations are maintained at 0.5 mg/ml.

4.3.7 Colorimetric imaging assessments: effect of high phenol red and ethylenediamine loadings on the observed colorimetric gas response at low humidity

Colorimetric images are shown for PSP-ED/ZIF-8 and ED/PSP:ZIF-8 with increased ethylenediamine loadings in **Figure 4.26** and **Figure 4.27**, respectively, exposed to 3,000 ppm CO_2 for 1-min at room temperature (0% RH). With increased ethylenediamine loading, the drop-cast sensor becomes more purple before controlled gas exposure. For PSP-ED/ZIF-8, the colorimetric response significantly decreases at higher ethylenediamine loadings, effectively not turning yellow at all at 20% (%v/v) ethylenediamine in methanol. For ED/PSP:ZIF-8, a colorimetric response is achieved across the entire range of ethylenediamine loadings used. However, similar to the PSP-ED/ZIF-8 sensor, the ED/PSP:ZIF-8 sensor does exhibit a reduced yellow response with increased ethylenediamine concentration on the surface of ZIF-8.

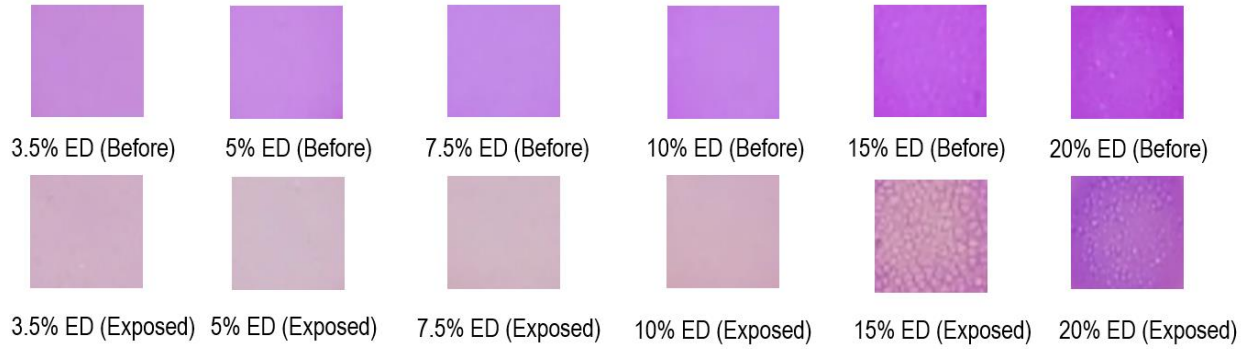

Fig. 4.26. Colorimetric images of PSP-ED/ZIF-8 exposed to 3,000 ppm CO_2 (at 0% RH).

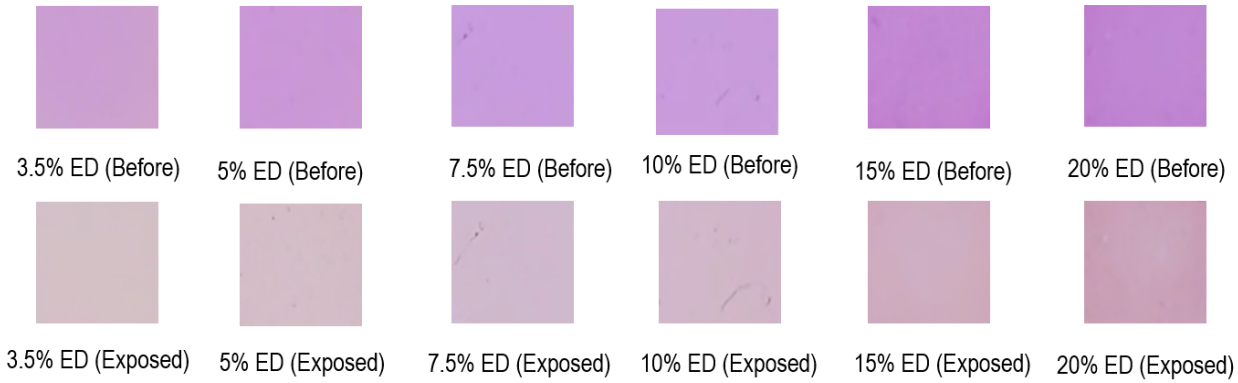

Fig. 4.27. Colorimetric images of ED/PSP:ZIF-8 exposed to 3,000 ppm CO_2 (at 0% RH).

Figure 4.28 depicts colorimetric images of PSP-ED/ZIF-8 exposed to 3,000 ppm CO_2 (at 0% RH) and room temperature for samples loaded with up to 20 mg/ml phenol red. At lower phenol red loadings, an obvious color change occurs, and the sensor becomes more yellow. However, with increased phenol red loadings, the color change effectively ceases to occur. As shown in **Figure 4.29**, the red, green, and blue (RGB) color distributions also decrease with increased phenol red loadings for "before exposure" and "exposed" CO_2 images. At 10 mg/ml phenol red and 20 mg/ml phenol red PSP-ED/ZIF-8 exposed to 3,000 ppm CO_2, the RGB distributions scarcely change before and during controlled gas exposure, indicating a suppression of the color change.

Fig. 4.28. Colorimetric images of PSP-ED/ZIF-8 exposed to 3,000 ppm CO_2 (at 0% RH) up to 20 mg/ml phenol red.

A

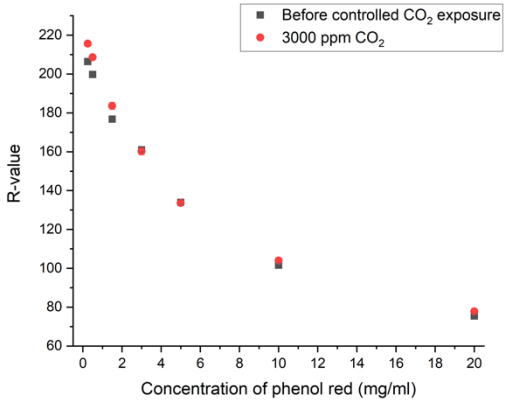

B

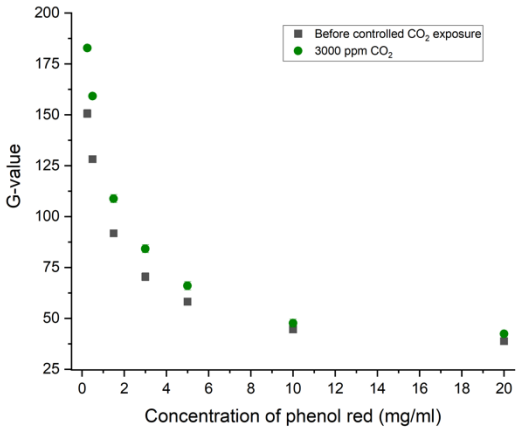

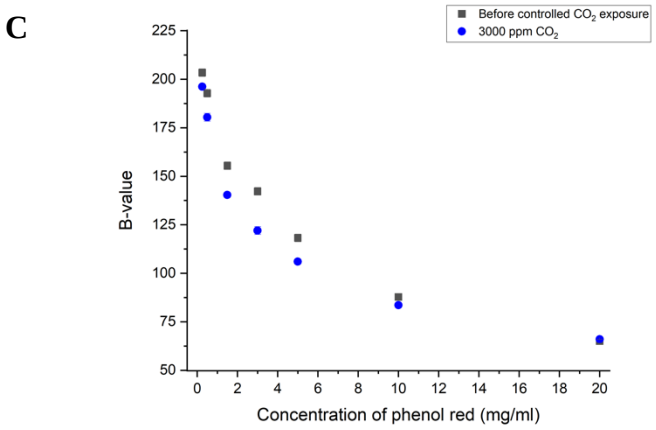

Fig. 4.29. Color distributions for 3,000 ppm CO_2 with PSP-ED/ZIF-8 with variable phenol red loadings. **(A)** R-distribution. **(B)** G-distribution. **(C)** B-distribution.

4.3.8 In-situ diffuse reflectance ultraviolet-visible (UV-Vis) spectra: quantifying the color change with high ethylenediamine loadings

To quantify the effect of high ethylenediamine concentration on the surface of ZIF-8 on the color change, an *in-situ* UV-Vis diffuse reflectance technique is employed. **Figure 4.30** shows a plot of the mean concentration of CO_2 (in ppm) versus mean CO_2 flowrate (in ml/min) collected at 0% relative humidity (22.7 ± 0.4 °C) using a wireless GasLab Plus CM-501 NDIR sensor.

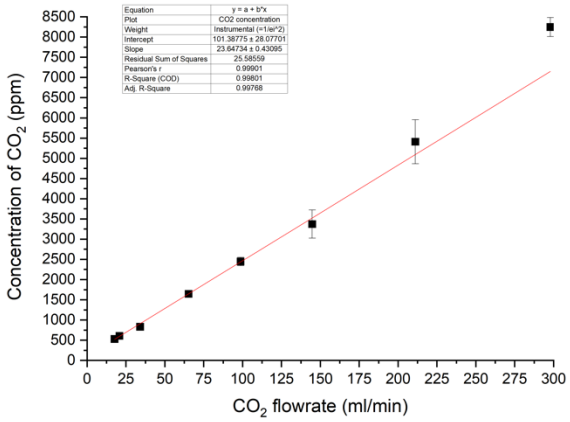

Fig. 4.30. Mean CO_2 concentration (ppm) versus mean CO_2 flowrate (ml/min) for *in-situ* UV-Vis spectral analysis. Total gas flowrate: 300 ml/min. Error bars are standard deviation values.

Figure 4.31 shows the 443/570 nm F(R) ratios for the first- and second-generation sensors exposed from 500 to 8300 ppm CO_2 (with increased ethylenediamine loadings: 3.5 to 20% ED, %v/v, in methanol). All phenol red loadings are 0.5 mg/ml. While the ED/PSP:ZIF-8 material exhibits a stronger colorimetric gas response than the PSP-ED/ZIF-8 material, both sensors exhibit a diminished colorimetric response with increased ethylenediamine loading. **Figure 4.32** demonstrates how the colorimetric gas response (at 3400 ppm CO_2) significantly drops for PSP-ED/ZIF-8 above 10% (%v/v) ethylenediamine loaded, whereas that of the ED/PSP:ZIF-8 sensor exhibits a stepped decrease indicating the existence of a color change even at such high ethylenediamine surface concentrations.

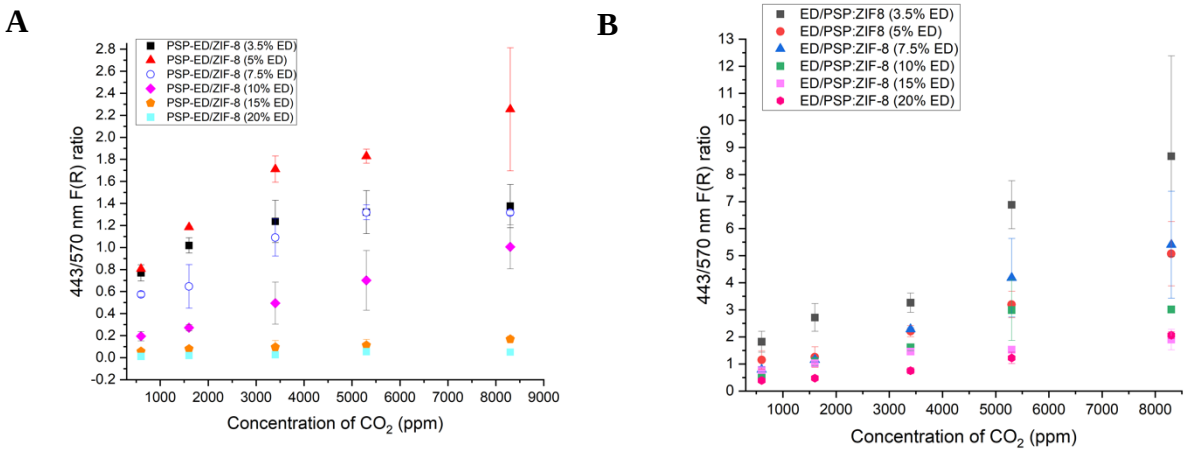

Fig. 4.31. 443/570 nm ratio for **(A)** PSP-ED/ZIF-8 and **(B)** ED/PSP:ZIF-8 exposed to dry CO_2. Total gas flowrate: 300 ml/min. Error bars are standard deviation values.

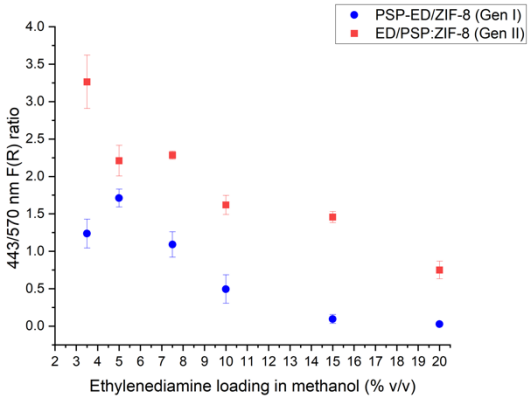

Fig. 4.32. 443/570 nm F(R) ratio vs. ethylenediamine concentration (%v/v) in methanol for PSP-ED/ZIF-8 (blue) and ED/PSP:ZIF-8 (red) exposed to 3400 ppm CO_2 (0% RH).

Figure 4.33 shows how the normalized F(R) values change at 15% and 20% ethylenediamine loadings, respectively, for PSP-ED/ZIF-8 and ED/PSP:ZIF-8. For both 15% and 20% ethylenediamine loadings, PSP-ED/ZIF-8 exhibits scarce changes in the colorimetric gas response with increased CO_2 levels, which is consistent with the colorimetric images depicted in **Figure 4.26**. However, the ED/PSP:ZIF-8 material continues to exhibit a quantifiable (but diminished) colorimetric gas response at both 15% and 20% (%v/v) ethylenediamine loadings (as shown in **Figure 4.27**). In accordance with the zwitterion mechanism described in **Equation 2.16** [140-145], it is possible that increasing the ethylenediamine loading positions ethylenediamine (rather than phenol red) as the primary base to deprotonate the zwitterion, thereby inhibiting the colorimetric gas response.

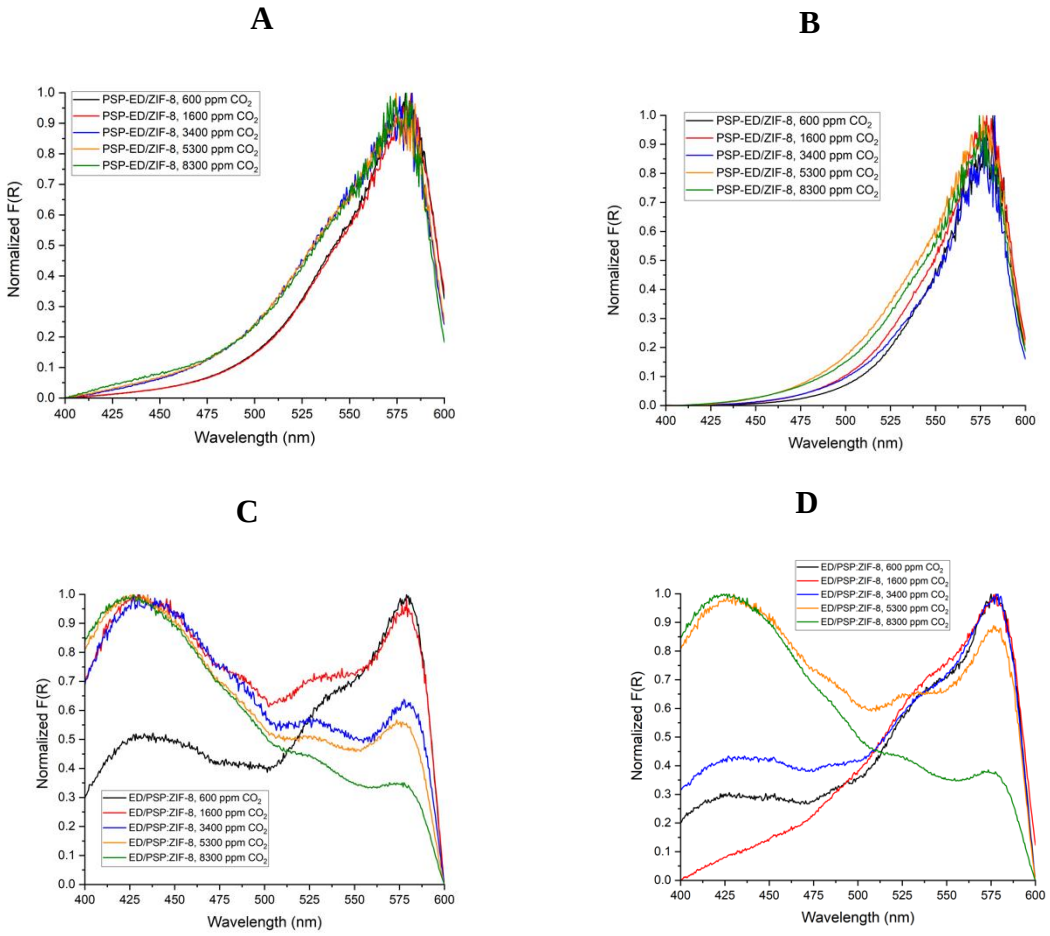

Fig. 4.33. Normalized F(R) ratios vs. wavelength (nm) for **(A)** PSP-ED/ZIF-8 (15% ED), **(B)** PSP-ED/ZIF-8 (20% ED), **(C)** ED/PSP:ZIF-8 (15% ED), and **(D)** ED/PSP:ZIF-8 (20% ED).

4.3.9 In-situ diffuse reflectance ultraviolet-visible (UV-Vis) spectra: high phenol red loading and the imperceptible color change

Diffuse reflectance UV-Vis spectra are collected for PSP-ED/ZIF-8 sensors scaled up to 20 mg/ml phenol red loading and exposed to 3,000 ppm CO_2 at 0% RH. **Table 4.6** displays the average CO_2 flowrate, average CO_2 concentration, and average temperature using an Agilent Technologies ADM1000 Universal Gas Flowmeter and wireless GasLab Plus CM-501 NDIR sensor. All *in-situ* UV-Vis diffuse reflectance spectra are collected at a total gas flow rate of 350 ml/min using the same system described in **Figure 3.2** [123].

Table 4.6 Average CO_2 flowrate, average CO_2 flowrate, and average temperature for UV-Vis spectral analysis

Average concentration of CO_2 (ppm)	Average CO_2 flowrate (ml/min)	Average temperature (°C)
2922 ± 100	125.3 ± 0.5	24.0 ± 0.6

Figure 4.34 shows the "before" and "exposed" diffuse reflectance (%R) versus wavelength (nm) for PSP-ED/ZIF-8. With increased phenol red loadings, the 570 nm resonant wavelength of phenol red becomes less sharp and shifts toward 600 nm. Upon exposure to gas, the 570 nm diffuse reflectance (%R) increases relative to its "before exposure" state, demonstrating the color change as the sensor becomes more yellow. However, as depicted in **Figure 4.35**, the difference in the diffuse reflectance values diminishes above 5 mg/ml phenol red, indicating a suppression of the color change with increased phenol red concentration on the surface of ZIF-8. At these elevated phenol red surface concentrations, the available surface area for CO_2 adsorption could be significantly reduced, limiting the capacity for color-based indoor gas detection. Such observations (similarly obtained from **Figure 4.8** and **Figure 4.9**) at these heightened dye levels necessitate the use of other analyses (such as surface area characterization and elemental analysis) to discern how phenol red adsorbs to ZIF-8 (with and without a constant ethylenediamine loading of 2%, %v/v, in methanol).

A **B**

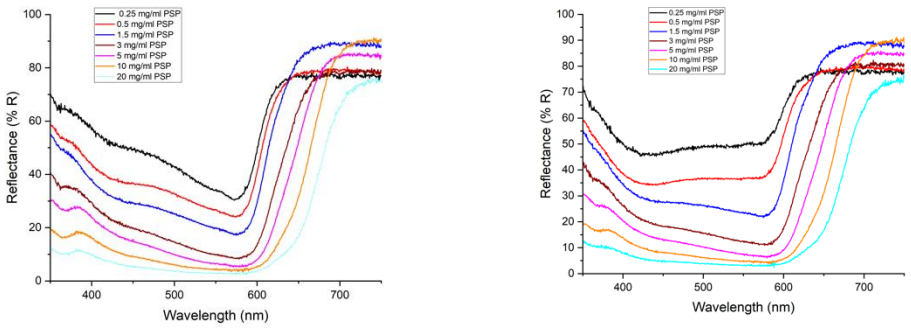

Fig. 4.34. Diffuse reflectance values for PSP-ED/ZIF-8. **(A)** Before exposure and **(B)** Exposed to 3,000 ppm CO_2 (0% RH).

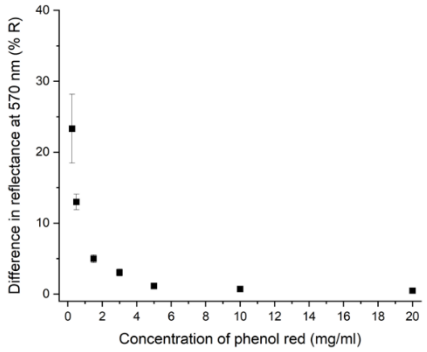

Fig. 4.35. Difference in reflectance at 570 nm (%R) versus concentration of phenol red (mg/ml) for PSP-ED/ZIF-8 before and exposed to 3,000 ppm CO_2.

4.3.10 Ultraviolet-visible (UV-Vis) spectra for thermodynamic investigation of phenol red/ZIF-8 adsorption with and without ethylenediamine

Liquid-phase, room temperature UV-Vis spectra are collected toward an initial estimation of how phenol red might adsorb to ZIF-8 (with and without ethylenediamine). First, multiple concentrations of phenol red in either (a) pure methanol or (b) a 2% ethylenediamine methanolic solution are prepared. Then, background UV-Vis spectra are collected for pure methanol and a 2% ethylenediamine solution using a Shimadzu UV-2600i UV-Vis spectrophotometer. The temperature for all experiments is set to 25°C using a Shimadzu Cell Positioner CPS-100 instrument. Absorbance data are collected for each phenol red concentration developed. Using the Beer-Lambert law [91-92], a linear calibration between the Absorbance (A.u.) versus concentration of phenol red (mg/L) is achieved. **Figure 4.36** displays this calibration for phenol red dissolved in pure methanol (λ_{max} = 423 nm) and **Figure 4.37** shows this calibration for phenol red dissolved in a 2% ethylenediamine (% v/v) solution in methanol (λ_{max} = 565 nm).

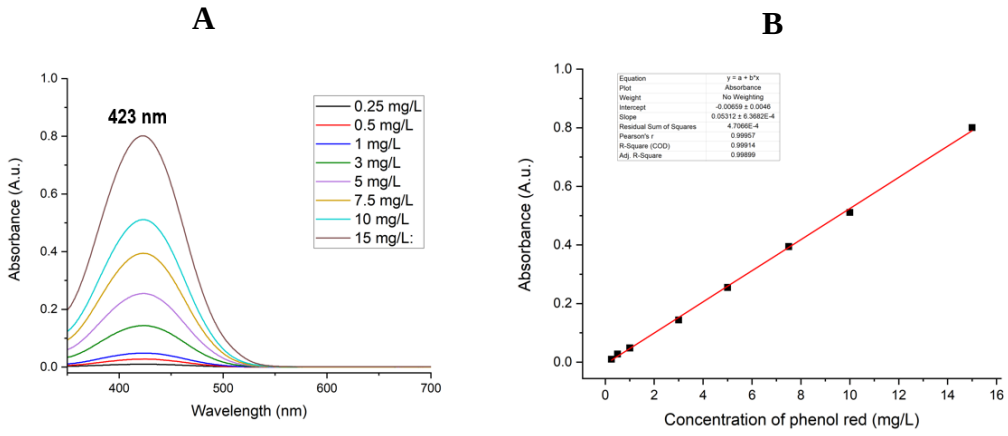

Fig. 4.36. (A) UV-Vis absorbance spectra for phenol red (in methanol). **(B)** Absorbance at 423 nm (A.u.) versus concentration of phenol red in methanol (mg/L) calibration.

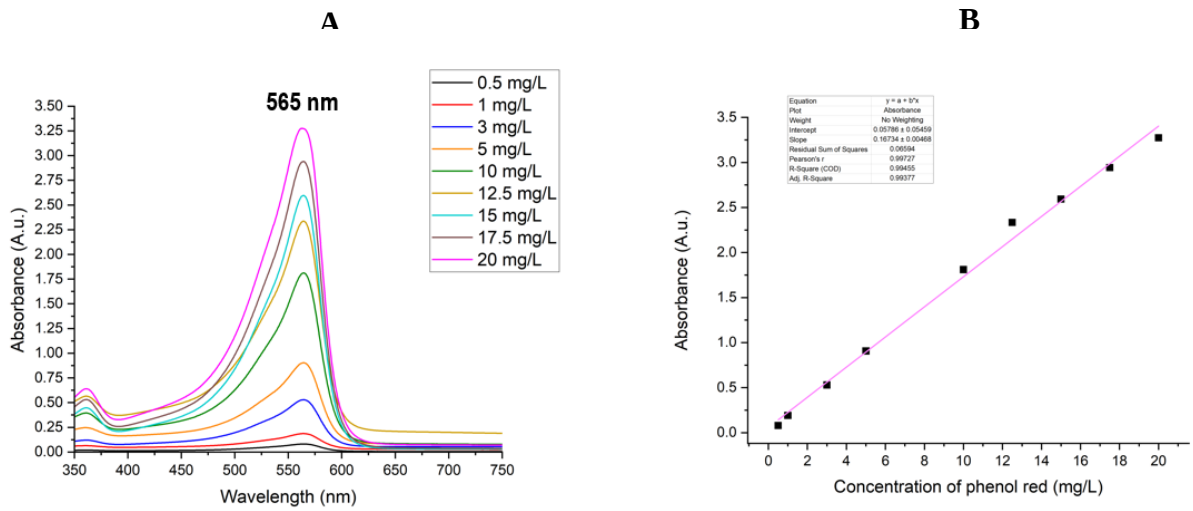

Fig. 4.37. **(A)** UV-Vis absorbance spectra for phenol red (in a 2% ethylenediamine, %v/v, methanolic solution). **(B)** Absorbance at 565 nm (A.u.) versus concentration of phenol red in 2% ethylenediamine-loaded methanol (mg/L) calibration.

Once the room temperature UV-Vis spectral calibrations are complete, 10 mg of pristine ZIF-8 are stirred in 20 ml of pure methanol or a 2% (%v/v) ethylenediamine solution in methanol for 24-hr at 1200 rpm. Then, supernatant solutions are separated from the dye-adsorbed MOF via centrifugation (6000 rpm at 10-min) using an Eppendorf Centrifuge 5430 R. Supernatant solutions are then transferred into cuvettes and their UV-Vis absorbance values are determined. Using the calibration curves shown in **Figure 4.36** and **Figure 4.37**, an equilibrium phenol red concentration, C_E, is determined in relation to the initial phenol red concentration, C_0. **Equation 4.1** is then used to attain equilibrium adsorbed amounts of phenol red to ZIF-8, q_E [197]. Finally, using **Equation 4.2** and **Equation 4.3**, the C_E and q_E values are used to determine whether phenol red binds to ZIF-8 according to the Langmuir adsorption model or the Freundlich adsorption model, respectively [197]. This entire process is depicted in **Figure 4.38**.

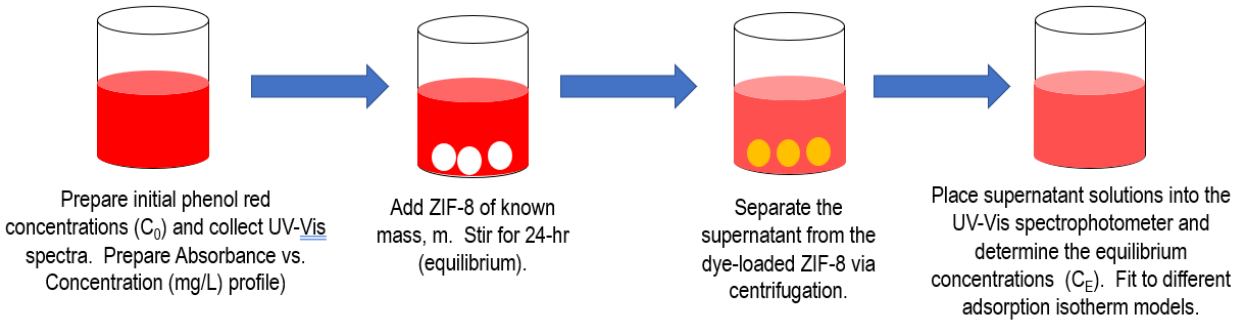

Fig. 4.38. Procedure for the determination of the thermodynamics of phenol red/ZIF-8 adsorption (shown here without ethylenediamine).

Figure 4.39 shows the Langmuir adsorption and Freundlich adsorption isotherms plotted for phenol red adsorbed to ZIF-8 (with and without ethylenediamine).

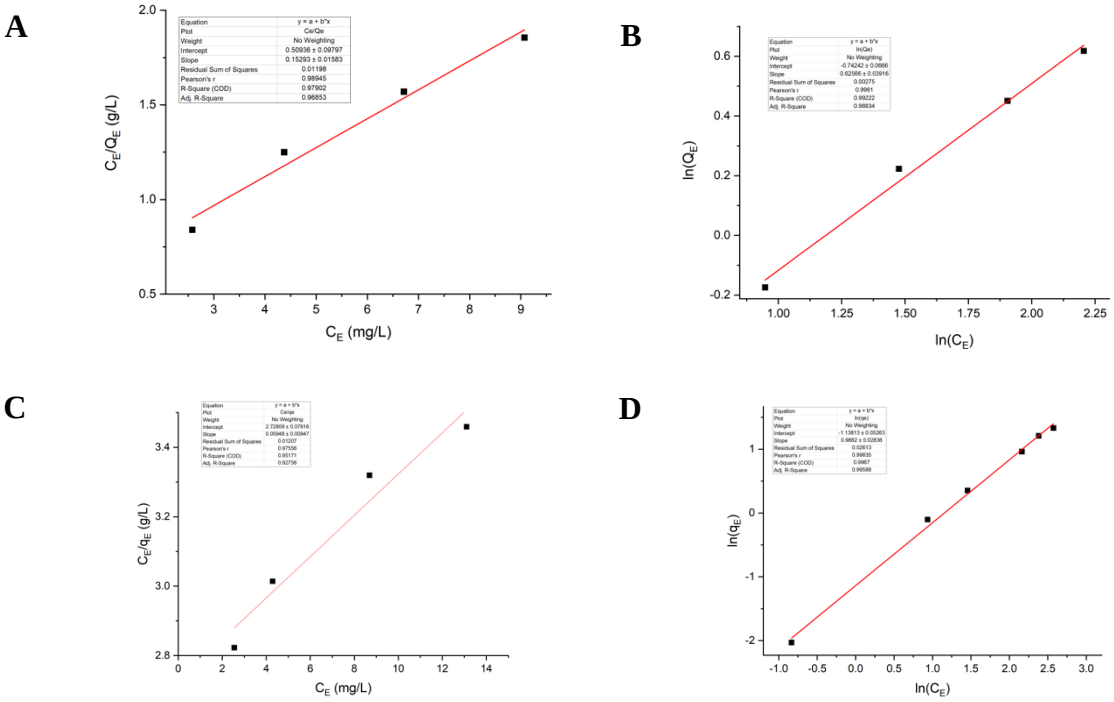

Fig. 4.39. Thermodynamic assessments of phenol red adsorption to ZIF-8. **(A)** Langmuir adsorption model (phenol red + methanol); **(B)** Freundlich adsorption model (phenol red + methanol); **(C)** Langmuir adsorption model (phenol red + ethylenediamine + methanol); and **(D)** Freundlich adsorption model (phenol red + ethylenediamine + methanol).

Table 4.7 shows the R-squared values for the room temperature adsorption of phenol red to ZIF-8 (with and without ethylenediamine). Without ethylenediamine, the Freundlich adsorption model demonstrates a larger R-squared value than the Langmuir adsorption model; however, the difference between the R-squared values is not very large. However, when ethylenediamine is introduced, the Freundlich adsorption model demonstrates a comparatively larger R-squared value than the Langmuir adsorption model. These results imply that ethylenediamine might enhance the heterogeneity of the surface for phenol red adsorption [197]. In the absence of ethylenediamine, the Freundlich adsorption model seems to well represent phenol red adsorption; however, the Langmuir adsorption isotherm could potentially be a meaningful fit.

Table 4.7. R-squared values for Langmuir and Freundlich adsorption models describing phenol red adsorption onto ZIF-8 (in the absence and presence of ethylenediamine).

UV-Vis system	Langmuir adsorption model: R-squared	Freundlich adsorption model: R-squared
Phenol red adsorbed to ZIF-8 (in methanol): PSP/ZIF-8.	0.989	0.996
Phenol red adsorbed to ZIF-8 (in a 2%, %v/v, ethylenediamine methanolic solution): PSP-ED/ZIF-8.	0.976	0.998

4.3.11 Brunauer, Emmett, Teller (BET) theory: effect of ethylenediamine on high phenol red loading and available ZIF-8 surface area

In addition to the preliminary UV-Vis spectra collected to evaluate the effect of ethylenediamine on phenol red adsorption to ZIF-8, BET surface area analysis is conducted using the same instrumentation described in Chapter 2 [123]. **Figure 4.40** shows the BET isotherms for PSP/ZIF-8 and PSP-ED/ZIF-8 at 0, 5, 10, and 20 mg/ml phenol red adsorbed to ZIF-8.

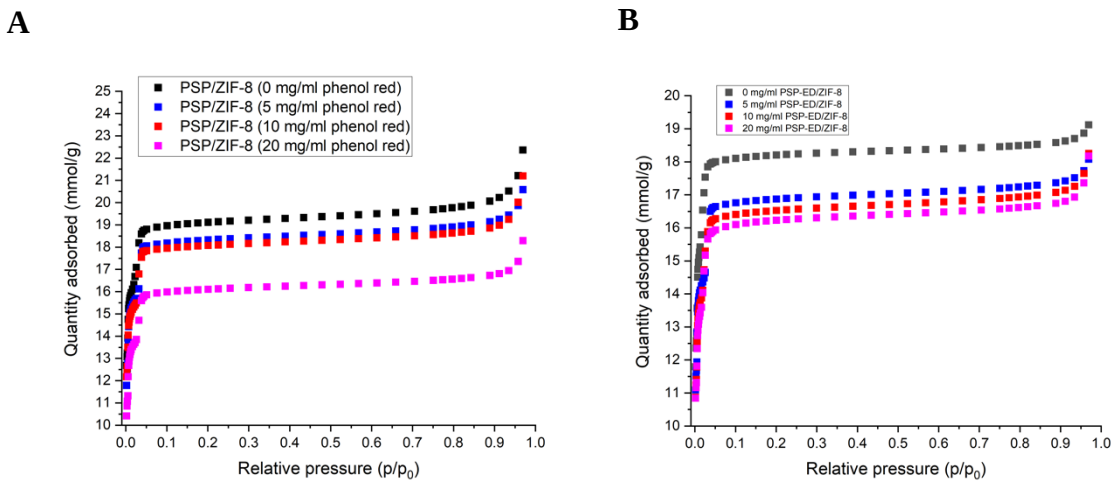

Fig. 4.40. BET adsorption isotherms for **(A)** PSP/ZIF-8 and **(B)** PSP-ED/ZIF-8. Phenol red loadings: 0, 5, 10, and 20 mg/ml in methanol-based solvent.

Table 4.8 and **Table 4.9** show the BET and Langmuir surface area values for PSP/ZIF-8 and PSP-ED/ZIF-8 powders, respectively. For both samples, increased phenol red loading generally decreases both the BET and Langmuir surface areas of ZIF-8, indicating phenol red adsorption onto the MOF. Below 20 mg/ml phenol red loaded, the PSP-ED/ZIF-8 materials exhibit a smaller BET surface than PSP/ZIF-8. These results could be attributed to the fact that ethylenediamine remains adsorbed on the solid PSP-ED/ZIF-8 powders, as evidenced by the IR-active N-H

stretches characteristic of ethylenediamine identified in **Figure 4.24** [123]. Moreover, the reduction of BET surface area in the PSP-ED/ZIF-8 samples from increased phenol red sorption could be answerable for the scarce color change observed from the *in-situ* UV-Vis diffuse reflectance spectra depicted in **Figure 4.35.** Above 5 mg/ml phenol red, the change in diffuse reflectance values at 570 nm (before and during gas exposure) approach zero. Here, the BET and Langmuir surface areas for PSP-ED/ZIF-8 continue to decrease for PSP-ED/ZIF-8, potentially eliminating sites for CO_2 chemisorption through interaction with ethylenediamine molecules [140-145]. To better situate these data (with and without ethylenediamine), however, comparative elemental analysis measurements are required.

Table 4.8. BET and Langmuir surface area values for PSP/ZIF-8.

Sample	BET surface area (m^2/g)	Langmuir surface area (m^2/g)
PSP/ZIF-8 (0 mg/ml phenol red)	1792.7	2050.3
PSP/ZIF-8 (5 mg/ml phenol red)	1695.3	1933.1
PSP/ZIF-8 (10 mg/ml phenol red)	1683.4	1940.5
PSP/ZIF-8 (20 mg/ml phenol red)	1496.4	1706.5

Table 4.9. BET and Langmuir surface area values for PSP-ED/ZIF-8.

Sample	BET surface area (m^2/g)	Langmuir surface area (m^2/g)
PSP-ED/ZIF-8 (0 mg/ml phenol red)	1743.3	1832.2
PSP-ED/ZIF-8 (5 mg/ml phenol red)	1577.5	1724.0
PSP-ED/ZIF-8 (10 mg/ml phenol red)	1562.8	1713.0
PSP-ED/ZIF-8 (20 mg/ml phenol red)	1533.7	1703.9

4.3.12 Carbon, hydrogen, nitrogen, and sulfur (CHNS) elemental composition: quantitative assessment of phenol red adsorption onto ZIF-8 in the absence and presence of ethylenediamine

Carbon, hydrogen, nitrogen, and sulfur (CHNS) elemental analysis is implemented using the same technique described in Chapter 4.2 to compare how much phenol red is adsorbed to ZIF-8 with and without ethylenediamine. **Table 4.10** shows the CHNS elemental composition reported for

phenol red (Thermo Scientific™, AC151431000). The reported CHNS elemental composition for phenol red agrees with values expected from the known chemical structure [117-118].

Table 4.10 CHNS elemental composition for solid phenol red powder.

Sample	C%	H%	N%	S%
Phenol red (PSP)	63.66	4.06	0	8.68

Table 4.11 and **Table 4.12** show the CHNS elemental composition for PSP/ZIF-8 and PSP-ED/ZIF-8, respectively. With increased phenol red loadings, both PSP/ZIF-8 and PSP-ED/ZIF-8 exhibit an increased carbon content (from phenol red adsorption), decreased nitrogen content (from the mass of ZIF-8 and volume of ethylenediamine set constant), and increased sulfur content (from phenol red adsorption). Compared to the PSP/ZIF-8 samples, the PSP-ED/ZIF-8 samples demonstrate higher hydrogen and nitrogen content at all phenol red loadings. This observation is ascribed to the presence of ethylenediamine in the solid PSP-ED/ZIF-8 powders. Moreover, at 5 mg/ml phenol red, PSP-ED/ZIF-8 demonstrates a larger sulfur content. However, with increased phenol red loadings, PSP/ZIF-8 exhibits a larger sulfur content than PSP-ED/ZIF-8.

Table 4.11 CHNS elemental composition for PSP/ZIF-8 samples.

Sample	C%	H%	N%	S%
PSP-ED/ZIF-8 (0 mg/ml PSP)	41.93	4.43	24.67	0
PSP/ZIF-8 (5 mg/ml PSP)	42.56	4.75	22.92	0.14
PSP/ZIF-8 (10 mg/ml PSP)	42.96	4.44	22.43	0.85
PSP/ZIF-8 (20 mg/ml PSP)	43.45	4.53	21.84	1.24

Table 4.12 CHNS elemental composition for PSP-ED/ZIF-8 samples.

Sample	C%	H%	N%	S%
PSP-ED/ZIF-8 (0 mg/ml PSP)	38.46	5.18	23.99	0
PSP-ED/ZIF-8 (5 mg/ml PSP)	40.65	5.14	23.68	0.19
PSP-ED/ZIF-8 (10 mg/ml PSP)	40.68	5.15	23.19	0.74
PSP-ED/ZIF-8 (20 mg/ml PSP)	41.84	4.99	22.56	0.95

To acquire a quantitative grasp of how these values (with and without ethylenediamine) compare, two trials are collected for PSP/ZIF-8 at 10 mg/ml phenol red loading. These results are shown in **Table 4.13**.

Table 4.13 CHNS elemental composition of PSP/ZIF-8 (10 mg/ml phenol red) for two trials.

Trial	C%	H%	N%	S%
1	42.96	4.44	22.43	0.85
2	42.81	4.74	22.32	0.77

As observed in **Table 4.13**, the average sulfur content (associated solely with adsorbed phenol red) is 0.81 ± 0.6%. This value, as well as the 0.77% sulfur content reported from Trial 2, are not substantially larger than the sulfur content reported for PSP-ED/ZIF-8 at 10 mg/ml phenol red. In addition, the co-adsorption of ethylenediamine in the PSP-ED/ZIF-8 samples could result in a smaller sulfur content (and apparent smaller loading of phenol red). To best address this hypothesis, PSP-ED/ZIF-8 powders should be set in a controlled, heated environment to volatilize the ethylenediamine molecules (while leaving the phenol red molecules unperturbed). Once the loss of ethylenediamine is confirmed via FTIR spectra, another CHNS elemental analysis can be completed for the PSP-ED/ZIF-8 samples. Here, it could be possible that ethylenediamine (i) functions as a "chaperone" molecule that enhances phenol red adsorption to ZIF-8 or (ii) inhibits phenol red adsorption through modulation of relevant van der Waals and electrostatic interactions [197].

In the preparation of both PSP/ZIF-8 and PSP-ED/ZIF-8 powders, an 80 mg of ZIF-8 are used per 1 ml of colorimetric solvent. In using **Equation 4.1**, an equilibrium adsorption of phenol red onto ZIF-8, q_E (mg phenol red/g ZIF-8) can be determined at 5, 10, and 20 mg/ml phenol red (assuming that all the dye is adsorbed onto the MOF such that C_E is 0 mg/ml). Through this calculation, the maximum sulfur content, S_{MAX}, can be determined as a function of initial concentration, C_0. The determination of S_{MAX} is illustrated by **Equation 4.4** [197].

$$S_{MAX} = \frac{\frac{C_{o,PSP}}{C_{ZIF-8}} m_{ZIF-8} \frac{1\ g\ PSP}{1000\ mg\ PSP} \left(\frac{1}{\boldsymbol{M_{PSP}}}\right) \frac{1\ mol\ S}{1\ mol\ PSP} \boldsymbol{M_S}}{m_{ZIF-8} + \frac{C_{o,PSP}}{C_{ZIF-8}} m_{ZIF-8} \frac{1\ g\ PSP}{1000\ mg\ PSP}} \times 100\% \qquad \textbf{(Eq. 4.4)}$$

Where:
S_{MAX} is the maximum sulfur content (%),
$C_{0,PSP}$ is the initial concentration of phenol red (mg dye/ml solvent),
C_{ZIF-8} is the concentration of ZIF-8 (g ZIF-8/ml dye-loaded solvent),
m_{ZIF-8} is the mass of ZIF-8 (g),
M_{PSP} is the molar mass of phenol red (g/mol),
and M_S is the molar mass of sulfur (g/mol).

Using **Equation 4.4** and assuming 1 g of ZIF-8, S_{MAX} values are computed and plotted (as a function of initial phenol red loading)—along with the sulfur composition measured for PSP/ZIF-8 and PSP-ED/ZIF-8—in **Figure 4.41**. Assuming that ZIF-8 completely adsorbs phenol red, the S_{MAX} values reported are 0, 0.53, 1, and 1.81% for 0, 5, 10, and 20 mg/ml phenol red blended with

ZIF-8, respectively. As observed from **Figure 4.41**, each sulfur composition experimentally determined for the PSP/ZIF-8 and PSP-ED/ZIF-8 are below S_{MAX} and reasonable for the concentration of ZIF-8 adsorbent used.

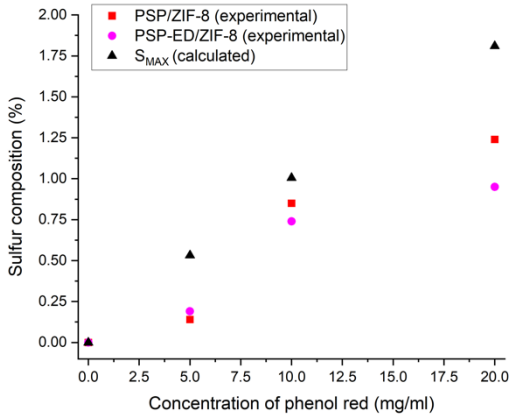

Fig. 4.41. Sulfur composition (%) as a function of the concentration of phenol red (mg/ml). PSP/ZIF-8 (red). PSP-ED/ZIF-8 (magenta). S_{MAX} (black).

Up to this subsection, the role of ethylenediamine on phenol red adsorption onto ZIF-8 has been assessed through PXRD pattern collection, SEM collection, FTIR spectral analysis, colorimetric imaging analysis, UV-Vis diffuse reflectance spectral analysis, BET surface area characterization, and CHNS elemental analysis. In Chapter 4.4.1, other spectroscopic techniques for probing the role of ethylenediamine on phenol red/ZIF-8 adsorption will be discussed. Similarly, the role of ethylenediamine on the colorimetric gas response (in dry atmosphere) in the first- and second-generation sensors has primarily been evaluated through colorimetric imaging and UV-Vis diffuse reflectance spectroscopic analysis. In the final subsection of Chapter 4.3, gas-dosed FTIR spectroscopic techniques will be used to differentiate how CO_2 is adsorbed by pristine ZIF-8 and ethylenediamine-loaded ZIF-8 to better illustrate the color change sensing dynamics.

4.3.13 Gas-dosed Fourier transform infrared (FTIR) spectra: elucidating ZIF-8-CO_2 physisorptive and ethylenediamine-CO_2 chemisorptive interactions

In this subsection, the physisorptive interactions between ZIF-8 and CO_2 and the chemisorptive interactions between ethylenediamine-bound ZIF-8 and CO_2 are established. Here, possible shifts of IR-active modes in ZIF-8 associated with the linker, as well as novel peak emergences upon exposure to dry CO_2, are used to determine the formation of reaction products characteristic of the proposed zwitterion mechanism [99, 123].

Gas-dosed FTIR spectroscopic measurements are performed to evaluate CO_2 adsorption onto ZIF-8 (with and without ethylenediamine). For these experiments, 100% CO_2 (1,000,000 ppm) is drawn from a food grade Airgas cylinder (20-lb aluminum) at 10 psi and directed into a Bruker Vertex80 FTIR spectrometer. A controlled gas atmosphere is achieved through use of a glove bag

taped down to the spectrometer. FTIR absorbance measurements are recorded as a function of wavenumber (4000 to 400 cm^{-1}). **Figure 4.42** shows the gas dosing FTIR spectrometer arrangement.

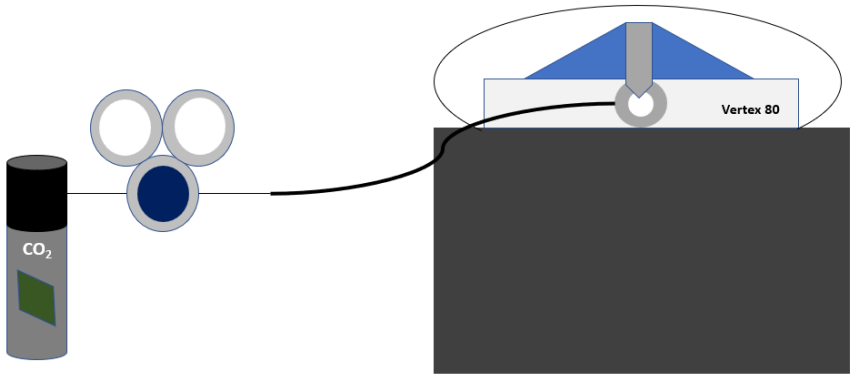

Fig. 4.42. Gas delivery of pure CO_2 into the Bruker Vertex80 FTIR spectrometer. ZIF-8-based samples (shown as a white circle) are exposed to pure CO_2 (contained within a glove bag).

Figure 4.43 depicts FTIR absorbance spectra for pristine ZIF-8 exposed to pure CO_2 over 12-min for select wavenumber ranges. As observed, the 421 cm^{-1} IR active mode (Zn-N stretch), 1147 cm^{-1} IR active mode (=C-H in plane deformation), 1179 cm^{-1} IR active mode (=C-H in plane deformation), 1311 cm^{-1} IR active mode (CH_2 wagging), 1384 cm^{-1} IR active mode (CH_3 antisymmetric bend), 1427 cm^{-1} IR active mode (CH_2 antisymmetric bend), 1584 cm^{-1} IR active mode (C=N stretch), 2931 cm^{-1} IR active mode (aliphatic C-H stretch), and 3136 cm^{-1} IR active mode (aromatic C-H stretch) do not exhibit a major shift upon prolonged exposure to CO_2 at 1-min, 3-min, 5-min, 7-min, 10-min, and 12-min [204].

Figure 4.44, however, shows FTIR absorbance spectra for pristine ZIF-8 exposed to pure CO_2 over 12-min for 2500 to 2200 cm^{-1}. The IR-active mode at 2348.2 cm^{-1} is associated with the C=O asymmetric stretch in the gaseous state [211]. The IR-active modes emerging at 2360.7 cm^{-1} and 2341.5 cm^{-1}, respectively, are associated with CO_2 molecules adsorbed to ZIF-8 [211]. The emergence of similar IR-active modes within the C=O asymmetric stretch region (2300 to 2400 cm^{-1}) has been observed in other literature, such as with the MOF, JUK-8 [211]. Moreover, as time progresses from 3-min to 12-min, the IR-active mode at 2341.5 cm^{-1} experiences a red shift to 2337.6 cm^{-1}, which is attributed to CO_2 adsorption to the pristine ZIF-8. While not immensely obvious from the gas-exposed measurements shown here, FTIR measurements collected under high pressure (~ 1 GPa) have described the "interaction between CO_2 and [ZIF-8] on the specific site of the imidazole ring," such as the C=C stretching mode of the ZIF-8 linker [194].

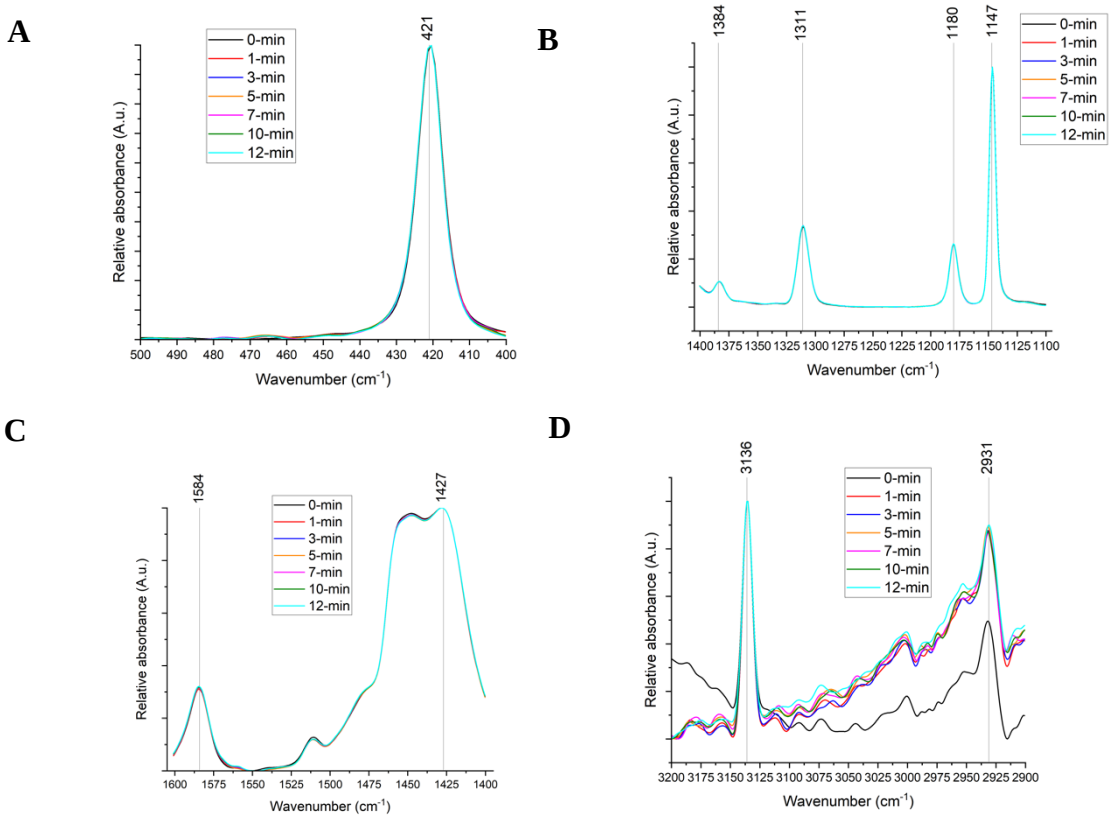

Fig. 4.43. Normalized Absorbance (A.u.) vs. wavenumber (cm^{-1}) for pristine ZIF-8 exposed to CO_2. Range: **(A)** 500 to 400 cm^{-1}; **(B)** 1400 to 1100 cm^{-1}; **(C)** 1600 to 1400 cm^{-1}; and **(D)** 3200 to 2900 cm^{-1}. 0-min: black. 1-min: red. 3-min: blue. 5-min: orange. 7-min: magenta. 10-min: olive. 12-min: cyan

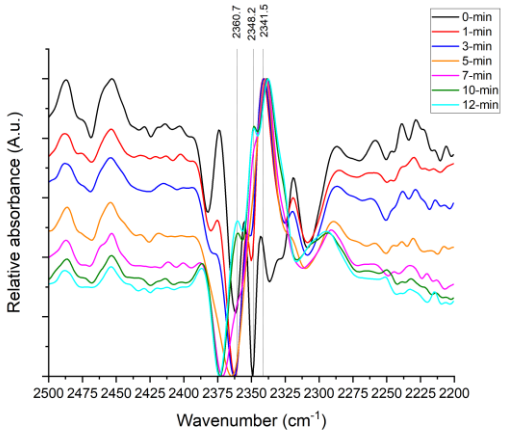

Fig. 4.44. Normalized Absorbance (A.u.) vs. wavenumber (cm^{-1}) for pristine ZIF-8 exposed to CO_2. Range: 2500 to 2200 cm^{-1}. 0-min: black. 1-min: red. 3-min: blue. 5-min: orange. 7-min: magenta. 10-min: olive. 12-min: cyan.

FTIR absorbance spectra for ethylenediamine-loaded samples are collected to determine chemisorptive CO_2 interactions associated with the zwitterion mechanism and the underlying colorimetric sensing dynamics [99, 123, 140-145]. As illustrated in prior literature, ethylenediamine can both react with CO_2 to produce the zwitterion and function as a deprotonating base [140-145, 203]. To distinguish protonated amine species from carbamates and other reaction products [140-145], FTIR absorbance spectra are collected for ethylenediamine in different pH environments. Glacial acetic acid is used to reduce the pH of ethylenediamine. Specifically, a 50%, %v/v, acetic acid solution is developed in methanol. Then, a second solution is made, which is 5% ethylenediamine (%v/v) and 95% (%v/v) of the glacial acetic acid methanolic solution. FTIR absorbance spectra for relevant solutions are shown in **Figure 4.45**.

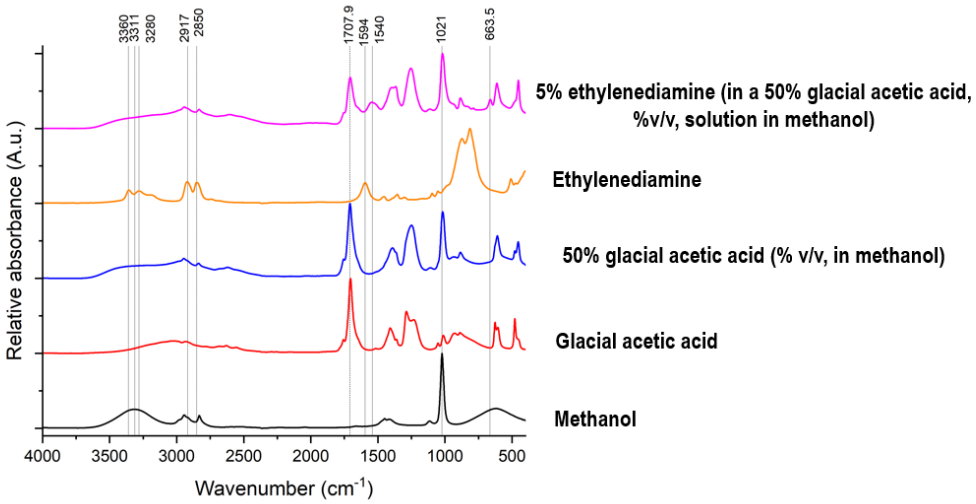

Fig. 4.45. Relative absorbance (A.u.) versus wavenumber (cm^{-1}) data for methanol (black), glacial acetic acid (red), 50% glacial acetic acid (blue), ethylenediamine (orange), and a 5% ethylenediamine solution (blended with acetic acid and methanol)- (magenta).

Multiple IR-active modes are identified. For methanol, 3311 cm^{-1} and 1021 cm^{-1} IR-active modes are associated with O-H stretching and C-O stretching, respectively [210]. The 1707.9 cm^{-1} IR-active mode is associated with the C=O stretch in glacial acetic acid [210]. Several IR-active modes are identified for ethylenediamine: N-H bend (1594 cm^{-1}), 2850 cm^{-1} (C-H stretch), 2917 cm^{-1} (C-H stretch), 3280 cm^{-1} (N-H stretch), and 3360 cm^{-1} (N-H stretch) [123, 210]. When blended with acetic acid and methanol, ethylenediamine shows two additional IR-active modes: 663.5 cm^{-1} (N-H wagging) [187] and 1540 cm^{-1} (N-H bend) [210].

Figure 4.46 displays the FTIR absorbance spectra for ethylenediamine-loaded ZIF-8 (ED/ZIF-8) at 5%, %v/v, ethylenediamine in methanol. As observed with pristine ZIF-8, no significant shift is observed with the 419 cm^{-1} IR-active mode associated with the Zn-N coordination bond as pure CO_2 is applied for 7-min [204]. With prolonged gas exposure, a broad absorbance peak at ~675 cm^{-1} appears, which could be attributed to -NH_2 wagging [187]. IR-active peaks also appear at

1223 cm^{-1} and 1285.5 cm^{-1}, which are associated with C-N stretching from carbamate formation [212]. An N-COO^- (carbamate) stretch is identified at 1327 cm^{-1} [212]. Similarly, an IR-active mode appears at 1351 cm^{-1} with prolonged CO_2 exposure, which is in a similar position as what has been located in prior literature [213]. With prolonged gas exposure, an N-H bend (associated with protonated ethylenediamine) appears at 1562 cm^{-1} [214]. The 1457 cm^{-1} IR-active mode associated with the C=C stretch of the imidazolate linker [204] shifts to lower wavenumber with time, possibly indicating where CO_2 may be adsorbing on the ethylenediamine-bound ZIF-8. In addition to a shoulder at 2326 cm^{-1}, IR-active modes at 2350 and 2361 cm^{-1} appear in the presence of CO_2, located in similar positions to the spectra collected for pristine ZIF-8. Finally, the N-H stretch of the ethylenediamine (at 3350 cm^{-1}) progressively vanishes with prolonged exposure to CO_2, which could be indicative of zwitterionic carbamate formation [213].

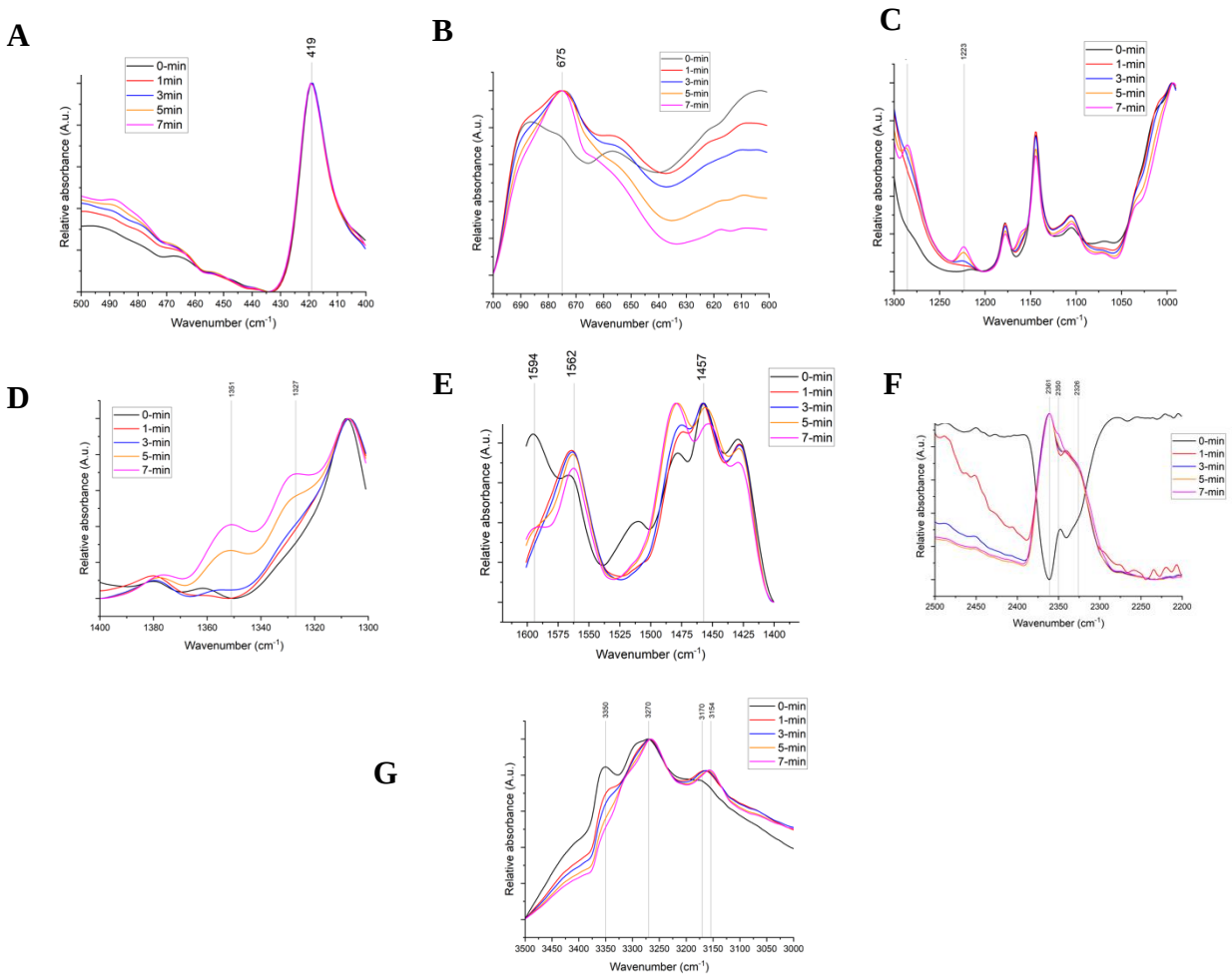

Fig. 4.46. FTIR absorbance spectra for ED/ZIF-8 (5% ED) exposed to pure CO_2 (10 psi). **(A)** 500 to 400 cm^{-1}; **(B)** 700 to 600 cm^{-1}; **(C)** 1300 to 990 cm^{-1}; **(D)** 1400 to 1300 cm^{-1}; **(E)** 1600 to 1400 cm^{-1}; **(F)** 2500 to 2200 cm^{-1}; and **(G)** 3500 to 3000 cm^{-1}. Measurements are taken at 0-min (black), 1-min (red), 3-min (blue), 5-min (orange), and 7-min (magenta).

FTIR absorbance spectra are also collected at higher ethylenediamine loadings (10% and 15% ethylenediamine, %v/v, in methanol). These FTIR absorbance spectra are shown in **Figure 4.47**. In both ED/ZIF-8 (10%) and ED/ZIF-8 (15%), IR-active modes at 668 and 669.2 cm^{-1}, respectively, are assigned to O=C=O bending [215]. Emergent absorbance peaks near 680 cm^{-1} are attributed to -NH_2 wagging [187]. Similar red shifts are observed between 1300 and 1400 cm^{-1}: ED/ZIF-8 (10%) transitions from 1381 to 1379 cm^{-1} and from 1308 to 1305 cm^{-1} while ED/ZIF-8 (15%) transitions from 1382 to 1379 cm^{-1} and from 1310 to 1306 cm^{-1}. However, neither material exhibits the 1327 cm^{-1} N-COO^- carbamate IR-active mode shown in ED/ZIF-8 (5%) [212]. Relative to the large loss of the 3350 cm^{-1} N-H stretch observed in ED/ZIF-8 (5%), neither ED/ZIF-8 (10%) nor ED/ZIF-8 (15%) demonstrates such a loss with under 10-min of pure CO_2 exposure. As mentioned in Chapter 2, highly-concentrated aqueous amine solutions have been associated with a "termolecular-kinetic model" through laminar jet absorber experiments [162], which determined an order of reaction that "ranged from 1.2 to 1.5 within the temperature range 293– 333 K." However, at lower aqueous amine loadings, previous literature has reported first order reaction kinetics [162]. Here, the apparent difference in FTIR absorbance spectral behavior from ED/ZIF-8 (5%) versus ED/ZIF-8 (10%) and ED/ZIF-8 (15%) is associated with a probable change of reaction order (with respect to the ethylenediamine), which also results in the differences in the color change obtained through colorimetric imaging and *in-situ* UV-Vis diffuse reflectance spectroscopic analysis [162].

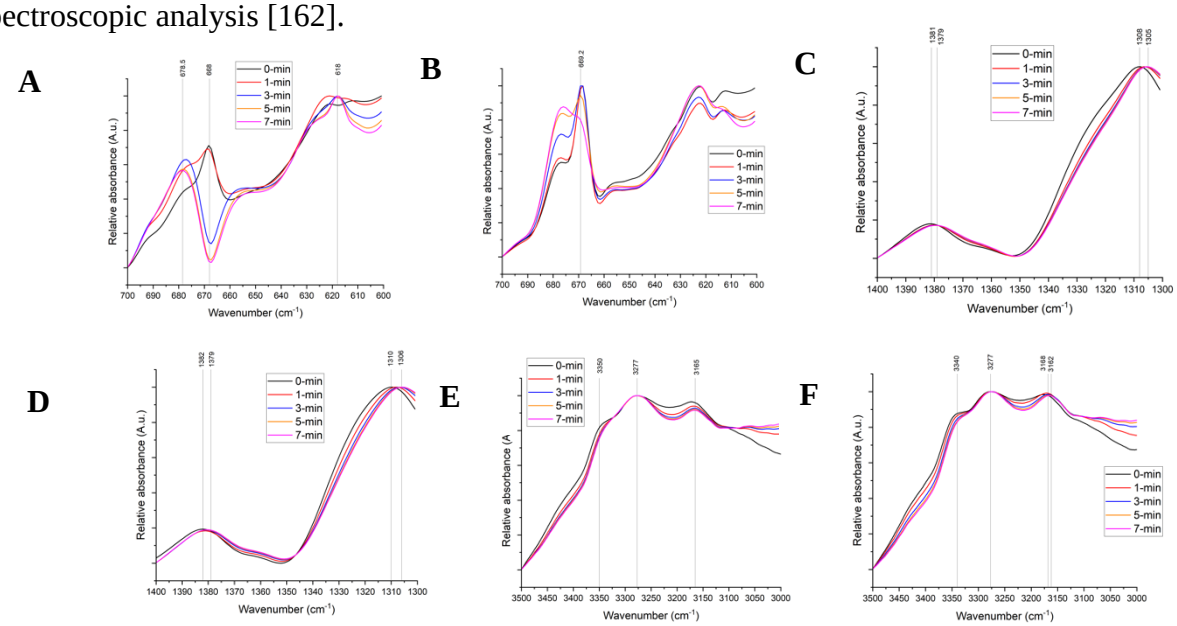

Fig. 4.47. FTIR absorbance spectra for ED/ZIF-8 (10% ED and 15% ED) exposed to pure CO_2 (10 psi). **(A)** (10% ED) 700 to 600 cm^{-1}; **(B)** (15% ED) 700 to 600 cm^{-1}; **(C)** (10% ED) 1400 to 1300 cm^{-1}; **(D)** (15% ED) 1400 to 1300 cm^{-1}; **(E)** (10% ED) 3500 to 3000 cm^{-1}; **(F)** (15% ED) 3500 to 3000 cm^{-1}. Measurements are taken at 0-min (black), 1-min (red), 3-min (blue), 5-min (orange), and 7-min (magenta).

Figure 4.48 shows FTIR absorbance spectra for PSP-ED/ZIF-8 (5 mg/ml phenol red; 5% ED) exposed to pure CO_2 (0-min, 7-min, and 10-min). Upon prolonged gas exposure, the N-H stretch (3350 cm^{-1}) shifts. The peak at 676 cm^{-1} is assigned to -NH_2 wagging [187]. However, the 613 cm^{-1} IR-active mode ascribed to phenol red does not appear to substantially change upon exposure to dry CO_2. Therefore, the proposed formation of a protonated phenol red species is not well defined from these studies.

In the subsequent and final subsection of this chapter, advanced techniques for analyzing dye/MOF and amine/MOF interactive chemistries toward colorimetric indoor gas sensing will be discussed.

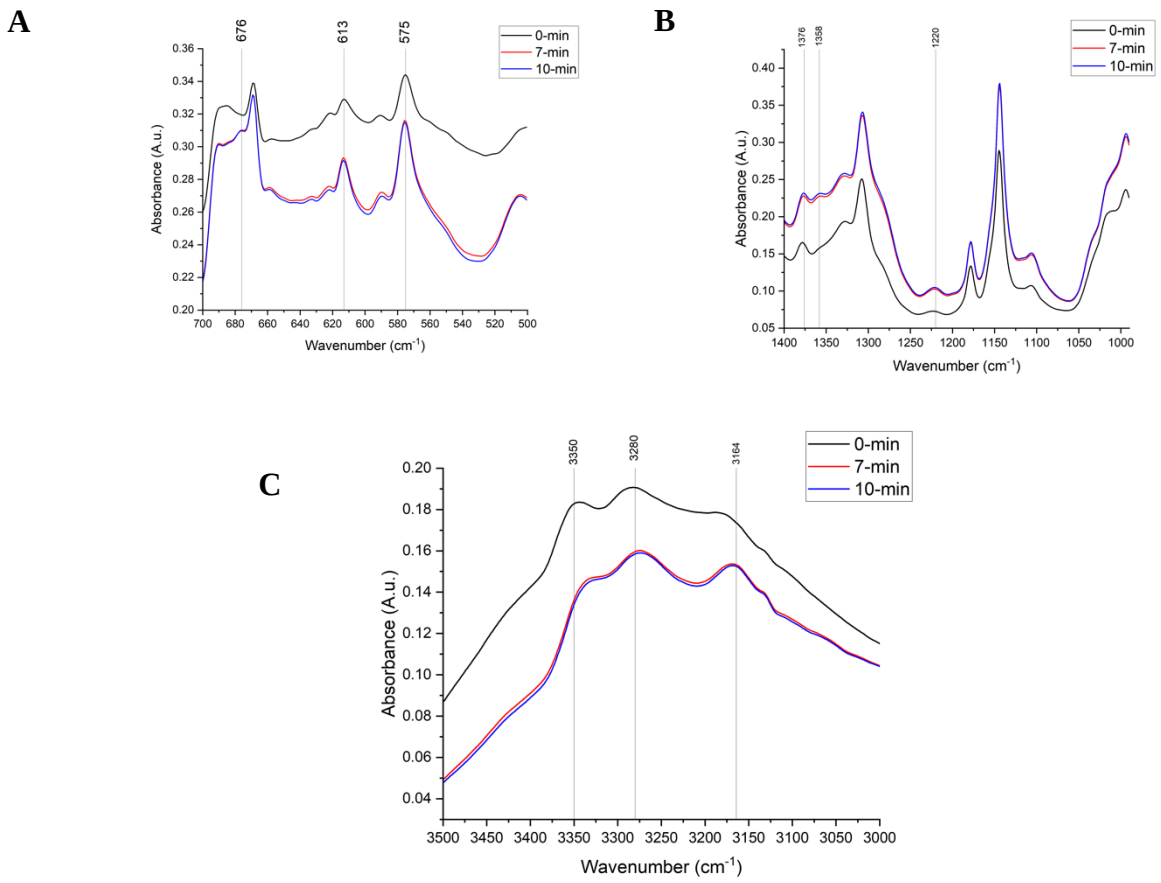

Fig. 4.48. FTIR absorbance spectra for PSP-ED/ZIF-8 (5 mg/ml PSP and 5% ED) exposed to pure CO_2 (10 psi). **(A)** 700 to 500 cm^{-1}; **(B)** 1400 to 1000 cm^{-1}; and **(C)** 3500 to 3000 cm^{-1}. Measurements are taken at 0-min (black), 7-min (red), and 10-min (blue).

4.4 Advanced spectroscopic techniques for analyzing MOF/dye/amine interactive chemistries

This subsection illustrates additional techniques that can be implemented toward a comprehensive analysis of dye and amine adsorption onto MOFs toward colorimetric analyte monitoring. Though phenol red and ethylenediamine adsorption has been characterized by PXRD pattern collection, SEM imaging analysis, FTIR spectra, UV-Vis spectra, colorimetric imaging and RGB distribution analysis, BET surface area characterization, and CHNS elemental analysis, more rigorous techniques can be employed to elucidate the thermodynamics of colorimetric ingredient adsorption onto MOFs. Nonlinear optical methods and X-ray photoelectron spectroscopy, then, will be established as essential techniques for optimal colorimetric gas sensing.

4.4.1 Second-harmonic spectroscopy for ascertaining dye-MOF adsorption thermodynamics

Nonlinear optical processes involve "the modification of the optical properties of a material system by the presence of light" in which "the response of a material system to an applied optical field depends in a nonlinear manner on the strength of the optical field" [216]. **Equation 4.5** describes the induced polarization (or dipole moment per unit volume), P(t), "of a material system depends on the strength *E*(t) of an applied optical field," representing the electric field strength *E*(t) as a power series [216].

$$P(t) = \epsilon_0\left[\chi^{(1)}E(t) + \chi^{(2)}E^2(t) + \chi^{(3)}E^3(t) + \cdots\right]$$

$$\equiv P^{(1)}(t) + P^{(2)}(t) + P^{(3)}(t) + \cdots \qquad \textbf{(Eq. 4.5)}$$

Where: ϵ_0 is the permittivity of free space, $\chi^{(1)}$ is the "constant of proportionality" linear susceptibility, $\chi^{(2)}$ is the second-order nonlinear optical susceptibility, $\chi^{(3)}$ is the third-order nonlinear optical susceptibility, $P^{(2)}(t)$ is the second-order nonlinear polarization, and $P^{(3)}(t)$ is the third-order nonlinear polarization [216].

Second harmonic generation (SHG) is a nonlinear optical process in which two photons with equal frequency, **ω**, interact with a medium and produce a photon of double energy, 2 ω, such that the second-order nonlinear susceptibility, $\chi^{(2)}$, is nonzero [216]. Spectroscopic applications of this nonlinear process have rigorously attended to the properties of interfaces, including "liquid/ gas, solid/gas, and the buried liquid/liquid, liquid/solid, and solid/solid interfaces" [217]. There is a general assumption that SHG processes are "forbidden" in centrosymmetric systems due to symmetry; namely, "for every molecule oriented in one direction, there is a neighboring one oriented in the opposite direction" such that the "nonlinear polarizations induced in these oppositely oriented molecules by the incident light are of opposite phase with respect to each other and thus cancel" and "the net second-order polarization is zero" [217]. However, "fluctuations in molecular density and molecular orientation in isotropic bulk solutions can disrupt the phase cancellation" [217]. In addition, SHG processes can occur from "individual large noncentrosymmetric entities in bulk solution" [217].

Nonlinear scattering techniques, such as second harmonic scattering (SHS), can be used to acquire interfacial insights about the "surface chemistry of particles in liquids" [218]. Second harmonic techniques have been used to determine information about dye adsorption to select adsorbents, such as cationic malachite green adsorption onto polystyrene sulfate (PSS) microspheres [217]. Here, the total second harmonic signal, $I_{2\omega}^{total}$, is represented by **Equation 4.6** [217]

$$I_{2\omega}^{total} = \sum_{j=1}^{n} \sum_{k=1}^{n} E_j^{2\omega} E_k^{2\omega} e^{i(\phi_j - \phi_k)} \quad \textbf{(Eq. 4.6)}$$

Where: $I_{2\omega}^{total}$ is the total second harmonic signal, "$E_j^{2\omega}$ is the second harmonic electric field generated by the *j*th… microsphere and φ_j is the phase of the second harmonic electric field generated by sphere j" [217].

When the density of adsorbent species (here, microspheres), n, is low, "the SHG from each microsphere is independent of other spheres, and their phases are random" such that *j*=*k* and **Equation 4.6** simplifies to **Equation 4.7** [217].

$$I_{2\omega}^{total} = n(E^{2\omega})^2 = nI_{2\omega} \quad \textbf{(Eq. 4.7)}$$

Where: $I_{2\omega}$ is the second harmonic intensity from a single adsorbent (or microsphere) [217].

Equation 4.7 enables the investigation of the energetics informing the transport "molecules from the bulk of a solution to an interface"—specifically, dye molecules in an aqueous (or nonaqueous solution) to the particle/solution interface [217]. The equilibrium achieved between dye molecules at in the bulk liquid and adsorbed to the particle interface can be approximated through the Langmuir adsorption model, which assumes a planar surface in which the adsorption of dye species, D, to unoccupied sites, S, on the particle is described by **Equation 4.8** [200, 217].

$$D + S \underset{k_{-1}}{\overset{k_1}{\Longleftrightarrow}} DS \quad \textbf{(Eq. 4.8)}$$

Where: k_1 is the forward reaction rate constant and k_{-1} is the reverse reaction rate constant.

Using **Equation 4.8**, a reaction equilibrium constant, K, and Gibbs free energy of adsorption, ΔG_{ADS}, for dye adsorption to the particles can be determined as **Equation 4.9** [217].

$$K = e^{-\frac{\Delta G_{ADS}}{RT}} = \frac{k_1}{k_{-1}} = \frac{[DS]}{[D][S]} \quad \textbf{(Eq. 4.9)}$$

Where: [DS] is the concentration of adsorbed sites, [D] is the concentration of bulk dye molecules, and [S] is the concentration of empty surface sites [200, 217].

The relative second harmonic scattering intensity saturates with dye concentration according to the modified Langmuirian model expressed in **Equation 4.10** [200, 217].

$$\theta_D = \frac{N}{N_{MAX}} = \frac{\left[\left(C_D + N_{MAX} + \frac{55.5}{K}\right) - \left(\left(C_D + N_{MAX} + \frac{55.5}{K}\right)^2 - 4C_D N_{MAX}\right)^{0.5}\right]}{2N_{MAX}} \quad \textbf{(Eq. 4.10)}$$

Where: θ_D is the fractional coverage of dye molecules on the particles, N is the number of adsorbed dye molecules per liter, C_D is the total concentration of the dye molecule, N_{MAX} is the maximum surface number density of dye molecules, K is the adsorption equilibrium constant, and 55.5 is the molarity of water [200, 217].

In using **Equation 4.8** and **Equation 4.9**, the Gibbs free energy of adsorption and number of adsorption sites can be determined with respect to dye molecules and select adsorbents [200, 217]. In terms of the future of this work, second harmonic spectroscopic techniques will be vital toward the clear elucidation of the adsorption dynamics between select MOF adsorbents and halochromic compounds used for color-based indoor analyte monitoring. Given that basic primary amine species (such as ethylenediamine) change the structure of adsorbed dyes (such as phenol red) on MOFs (such as ZIF-8), differences in the Gibbs free energy of adsorption of dyes to MOFs in variable pH must be determined. Through such measurements, an appropriate assessment of the influence of specific intermolecular forces can be conducted. For example, previous research demonstrated that the adsorption of malachite green to negatively charged, neutral, and positively charged polystyrene microspheres largely involved non-Coloumbic interactions between malachite green and polystyrene microspheres, such as van der Waals forces [217]. Similar studies should be conducted involving ZIF-8 and phenol red across a controlled pH range so as to (i) achieve phenol red in neutral and anionic states [117-118] and (ii) maintain the structural integrity of ZIF-8 in solvent environment [99, 134]. For these studies, **Equation 4.10** should also be modified such that the molarity of methanol, the characteristic solvent for all the zwitterionic colorimetric gas studies in this dissertation, is accounted for in the determination of the adsorption thermodynamics [200, 217]. Such studies, when complemented by other quantitative techniques such as the CHNS elemental composition data reported in **Table 4.11** and **Table 4.12**, will produce important knowledge about how dyes bind to MOFs for gas sensing.

As second harmonic spectroscopic experiments continue to be troubleshooted for the system in UC Berkeley College of Chemistry—involving important steps such as identifying appropriate ZIF-8 concentrations to satisfy **Equation 4.7**, targeting phenol red concentrations such that **Equation 4.9** and **Equation 4.10** can provide useful thermodynamic adsorption data, and determining how ethylenediamine species modify dye/MOF adsorption thermodynamics through observed differences in second harmonic scattering in nonaqueous media—there remains optimism about potential applications for more complicated, color-based sensing systems.

4.4.2 X-ray photoelectron spectroscopy (XPS): identifying phenol red residence with respect to the porous ZIF-8 adsorbent

X-ray photoelectron spectroscopy (XPS) is an analytical technique "based on energy analysis of secondary electrons that are emitted as a result of excitation by photons" [219]. When X-rays "interact with the electrons in the atomic shell and photoelectrons… are generated," some

"electrons move through the solid to the surface and are subject to various scattering processes," and then "electrons reaching the surface are emitted in the vacuum (after surmounting the work function threshold)" [219]. The kinetic energy, E_K, of a photoelectron is measured from the difference between an X-ray of energy, *hv*, and the binding energy of a core electron level, E_B, and the work function of the analyzer, Φ_A (as shown in **Equation 4.11**) [219].

$$E_K = hv - E_B - \Phi_A \qquad \textbf{(Eq. 4.11)}$$

The main instrumentation for XPS chemical analysis involves a vacuum system, "the specimen on a sample holder with *x*-*y*-*z* movement stage," an "excitation source," and "the electron energy analyzer with detector" [219]. There are "basic pressure requirements" for the vacuum system, which include the prevention of "electron scattering on gas molecules in the path from the sample to the analyzer" and the avoidance of "attenuation and distortion of the spectra by surface contamination" [219]. For the XPS experiments described in this chapter, *ultrahigh vacuum (UHV)* is used, which is 10^{-8} to 10^{-11} Torr [219]. Synchrotron radiation is incorporated as the X-ray source, which accelerates electrons to emit radiation to generates a "high photon flux" that produces "high energy resolution" unachievable in conventional XPS measurements [219]. Moreover, synchrotron radiation allows for "tunable photon energy," which entails non-destructive *depth profiling* for the assessment of chemical variations between surface and bulk regions [219]. The electron energy analyzer (with detector) can operate "like band-pass filters," or "open a window for only a small energy band around a given energy" [219].

XPS spectra are characteristically expressed in "intensity (counts per second) as a function of binding energy" [219], where the abscissa can also be converted to kinetic energy [219]. Changes "in the bonding state of an atom" induces changes in "the observed spectral characteristics" of the system under study, including binding energy and peak width and shape [219]. Chemical bonding involves such changes, where a "change of the binding energy" (known as a *chemical shift*) occurs with respect to differences in "the effective charge potential change on an atom" [219].

Previous literature has implemented changes in excitation energy (or *depth profiling*) to characterize aqueous CO_2-amine systems [203]. Lewis et al. [203] conducted "soft X-ray photoelectron spectroscopy… measurements from a vacuum liquid microjet of aqueous solutions of pure [monoethanolamine]… and CO_2-treated [monoethanolamine]" to "better understand the CO_2–amine solution interactions at the molecular level" [203]. Through probing C 1s and N 1s spectra (at the surface and in the bulk), Lewis et al. determined that "neutral [monoethanolamine] exhibits a relatively enhanced concentration at the surface of the aqueous solution, whereas the production of the reaction of [monoethanolamine] with CO_2, carbamate and carbamic acid, show a preference for the bulk solution" [203]. Such findings were critical toward understanding "the behavior of CO_2 at the liquid/vapor interface," which inform important advancements in CO_2 capture (and other carbon-based system scientific investigation) [203].

As mentioned from discussion of the CHNS elemental analysis data shown for PSP/ZIF-8 and PSP:ZIF-8 in **Table 4.4** and **Table 4.5**, respectively, the amount of phenol red adsorbed to ZIF-8

appears to be quite similar (below 5 mg/ml phenol red). Thus, the large differences in the observed color change in the presence of CO_2 is not concluded to be due to how much phenol red is loaded. Instead, the differences in the magnitude of the color change achieved between PSP-ED/ZIF-8 and ED/PSP:ZIF-8 upon exposure to the same levels of indoor CO_2 is ascribed to where phenol red adsorbs to ZIF-8: phenol red is suspected to bind to the external surface area in PSP-ED/ZIF-8 and to the internal pores (within the 11.6 Å pore cage) in ED/PSP:ZIF-8 [123]. While colorimetric gas exposure and UV-Vis spectroscopic analysis on washed sensors [123], as well as BET surface area characterization and CHNS elemental composition data, support this hypothesis, spectral comparisons from XPS investigation can provide more conclusive assessments of where phenol red is located on ZIF-8 toward elucidation of the colorimetric gas sensing mechanism.

With use of synchrotron radiation, depth dependence studies can be conducted such that elemental spectra can be evaluated as a function of excitation energy [203. 219]. Here, the relevant samples are (i) Pristine ZIF-8, (ii) PSP/ZIF-8, and (iii) PSP:ZIF-8. For ZIF-8, the following spectra are selected: Zn 3s, C 1s, N 1s, and O 1s. For phenol red, the following spectra are expected: S 2p, C 1s, and O 1s. For phenol red-adsorbed ZIF-8 samples, the following spectra are selected: Zn 3s, S 2p, C 1s, N 1s, and O 1s.

In collecting the XPS data for the three samples, spectra are plotted in Intensity (in counts per second, cps) versus Kinetic Energy (in eV). Through the rearrangement of **Equation 4.11** (subtracting the kinetic energy from the excitation energy), the binding energy, BE, can be determined for each element [219]. In fitting the spectral peaks, binding energy positions for Zn 3s, S 2p, N 1s, C 1s, and O 1s should be consistent with values from literature [220-230]. In systems (such as ZnO), Zn 3s binding energy peaks appear between 139 and 140 eV [220]. Previous research has associated binding energies between 167 and 169 eV with the S $2p^{3/2}$ and S $2p^{1/2}$ elemental spectra of phenol red [221-222]. For ZIF-8, C 1s elemental spectra binding energies associated with the C-C and C-N bonds of the imidazolate linker exist between 283 and 286 eV [223-226, 228-230], as well as adventitious (or spurious) carbon [228]. In addition, N 1s elemental spectra attributed to the nitrogen species of the imidazolate linker (namely, the C-N bond) are identified ~399 eV [225-230]. O 1s spectra (in ZIF-8) have been associated with -OH species at 532-533 eV [228,230] and Zn-O species at 530.66 eV [230]. For polymer phenol red, O 1s spectra with a binding energy peak at 531.7 eV are associated with the -C=O bond [221].

Several outcomes can be expected from the depth dependence XPS measurements. At lower excitation energy, the intensities associated with PSP/ZIF-8 could be larger than those from PSP:ZIF-8; however, with increased excitation energy (i.e., depth into the surface of the sample), the S 2p peak intensities associated with PSP:ZIF-8 could significantly increase. These results could imply phenol red adsorption onto the external surface of ZIF-8 (for PSP/ZIF-8) and to the internal pores of ZIF-8 (for PSP:ZIF-8), thus confirming the hypothesis. In addition, changes in peak position of Zn 3s, C 1s, N1s, and O 1s spectra between the pristine ZIF-8 and phenol red-adsorbed samples could differentiate phenol red adsorption. In prior studies, the aqueous adsorption of malachite green (MG) on the "highly porous" MOF, MIL-100(Fe), resulted in "a shift to lower energy for the Fe 2p peak in MIL-100(Fe) (from 725.3 eV and 711.7 eV to 724.9 eV and 711.2 eV, respectively)," which was attributed to "the interaction between the Lewis base –

$N(CH3)_2$ in MG and the Lewis acid Fe sites of MIL-100(Fe)" and associated replacement of water molecules occupying the open metal sites of the MOF [231]. In a separate study, methylene blue (MB) adsorption onto MXene adsorbents resulted in a shift of the N 1s Mxene peak to lower binding energy, which was assigned "to the negative charge of MXene being strongly bonded to the positive charge of MB" and assessed as an electrostatic interaction between MXene and MB [232]. As observed in **Figure 4.23**, increasing concentrations of phenol red adsorbed onto ZIF-8 produced a shift in 1584 cm^{-1} C=N vibrational mode of ZIF-8 [123, 204]. Moreover, CHNS elemental composition data shown in **Table 4.4** and **Table 4.5** demonstrate obvious increases in the carbon content (% C) and decreases in the nitrogen content (% N) between pristine ZIF-8 and dye-adsorbed samples. Here, binding energy shifts in the C 1s and N 1s spectra could also inform which regions of the imidazolate linker of ZIF-8 interact with phenol red in the first- and second-generation sensors.

Full depth-dependence XPS analysis of colorimetric gas sensing mechanism involving the PSP-ED/ZIF-8 and ED/PSP:ZIF-8 (using synchrotron radiation) remain ongoing at Beamline 11.0.2 at the Advanced Light Source (ALS) of the Lawrence Berkeley National Laboratory (LBNL) in Berkeley, CA. As discussed in Chapter 6.2., liquid-jet XPS measurements (with depth dependence) will also be implemented in methanolic solvent to (i) elucidate the role of water as an interferent in the colorimetric gas sensing mechanism and (ii) establish the role of ZIF-8 as an effective adsorbent through studying gas/liquid interfaces (involving ethylenediamine and CO_2 in methanol) and gas/solid interfaces (involving ethylenediamine-functionalized ZIF-8 and CO_2 in methanol).

4.5 Summary

In this chapter, mechanistic information involving (i) differences between PSP-ED/ZIF-8 and ED/PSP:ZIF-8 and (ii) the role of ethylenediamine on colorimetric gas sensing and phenol red/ZIF-8 adsorption were elaborated. *In-situ* diffuse reflectance UV-Vis spectra revealed that while PSP-ED/ZIF-8 continues to exhibit a color change at 5 mg/ml phenol red loaded into the system, ED/PSP:ZIF-8 does not. PXRD, FTIR, and CHNS elemental composition measurements confirmed that ZIF-8 does not crystallize in a precursor broth loaded with more than 5 mg/ml phenol red, establishing an upper limit for the concentration of phenol red which can be directly incorporated into the MOF reaction broth toward colorimetric gas sensing. CHNS elemental analysis demonstrated that PSP/ZIF-8 and PSP:ZIF-8 possessed similar sulfur content (%S) at the same loadings of phenol red; these results implied that phenol red location on ZIF-8, not the amount of adsorbed phenol to the MOF surface, likely determined the large differences in the colorimetric gas response achieved in PSP-ED/ZIF-8 and ED/PSP:ZIF-8. Such observations motivated recommended XPS studies to determine differences in phenol red location on ZIF-8 between both sensors. In a related study, PXRD patterns confirmed the chemical stability of ZIF-8 in the presence of up to 20 mg/ml phenol red (in both pure methanol and ethylenediamine-loaded methanolic environment). Other conventional FTIR transmittance spectra revealed that phenol red likely adsorbs to select regions of the imidazolate ligand. Solution-phase UV-Vis absorbance spectra suggested that phenol red adsorption onto ZIF-8 (with and without ethylenediamine) is well represented through the Freundlich adsorption isotherm. Controlled heating of the PSP-

ED/ZIF-8 samples (so as to vaporize ethylenediamine molecules but preserve adsorbed phenol red molecules) was recommended to better understand the preliminary CHNS elemental composition data (in which samples with only phenol red exhibit a larger sulfur content at higher phenol red loadings). In addition, second harmonic spectroscopic measurements were recommended to better elucidate phenol red/ZIF-8 adsorption thermodynamics in both methanol and ethylenediamine-loaded methanol environments. Finally, gas-dosed FTIR absorbance spectra indicated the formation of protonated ethylenediamine and carbamate species upon exposure to pure CO_2. Differences in these FTIR absorbance spectra across various ethylenediamine loadings (5, 10, and 15%) were suspected to be from the emergence of termolecular kinetics associated with concentrated amine solutions [162]. These observations were situated beside separate *in-situ* diffuse reflectance UV-Vis spectra, which revealed suppression of the color change at higher ethylenediamine loadings.

In Chapter 5, a third-generation, ZIF-8-based colorimetric CO_2 sensor is briefly introduced and compared against the first-generation sensor, PSP-ED/ZIF-8, and the second-generation sensor, ED/PSP:ZIF-8.

4.6 Acknowledgements of co-authors for in-progress publishable work

Chapter 4 of this dissertation involves publishable work separated into two, possible manuscripts. For the first work, "Spectroscopic differentiation of dye- and amine-loaded metal-organic framework-based colorimetric gas sensors for indoor carbon dioxide detection," I would like to thank all the co-authors for their instrumental support, intellectual insights, and encouragement: Andreas Siebert, Isaac Zakaria, Mario Gotters, Erika Riffe, Elena Kreimer, Alireza Pourghaderi, Stuart McElhany, Yaprak Ozbakir, Chithra Asokan, Natalie Lefton, Branden Leonhardt, Matthew N. Dods, Tayler Hunter, Ishan Gupta, Carlo Carraro, Roya Maboudian, Bryan McCloskey, Markita Landry, and Monika Blum. For the second work, "Spectroscopic determination of the role of surface basicity on dye/metal-organic framework adsorption for colorimetric chemical species monitoring," I similarly extend my gratitude to all co-authors for their instrumental support, intellectual insights, and encouragement: Erika Riffe, Yaprak Ozbakir, Chithra Asokan, Alireza Pourghaderi, Stuart McElhany, Natalie Lefton, Branden Leonhardt, Elena Kreimer, Tayler Hunter, Ishan Gupta, Carlo Carraro, Roya Maboudian, Bryan McCloskey, Markita Landry, Richard Saykally, and Monika Blum.

This research used resources of the Advanced Light Source, which is a DOE Office of Science User Facility under contract no. DE-AC02-05CH11231. Special thanks are given to Dr. Monika Blum, Dr. Andreas Siebert, Isaac Zakaria, and Mario Gotters for collection of XPS spectra at Beamline 11.0.2. This chapter also acknowledges support in the form of a National Science Foundation Graduate Research Fellowship (NSF GRFP) and UC Dissertation-Year Fellowship. The authors also acknowledge the Lawrence-Berkeley National Laboratory Catalysis Facility and Dr. Chithra Asokan for assistance with FTIR measurements. Dr. Nick Settineri of the UCB CheXray facility is acknowledged for assistance with the collection of PXRD patterns. The authors also acknowledge the UC Berkeley College of Chemistry Microanalytical Facility and Dr. Elena Kreimer for the collection of CHNS elemental composition data. Work at the Molecular

Foundry was supported by the Office of Science, Office of Basic Energy Sciences, of the U.S. Department of Energy under Contract No. DE-AC02-05CH11231. Erika Riffe and the Saykally research group are greatly appreciated for fundamental knowledge and future applications of second harmonic spectroscopic techniques for color-based analyte detection. Additional funds from the UC Berkeley Department of Chemical & Biomolecular Engineering toward CHNS, BET, and PXRD measurements are also acknowledged.

Chapter 5: Mixed-Dye Colorimetric Gas Sensors for Robust Indoor Air Quality Monitoring

In this chapter, a third-generation colorimetric gas sensor constructed from the combination of phenol red-adsorbed and other dye-adsorbed ZIF-8 species is achieved toward the promotion of an intense color change in the presence of CO_2 (at low and intermediate humidity). Then, preliminary work involving anthocyanin-loaded MOFs is engaged as vital toward enabling highly sensitive, highly selective, and multi-color gas responses in indoor air systems.

5.1 Introduction to the reduction of interference in colorimetric gas sensing

In Chapter 3, the second-generation gas sensor, ED/PSP:ZIF-8—developed from the direct incorporation of phenol red into the ZIF-8 precursor broth—was demonstrated to exhibit a stronger colorimetric gas response to CO_2 in variable humidity and across a range of acetone levels than that of the first-generation gas sensor, PSP-ED/ZIF-8 [123]. However, with rising humidity levels, ED/PSP:ZIF-8 experienced a diminished color change in the presence of CO_2 [123]. Thus, research efforts to rectify humidity interference remained imperative.

The wide range of humidity existent across air systems on Earth imposes certain challenges for environmental gas sensing [169]. However, various efforts have succeeded in the mitigation of humid interference of colorimetric analyte detection [169]. Nafion tubing, which "is a copolymer of tetrafluoroethylene and perfluoro-3,6-dioxa-4- methyl-7-octene-sulfonic acid," has been integrated into colorimetric sensors and shown to facilitate an uninterrupted parts per billion (ppb)-level nitric oxide (NO) detection at 100% RH [169]. In addition, the incorporation of "matrices of substrates" of hydrophobic character, such as ethyl cellulose as a plastic film—coupled with a phase transfer agent and pH indicator—produced a solid-state, colorimetric CO_2 sensor with stable sensing performance at 100% RH and 37 °C [169]. In recent studies, the integration of "water-rich hydrogel[s]" into "hydrophilic colorimetric sensing system[s]" has been proven to "buffer the humidity influence on the colorimetric gas sensing" [233].

In this dissertation, phenol red is a hydrophilic halochromic compound [169] and ethylenediamine is a hydrophilic primary amine [167]. Moreover, water is suspected to be functional as a base in the underlying zwitterion mechanism, possibly competing with phenol red for deprotonation of the zwitterion [99, 123]. Thus, humid interference has been observed (with distinct magnitude) between the first-generation sensor, PSP-ED/ZIF-8, and the second-generation sensor, ED/PSP:ZIF-8 [99, 123]. Toward the desired fabrication of a water-robust indoor colorimetric gas sensor, an approach is pursued in this chapter in which other halochromic compounds are blended with ZIF-8 reaction precursors (via dye-precursor synthesis), reacted, mixed with ED/PSP:ZIF-8, and then exposed to indoor levels of CO_2 in variable humidity.

5.2 Development and characterization of the third-generation colorimetric gas sensor, ED/UI-PSP:ZIF-8.

The intuition for the incorporation of a multi-dye synthesis approach is to potentially suppress the capacity of humidity to participate as a base in the zwitterion mechanism [99, 123, 140-145]. In the previous chapter, an increased phenol red loading (through the first-generation approach) resulted in a reduced colorimetric gas response at higher dye loadings. Similarly, an increased phenol red loading (through the second-generation approach) inhibited the crystallization of ZIF-8 at higher dye loadings. Rather than simply increasing the phenol red concentration through the first- or second-generation sensor synthesis method, a second, pH-sensitive material is selected and blended with phenol red-loaded ZIF-8 to colorimetrically sense indoor CO_2.

5.2.1 Development of UI:ZIF-8 and ED/UI-PSP:ZIF-8

A universal pH indicator (referred to as UI) is selected to produce the third-generation sensor. UI is acquired from Lab Supplies pH indicator Test Drops (pH Range: 2.0 – 10.0). UI is composed of ethanol, methyl red, and phenolphthalein. UI is chosen because of its multiple colors achieved across a range of pH. (Efforts to generate a multi-color gas sensor is discussed in greater detail in Chapter 5.3). **Figure 5.1** shows the components of UI.

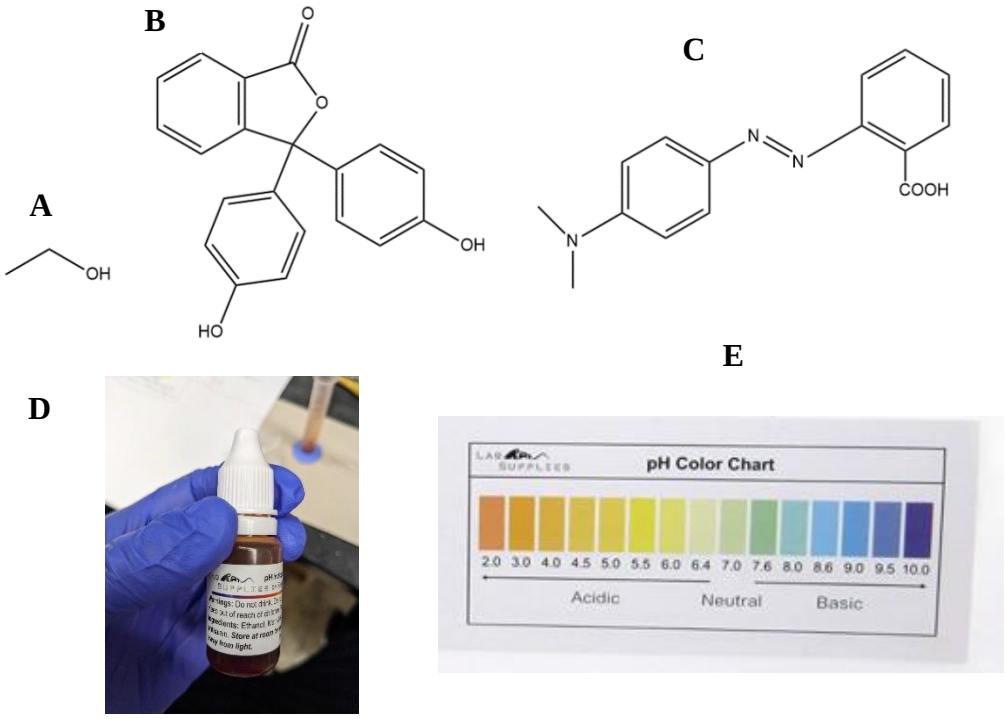

Fig. 5.1 Universal pH indicator (UI). **(A)** Ethanol; **(B)** Phenolphthalein; **(C)** Methyl red; **(D)** the universal pH indicator; and **(E)** the pH range of the UI. All chemical structures are prepared in ChemDraw.

The synthesis of the third-generation sensor, ED/UI-PSP:ZIF-8 is depicted in **Figure 5.2**. 300 mg of zinc nitrate hexahydrate are dissolved in 10 ml methanol and 5 ml UI. In a second beaker, 827 mg of 2-methylimidazole are dissolved in 10 ml methanol and 5 ml UI. Then, the second beaker is poured into the first beaker, and the reaction broth is allowed to react at room temperature for 48-hr to form UI:ZIF-8. After preparing an 80 mg/ml ED/PSP:ZIF-8 solution (through the procedure outlined in Chapter 3), UI:ZIF-8 (as-synthesized) is mixed with ED/PSP:ZIF-8 in the following volume ratio: 200 ul ED/PSP:ZIF-8 : 300 ul UI:ZIF-8. The resulting mixture is ED/UI-PSP:ZIF-8. UI:ZIF-8 is also dried at room temperature and used for CHNS elemental analysis and FTIR transmittance spectra. PXRD pattern collection (using Rigaku Miniflex 6G Benchtop Powder XRD (ChexFLEX: RUA #2172; 40kV/15 mA; X-ray Source: Sealed Source Tube (Cu-Kα Radiation); scan rate: 3.0°/min; and 1D scan mode) occurs using as-synthesized UI:ZIF-8 (drop-cast).

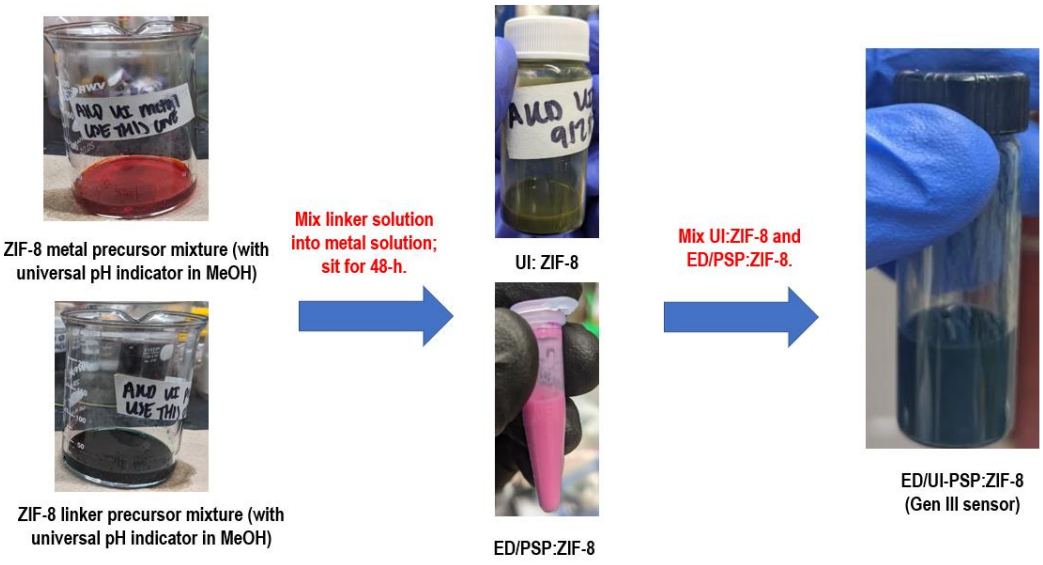

Fig. 5.2 Synthesis of ED/UI-PSP:ZIF-8 (third-generation colorimetric gas sensor).

5.2.2 Material characterization of UI:ZIF-8 and ED/UI-PSP:ZIF-8

Figure 5.3 shows the PXRD pattern for drop-cast UI:ZIF-8 (as-synthesized) and FTIR transmittance spectra for UI-based materials. As depicted, the major diffraction peaks characteristic of ZIF-8 are present [99, 123], indicating the successful crystallization of the MOF. Additionally, FTIR transmittance spectra (collected using a Bruker Vertex80) are collected for the various spectra. UI:ZIF-8 (powder), UI:ZIF-8 (as-synthesized), and ED/UI-PSP:ZIF-8 exhibit the 421 cm^{-1} mode associated with the Zn-N coordination bond, confirming the formation of ZIF-8 [123]. ED/UI-PSP:ZIF-8 also possesses two N-H stretches at 3280 and 3360 cm^{-1}, indicating the stable incorporation of ethylenediamine [123]. Several peaks appearing between 1000 and 1500 cm^{-1} in UI:ZIF-8 (as-synthesized) and ED/UI-PSP:ZIF-8 are associated with IR-active vibrations from the universal pH indicator.

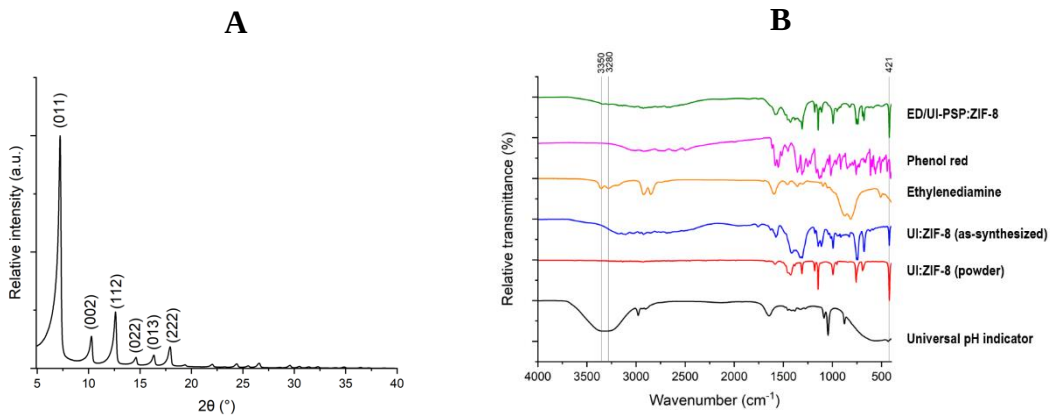

Fig. 5.3 (A) PXRD pattern for solid UI:ZIF-8 (as-synthesized). **(B)** FTIR transmittance spectra for UI (black), UI:ZIF-8, powder (red), UI:ZIF-8, as-synthesized (blue), ethylenediamine (orange), phenol red (magenta), and ED/UI-PSP:ZIF-8 (olive).

Table 5.1 shows the CHNS elemental composition data for UI:ZIF-8 powder. The elemental contents are consistent with that of pristine ZIF-8 (with slightly larger hydrogen content associated with the adsorption of the UI to ZIF-8).

Table 5.1 CHNS elemental composition for solid UI:ZIF-8 (powder)

Sample	C%	H%	N%	S%
UI:ZIF-8	42.78	4.72	23.82	0

5.2.3 Preservation of the color change in intermediate humidity: colorimetric imaging

Colorimetric images are recorded for PSP-ED/ZIF-8, ED/PSP:ZIF-8, and ED/UI-PSP:ZIF-8 exposed to 3,000 ppm CO_2 at 0 and 35% RH (T: 28.7 ± 2 °C). and shown in **Figure 5.4**. Gas exposures are conducted using a LabView-operated gas dosing system. As demonstrated in Chapter 3, the ED/PSP:ZIF-8 sensor outperforms the PSP-ED/ZIF-8 sensor across humidity. However, both sensors suffer with increased humidity. In contrast, the ED/UI-PSP:ZIF-8 sensor exhibits an intense, pink-to-green color change in the presence of both dry and humid CO_2. The maintenance of the color change of the ED/UI-PSP:ZIF-8 sensor at the same CO_2 level (but with varied humidity) is attributed to the integration of a UI-adsorbed ZIF-8 to the second-generation sensor, ED/PSP:ZIF-8. Whereas Chapter 4 demonstrated the undesirable effect of increased phenol red loading on the color change, the addition of a second layer of dye-adsorbed ZIF-8 is speculated to (i) provide additional surface sites for CO_2 chemisorption and (ii) reduce humid participation in the zwitterion mechanism through increasing the concentration of dye species in the system.

Given this improvement at modest humidity levels, quantitative UV-Vis diffuse reflectance spectra are collected to assess ED/UI-PSP:ZIF-8 sensing performance in plausible indoor air conditions consisting of CO_2, humidity, and VOCs.

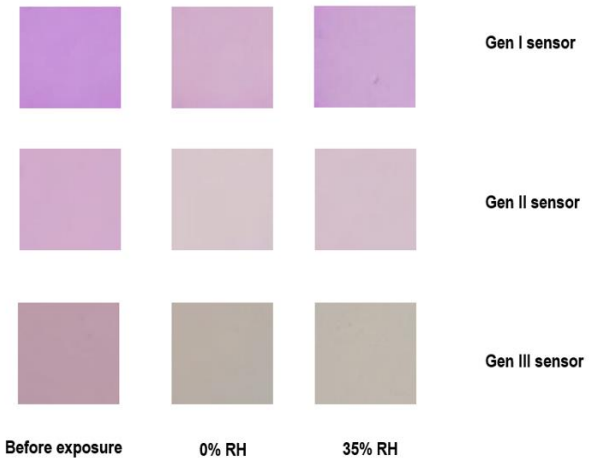

Fig. 5.4 Colorimetric gas exposures for PSP-ED/ZIF-8 (Gen I sensor), ED/PSP:ZIF-8 (Gen II sensor), and ED/UI-PSP:ZIF-8 (Gen III sensor). Temperature (°C) and relative humidity (%) are determined using a wireless GasLab Plus CM-501 NDIR sensor.

5.2.4 Evaluating the color change in real indoor conditions: UV-Vis diffuse reflectance spectra in carbon dioxide, humidity, and acetone ternary environment

Ternary *in-situ* diffuse reflectance UV-Vis spectra are collected to examine how ED/UI-PSP:ZIF-8 performs at 3,000 ppm CO_2 in (i) dry CO_2 environment, (ii) humid CO_2 environment, and (iii) humid CO_2 environment in the presence of acetone. The *in-situ* UV-Vis diffuse reflectance spectral technique shown in **Figure 3.2** is reimplemented for these studies. **Figure 5.5-A** profiles the average CO_2 concentration (in ppm) versus the average CO_2 flowrate (ml/min). Milli-Q water inside a glass vessel in submerged in a water bath heated to 28 °C (via a OMEGA Thermoregulator) is used to generate a humid system (as depicted in **Figure 5.5-B**). **Table 5.2** shows mean CO_2 flowrates (ml/min), relative humidity (%), and temperature (°C), for humid CO_2 systems (with and without acetone). Acetone flowrates (in nitrogen background) are set to 113 ± 3 ml/min.

Table 5.2 Mean CO_2 flowrates (ml/min), CO_2 concentration (ppm), relative humidity (%), and temperature (°C) for humid CO_2 UV-Vis diffuse reflectance spectra (with and without acetone). Total gas flow: 350 ml/min.

Condition	**CO_2 flowrate (ml/min)**	**CO_2 concentration (ppm)**	**Relative humidity (%)**	**Temperature (°C)**
Humid CO_2 (without acetone)	141 ± 2	3120 ± 120	82.4 ± 2	25.11± 0.8
Humid CO_2 (with acetone)	141 ± 2	3120 ± 86	83.4 ± 5	25.02 ± 0.6

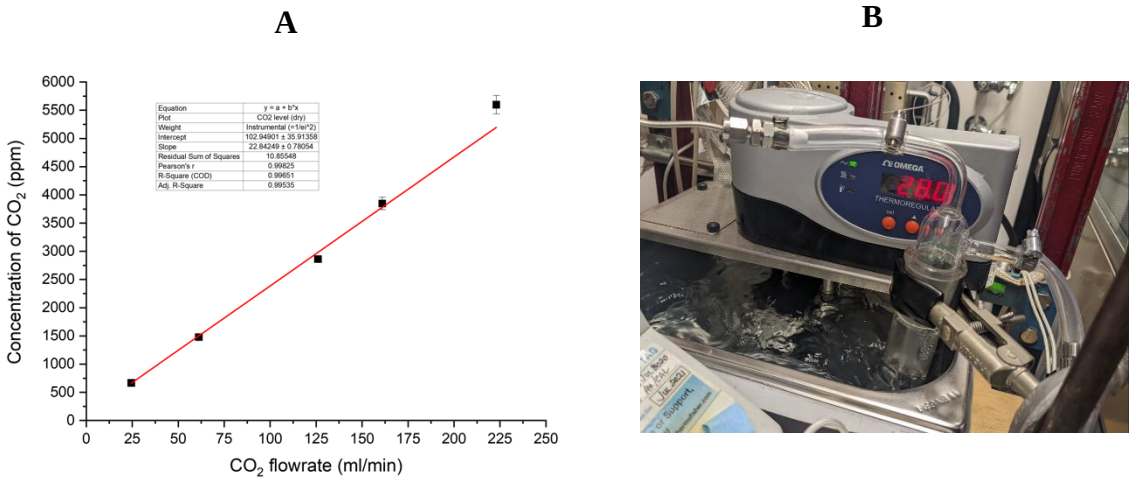

Fig. 5.5 (A) Concentration of CO_2 (ppm) versus CO_2 flowrate (ml/min) for CO_2 measurements at 0% RH (T: 24.5 ± 0.8 °C). Error bars are standard deviation values. **(B)** Heating system used to stabilize humid gas flow.

Figure 5.6-(A) displays the normalized reflectance (% R) vs. wavelength (nm) spectra for PSP:ZIF-8 (as-synthesized), ED/PSP:ZIF-8, UI:ZIF-8 (as-synthesized), and ED/UI-PSP:ZIF-8. Several wavelengths of interest for colorimetric assessment emerge: (i) 416.5 nm reflectance minimum (violet region; associated with UI:ZIF-8); (ii) 517 nm reflectance maximum (green region; associated with UI:ZIF-8); (iii) 578 nm reflectance minimum (yellow region: associated with ED/PSP:ZIF-8); and (iv) 620 nm reflectance "shoulder" (orange region: associated with the UI:ZIF-8).

All gas exposure measurements show normalized F(R) values versus wavelength (nm) at 11-min controlled gas delivery (as shown in **Fig. 5.6-(B)**). Upon prolonged dry CO_2 exposure, the F(R) minimum at 517 nm shifts to 535.5 nm (as the sensor becomes greener). In addition, the F(R) peak at 578 nm and F(R) "shoulder" at 620 nm become a wide region. However, at elevated humidity (> 80% RH), an F(R) peak forms at 620 nm while the peaks at 517 nm and 578 nm remain unshifted. Finally, the humid CO_2 exposure (with acetone) also produces a 620 nm peak relative to that at 578 nm. Though the color change appeared stable at low and intermediate humidity, the UV-Vis diffuse reflectance spectra demonstrate that the ED/UI-PSP:ZIF-8 sensor still suffers under high humidity. Improvements to this sensor could entail several strategies, such as the incorporation of hydrophobic substrates [169] and hydrophobic MOF linkers [99, 170].

In the next section, efforts to generate multi-color responses to indoor CO_2 will be succinctly discussed.

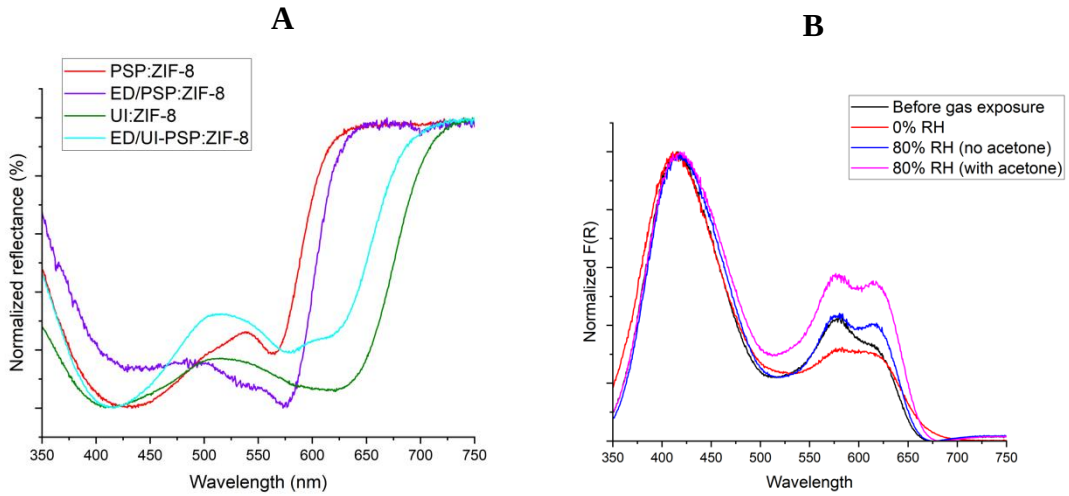

Fig. 5.6 (A) UV-Vis diffuse reflectance spectra for PSP:ZIF-8 (red), ED/PSP:ZIF-8 (violet), UI:ZIF-8 (olive), and ED/UI-PSP:ZIF-8 (cyan) before controlled gas delivery. **(B)** Normalized F(R) vs. wavelength (nm) for ED/UI-PSP:ZIF-8 before controlled gas delivery-black; ED/UI-PSP:ZIF-8 exposed to ~3000 ppm CO_2 (0% RH)-red; ED/UI-PSP:ZIF-8 exposed to ~3000 ppm CO_2 (~80% RH)- blue; and ED/UI-PSP:ZIF-8 exposed to ~3000 ppm CO_2 (~80% RH) under 113 ± 2ml/min acetone flow - magenta. Total gas flow: 350 ml/min.

5.3 Introduction to anthocyanin-based colorimetric gas sensing

As mentioned in the previous section, part of the impetus for selecting UI was to achieve different colors upon exposure to distinct indoor levels of CO_2. In earlier chapters, the sole use of phenol red resulted in only fuchsia-to-yellow or fuchsia-to-red/yellow color changes; however, the human eye struggles to discern these differences at elevated gas levels. Moreover, given that the construction of a cheap and user-friendly sensor is part of the fabrication criteria, it is imperative that a colorimetric sensor can provide meaningful data outside expensive spectroscopic equipment.

When drop-cast on cellulose filter paper and allowed to dry in ambient environment at room temperature, ED/UI-PSP:ZIF-8 undergoes several color changes before becoming green (as shown in **Figure 5.7**). However, when exposed to elevated levels of dry CO_2, the sensor simply becomes greener. The ideal sensor would generate the unique colors observed in **Figure 5.7** upon direct exposure to indoor CO_2 levels (500-5,000 ppm).

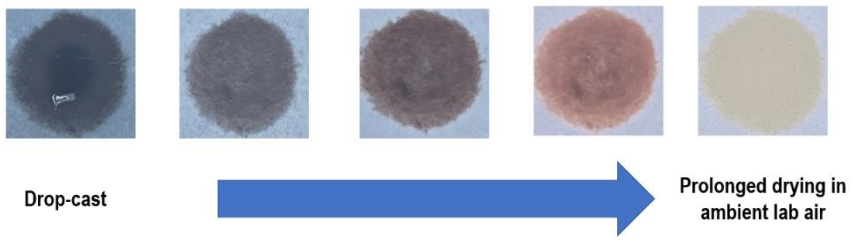

Fig. 5.7 Progression of the color of ED/UI-PSP:ZIF-8 in ambient lab environment.

Toward the achievement of such multi-color sensors, anthocyanin-based halochromic compounds are screened and integrated into ZIF-8 precursor mixtures. Anthocyanins are pigments existent in plants (such as red cabbage, berries, and other fruits and edible flowers) which produce a range of colors [234]. The fundamental structure of an anthocyanin is given in **Figure 5.8** [234]. As halochromic compounds, anthocyanin color shifts with pH [234]. Several colors can be achieved from acidic to neutral to basic environment, such as red-to-purple-to-blue transitions [234]. This behavior is associated with the various HOMO-LUMO transitions achievable upon change of the chemical conjugation of anthocyanins upon change of pH [116. 234-235]. Anthocyanin-based materials have been employed in food quality and food safety [235].

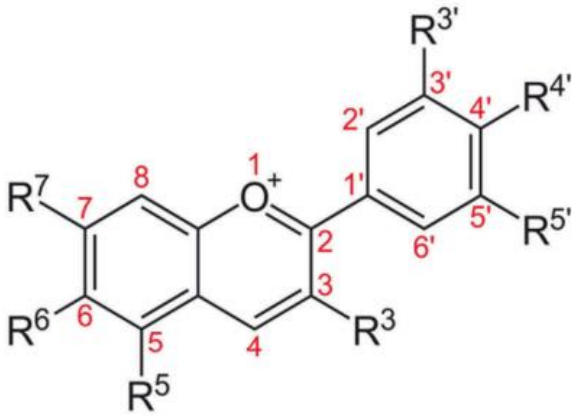

Fig. 5.8 Chemical structure of a simple anthocyanin. Acquired from Khoo et al. [234].

In this section, two anthocyanin-based compounds—red cabbage and cherry juice—are blended with ZIF-8 reaction precursors and exposed to the same gas conditions described in Chapter 5.2. Red cabbage powder (water soluble food dye from Fluxias GmbH) and tart cherry juice (from concentrate from OPEN NATURE, 100% juice) are used. Red cabbage-incorporated ZIF-8 (RC:ZIF-8) is attempted through dissolving 1.04 g zinc nitrate hexahydrate in 60 ml methanol, and then adding 400 mg red cabbage to this solution. In a separate beaker, 1.04 g 2-methylimidazole are dissolved in 60 ml methanol, and 400 mg red cabbage are also added to this solution. After prolonged sonication, the 2-methylimidazole-red cabbage solution is slowly poured into the zinc nitrate hexahydrate-red cabbage solution, and reacted for 48-hr at room temperature. Cherry juice-incorporated ZIF-8 (CJ:ZIF-8) is also attempted through dissolving 300 mg zinc nitrate hexahydrate in 10 ml methanol and 5 ml cherry juice. In a second beaker, 827 mg 2-methylimidazole are dissolved in 10 ml methanol and 5 ml cherry juice. The 2-methylimidazole-cherry juice solution is then slowly poured into the zinc nitrate hexahydrate-cherry juice solution, and then reacted at room temperature for 48-hr. Images of the attempted RC:ZIF-8 and CJ:ZIF-8 are depicted in **Figure 5.9**. While the RC:ZIF-8 appears with a dark blue color, the CJ:ZIF-8 appears with a brown-red color.

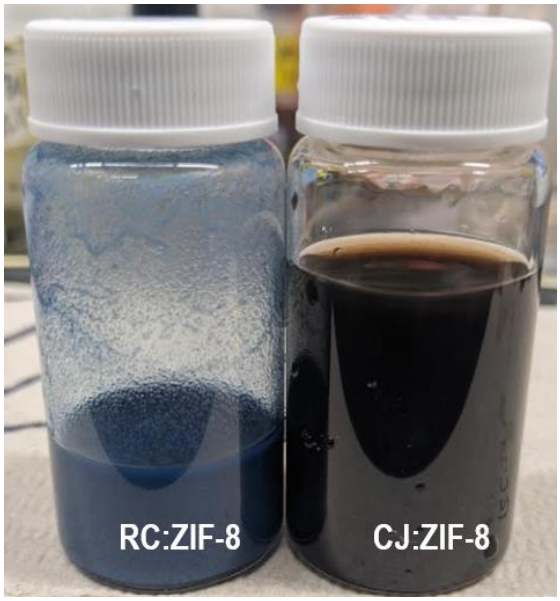

Fig. 5.9 RC:ZIF-8 and CJ:ZIF-8 solutions.

PXRD diffraction scans are shown for RC:ZIF-8 and CJ:ZIF-8 drop-cast on sample holders in **Figure 5.10**. RC:ZIF-8 possesses the major diffraction peaks assigned to ZIF-8 formation; however, none of those peaks appear for the cherry juice-based sample, indicating the failure of ZIF-8 formation in the presence of CJ.

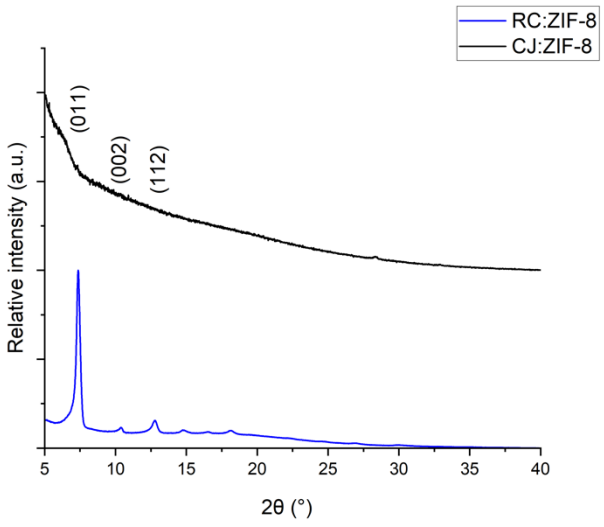

Fig. 5.10 PXRD patterns for attempted RC:ZIF-8 (blue) and CJ:ZIF-8 (black).

Third-generation sensors are constructed from RC:ZIF-8 (and the attempted CJ:ZIF-8 sample). The ED/RC-PSP:ZIF-8 sensor is prepared from mixing 350 ul of ED/PSP:ZIF-8 with 150 ul of RC:ZIF-8 (as-synthesized). The ED/CJ-PSP:ZIF-8 sensor is developed from mixing 400 ul of ED/PSP:ZIF-8 with 200 ul of the attempted CJ:ZIF-8 (as-synthesized). Colorimetric images are collected for ED/RC-PSP:ZIF-8 and ED/CJ-PSP:ZIF-8 exposed to 3,000 ppm CO_2 at 0 and 35% RH (T: 28.7 ± 2 °C). and displayed in **Figure 5.11**. As observed, the ED/RC-PSP:ZIF-8 sensor exhibits a weakened color change in humidity; similarly, the ED/CJ-PSP:ZIF-8 sensor exhibits a weak color change in general (at both low and intermediate humidity).

Through dye/MOF engineering optimization—including screening more anthocyanin-based dyes and incorporating hydrophobic molecules—humid-robust, multi-color changes in the presence of CO_2 should be pursued (as depicted in **Figure 5.12**).

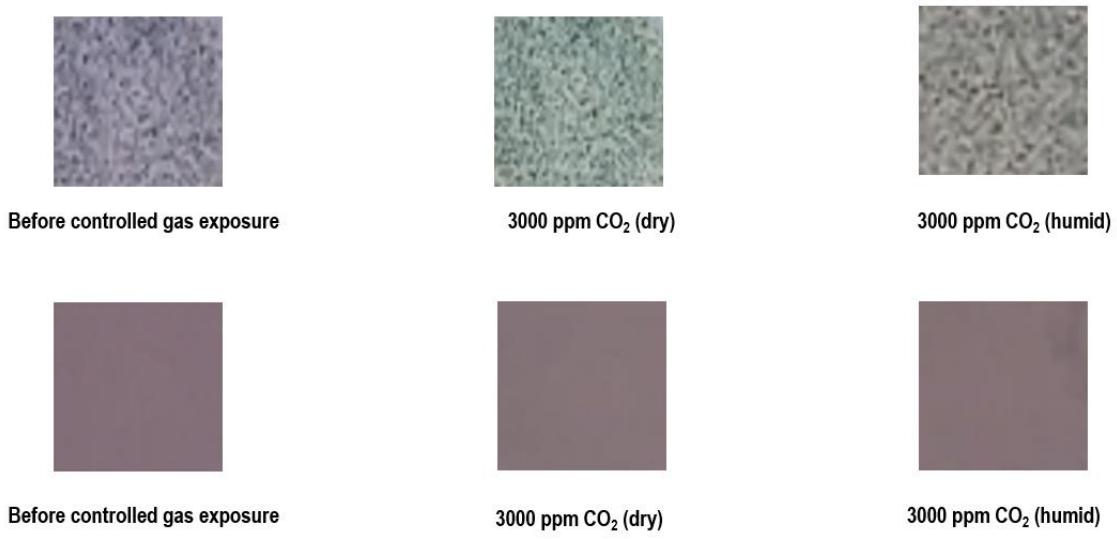

Fig. 5.11 Colorimetric images of ED/RC-PSP:ZIF-8 (top row) and ED/CJ-PSP:ZIF-8 (bottom row) exposed to indoor CO_2 levels.

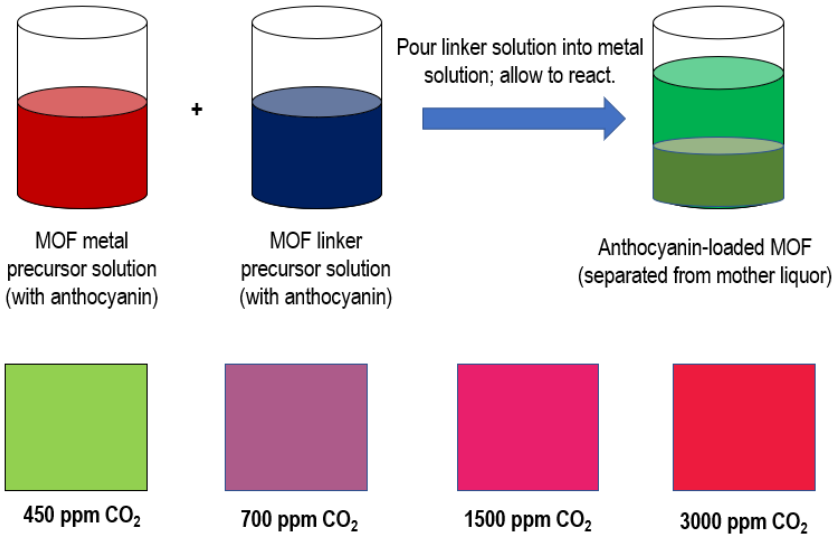

Fig. 5.12 Idealized colorimetric gas response achieved from dye-precursor synthesis involving MOFs and select anthocyanin-based compounds.

5.4 Summary

In this chapter, third-generation, ZIF-8-based indoor colorimetric CO_2 sensors were developed from mixing ED/PSP:ZIF-8 with universal pH indicator- and anthocyanin-loaded ZIF-8 adsorbents. Compared to the PSP-ED/ZIF-8 and ED/PSP:ZIF-8 materials, the ED/UI-PSP:ZIF-8 material exhibited a stronger color change in both low and intermediate humidity. However, *in-situ* diffuse reflectance UV-Vis spectra revealed that the sensor performance suffered at elevated humidity (with and without VOCs present). In addition, while preliminary anthocyanin-based materials exhibited distinct color changes from those of PSP-ED/ZIF-8 and ED/PSP:ZIF-8 in dry environment, both still suffered with increased humidity. Incorporation of select anthocyanins, as well as hydrophobic functional groups, were recommended for the realization of the ideal indoor gas sensor.

5.5 Acknowledgement of co-authors for in-progress publishable work

The work in this chapter involves a publishable chapter, "Mixed-dye metal-organic framework-based colorimetric gas sensors for robust indoor air quality monitoring." I extend my gratitude to all the co-authors for their contributions to this study: Alireza Pourghaderi, Stuart McElhany, Elena Kreimer, Tayler Hunter, Ishan Gupta, Natalie Lefton, Branden Leonhardt, Hanxiao Liu, Carlo Carraro, Roya Maboudian, Bryan McCloskey, and Markita Landry.

This chapter also acknowledges support in the form of a National Science Foundation Graduate Research Fellowship (NSF GRFP) and UC Dissertation-Year Fellowship. The authors also acknowledge the Lawrence-Berkeley National Laboratory Catalysis Facility and Dr. Chithra Asokan for the FTIR measurements. Dr. Nick Settineri of the UCB CheXray facility is

acknowledged for assistance with the collection of PXRD patterns. The authors also acknowledge the UC Berkeley College of Chemistry Microanalytical Facility and Dr. Elena Kreimer for the collection of CHNS elemental composition data. Additional funds from the UC Berkeley Department of Chemical & Biomolecular Engineering toward CHNS, BET, and PXRD measurements are also acknowledged.

Chapter 6: Conclusion and Outlook

6.1 Conclusion

This dissertation presented three generations of metal-organic framework (MOF)-based colorimetric gas sensors for the indoor monitoring of carbon dioxide (CO_2) levels implicated in human health.

In Chapter 1, we illustrated the deleterious consequences of carbon dioxide (as well as volatile organic compounds, VOC) accumulation indoors. In framing this problem, we grounded environmental violence as a symptom of a larger antiblack, colonial "World" for which breathable air is a political zone. Through an assessment of the advantages and disadvantages of the commercial nondispersive infrared (NDIR) gas sensor, we proposed a colorimetric route of indoor carbon dioxide detection toward the realization of a low-cost, passive, simple, scalable, and user-friendly device attendant to concerns about modern indoor air quality.

In Chapter 2, we constructed a first-generation colorimetric gas sensor, PSP-ED/ZIF-8, through the post-synthetic decoration of the MOF, ZIF-8, with the pH indicator, phenol red, and the primary amine, ethylenediamine, in methanol. Through powder X-ray diffraction (PXRD), we demonstrated the structural integrity of ZIF-8 in the presence of phenol red and ethylenediamine. Moreover, through a LabView-operated gas manifold process, we collected colorimetric images that displayed the sensor's sensitivity to < 1,000 ppm CO_2 (with the sensor transitioning from fuchsia to yellow). An *ex-situ* ultraviolet-visible (UV-Vis) diffuse reflectance spectroscopic technique demonstrated an increasing colorimetric response from 700 to 7,500 ppm CO_2 (in dry environment) through probing the 443 nm and 570 nm resonant wavelengths associated with phenol red. However, in the presence of humidity, both the colorimetric images and *ex-situ* UV-Vis diffuse reflectance spectra revealed an inhibited colorimetric response. Such results motivated efforts to both comprehend the mechanism of colorimetric carbon dioxide sensing and mitigate humid interference.

In Chapter 3, we developed a second-generation colorimetric gas sensor based on dye-precursor synthesis: namely, blending phenol red directly into the ZIF-8 metal and linker methanolic precursor solutions. The resulting MOF, termed PSP:ZIF-8, was then blended with ethylenediamine to produce the second-generation colorimetric gas sensor, ED/PSP:ZIF-8. PXRD patterns and Fourier transform infrared (FTIR) transmittance spectra determined that ZIF-8 was successfully achieved in both PSP:ZIF-8 and ED/PSP:ZIF-8. Colorimetric images and an *in-situ* UV-Vis diffuse reflectance spectroscopic technique determined that ED/PSP:ZIF-8 exhibited a stronger color change than PSP-ED/ZIF-8 in the presence of humidity and in the presence of VOCs (such as acetone). Complementary FTIR transmittance and UV-Vis diffuse reflectance spectroscopic studies illustrated potential differences in how phenol red adsorbed to either sensor. While the FTIR transmittance spectra showed that successively washing both sensors removed ethylenediamine from the system, the UV-Vis diffuse reflectance spectra demonstrated a large increase in the reflectance of the 570 nm signature of phenol red for PSP-ED/ZIF-8 (whereas that

for ED/PSP:ZIF-8 decreased by a smaller magnitude). In addition, colorimetric images taken of both washed sensors revealed that neither sensor demonstrated a strong color change to CO_2 without re-addition of ethylenediamine; however, while washed ED/PSP:ZIF-8 sensors only required ethylenediamine to recover a strong colorimetric gas response, washed PSP-ED/ZIF-8 sensors required *both* the replenishment of phenol red and ethylenediamine to change color. From these results, we hypothesized that phenol red resided on the external surface of ZIF-8 in the PSP-ED/ZIF-8 sensor and within the internal pores of ZIF-8 in the ED/PSP:ZIF-8 sensor. Moreover, though ED/PSP:ZIF-8 outperformed PSP-ED/ZIF-8 across all environments tested, the sensor still exhibited a visible colorimetric loss with increased humidity. Here, we employed the previously-studied zwitterion mechanism in which chemical reactions between CO_2, amines, and other bases in the system generate carbamates and protonated bases. We hypothesized that two mechanisms of water interference could prevail: physisorptive interactions of humidity with hydrophilic regions of the sensor and participation of water as a base in the deprotonation of the zwitterion. Thus, the motivation to better elucidate the interplay of ZIF-8, phenol red, and ethylenediamine (and their interactions with CO_2) remained.

In Chapter 4, we rigorously examined mechanistic insights of how ZIF-8, phenol red, and ethylenediamine interact (in methanolic solvent) toward elucidating the colorimetric sensing mechanism and clarifying differences between PSP-ED/ZIF-8 and ED/PSP:ZIF-8. In first probing the role of phenol red, we increased the concentration of phenol red in both the PSP-ED/ZIF-8 and ED/PSP:ZIF-8 sensors and collected colorimetric images and *in-situ* UV-Vis diffuse reflectance spectra. We observed that the colorimetric gas response dwindled for both sensors with increased phenol red, which was associated with a loss of Brunaeur-Emmett-Teller (BET) surface area of ZIF-8 accessible for gas adsorption. However, at 5 mg/ml phenol red in the ED/PSP:ZIF-8 sensor, we observed noise across all CO_2 concentrations. FTIR transmittance spectra, PXRD patterns, and carbon-nitrogen-hydrogen-and-sulfur (CHNS) elemental analysis determined that ZIF-8 does not fully crystallize at and above 5 mg/ml phenol red loaded through dye-precursor synthesis. In transition to the role of ethylenediamine, we first investigated how the intermolecular forces between ZIF-8 and phenol red were modulated by the basic amine. While UV-Vis absorbance spectra suggested that phenol red adsorbed to ZIF-8 through a Freundlich adsorption mechanism (with and without ethylenediamine), CHNS elemental analysis demonstrated that phenol red-adsorbed ZIF-8 (without ethylenediamine) demonstrated larger sulfur content at higher phenol red loadings. However, efforts to completely vaporize ethylenediamine (after its co-adsorption with phenol red onto ZIF-8) were recommended for future experiments to best confirm whether ethylenediamine enhances or inhibits phenol red adsorption onto ZIF-8. Preliminary FTIR transmittance spectra on phenol red-adsorbed ZIF-8 (without ethylenediamine) demonstrated shifts in the C=N bond of the imidazolate linker, which was attributed to van der Waals interactions between the ZIF-8 linker and phenol red. *In-situ* UV-Vis diffuse reflectance spectra collected on PSP-ED/ZIF-8 and ED/PSP:ZIF-8 sensors exhibited a suppressed color change in the presence of dry CO_2 with increased ethylenediamine loadings. Gas-dosed FTIR absorbance spectra on pristine ZIF-8 and amine-functionalized ZIF-8 (ED/ZIF-8) revealed (i) physisorption of CO_2 onto ZIF-8 in the pristine ZIF-8 and (ii) formation of protonated ethylenediamine and carbamate species in ED/ZIF-8 upon exposure to pure CO_2. However, as ethylenediamine loadings were scaled from 5% to 10% and 15%, (%v/v in methanol), the observed reduction of the N-H stretch associated with the zwitterionic chemical reaction occurred less dramatically. This observation was ascribed

to a possible emergence of termolecular kinetics associated with increased primary amine loading. This possible change in the reaction order kinetics of ethylenediamine was coupled with the observed reduction of the colorimetric gas response in the UV-Vis spectra, with ethylenediamine considered to be competing with phenol red for deprotonation of the zwitterion. Finally, second harmonic and X-ray photoelectron spectroscopic techniques were discussed toward a comprehensive analysis of dye adsorption onto MOFs toward colorimetric analyte monitoring.

In Chapter 5, third-generation colorimetric gas sensors were constructed through using dye-precursor synthesis with phenol red-adsorbed ZIF-8 and other dye-adsorbed ZIF-8 molecules and blending with ethylenediamine. The combination of phenol red and a universal pH indicator (on ZIF-8) produced ED/UI-PSP:ZIF-8, which maintained the structural integrity of ZIF-8 and exhibited an improved colorimetric gas response at low and intermediate humidity. However, *in-situ* diffuse reflectance UV-Vis spectra revealed that this sensor failed at higher humidity. Toward the fulfillment of a multi-color gas response, anthocyanin-based sensors were proposed. Preliminary colorimetric gas exposures for red cabbage- and cherry juice-loaded ZIF-8 sensors exhibited novel colors upon exposure to CO_2; however, relative humidity remained detrimental to the observed color change, prompting strategies to stably incorporate hydrophobic compounds into the MOF-based colorimetric sensor system.

6.2 Outlook

As mentioned throughout this dissertation, several corrective synthesis strategies and experimental insights remain to be pursued. Most importantly, the role of water as a colorimetric interferant (and its mechanism of interference) require further experimental depth. It remains unclear whether water disrupts the color change through (i) hydrophilic interactions with colorimetric gas sensor components, (ii) competition with dye molecules for zwitterion deprotonation, or (iii) some combination of these interactions. Toward this end, liquid-jet XPS studies at Beamline 11.0.2 at the Advanced Light Source at the Lawrence Berkeley National Laboratory are being designed. In related research, primary amines (such as ethylenediamine) have been used in aqueous systems for the absorption of ultradilute CO_2 streams. My colleagues and I remain interested in the role of amine-functionalized MOFs (such as ZIF-8) loaded into nonaqueous systems (such as methanol) in the extent to which zwitterionic reaction products form in the presence of CO_2 (across humidity). One current challenge is the incorporation of ZIF-8 systems (< 100 nm) into the liquid jet to form a flat sheet without agglomeration. Once this challenge is surmounted, the role of both ZIF-8 and water can be elucidated to best inform the interactions between ZIF-8, phenol red, ethylenediamine, carbon dioxide, and water (in methanol). Moreover, we remain optimistic that these experimental improvements (and their insights) will facilitate the XPS-based mechanistic assessment of other MOFs (of distinct metal and linker chemistries) relevant to a wide array of applications.

Second harmonic spectroscopic studies remain in progress to determine the Gibbs free energy of adsorption and maximum surface number density of dye molecules with respect to phenol red on ZIF-8 (with and without ethylenediamine). Coupled with the CHNS elemental analysis, UV-Vis absorbance spectra, and FTIR transmittance spectra described in Chapter 4, these studies will explicate changes in the intermolecular forces that define phenol red adsorption to ZIF-8 upon

inclusion of ethylenediamine. With certain experimental modifications, second harmonic spectroscopies can also be implemented to (i) evaluate MOF crystallization [199] and (ii) determine the molecular orientation of adsorbed dye molecules [202]. As observed in Chapter 4, ZIF-8 fails to crystallize in phenol red through dye-precursor synthesis at elevated dye loadings. Second harmonic spectroscopic techniques can expound how ZIF-8 crystallization occurs in the presence of dye, which can be used for more complicated dye-loaded systems (such as with anthocyanins). Related to molecular orientation, second harmonic spectroscopic techniques can be coupled with FTIR transmittance spectra to determine how phenol red (and other dyes) adsorb to ZIF-8, which could be used to inform proficiency in sensing gaseous analytes.

In addition to these established techniques, novel experiments should be developed for the materialization of an excellent colorimetric gas sensor. Selective dye engineering of anthocyanin-based compounds into MOFs to achieve the color changes depicted in **Figure 5.12** should be compatible with cellular devices such that red, green, and blue (RGB) distributions can be standardized for reliable use across various indoor air settings. Moreover, a multi-transduction technique could empower colorimetric gas sensing. In recent times, conductive MOFs have obtained considerable interest in gas sensing [236]. Despite characteristically "large energy gaps between their frontier orbitals" for which reported MOFs are expected to be insulators, research progress remains promising in developing libraries of conductive MOFs for which a change in resistance can be measured as a function of adsorbed analyte concentration [236]. Relevant charge transport can be described through "band-like" transport (involving delocalized electrons characteristic of strong covalent bonds) and "hopping transport" (involving "always thermally activated" electron transfer from "distinct sites with differing valences" characteristic of ionic materials) [236]. In MOFs, three major carrier transport pathways exist: (a) "through-bond," involving "metals and ligand moieties with well-matched energy levels and good orbital overlap" toward charge delocalization; (b) "extended conjugation," involving transition metals bonded to "ligands containing chelating functional groups" which are "conjugated with the organic core" and responsible for producing MOFs "with extended conjugation encompassing both the organic and inorganic components"; and (c) "through-space," which involve "organic components participating in π-π interactions with each other" [236]. Through the integration of conductive MOFs into colorimetric MOF systems, gas/solid interfacial phenomena can be advanced through relating amine-based HOMO-LUMO dye chemical conjugation transformations with changes in resistance from MOF-analyte interactions. In a practical sense, a modern sensor possessing both colorimetric and conductive capacities would provide RGB analysis and electrical signals which could be mapped (as a function of gas concentration) and made legible for portable use.

In order to be effective in various air systems, many questions should be posed and ruminated upon regarding colorimetric gas sensors. Who will determine how the sensors are fabricated and distributed? What safety measures are important for these sensors? What is a reasonable shelf life for such materials? Why are gas concentrations present at the levels they are, and how will the knowledge acquired through such sensors act upon such gas levels? It is my hope that this preliminary work will attend to these inquiries for anticipated sensor designs and applications.

References

1. .Diamond, D. "Grand Challenges and Opportunities in Sensor Science and Technology." *Front. Sens.*, **2020**, 1, 2, 1-3. DOI: https://doi.org/10.3389/fsens.2020.00002
2. Li, H.; Zhao, J.; Luo, L.; Du, J.; and Zeng, J. "Symmetry-Breaking Sites for Activating Linear Carbon Dioxide Molecules." *Accounts of Chemical Research*, **2021,** *54*, 6, 1454-1464. DOI: https://doi.org/10.1021/acs.accounts.0c00715
3. Buder, I; **2020.** Idowu, S.; Schmidpeter, R.; Capaldi, N.; Zu, L.; Del Baldo, M.; and Abreu, R. (eds.) "Greenhouse Gases." *Encyclopedia of Sustainable Management*, 1-8. DOI: https://doi.org/10.1007/978-3-030-02006-4_298-1
4. Matemilola, S. and Alabi, H.A. "Greenhouse Effect." *Encyclopedia of Sustainable Management,* **2021**, 1-4.
5. Kirk-Davidoff, D. "Chapter 3.4. The Greenhouse Effect, Aerosols, and Climate Change." *Green Chemistry*, **2018**, 211-234. DOI: http://dx.doi.org/10.1016/B978-0-12-809270-5.00009-1
6. Piekle, Jr., R.A. "What is Climate Change?" *Energy & Environment*, 15, 3, 2004. DOI: https://doi.org/10.1260/0958305041494576
7. Srinivasan, J. "Climate Change, Greenhouse Gases and Aerosols." *Resonance*, **2008**, 1146-1155. DOI: https://doi.org/10.1007/s12045-008-0114-x
8. "Indoor Air Quality." *United States Environmental Protection Agency*. Web. 3 January 2023. https://www.epa.gov/report-environment/indoor-air-quality#:~:text=Americans%2C%20on%20average%2C%20spend%20approximately,higher%20than%20typical%20outdoor%20concentrations.
9. Ana, G.R.; Alli, A.S.; Uhiara, D.C.; and Shendell, D.G. "Indoor air quality and reported health symptoms among hair dressers in salons in Ibadan, Nigeria." *J. Chem Health Saf.*, **2019**, 26, 1, 23-30. DOI: https://doi.org/10.1016/j.jchas.2018.09.004
10. Zhang, X.; Wargocki, P.; Lian, Z.; and Thyregod, C. "Effects of exposure to carbon dioxide and bioeffluents on perceived air quality, self-assessed acute health symptoms, and cognitive performance." *Indoor Air*, **2016**, 27, 1, 47-64. DOI: https://doi.org/10.1111/ina.12284
11. Azuma, K.; Kagi, N.; Yanagi, U; and Osawa, H. "Effects of low-level inhalation exposure to carbon dioxide in indoor environments: A short review on human health and psychomotor performance." *Environmental International 121*, **2018**, 51-56. DOI: https://doi.org/10.1016/j.envint.2018.08.059
12. Wang, N.; Ernle, L.; Beko, G.; Wargocki, P.; and Williams, J. "Emission Rates of Volatile Organic Compounds from Humans." *Environmental Science & Technology* **2022** *56*, 8, 4838-4848. DOI: https://doi.org/10.1021/acs.est.1c08764

13. "What are volatile organic compounds (VOCs)?" *United States Environmental Protection Agency*. Web. 4 January 2023. https://www.epa.gov/indoor-air-quality-iaq/what-are-volatile-organic-compounds-vocs

14. Yu, C.W.F. and Kim, J.T. "Building Pathology, Investigation of Sick Buildings -- VOC Emissions." *Indoor Built Environ*, **2010**, 19, 1, 30-39. DOI: https://doi.org/10.1177/1420326X09358799

15. Allen, J.G.; MacNaughton, P.; Satish, U.; Santanam, S.; Vallarino, J.; and Spengler, J.D. " Associations of Cognitive Function Scores with Carbon Dioxide, Ventilation, and Volatile Organic Compound Exposures in Office Workers: A Controlled Exposure Study of Green and Conventional Office Environments." *Environmental Health Perspectives*, **2016**, 124, 6, 805-812. DOI: https://doi.org/10.1289/ehp.1510037

16. Chang, C-J; Yang, H-H; Wang, Y-F; and Li, M-S. "Prevalence of Sick Building Syndrome-Related Symptoms among Hospital Workers in Confined and Open Working Spaces." *Aerosol and Air Quality Research*, **2015**, 15, 2378-2384. DOI: 10.4209/aaqr.2015.01.0040

17. Ghaffarianhoseini, A.; AlWaer, H.; Omrany, H.; Ghaffarianhoseini, A.; Alaluoch, C.; Clements-Croome, D.; and Tookey, J. "Sick building syndrome: are we doing enough?" *Architectural Science Review*, **2018**, 61, 3, 99-121. DOI: https://doi.org/10.1080/00038628.2018.1461060

18. Satish, U.; Mendell, M.J.; Shekhar, K.; Hotchi, T.; Sullivan, D.; Streufert, S.; and Fisk, W.J. "Is CO_2 an Indoor Pollutant? Direct Effect of Low-to-Moderate Concentrations on Human Decision-Making Performance" *Environ. Health Perspect.*, **2012**; 120(12): 1671–1677. DOI: 10.1289/ehp.1104789

19. R.-Y. Chen, K.-F. Ho, T.-Y. Chang, G.-B. Hong, C.-W. Liu, K.-J. Chuang "In-vehicle carbon dioxide and adverse effects: an air filtration-based intervention study." *Sci. Total Environ*, **2020**, 723, 138047, DOI: 10.1016/j.scitotenv.2020.138047

20. Snow, S.; Boyson, A.S.; Paas, K.H.W.; Gough, H.; King, M-F; Barlow, J.; Noakes, C.J.; and schraefel, M.C. "Exploring the physiological, neurophysiological, and cognitive performance effects of elevated carbon dioxide concentrations indoors." *Building and Environment*, **2019**, 156, 243-252. DOI: https://doi.org/10.1016/j.buildenv.2019.04.010

21. Zhang, X.; Wargocki, P.; and Lian, Z. " Physiological responses during exposure to carbon dioxide and bioeffluents at levels typically occurring indoors." *Indoor Air*, **2017**; 27: 65–77 DOI: https://doi.org/10.1111/ina.12286

22. Wang, J.; Long, E.; and Zhang, X. "Characteristics of human bioeffluents "common core" quantity varying with occupant density in region." *HVAC&R Research*, **2014,** 20, 188–193 DOI: https://doi.org/10.1080/10789669.2013.852902

23. Fenske, J.D. and Paulson, S.E. "Human Breath Emissions of VOCs." *Air & Waste Manage. Assoc.*, **1999**, 594-598. DOI: https://doi.org/10.1080/10473289.1999.10463831

24. Nakaoka, H.; Todaka, E.; Seto, H.; Saito, I.; Hanazato, M.; Watanabe, M.; and Mori, C. "Correlating the symptoms of sick-building syndrome to indoor VOCs concentration levels and odour." *Indoor and Built Environment*. **2014**, 23, 6, 804-813. DOI: https://doi.org/10.1177/1420326X13500975

25. Du, B.; Tandoc, M.C.; Mack, M.L.; and Siegel, J.A. "Indoor CO_2 concentrations and cognitive function: A critical review." *Indoor Air*, **2020**, 30, 1067-1082. DOI: https://doi.org/10.1111/ina.12706

26. Zhang, X.; Mishra, A.; and Wargocki, P. "Effects from Exposures to Human Bioeffluents and Carbon Dioxide." *Handbook of Indoor Air Quality*, **2022.** DOI: https://doi.org/10.1007/978-981-10-5155-5_63-1

27. Domínguez-Amarillo, S.; Fernandez-Agilera, J.; Cesteros-Garcia, S.; and Gonzalez-Lezcano, R.A. "Bad air can also kill: residential indoor air quality and pollutant exposure risk during the COVID-19 crisis." *Int. J. Environ. Res. Public Health*, **2020**, 17, 7183. DOI: https://doi.org/10.3390/ijerph17197183

28. Sun, C.; and Zhai, Z. "The efficacy of social distance and ventilation effectiveness in preventing COVID-19 transmission." *Sustainable Cities and Society*, **2020**, 62, 102390. DOI: https://doi.org/10.1016/j.scs.2020.102390

29. Isphording, I.E.; and Pestel, N. "Pandemic meets pollution: Poor air quality increases deaths by COVID-19." *Journal of Environmental Economics and Management*, **2021**, 108, 102448. https://doi.org/10.1016/j.jeem.2021.102448

30. Ha, W.; Zabarsky, T.F.; Eckstein, E.C.; Alhmidi, H.; Jencson, A.L.; Cadnum, J.L.; Donskey, C.J. "Use of carbon dioxide measurements to assess ventilation in an acute care hospital." *American Journal of Infection Control*, **2022**, 50, 2, 229-232. DOI: https://doi.org/10.1016/j.ajic.2021.11.017

31. Poydenot, F.; Abdourahamane, I.; Caplain, E.; Der, S.; Haiech, J.; Jallon, A.; Khoutami, I.; Loucif, A.; Marinov, E.; and Andreotti, B. " Risk assessment for long- and short-range airborne transmission of SARS-CoV-2, indoors and outdoors." *PNAS Nexus*, **2022**, 1, 1–10. DOI: https://doi.org/10.1093/pnasnexus/pgac223

32. Nair, A.N.; Anand, P.; George, A.; and Mondal, N. "A review of strategies and their effectiveness in reducing indoor airborne transmission and indoor air quality." *Environmental Research*, **2022**, 213, 113579. DOI: https://doi.org/10.1016/j.envres.2022.113579

33. Fernández-de-las-Peñas. C. "Long COVID: current definition." *Infection*, **2022**, 50, 285-286. DOI: https://doi.org/10.1007/s15010-021-01696-5

34. Crook, H.; Raza, S; Nowell, J.; Young, M.; and Edison, P. "Long COVID—mechanisms, risk factors, and management." *BMJ*, **2021**, 374. DOI: https://doi.org/10.1136/bmj.n1648

35. Raveendran, A.V.; Jayadevan, R.; and Sashidharan, S. "Long COVID: An overview." *Diabetes & Metabolic Syndrome: Clinical Research & Reviews*, **2021**, 15, 869-875. DOI: https://doi.org/10.1016/j.dsx.2021.04.007

36. "Carbon dioxide peaks near 420 parts per million at Mauna Loa observatory." *National Oceanic and Atmospheric Administration*, **2021**. Web. 5 January 2022. https://research.noaa.gov/article/ArtMID/587/ArticleID/2764/Coronavirus-response-barely-slows-rising-carbon-dioxide

37. Paterson, M. and Stripple, J. "My Space: governing individuals' carbon emissions." *Environment and Planning D: Society and Space*, **2010**, 28, 341-362. DOI: https://doi.org/10.1068/d4109

38. Kause, A.; de Bruin, W.B.; Milwward-Hopkins, J.; and Olsson, H. "Public perceptions of how to reduce carbon footprints of consumer food choices." *Environ. Res. Lett*, **2019**, 14, 114005. DOI: https://doi.org/10.1088/1748-9326/ab465d

39. Paap, W.R. "The Concept of Power: Treatment in Fifty Introductory Sociology Textbooks." *Teaching Sociology*, **1981**, 9, 1, 57-68.

40. Táíwò, O.O. *Reconsidering Reparations.* Oxford University Press, **2022**, 21.

41. Grosfoguel, R. "The Structure of Knowledge in Westernized Universities: Epistemic Racism/Sexism and the Four Genocides/Epistemicides of the Long 16th Century." *Human Archtiecture: Journal of the Sociology of Self-Knowledge*, **2013**, XI, 1, 73-90. DOI: **https://doi.org/10.25058/20112742.153**

42. Robinson, C. *Black Marxism: The Making of the Black Radical Tradition.* **2000**. p. 10

43. Horne, G. *The Dawning of the Apocakypse: The Roots of Slavery, White Supremacy, Settler Colonialism, and Capitalism in the Long Sixteenth Century*, **2020**. p. 7-8.

44. Horne, G. *The Dawning of the Apocakypse: The Roots of Slavery, White Supremacy, Settler Colonialism, and Capitalism in the Long Sixteenth Century*, **2020**. p. 35.

45. Leong, N. "Racial Capitalism." *Harvard Law Review*, **2013**, 126, 8, 2151-2226. DOI: https://www.jstor.org/stable/23415098

46. Robinson, C. *Black Marxism: The Making of the Black Radical Tradition.* **2000**. pp. 2, 10, 19.

47. Robinson, C. *Black Marxism: The Making of the Black Radical Tradition.* **2000**. pp. xiii.

48. Liboiron, M. *Pollution is Colonialism*. Duke University Press, *Durham and London.* **2021**. p. 9.

49. Horne, G. *The Dawning of the Apocakypse: The Roots of Slavery, White Supremacy, Settler Colonialism, and Capitalism in the Long Sixteenth Century*, **2020**. p. 16.

50. Liboiron, M. *Pollution is Colonialism*. Duke University Press, *Durham and London.* **2021**. p. 14

References

51. Robinson, C. *Black Marxism: The Making of the Black Radical Tradition.* **2000**. p. 4.

52. Smallwood, S.E. *Saltwater Slavery: A Middle Passage from Africa to America Diaspora*. Harvard University Press. **2007.** pp. 6-12, 23, 30, 32.

53. Smallwood, S.E. *Saltwater Slavery: A Middle Passage from Africa to America Diaspora*. Harvard University Press. **2007.** p. 14.

54. Samuelson, M. "Thinking with sharks: racial terror, species extinction and other Anthropocene fault lines." *Australian Humanities Review*, **2018**, 63, 31-47. http://australianhumanitiesreview.org/2018/12/02/thinking-with-sharks-racial-terror-species-extinction-and-the-other-anthropocene-fault-lines/

55. Lewis, S.L. and Maslin, M.A. "Defining the Anthropocene." *Nature*, **2015**, 519, 171-180. DOI: https://doi.org/10.1038/nature14258

56. Leung, D.Y.C. "Outdoor-indoor air pollution in urban environment: challenges and opportunity." *Front. Environ. Sci.*, **2015**, 2, 69, 1-7. DOI: https://doi.org/10.3389/fenvs.2014.00069

57. Karnauskas, K.B.; Miller, S.I.; and Schapiro, A.C. "Fossil Fuel Combustion Is Driving Indoor CO_2 Toward Levels Harmful to Human Cognition." *GeoHealth*, **2020**, 4, 5, 1-8. DOI: https://doi.org/10.1029/2019GH000237

58. Malm, A. *Fossil Capital: The Rise of Steam Power and the Roots of Global Warming*. Verso, **2016**. pp. 7; 11-13; 17-18.

59. Malm, A. *Fossil Capital: The Rise of Steam Power and the Roots of Global Warming*. Verso, **2016**. pp. 7-8, 13, 17, 19.

60. Malm, A. *Fossil Capital: The Rise of Steam Power and the Roots of Global Warming*. Verso, **2016**. pp. 93; 117-118; 170; 192.

61. Malm, A. *Fossil Capital: The Rise of Steam Power and the Roots of Global Warming*. Verso, **2016**. pp. 93; 119; 123-124; 215-216.

62. Malm, A. *Fossil Capital: The Rise of Steam Power and the Roots of Global Warming*. Verso, **2016**. pp. 58-63; 124; 223-224; 234-236.

63. Malm, A. *Fossil Capital: The Rise of Steam Power and the Roots of Global Warming*. Verso, **2016**. pp. 58-63; 124; 273-277; 279-292; 309; 314; 325-326.

64. Malm, A. *Fossil Capital: The Rise of Steam Power and the Roots of Global Warming*. Verso, **2016**. pp. 315-317.

65. "History of Reducing Air Pollution from Transportation in the United States." *United States Environmental Protection Agency*. Web. 14 January 2023. https://www.epa.gov/transportation-air-pollution-and-climate-change/history-reducing-air-pollution-transportation

66. Schipper, L.; Saenger, C.; and Sudardshan, A. "Transport and Carbon Emissions in the United States: The Long View." *Energies*, **201**, 4, 4, 563-581. DOI: https://doi.org/10.3390/en4040563

67. Bildirici, M.E. "The effect sof militarization on biofuel consumption." *Journal of Cleaner Production*, **2017**, 152, 420-428. DOI: http://dx.doi.org/10.1016/j.jclepro.2017.03.103

68. Belcher, O.; Bigger, P.; Neimark, B.; and Kennelly, C. "Hidden carbon costs of the 'everywhere war': Logistics, geopolitical ecology, and the carbon boot-print of the US military." *Trans. Inst. Br. Geogr.*, **2020**, 45, 65-80. DOI: https://doi.org/10.1111/tran.12319

69. Bush, V. "Science the Endless Frontier: A Report to the President by Vannevar Bush, Director of the Office of Scientific Research and Development, July 1945." Web. 14 January 2023. https://www.nsf.gov/od/lpa/nsf50/vbush1945.htm

70. Malm, A. *Fossil Capital: The Rise of Steam Power and the Roots of Global Warming*. Verso, **2016**. pp. 267; 269-270.

71. Smallwood, S.E. *Saltwater Slavery: A Middle Passage from Africa to America Diaspora*. Harvard University Press. **2007.** pp. 34-36.

72. Smallwood, S.E. *Saltwater Slavery: A Middle Passage from Africa to America Diaspora*. Harvard University Press. **2007.** pp. 39-41.

73. Smallwood, S.E. *Saltwater Slavery: A Middle Passage from Africa to America Diaspora*. Harvard University Press. **2007.** pp. 43-45.

74. Smallwood, S.E. *Saltwater Slavery: A Middle Passage from Africa to America Diaspora*. Harvard University Press. **2007.** pp. 49.

75. Smallwood, S.E. *Saltwater Slavery: A Middle Passage from Africa to America Diaspora*. Harvard University Press. **2007.** pp. 53, 55.

76. Smallwood, S.E. *Saltwater Slavery: A Middle Passage from Africa to America Diaspora*. Harvard University Press. **2007.** pp. 56-61.

77. ."Constitution of the United States: Thirteenth Amendment- Section 1." Web. 15 January 2023. https://constitution.congress.gov/constitution/amendment-13/#:~:text=Neither%20slavery%20nor%20involuntary%20servitude,place%20subject%20to%20their%20jurisdiction.

78. "Frank Wilderson: The Politics of Pessimism in an Anti-Black World." **2020**. Web. 15 January 2023. Frank Wilderson: The Politics of Pessimism in an Anti-Black World - YouTube

79. "Frank B. Wilderson in conversation with Justin Desmangles, discusses his latest work, Afropessimism." **2021**. Web. 15 January 2023. Frank B. Wilderson in conversation with Justin Desmangles, discusses his latest work, Afropessimism - YouTube

80. Karera, A. "Blackness and the Pitfalls of Anthropocene Ethics." *Critical Philosophy of Race*, **2019**, 7, 1. SPECIAL ISSUE: RACE AND THE ANTHROPOCENE AND RACE, IMMIGRATION, AND REFUGEES. DOI: https://doi.org/10.5325/critphilrace.7.1.0032

81. Hecht, G. "An elemental force: Uranium production in Africa, and what it means to be nuclear." *Bulletin of the Atomic Scientists*, 68, 2, 22-33 DOI: https://doi.org/10.1177/0096340212440352

82. Srivastava, R.R.; Pathak, P.; and Perween, M. "Environmental and Health Impact Due to Uranium Mining." pp. 76-77. *Uranium in Plants and the Environment*, **2020.**

83. Blodgett, A.D. "An Analysis of Pollution and Community Advocacy in 'Cancer Alley': Setting an Example for the Environmental Justice Movement in St James Parish, Louisiana." *Local Environment*, **2006**, 11, 6, 647-661. https://doi.org/10.1080/13549830600853700

84. Johnson, K.A.; Dolan, M.K.; and Sonnett, J. "Speaking of Looting: An Analysis of Racial Propaganda in National Television Coverage of Hurricane Katrina." *Howard Journal of Communications*, **2011**, 3, 302-318. DOI: https://doi.org/10.1080/10646175.2011.590404

85. Carter, B. "Newark homes not so sweet with toxic vapor seeping inside." **2014**. Web. 15 January 2023. https://www.nj.com/essex/2014/04/newark_homes_not_so_sweet_with_toxic_vapors_seeping_inside.html

86. ."Environmental Justice in The Ironbound." Web. 15 January 2023. https://www.ejintheironbound.com/

87. Pirtle Laster, W.N. "Racial Capitalism: A Fundamental Cause of Novel Coronavirus (COVID-19) Pandemic Inequities in the United States." *Health Education & Behavior*, **2020**, 47, 4, 504-508. DOI: https://doi.org/10.1177/1090198120922942

88. "Joy James on the Academy, Captive Maternal, Central Park Five, Prison Abolition, and Simulacra." **2019.** Web. 15 January 2023. https://www.youtube.com/watch?v=6nh-T9KkHR8&t=4033s

89. "FUC 015 | Joy James -- The Algorithm of Anti-Racism." **2020**. Web. 15 January 2023. https://www.youtube.com/watch?v=4zmFqyJwB6I&t=3361s

90. McGrath, M.J. and Scanaill, C.N. *Sensors Technologies: Healthcare, Wellness, and Environmental Applications.* Apress Media, **2014.** https://link.springer.com/content/pdf/10.1007/978-1-4302-6014-1.pdf?pdf=button%20sticky

91. Jia, X.; Roels, J.; Baets, R.; and Roelkens, G. "On-Chip Non-Dispersive Infrared CO_2 Sensor Based on an Integrating Cylinder." *Sensors*, **2019**, 19, 4260. DOI: https://doi.org/10.3390/s19194260

92. Dinh, T-V.; Choi, I-Y; Son, Y-S.; and Kim, J-C. " A review on non-dispersive infrared gas sensors: Improvement of sensor detection limit and interference correction." *Sensors and Actuators B*, **2016**, 231, 529-538. DOI: https://doi.org/10.1016/j.snb.2016.03.040

93. Chatterjee, C. and Sen, A. "Sensitive colorimetric sensors for visual detection of carbon dioxide and sulfur dioxide." *J. Mater. Chem. A*, 2015,3, **5642-5647. DOI: https://doi.org/10.1039/C4TA06321J**

94. Sempionatto, J.R.; Jeerapan, I.; Krishnan, S.; and Wang, J. "Wearable Chemical Sensors: Emerging Systems for On-Body Analytical Chemistry." *Anal. Chem.*, **2020**, 92, 1, 378-396. DOI: https://doi.org/10.1021/acs.analchem.9b04668

95. Stetter, J.R. and Penrose W.R. "Understanding Chemical Sensors and Chemical Sensor Arrays (Electric Noses): Past, Present, and Future." *Sensor Applications*, **2002**, 10, 1, 189-229.

96. Gilchrist, A. and Nobbs, J. "Colorimetry, Theory." *Encyclopedia of Spectroscopy and Spectrometry, Third Edition*. **2017.** DOI: http://dx.doi.org/10.1016/B978-0-12-803224-4.00124-2

97. Liu, B.; Zhuang, J.; and Wei, G. "Recent advances in the design of colorimetric sensors for environmental monitoring." *Environ. Sci. Nano.*, **2020**, 7, 2195. DOI: https://doi.org/10.1039/D0EN00449A

98. Alberti, G.; Zanoni, C.; Magnaghi, L.R.; and Biesuz, R. "Disposable and Low-Cost Colorimetric Sensors for Environmental Analysis." *Int. J. Environ. Res. Public Health*, **2020**, 17, 8331. DOI: https://doi.org/10.3390/ijerph17228331

99. Davey, A.K.; Gao, X.; Xia, Y.; Li, Z.; Dods, M.N.; Delacruz, S.; Pan, A.; Swamy, S.; Gardner, D.W.; Carraro, C.; and Maboudian, R. "Amine-functionalized metal-organic framework ZIF-8 toward colorimetric CO_2 sensing in indoor air environment." *Sensors and Actuators B: Chemical*, **2021**, 130313. DOI: https://doi.org/10.1016/j.snb.2021.130313

100. Zhou, H.-C.; Long, J.R.; and Yaghi, O.M. "Introduction to Metal--Organic Frameworks." *Chem. Rev.*, **2012**, 112, 2, 674-674. DOI: https://doi.org/10.1021/cr300014x

101. Sharmin, E and Zafar, F. "Introductory Chapter: Metal Organic Frameworks (MOFs)." *Metal-Organic Frameworks*, **2016.** DOI: http://dx.doi.org/10.5772/64797

102. Varma, R.S.; Baul. A.; Wadhwa, R.; and Gulati, S. "Introduction to Metal Organic Frameworks (MOFs)." *Metal-Organic Frameworks (MOFs) as Catalysts*, **2022**. 4-29. DOI: https://doi.org/10.1007/978-981-16-7959-9_1

103. Duan, C.; Yu, Y.; Xiao, J.; Li, Y.; Yang, P.; Hu, F.; and Xi, H. "Recent advancesments in metal-organic frameworks for green applications." *Green Energy & Environment*, **2021**, 6, 1, 33-49. DOI: https://doi.org/10.1016/j.gee.2020.04.006

104. Yaghi, O.M.; Kalmutzki, M.J.; and Diercks, C.S. "Zeolitic Imidazolate Frameworks." *Introduction to Reticular Chemistry: Metal-Organic Frameworks and Covalent Organic Frameworks*, Chapter 20, **2019.** DOI: https://doi.org/10.1002/9783527821099.ch20

105. Park, K.S.; Ni, Z.; Côté, A.P.; Choi, J.Y.; Huang, R.; Uribe-Romo, F.J.; Chae, H.K.; O'Keeffe, M.; and Yaghi, O.M. "Exceptional chemical and thermal stability of zeolitic

imidazolate frameworks." *Proc. Natl. Acad Sci USA* **(2006)**; 103(27): 10186-10191. DOI: https://doi.org/10.1073/pnas.0602439103

106. Beh, J.J.; Lim, J.K.; Ng, E.P.; and Ooi, B.S. "Synthesis and size control of zeolitic imidazolate frameworks-8 (ZIF-8): From the perspective of reaction kinetics and thermodynamics of nucleation." *Materials Chemistry and Physics*, **2018**, 216, 393-401. DOI: https://doi.org/10.1016/j.matchemphys.2018.06.022

107. Lee, Y.R.; Jang, M.S.; Cho, H.Y.; Kwon, H.J.; Kim, S; Ahn W.S. "ZIF-8: A comparison of synthesis methods." *Chemical Engineering Journal.* 271, **2015,** 276-280. DOI: https://doi.org/10.1016/j.cej.2015.02.094

108. Hendon, C.H.; Rieth, A.J.; Korzynski, M.D.; and Dinca, M. "Grand Challenges and Future Opportunities for Metal--Organic Frameworks." *ACS Cent. Sci.* **2017**, 3, 554−563. DOI: https://doi.org/10.1021/acscentsci.7b00197

109. Bergaoui, M.; Khalfaoui, M.; Awadallah-F, A.; and Al-Muhtaseb, S. "A review of the features and applications of ZIF-8 and its derivatives for separating CO_2 and isomers of C_3^- and C_4^- hydrocarbons." *Journal of Natural Gas Science and Engineering*, **2021**, 96, 104289. DOI: https://doi.org/10.1016/j.jngse.2021.104289

110. Gong, X.; Wang, Y.; and Kuang, T. "ZIF-8-Based Membranes for Carbon Dioxide Capture and Separation." *ACS Sustainable Chem. Eng.*, **2017**, 5, 12, 11204-11214. DOI: https://doi.org/10.1021/acssuschemeng.7b03613

111. Perez-Pellitero, J.; Amrouche, H.; Siperstein, F.R.; Pirngruber, G.; Nieto-Draghi, C.; Chaplais, G.; Simon-Masseron, A.; Bazer-Bachi, D.; Peralta, D; and Bats, N. "Adsorption of CO_2, CH_4, and N_2 on Zeolitic Imidazolate Frameworks: Experiments and Simulations" *Chem. Eur. J.* **2010**, 16, 1560 – 1571. DOI: https://doi.org/10.1002/chem.200902144

112. Lee, Y.R.; Do, X.H.; Cho, K.Y.; Jeong, K.; and Baek, K.-Y.. "Amine-Functionalized Zeolitic Imidazolate Framework-8 (ZIF-8) Nanocrystals for Adsorption of Radioactive Iodine." *ACS Appl. Nano Mater.*, **2020**, 3, 10, 9852-9861. DOI: https://doi.org/10.1021/acsanm.0c01914

113. Zhang, H.; Shi, X.; Li, J.; Kumar, P.; and Liu, B. "Selective Dye Adsorption by Zeolitic Imidazolate Framework-8 Loaded UiO-66-NH_2." *Nanomaterials*, **2019**, 9, 9, 1283. DOI: https://doi.org/10.3390/nano9091283

114. Van der Schueren, L. and De Clerck, K. "Coloration and application of pH-sensitive dyes on textile materials." *Coloration Technology*, **2012**, 128, 2. DOI: https://doi.org/10.1111/j.1478-4408.2011.00361.x

115. "1.10: Pi Conjugation." *LibreTexts*, **2019.** Web. 18 January 2023. https://chem.libretexts.org/Courses/Purdue/Purdue%3A_Chem_26505%3A_Organic_Chemistry_I_(Lipton)/Chapter_1._Electronic_Structure_and_Chemical_Bonding/1.10%3A_Pi_Conjugation#:~:text=group.%5B4%5D-,Conjugated%20systems%20in%20pigments,in%20a%20strong%20orange%20color.

116. "A Brief Discussion on Color." *University of Massachussetts Amherst.* 1-4. Web. 18 January 2023. https://people.chem.umass.edu/samal/269/color.pdf

117. Ito, S. "Structural features of bromocresol purple and its binding sites on human serum albumin for a proton-exchange reaction." *International Journal of Pharmaceutical Chemistry,* **2016,** 6, 3.

118. Sahin, Y.; Kacus, H.; Aydogan, S.; Yilmaz, M.; and Incekara, U. "Enhanced Electrical and Optical Characteristics of Co/Phenol Red (PR)/Silicon Hybrid Heterojunction for Photodiode and Thermal Applications." *Journal of Electronic Materials*, **2020**, 49, 8. DOI: https://doi.org/10.1007/s11664-020-08217-4

119. Hamdy, L.B.; Goel, C.; Rudd, J.A.; Barron, A.R.; and Andreoli, E. "The application of amine-based materials for carbon capture and utilisation: an overarching view." *Mater. Adv.*, **2021**, 2, 5843. DOI: https://doi.org/10.1039/D1MA00360G

120. Asghar, A.; Iqbal, N.; Aftab, L.; Noor, T.; Kariuki, B.M.; Kidwell, L.; and Easun, T.L. "Ethylenediamine loading into a manganese-based metal-organic framework enhances water stability and carbon dioxide uptake of the framework." *R. Soc. open. sci.*, **2020**, 7, 191934. DOI: http://dx.doi.org/10.1098/rsos.191934

121. Ahmadijokani, F.; Tajahmadi, S.; Bahi, A.; Molavi, H.; Rezakazemi, M.; Ko, F.; Aminabhavi, T.M.; and Arjmand, M. "Ethylenediamine-functionalized Zr-based MOF for efficient removal of heavy metal ions from water." *Chemosphere*, **2021**, 264, Part 2,128466. DOI: https://doi.org/10.1016/j.chemosphere.2020.128466

122. Cravillon, J.; Munzer; S; Lohmeier, S.J.; Feldhoff, A; Huber, K; Wiebcke, M "Rapid Room-Temperature Synthesis and Characterizatin of Nanocrystals of a Prototypical Zeolitic Imidazolate Framework" *Chem. Mater.* 2009, 21, 8, 1410-1412. DOI: https://doi.org/10.1021/cm900166h

123. Davey, A.K.**;** Li, Z.; Lefton, N.; Leonhardt, B.; Pourghaderi, A.; McElhany, S.; Popple, D.; Dai, C.; Kahn, S.; Dods, M.N.; Zettl, A.; Carraro, C.; and Maboudian R. "Enhanced ZIF-8 enabled colorimetric CO_2 sensing through dye-precursor synthesis." *Sensors and Actuators B: Chemical*, **2023**, 374, 132783. DOI: https://doi.org/10.1016/j.snb.2022.132783

124. Dutrow, B.L. and Clark, C.M. "X-ray Powder Diffraction (XRD)." *Geochemical Instrumentation and Analysis.* Web. 18 January 2023. https://serc.carleton.edu/research_education/geochemsheets/techniques/XRD.html#:~:text=X%2Dray%20diffraction%20is%20based,and%20directed%20toward%20the%20sample.

125. Ameh, E.S. "A review of basic crystallography and x-ray diffraction applications." *Int. J. Adv. Manuf. Technol.*, **2019**, 105, 3289-3302. DOI: https://doi.org/10.1007/s00170-019-04508-1

126. Swapp, S. "Scanning Electron Microscopy (SEM)." *Geochemical Instrumentation and Analysis.* Web. 19 January 2023. https://serc.carleton.edu/research_education/geochemsheets/techniques/SEM.html

127. Lowell, S.; Shields, J.E.; Thomas, M.A.; and Thommes, M. *Characterization of Porous Solids and Powders: Surface Area, Pore Size and Density*. Springer, **2006**. 18-24; 59.

128. Hunt, I. "Chapter 13: Spectroscopy. Ultraviolet-Visible (uv-vis) Spectroscopy." University of Calgary. Web. 19 January 2022. https://www.chem.ucalgary.ca/courses/353/Carey5th/Ch13/ch13-uvvis.html#:~:text=Ultraviolet%2DVisible%20(uv%2Dvis)%20Spectroscopy&text=The%20lowest%20energy%20transition%20is,and%20creates%20an%20excited%20state.

129. Blitz, J.P. "Diffuse Reflectance Spectroscopy." *Modern Techniques in Applied Molecular Spectroscopy*, **1998**. Edited by Francis M. Mirabella. Techniques in Analytical Chemistry Series. John Wiley & Sons, Inc.

130. Hecht, H.G. "The Interpretation of Diffuse Reflectance Spectra." *Journal of Research of the National Bureau of Standards---A. Physics and Chemistry*, **1976**, 80A, 4. DOI: *https://doi.org/10.6028%2Fjres.080A.056*

131. "CSD Single Crystal CCDC VELVOY." *CCDC*. 602542. https://www.ccdc.cam.ac.uk/structures/search?identifier=VELVOY (accessed 2020/1/18).

132. Zhang, Y.; Jia, Y.; Li, M.; and Hou, L. "Influence of the 2-methylimidazole/zinc nitrate hexahydrate molar ratio on the synthesis of zeolitic imidazolate framework-8 crystals at room temperature." *Scientific Reports*, **2018**, 8, 9597. DOI: 10.1038/s41598-018-28015-7

133. Ding, M.; Cai, X.; and Jiang, H-L. "Improving MOF stability: approaches and applications." *Chem Sci.*,**2019**, 10, 10209. DOI: 10.1039/c9sc03916c

134. Bosch, M.; Zhang, M.; and Zhou, H-C. "Increasing the Stability of Metal-Organic Frameworks." *Advances in Chemistry*, **2014**, 182327. DOI: https://doi.org/10.1155/2014/182327

135. Ta, D.N.; Nguyen, H.K.D.; Trinh, B.X.; Le, Q.T.N.; Ta, H.N.; and Nguyen, H.T. "Preparation of Nano-ZIF-8 in Methanol with High Yield." *Can. J. Chem. Eng.* **2018**, 96, 1518-1530. DOI: https://doi.org/10.1002/cjce.23155

136. Avci, C.; Yazdi, A.; Tarres, M.; Bernoud, E.; Bastus, N.G.; Puntes, V.; Imaz, I.; Ribas, X.; Maspoch, D. "Sequential Deconstruction—Reconstruction of Metal-Organic Frameworks: An Alternative Strategy for Synthesizing (Multi)-Layered ZIF Composites." *ACS Appl. Mater. Interfaces* **2018**, 10, 23952-23960. DOI: http://dx.doi.org/10.1021/acsami.8b05098

137. Yahia, M.; Phan Le, Q.N.; Ismail, N.; Essalhi, M.; Sundman, O.; Rahimpour, A.; Dal-Cin, M.M.; ad Tavajohi, N. "Effect of incorporating different ZIF-8 crystal sizes in the polymer of intrinsic microporosity, PIM-1, for CO_2**."** *Microporous and Mesoporous Materials*, **2021**, 312, 110761. DOI: https://doi.org/10.1016/j.micromeso.2020.110761

138. Held, P. "Using Phenol Red to Assess pH in Tissue Culture Media. Using the Cytation 5 Cell Imaging Microplate Reader to Monitor Cell Culture." *Biotek*¸ **2018.** https://www.biotek.com/resources/application-notes/using-phenol-red-to-assess-ph-in-tissue-culture-media/ (accessed 2020/9/20).

139. Zhang, Z.; Xian, S.; Xia, Q.; Wang, H.; Li, Z.; Li, J. "Enhancements of CO_2 Adsorption and CO_2/N_2 Selectivity on ZIF-8 via Postsynthetic Modification" *AIChE*, **2013,** Vol. 59, No. 6, 2195-2206. DOI: 10.1002/aic.13970

140. Caplow, M. "Kinetics of Carbamate Formation and Breakdown." *J. Am. Chem. Soc.* 1968, 90, 24, 6795–6803. DOI: https://doi.org/10.1021/ja01026a041

141. Danckwerts, P.V. "The reaction of CO_2 with ethanolamines." *Chemical Engineering Science*. **1979.** Vol. 34. pp 443-446. DOI: https://doi.org/10.1016/0009-2509(79)85087-3

142. Sada, E.; Kumazawa, H.; and Han, Z.Q**. "**Kinetics of reaction between carbon dioxide and ethylenediamine in nonaqueous solvents" *Chem. Eng. J.*, **1985**, 31, 109–115. DOI: https://doi.org/10.1016/0300-9467(85)80049-6

143. Sada, E.; Kumazawa, H.; Osawa, Y; Matsuura, M; Han, Z.Q. "Reaction kinetics of carbon dioxide with amines in non-aqueous solvents" *The Chemical Engineering Journal*, **1986,** *33*, 87- 95. DOI: https://doi.org/10.1016/0300-9467(86)80038-7

144. Littel, R.J.; Versteeg, G.F.' Van Swaaij, W.P.M. "Kinetics of CO_2 with Primary and Secondary Amines in Aqueous Solutions – I. Zwitterion Deprotonation Kinetics for DEA and DIPA in Aqueous Blends of Alkanolamines." *Chemical Engineering Science*, **1992**, 47, 3, 2027-2035. DOI: https://doi.org/10.1016/0009-2509(92)80319-8

145. Couchax, G.; Barth, D.; Jacquin, M.; Faraj, A.; Grandjean, J. "Kinetics of Carbon Dioxide with Amines. I. Stopped-Flow Studies in Aqueous Solutions. A Review." *Oil & Gas Science and Technology – Rev. IFP Energies nouvelles*. **2014**. 69, 5, 865-884. DOI: https://doi.org/10.2516/ogst/2013150

146. Wesierska-Gadek, J.; Schreiner, T.; Maurer, M.; Waringer, A.; and Ranftler, C. "Phenol Red in the Culture Medium Strongly Affects the Susceptibility of Human MFC-7 Cells to Roscovitine." *Cellular & Molecular Biology Letters*, **2007**, 12, 280-293. DOI: https://doi.org/10.2478/s11658-007-0002-5

147. Gassensmith, J.J.; Furukawa, H.; Smaldone, R.A.; Forgan, R.S.; Botros, Y.Y.; Yaghi, O.M.; and Stoddart, J.F. "Strong and Reversible Binding of Carbon Dioxide in a Green Metal-Organic Framework." *J. Am. Chem. Soc.* **2011,** 133, 15312–15315. DOI: https://doi.org/10.1021/ja206525x

148. Jain H; Vargese, C. "Use of Disposable End Tidal Carbon Dioxide Detector Device for Checking Endotracheal Tube Placement." *Journal of Clinical and Diagnostic Research*, **2007**, 1, 10-16.

149. Karlsson, H.; and Svensson, H. "Rate of absorption of CO_2 absorption systems using a wetted wall column." *Energy Procedia*, **2017**, 114, 2009-2023. DOI: https://doi.org/10.1016/j.egypro.2017.03.1335

150. Moioili a, S.; Pellegrini, L.A; and Gamba, S. "Simulation of CO_2 capture by MEA scrubbing with a rate-based model." *Procedia Engineering*, **2012**, 42. 1651-1661. DOI: https://doi.org/10.1016/j.proeng.2012.07.558

151. Mebane, D.S.; Kress, J.D.; Storlie, C.B.; Fauth, D.J.; Gray, M.L.; and Li, K. "Transport, Zwitterions, and the Role of Water of CO_2 Mesoporous Silica-Supported Amine Sorbents." *J. Phys. Chem. C* **2013**. 117, 26617-26627. DOI: https://doi.org/10.1021/jp4076417

152. Ben Said, R.; Koelle, J.M.; Essalah, K.; Tangour, B.; and Sayari, A. "Unified Approach to CO_2-Amine Reaction Mechanisms." *ACS Omega*, **2020**, 5, 26125-26133. DOI: https://doi.org/10.1021/acsomega.0c03727

153. da Silva, E.F.' and Svendsen, H.F. "Ab Initio Study of the Reaction of Carbamate Formation and Alkanolamines." *Ind. Eng. Chem. Res.*, **2004**, 43, 3413-3418. DOI: https://doi.org/10.1021/ie030619k

154. Crooks, J. E.; Donnellan, J. P. "Kinetics and Mechanism of the Reaction between Carbon Dioxide and Amines in Aqueous Solution." *J. Chem. Soc.*, Perkin Trans. 2 **1989**, 44, 331–333. DOI: https://doi.org/10.1039/P29890000331

155. Vaidya, P.D.; and Kenig, E.Y. "Termolecular Kinetic Model for CO_2-Alkanolamine Reactions: An Overview." *Chem. Eng. Technol.* **2010**, 33, 10, 1577-1581. DOI: https://doi.org/10.1002/ceat.201000050

156. Xie, H-B.; Zhou, Y.; Zhang, Y.; and Johnson, J.K. "Reaction Mechanism of Monoethanolamine with CO_2 in Aqueous Solution from Molecular Modeling." *J. Phys. Chem. A.*, **2010**, 114, 11844-11852. DOI: https://doi.org/10.1021/jp107516k

157. Flaig, R.W.; Obsorn Popp, T.M.; Fracaroli, A.M.; Kapustin, E.A.; Kalmutzski, M.J.; Atamimi, R.M.; Fathieh, F.; Reimer, J.A.; and Yaghi, O.M. "The Chemistry of CO_2 Capture in an Amine-Functionalized Metal-Organic Framework under Dry and Humid Conditions." *J. Am. Chem. Soc.* **2017**, 139, 12125-12128. DOI: https://doi.org/10.1021/jacs.7b06382

158. Versteeg, G.F.; Van Dijck, L.A.J.; and Van Swaaij, W.P.M. "On the Kinetics Between CO_2 and Alkanolamines both in Aqueous and Nonaqueous Solutions. An Overview." *Chem. Eng. Comm.*, **1996**, Vol. 144, pp.113-158 DOI: https://doi.org/10.1080/00986449608936450

159. Vaidya, P.D.; and Kenig, E.Y. "CO_2-Alkanolamine Reaction Kinetics: A Review of Recent Studies." *Chem. Eng. Technol*. **2007**, 30, 11, 1467–1474. DOI: https://doi.org/10.1002/ceat.200700268

160. Aboudheir, A; Tontiwachwuthikul, P.; Chakma, A.; and Idem, R. "Novel Design for the Nozzle of a Laminar Jet Absorber." *Ind. Eng. Chem. Res*. **2004**, 43, 2568-2574. DOI: https://doi.org/10.1021/ie0341606

161. Vaidya, P.D.; and Mahajani, V.V. "Kinetics of the Reaction of CO_2 with Aqueous Formulated Solution Containing Monoethanolamine, N-Methyl-2-pyrrolidone, and Diethylene Glycol." *Ind. Eng. Chem. Res*. **2005**, 44, 1868-1873. DOI: https://doi.org/10.1021/ie049226r

162. Aboudheir, A., Tontiwachwuthikul, P., Chakma, A. and Idem, R. "Kinetics of the Reactive Absorption of Carbon Dioxide in High CO_2-Loaded, Concentrated Aqueous

Monoethanolamine Solutions." *Chemical Engineering Science*, **2003**, 58, 5195-5210. DOI: https://doi.org/10.1016/j.ces.2003.08.014

163. Zhang,H.; Snurr, R.Q. "Computational Study of Water Adsorption in the Hydrophobic Metal-Organic Framework ZIF-8: Adsorption Mechanism and Acceleration of the Simulations" *J. Phys. Chem. C* **2017**, 121, 43, 24000–24010. DOI: https://doi.org/10.1021/acs.jpcc.7b06405

164. Küsgens, P.; Rose, M.; Senkovska, I.; Fröde, H.; Henschel, A.; Siegle, S.; and Kaskel, S. "Characterization of metal-organic frameworks by water adsorption." *Microporous and Mesoporous Materials*, **2009**, 120, 325–330. DOI: https://doi.org/10.1016/j.micromeso.2008.11.020

165. Gao, M.; Wang, J.; Rong, Z.; Shi, Q.; and Dong, J. "A combined experimental-computational investigation on water adsorption in various ZIFs with the SOD and RHO topologies." *RSC Adv.*, **2018**, 8, 39627. DOI: https://doi.org/10.1039/C8RA08460B

166. Pokhrel, J.; Bhoria, N; Anastasiou, S.; Tsoufis, T.; Gournis, D.; Romanos, G; Karanikolos, G.N. "CO_2 adsorption behavior of amine-functionalized ZIF-8, graphene oxide, and ZIF-8/graphene oxide composites under dry and wet conditions" *Microporous and Mesoporous Materials* **2018**, 267. 53–67. DOI: https://doi.org/10.1016/j.micromeso.2018.03.012

167. Didas, S.A.; Kulkarni, A.R.' Sholl, D.S.; and Jones, C.W. "Role of Amine Structure on Carbon Dioxide Adsorption from Ultradilute Gas Streams such as Ambient Air." *ChemSusChem*, **2012**, 5, 2058-2064. DOI: https://doi.org/10.1002/cssc.201200196

168. Lin, C. ; Xian, X. ; Qin, X. ; Wang, D. ; Tsow, F. ; Forzani, E. ; and Tao, N. "High Performance Colorimetric Carbon Monoxide Sensor for Continuous Personal Exposure Monitoring." *ACS Sens.*, **2018**, 3, 327-333. DOI: https://doi.org/10.1021/acssensors.7b00722

169. Yu, J. ; Wang, D. ; Tipparaju., V.V. ; Tsow, F. ; and Xian, X. "Mitigation of Humidity Interference in Colorimetric Sensors." *ACS Sens.* **2021**, 6, 303-320. DOI: https://doi.org/10.1021/acssensors.0c01644

170. Liu, X.; Li, Y.; Ban, Y.; Peng, Y.; Jin, H.; Bux, H.; Xu, L.; Caro, J.; and Yang, W. "Improvement of hydrothermal stability of zeolitic imidazolate frameworks." *Chem. Commun*, **2013**, 49, 9140. DOI: https://doi.org/10.1039/C3CC45308A

171. Van Vleet, M.J.; Weng, T.; Li, X.; and Schmidt, J.R. "In Situ, Time-Resolved, and Mechanistic Studies of Metal-Organic Framework Nucleation and Growth." *Chem. Rev.*, **2018**, 118, 3681-3721. DOI: http://dx.doi.org/10.1021/acs.chemrev.7b00582

172. Carpenter, B.P.; Talosig, A.R.; Mulvey, J.T.; Merham, J.G.; Esquivel, J.; Rose, B.; Ogata, A.F.; Fishman, D.A.; Patterson, J.P. *Chem. Mater.*, **2022**, 34, 18, 8336-8344. DOI: https://doi.org/10.1021/acs.chemmater.2c01903

173. Mazlan, N.A.; Butt, F.S.; Lewis, A.; Yang, Y.; Yang, S.; and Huang, Y. "The Growth of Metal-Organic Frameworks in the Presence of Graphene Oxide: A Review." *Membranes*, **2022**, 12, 5, 501. DOI: https://doi.org/10.3390/membranes12050501

174. Escalante Sierra, C.F. "Fundamentals of transmission electron microscopy, the technique with the best resolution in the world." *Transmission electron microscopy*, **2019**, 1-6. https://www.researchgate.net/publication/330999184_Fundamentals_of_transmission_electron_microscopy_the_technique_with_the_best_resolution_in_the_world

175. Michler, G.H. *Electron Microscopy of Polymers*, **2008**, 17-18.

176. "5.5: The Harmonic Oscillator and Infrared Spectra." LibreTexts, **2020**. Web. 21 January 2023. https://chem.libretexts.org/Courses/Pacific_Union_College/Quantum_Chemistry/05%3A_The_Harmonic_Oscillator_and_the_Rigid_Rotor/5.05%3A_The_Harmonic_Oscillator_and_Infrared_Spectra

177. "Acetone: The National Institute for Occupational Safety and Health (NIOSH)." *CDC*. U.S. Department of Health & Human Services. https://www.cdc.gov/niosh/npg/npgd0004.html (accessed 2022/18/3).

178. "Ethyl alcohol: The National Institute for Occupational Safety and Health (NIOSH)." *CDC*. U.S. Department of Health & Human Services. https://www.cdc.gov/niosh/npg/npgd0262.html (accessed 2022/18/3).

179. Zhang, Y.; Jia, Y.; and Hou, L. "Synthesis of zeolitic imidazolate framework-8 on polyester fiber for $PM_{2.5}$ removal." *RSC. Adv.*, **2018**, 8, 31471-31477. DOI: https://doi.org/10.1039/C8RA06414H

180. Zhang, C.; Han, C.; Sholl, D.S.; and Schmidt, J.R. "Computational Characterization of Defects in Metal-Organic Frameworks: Spontaneous and Water-Induced Point Defects in ZIF-8." *J Phys. Chem. Lett.*, **2016**, 7, 3, 459-464. DOI: https://doi.org/10.1021/acs.jpclett.5b02683

181. Liu, X.; Kozlowska, M.; Okkali, T.; Wagner, D.; Higashino, T.; Brenner-Weiß; Marschner, S.M.; Fu, Z.; Zhang, Q.; Imahori, H.; Brase, S.; Wenzel, W.; Wçll, C.; and Heinke, L. "Photoconductivity in Metal-Organic Framework (MOF) Thin Films." *Angew. Chem. Int. Ed.* **2019**, 58, 9590 –9595. DOI: https://doi.org/10.1002/anie.201904475

182. Yi, F-Y; Wang, Y.; Li, J-P; Wu, D.; Lan, Y-Q; and Sun, Z-M. "An ultrastable porous metal-organic framework switch towards aromatic compounds." *Mater. Horiz*, **2015**, 2, 245. DOI: https://doi.org/10.1039/C4MH00210E

183. Zhong, M.; Kong, L.; Zhao, K.; Zhang, Y-H; Li, N.; and Bu, X-H. "Recent Progress of Nanoscale Metal-Organic Frameworks in Synthesis and Battery Applications." *Adv. Sci.*, **2021**, 8, 2001980. DOI: https://doi.org/10.1002/advs.202001980

184. Shahrak, M.N.; Gharamaninezhad, M.; and Eydifarash, M. "Zeolitic imidazolate framework-8 for efficient adsorption and removal of Cr(VI) ions from aqueous solution." *Environ. Sci. Pollut. Res.*, **2017**, 24, 9624-9634. DOI: https://doi.org/10.1007/s11356-017-8577-5

185. Kaur, H.; Mohanta, G.C.; Gupta, V.; Kukkar, D.; and Tyagi, S. "Synthesis and characterization of ZIF-8 nanoparticles for controlled release of 6-mercaptopurine drug."

Journal of Drug Delivery Science and Technology, **2017**, 41, 106-112. DOI: http://dx.doi.org/10.1016/j.jddst.2017.07.004

186. Web reference six. "Spectroscopy Tutorial: Reference. Table of Characteristic IR Absorptions." http://www.orgchemboulder.com/Spectroscopy/specttutor/irchart.shtml. (accessed 21/1/2022).

187. Web reference seven. "24.10: Spectroscopy of Amines." *Chemistry LibreTexts*^{tM}, **2021**. https://chem.libretexts.org/Bookshelves/Organic_Chemistry/Organic_Chemistry_(McMurry)/24%3A_Amines_and_Heterocycles/24.10%3A_Spectroscopy_of_Amines. (accessed 21/1/2022).

188. Bunzen, H. "Chemical Stability of Metal-Organic Frameworks for Applications in Drug Delivery." *ChemNanoMat*, **2021**, 998-1007. DOI: https://doi.org/10.1002/cnma.202100226

189. Wickenhisser, M.; Jeremias, F.; Henninger, S.K.; and Janiak, C. "Grafting of hydrophilic ethylene glycols or ethylenediamine on coordinatively unsaturated metal sites in MIL-100(Cr) for improved water adsorption characteristics." *Inorganica Chimica Acta*, **2013**, 407, 145-152. DOI: https://doi.org/10.1016/j.ica.2013.07.024

190. Siefker, Z.A.; Hodul, J.N.; Zhao, X.; Bajaj, N.; Brayton, K.M.; Flores-Hansen, C.; Zhao, W.; Chiu, G.T.-C.; Braun, J.E.; Rhoads, J.F.; and Boudouris, B.W. "Manipulating polymer composition to create low-cost, high-fidelity sensors for indoor CO_2 monitoring." *Sci. Rep.*, **2021**, 11, 13237. DOI: https://doi.org/10.1038/s41598-021-92181-4

191. Sun, Y.; Li, Y.; and Tan, J-C. "Framework flexibility of ZIF-8 under liquid intrusion: discovering time-dependent response and structural relaxation." *Phys. Chem. Chem. Phys.*, **2018**, 20, 10108. DOI: https://doi.org/10.1039/C8CP00447A

192. Fairen-Jimenez, D.; Moggach, S.A.; Wharmby, M.T.; Wright, P.A.; Parsons, S.; and Duren, T. "Opening the Gate: Framework Flexibility in ZIF-8 Explored by Experiments and Simulations." *J. Am. Chem. Soc.*, **2011**, 133, 23, 8900–8902. DOI: https://doi.org/10.1021/ja202154j

193. Zhang, K.; Lively, R.P.; Zhang, C.; Chance, R.R.; Koros, W.J.; Shol,, D.S.; and Nair, S. "Exploring the Framework Hydrophobicity and Flexibility of ZIF-8: From Biofuel Recovery to Hydrocarbon Separations." . *J. Phys. Chem. Lett.*, **2013**, 4, 21, 3618–3622. DOI: https://doi.org/10.1021/jz402019d

194. Hu, Y.; Liu, Z.; Xu, J.; Huang, Y.; and Song, Y. "Evidence of Pressure Enhanced CO_2 Storage in ZIF-8 Probed by FTIR Spectroscopy." *J. Am. Chem. Soc.*, **2013**, 135, 9287-9290. DOI: https://doi.org/10.1021/ja403635b

195. Khan, M.S.; Khalid, M.; and Shahid, M. "What triggers dye adsorption by metal organic frameworks? The current perspectives." *Mater. Adv.*, **2020**, 1, 1575. DOI: https://doi.org/10.1039/D0MA00291G

196. Ka-Man-Au, V. "Recent Advances in the Use of Metal-Organic Frameworks for Dye Adsorption." *Front. Chem.*, **2020**, 8, 708. DOI: https://doi.org/10.3389/fchem.2020.00708

197. Nanthamathee, C.; and Dechatiwongse, P. "Kinetic and thermodynamic studies of neutral dye removal from water using zirconium metal-organic framework analogues." *Material Chemistry and Physics*, **2021**, 258, 123924. DOI: https://doi.org/10.1016/j.matchemphys.2020.123924

198. Feng, Y.; Li, Y.; Xu, M.; Liu, S.; and Yao, J. "Fast adsorption of methyl blue on zeolitic imidazolate framework-8 and its adsorption mechanism." *RSC Adv.*, **2016**, 6, 109608. DOI: https://doi.org/10.1039/C6RA23870J

199. Van Cleuvenbergen, S.V.; Smith, Z.J.; Deschaume, O.; Bartic, C.; Waschmann-Hogiu, S.; Verbiest, T.; and van der Veen, M.A. "Morphology and structure of ZIF-8 during crystallization measured by dynamic angle-resolved second harmonic scattering." *Nature Communications*, **2018**, 9, 3418. DOI: https://doi.org/10.1038/s41467-018-05713-

200. Cole, W.T.S.; Wei, H.; Nguyen, S.C.; Harris, C.B.; Miller, D.J.; and Saykally, R.J. "Dynamics of Micropollutant Adsorption to Polystyrene Surfaces Probed by Angle-Resolved Second Harmonic Scattering." *The Journal of Physical Chemistry C*, **2019**, 123, 23, 14362-14369. DOI: https://doi.org/10.1021/acs.jpcc.9b01146

201. Campen, R.K.; Zheng, D-s; Wang, H-f; and Borguet, E. "Second Harmonic Generation as a Probe of Multisite Adsorption at Solid-Liquid Interfaces of Aqueous Colloid Suspensions." *J. Phys. Chem. C*, **2007**, 111, 25, 8805–8813. DOI: https://doi.org/10.1021/jp061730h

202. de Beer, A.G.F.; and Roke, S. "Obtaining molecular orientation from second harmonic and sum frequency scattering experiments in water: Angular distribution and polarization dependence." *The Journal of Chemical Physics*, **2010**, 132, 234702. DOI: https://doi.org/10.1063/1.3429969

203. Lewis, T.; Faubel, M.; Winter, B.; and Hemminger, J.C. "CO_2 Capture in Amine-Based Aqueous Solution: Role of the Gas-Solution Interface." *Angew. Chem. Int. Ed.* **2011**, 50, 10178 –10181. DOI: 10.1002/anie.201101250

204. Hadjivanov, K.I.; Panayotov, D.A.; Mihaylov, M.Y.; Ivanova, E.Z.; Chakarova, K.K.; Andonova, S.M.; and Drenchev, N.L. "Power of Infrared and Raman Spectroscopies to Characterize Metal-Organic Frameworks and Investigate Their Interactions with Guest Molecules." *Chem. Rev.*, **2021**, 121, 1286-1424. DOI: 10.1021/acs.chemrev.0c00487

205. Uba Zango, Z.; Jumbri, K.; Soraya Samdbudi, N.; Ramli, A.; Abu Bakar, N.H.H.; Saad, B.; Rozaini, M.N.H.; Isiyaka, H.A.; Jagaba, A.H.; Aldaghri, O.; and Sulieman, A. "A Critical Review on Metal-Organic Frameworks and Their Composites as Advanced Materials for Adsorption and Photocatalytic Degradation of Emerging Organic Pollutants from Wastewater." *Polymers*, **2020**, 12, 2648. DOI: https://doi.org/10.3390/polym12112648

206. Sriram, G.; Bendre, A.; Mariappan, E.; Altalhi, T.; Kigga, M.; Ching, Y.C.; Jung, H-Y; Bhaduri, B.; and Kurkuri, M. "Recent trends in the application of metal-organic frameworks (MOFs) for the removal of toxic dyes and their removal mechanism - a review."

Sustainaable Materials and Technologies, **2022**, e00378. DOI: https://doi.org/10.1016/j.susmat.2021.e00378

207. Noor, T.; Raffi, U.; Iqbal, N. Yaqoob, L.; and Zaman, N. "Kinetic evaluation and comparative study of cationic and anionic dyes adsorption on Zeolitic imidazolate frameworks based metal organic frameworks." *Mater. Res. Express*, **2019**, 6, 125088. DOI: https://doi.org/10.1088/2053-1591/ab5bdf

208. Zhang, J.; Li, F.; and Sun, Q. "Rapid and selective adsorption of cationic dyes by a unique metal-organic framework with decorated pore surface." *Applied Surface Science*, **2018**, 440, 1219-1226. DOI: https://doi.org/10.1016/j.apsusc.2018.01.258

209. .Thompson, M. "CHNS Elemental Analysers." *The Royal Society of Chemistry*, **2008**, Analytical Methods Committee, AMCTB No 29. Web. 28 January 2023. https://www.rsc.org/images/CHNS-elemental-analysers-technical-brief-29_tcm18-214833.pdf

210. "Infrared Spectroscopy Absorption Table." *LibreTexts Chemistry*, **2020**. Web. 14 February 2023. https://chem.libretexts.org/Ancillary_Materials/Reference/Reference_Tables/Spectroscopic_Reference_Tables/Infrared_Spectroscopy_Absorption_Table

211. Roztocki, K.; Rauche, M.; Bon, V.; Kaskel, S.; Brunner, E.; and Matoga, D. " Combining In Situ Techniques (XRD, IR, and 13C NMR) and Gas Adsorption Measurements Reveals CO2-Induced Structural Transitions and High CO2/CH4 Selectivity for a Flexible Metal−Organic Framework JUK-8." *ACS Appl. Mater. Interfaces,* **2021**, 13, 28503-28513. DOI: https://doi.org/10.1021/acsami.1c07268?rel=cite-as&ref=PDF&jav=VoR

212. Sun, C. and Dutta, P.K. "Infrared Spectroscopic Study of Reaction of Carbon Dioxide with Aqueous Monoethanolamine Solutions." *Ind. Eng. Chem. Res*. **2016**, 55, 6276−6283. DOI: http://dx.doi.org/10.1021/acs.iecr.6b00017

213. McDonald, T.M.; D'Alessandro, D.M.; Krishna, R.; and Long, J.R. " Enhanced carbon dioxide capture upon incorporation of N,N0 -dimethylethylenediamine in the metal–organic framework CuBTTri." *Chem. Sci.*, **2011**, 2, 2022-2028. DOI: https://doi.org/10.1039/C1SC00354B

214. Merger, Y.; Rumley-van Gurp, R.; Brasser, P.; de Koning, M.; and Goetheer, E. " Solvents for CO_2 capture. Structure-activity relationships combined with Vapour-Liquid-Equilibrium measurements." *Energy Procedia*, **2011**, 4, 259–266 10.1039/C1SC00354B

215. Isokoski, K.; Poteet, C.A.; and Linnartz, H. " Highly resolved infrared spectra of pure CO2 ice (15–75 K)." A&A 555, A85, **2013**. DOI: http://dx.doi.org/10.1051/0004-6361/201321517

References

216. Boyd, R.W. *Nonlinear Optics: Third Edition.* Academic Press, **2008**, pp. 1-6.

217. Eisenthal, K.B. "Second Harmonic Spectroscopy of Aqueous Nano- and Microparticle Interfaces." *Chem. Rev.*, **2006**, 106, 1462-1477. DOI: https://doi.org/10.1021/cr0403685

218. Roke, S. and Gonella, G. "Nonlinear Light Scattering and Spectroscopy of Particles and Droplets in Liquids." *Annu. Rev. Phys. Chem.*, **2012**, 63, 353-378. DOI: 10.1146/annurev-physchem-032511-14374

219. Hofmann, S. *Auger- and X-Ray Photoelectron Spectroscopy in Materials Science: A User-Oriented Guide.* Springer Series in Surface Sciences, *49*, **2013**. pp. 5, 11, 13, 22-23, 29, 43-45, 48-49, 297, 398-399

220. Naumkin, A.V.; Kraut-Vass, A.; Gaarenstroom, S.W.; and Powell, C.J. "NIST X-ray Photoelectron Spectroscopy Database." DOI: http://dx.doi.org/10.18434/T4T88K

221. Karabiberoglu, S. and Dursun, Z. "Over-Oxidized Poly (Phenol Red) Film Modified Glassy Carbon Electrode for Anodic Stripping Voltammetric Determination of Ultra-Trace Antimony (III)." *Electroanalysis*, **2017**, 29, 1069 – 1080 10. DOI: http://dx.doi.org/10.1002/elan.201600629

222 Al-Kandari, H.; Kasak, P.; and Mohamed, A.M.; Al-Kandari, S.; Chorvat, Jr., D.; and Abdullah, A.M. "Toward an Accurate Spectrophotometric Evaluation of the Efficiencies of Photocatalysts in Processes Involving Their Separation Using Nylon Membranes." *Catalysts* **2018**, 8, 12, 576. DOI: https://doi.org/10.3390/catal8120576

223 Feng, S.; Jia, X.; Yang, J.; Li, Y.; Wang, S.; and Song, H. "One-pot synthesis of core-shell ZIF-8@ZnO porous nanospheres with improved ethanol gas sensing." *Journal of Materials Science: Materials in Electronics*, **2020**, 31, 22534-22545. DOI: https://doi.org/10.1007/s10854-020-04764-y

224 Luanwuthi, S.; Krittayavathananon, A.; Srimuk, P.; and Sawangphruk, M. "*In situ* synthesis of permselective zeolitic imidazolate framework-8/graphene oxide composites: rotating disk electrode and Langmuir adsorption isotherm." *RSC Adv.*, **2015**, 5, 46617.

References

225 Pan, D.; Wang, L.; Li, Z.; Geng, B.; Zhang, C.; Zhan, J.; Yin, L.; and Wang, L. "Synthesis of graphene quantum dot/metal-organic framework nanocomposites as yellow phosphorsfor white light-emitting diodes." *New J. Chem.*, **2018**, 42, 5083. DOI: https://doi.org/10.1039/C7NJ04909A

226. Ebrahim, A.M.; Plonka, A.M.; Rui, N.; Hwang, S.; Gordon, W.O.; Balboa, A.; Senanayake, S.D.; and Frenkel, A.I. "Capture and Decomposition of the Nerve Agent Simulant, DMCP, Using the Zeolitic Imidazolate Framework (ZIF-8)." *ACS Appl. Mater. Interfaces* **2020**, 12, 52, 58326–58338. DOI: https://doi.org/10.1021/acsami.0c12985

227. Liu, J.; He, J.; Wang, L.; Li, R.; Chen, P.; Rao, X.; Deng, L.; Rong, L.; and Lei, J. "NiO-PTA supported on ZIF-8 as a highly effective catalyst for hydrocracking of Jatropha oil." *Scientific Reports*, **2016**, 6, 23667. DOI: https://doi.org/10.1038/srep23667

228 Papurello, R.L.; Lozano, L.A.; Ramos-Fernandez, E.V.; Fernandez, J.L.; Zamaro, J.M. "Post-Synthetic Modification of ZIF-8 Crystals and Films through UV Light Photoirradiation: Impact on the Physicochemical Behavior of the MOF." *ChemPhysChem*, **2019**, 20, 23, 3201-3209. DOI: https://doi.org/10.1002/cphc.201900863

229 Dangwal, S.; Ronte, A.; Lin, H.; Liu, R.; Zhu, J.; Lee, J-S.; Gappa-Fahlenkamp, H.; and Kim, S-J. "ZIF-8 membranes supported on silicalite-seeded substrates for propylene/propane separation." *Journal of Membrane Science*, **2021**, 626, 119165. DOI: https://doi.org/10.1016/j.memsci.2021.119165

230. Chakraborty, T.; Das, M.; Lin, C-Y.; Su, Y.; Yuan, B.; and Kao, C-H. "ZIF-8 Nanoparticles Based Electrochemical Sensor for Non-Enzymatic Creatinine Detection." *Membranes*, **2022**, 12, 159. DOI: https://doi.org/10.3390/membranes12020159

231 Huo, S-H. and Yan, X-P. "Metal-organic framework MIL-100(Fe) for the adsorption of malachite green from aqueous solution." *J. mater. Chem.*, **2012**, 22, 7449. DOI: https://doi.org/10.1039/C2JM16513A

232 Jun, B-M.; Heo, J.; Taheri-Qazvini, N.; Park, C.M.; and Yoon, Y. "Adsorption of selected dyes on $Ti_3C_2T_X$ MXene and Al-based metal-organic framework." *Ceramics International*, **2020**, 46, 2960-2968. DOI: https://doi.org/10.1016/j.ceramint.2019.09.293

233 Yu, J.; Tsow, Mora, S.J.; Tipparaju, V.V.; and Xian, X. "Hydrogel-incorporated colorimetric sensors with high humidity tolerance for environmental gases sensing." *Sensors & Actuators B: Chemical*, **2021**, 345, 130404. DOI: https://doi.org/10.1016/j.snb.2021.130404

234 Khoo, H.E.; Azlan, A.; Teng Tang, S.; and Lim, S. M. "Anthocyanidins and anthocyanins: colored pigments as food, pharmaceutical ingredients, and the potential health benefits." *Food & Nutrition Research*, **2017**, 61, 1361779. DOI: https://doi.org/10.1080/16546628.2017.1361779

235 Roy, S. and Rhim, J.-W. "Anthocyanin food colorant and its application in pH-responsive color change indicator films." *Critical Reviews in Food Science and Nutrition*, **2021**, 61, 14, 2297-2235. DOI: https://doi.org/10.1080/10408398.2020.1776211

236 Xie, L.S.; Skorupskii, G.; and Dinca, M. "Electrically Conductive Metal-Organic Frameworks." *Chem. Rev.*, **2020**, 120, 8536-8580. DOI: https://dx.doi.org/10.1021/acs.chemrev.9b00766?ref=pdf